

# **Wide band gap materials and devices for NO<sub>x</sub>, H<sub>2</sub> and O<sub>2</sub> gas sensing applications**

Dissertation zur Erlangung des  
akademischen Grades Doktor-Ingenieur (Dr.-Ing.)

vorgelegt der Fakultät Elektrotechnik und  
Informationstechnik der Technischen Universität Ilmenau

von Dipl.-Ing Majdeddin Ali  
geboren am 08.09.1976 in Homs, Syrien

1. Gutachter: Univ.-Prof. Dr. rer. nat. habil. Oliver Ambacher, Fraunhofer-Institut für Angewandte Festkörperphysik, Freiburg
2. Gutachter: PD Dr.-Ing. habil. Frank Schwierz, TU Ilmenau
3. Gutachter: Dr. Martin Eickhoff, Walter Schottky Institut, TU München

Tag der Einreichung: 28.06.2007

Tag der wissenschaftlichen Aussprache: 22.01.2008

## Abstract

In this thesis, field effect gas sensors (Schottky diodes, MOS capacitors, and MOSFET transistors) based on wide band gap semiconductors like silicon carbide (SiC) and gallium nitride (GaN), as well as resistive gas sensors based on indium oxide ( $\text{In}_2\text{O}_3$ ), have been developed for the detection of reducing gases ( $\text{H}_2$ ,  $\text{D}_2$ ) and oxidising gases ( $\text{NO}_x$ ,  $\text{O}_2$ ). The development of the sensors has been performed at the Institute for Micro- and Nanoelectronic, Technical University Ilmenau in co-operation with (GE) General Electric Global Research (USA) and Umwelt-Sensor-Technik GmbH (Geschwenda).

**Chapter 1:** serves as an introduction into the scientific fields related to this work. The theoretical fundamentals of solid-state gas sensors are provided and the relevant properties of wide band gap materials (SiC and GaN) are summarized.

In **chapter 2:** The performance of Pt/GaN Schottky diodes with different thickness of the catalytic metal were investigated as hydrogen gas detectors. The area as well as the thickness of the Pt were varied between  $250 \times 250 \mu\text{m}^2$  and  $1000 \times 1000 \mu\text{m}^2$ , 8 and 40 nm, respectively. The response to hydrogen gas was investigated in dependence on the active area, the Pt thickness and the operating temperature for 1 vol.% hydrogen in synthetic air. We observed a significant increase of the sensitivity and a decrease of the response and recovery times by increasing the temperature of operation to about  $350^\circ\text{C}$  and by decreasing the Pt thickness down to 8 nm. Electron microscopy of the microstructure showed that the thinner platinum had a higher grain boundary density. The increase in sensitivity with decreasing Pt thickness points to the dissociation of molecular hydrogen on the surface, the diffusion of atomic hydrogen along the platinum grain boundaries and the adsorption of hydrogen at the Pt/GaN interface as a possible mechanism of sensing hydrogen by Schottky diodes.

The response to deuterium  $\text{D}_2$ ,  $\text{NO}_x$ , and  $\text{O}_2$  of metal-oxide-semiconductor (MOS) and metal-metal oxide-oxide-semiconductor (MMOOS) structures with rhodium (Rh) gate were investigated in dependence on the operating temperature and gas partial pressures was investigated in **chapter 3**. The response of the sensor was measured as a shift in the capacitance-voltage (C-V) curve along the voltage axis. Positive and negative flat-band voltage shifts up to 1 V were observed for oxidizing and reducing gases, respectively. Depending on the type of insulator that is chosen, differences in the sensitivity of the sensor were observed.

In **chapter 4**: The performance of SiC-based field effect transistors (FETs) with different gate materials (mixture of metal oxides: indium oxide and tin oxide ( $\text{In}_x\text{Sn}_y\text{O}_z$ ), indium oxide and vanadium oxide ( $\text{In}_x\text{V}_y\text{O}_z$ ), as well as mixtures of metal oxides with metal additives) were investigated as  $\text{NO}_x$ ,  $\text{O}_2$ , and  $\text{D}_2$  gas detectors. The response to these gases was investigated in dependence on the operating temperature and gas partial pressures. The composition and microstructure of the sensing gate electrode are the key parameters that influence the sensing mechanism, and hence key performance parameters: sensitivity, selectivity, and response time. By choosing the appropriate temperature and catalyst material (gate material), devices that are significantly sensitive to certain gases may be realized. In addition, the temperature of maximum response varies dependent on the gas species being measured. This information, along with a careful choice of catalyst (gate material) can be used to enhance device selectivity.

In **chapter 5**: Polycrystalline and nano-structured  $\text{In}_2\text{O}_3$  thin films were investigated with the aim to obtain information about their  $\text{NO}_x$  and  $\text{O}_2$  gas sensing properties. The response to these gases was investigated in dependence on the operating temperature and gas partial pressures. The analysis in the presence of different partial pressures of  $\text{NO}_x$  has shown that both thin films are able to detect nitrogen oxide, but their responses exhibit different characteristics. In particular, nano-structured  $\text{In}_2\text{O}_3$  thin films were found to have the higher response to  $\text{NO}_x$ . This is most probably due to the enlarged overall active surface area of the sensing layer as a consequence of the small grain size (higher surface to volume ratio) so that the relative interactive surface area is larger, and the density of charged carriers per volume is higher. We have found that reducing the grain size of the sensing material to the  $\sim 10$  nm regime can have a substantial effect on performance. The optimum detection temperatures of the nano-structured  $\text{In}_2\text{O}_3$  occur in the range of  $100\text{-}175^\circ\text{C}$  for  $\text{NO}_x$  considering the sensitivity as well as the response time. In this range of temperatures the response to  $\text{O}_2$  is very low indicating that the sensor is very suitable for selective detection of  $\text{NO}_x$  at low temperatures. In addition, nano-structured  $\text{In}_2\text{O}_3$  thin films were found to be more suitable to be used in the field of application for detecting low partial pressures.

**Chapter 6**: offers conclusions of the current work. In this chapter we compare also all studied gas sensors according to their sensitivity, selectivity, and response

time and then we compare them with the related works by other authors available in the scientific literature.



## Zusammenfassung

Im Rahmen dieser Arbeit sind Feldeffektgassensoren (Schottky Dioden, MOS Kapazitäten, und MOSFET Transistoren) auf der Basis von Halbleitern mit großer Bandlücke (Siliziumkarbid (SiC) und Gallium Nitrid (GaN), sowie resistive Gassensoren, die auf aktiven Indiumoxid-Schichten ( $\text{In}_2\text{O}_3$ ) basieren, für die Detektion von reduzierenden Gasen ( $\text{H}_2$ ,  $\text{D}_2$ ) und oxidierenden Gasen ( $\text{NO}_x$ ,  $\text{O}_2$ ), entwickelt worden. Die Entwicklung der Sensoren ist am Institut für Mikro- und Nanoelektronik der Technischen Universität Ilmenau in Zusammenarbeit mit General Electric (GE) Global Research (USA) und der Umwelt- und Sensortechnik GmbH (Geschwenda) durchgeführt worden.

**Kapitel 1:** dient als eine Einführung in das mit dieser Arbeit verbundene wissenschaftliche Feld. Die theoretischen Grundlagen der Festkörper-Gassensoren werden dargestellt. Zusätzlich werden in diesem Kapitel die relevanten Eigenschaften der Materialien mit großer Bandlücke (SiC und GaN) präsentiert.

**Kapitel 2:** Pt/GaN Schottky Dioden mit verschiedener Dicke des katalytischen Metalls werden als Wasserstoffgasdetektoren vorgestellt. Die Fläche sowie die Dicke von Pt-gates wurden zwischen  $250 \times 250 \mu\text{m}^2$  und  $1000 \times 1000 \mu\text{m}^2$ , 8 und 40 nm, systematisch variiert. Die Sensorantwort (Sensorsreaktion) auf 1 vol.% Wasserstoff in synthetischer Luft wurde in Abhängigkeit von der aktiven Fläche, der Pt-Dicke, und der Betriebstemperatur untersucht. Durch Anheben der Betriebstemperatur auf ca.  $350^\circ\text{C}$  und durch Reduzierung der Dicke des Pt auf 8 nm beobachteten wir eine beträchtliche Erhöhung der Empfindlichkeit sowie eine Verkürzung der Ansprech- und Erholzeiten. Untersuchungen am Elektronenmikroskop zeigten, dass das dünnere Platin eine höhere Korngrenzendichte aufwies. Die Erhöhung der Empfindlichkeit gemeinsam mit der Reduzierung der Dicke des Pt deuten auf die Dissoziation von molekularem Wasserstoff an der Oberfläche, die Diffusion atomaren Wasserstoffs entlang der Korngrenzen des Platins und die Adsorption von Wasserstoff an der Pt/GaN Grenzfläche als ein möglicher Mechanismus der Detektion von Wasserstoff durch Schottky Dioden hin.

Die Reaktion auf  $\text{D}_2$ ,  $\text{NO}_x$ , and  $\text{O}_2$  von Metall-Oxid-Halbleiter (MOS) Strukturen mit Rhodium Schottky-Kontakten mit einer Dicke von 30 nm in Abhängigkeit von der Betriebstemperatur und der Gaspartialdrücke wurde in **Kapitel 3** untersucht. Die Reaktion dieses Gates wurde als Verschiebung entlang der Spannungsachse in der Kapazität-Spannungs Kurve (C-V) nachgewiesen. Positive und negative Flachband-

Verschiebungen jeweils bis zu 1 V wurden für oxidierende und reduzierende Gase beobachtet. Abhängig vom gewählten Typ des Isolators wurden Unterschiede in den Empfindlichkeiten beobachtet.

In **Kapitel 4:** SiC-basierten FETs mit verschiedenen Materialien für das Gate (Gemisch aus Metalloxiden: Indiumoxide und Zinnoxid ( $\text{In}_x\text{Sn}_y\text{O}_z$ ), Indiumoxid und Vanadiumoxid ( $\text{In}_x\text{V}_y\text{O}_z$ ) sowie ein Gemisch aus Metalloxiden mit Zugabe einer entsprechenden Menge Metallzusätzen) wurden als  $\text{NO}_x$ ,  $\text{O}_2$ , und  $\text{D}_2$  Gasdetektoren untersucht. Die Reaktion auf diese Gase wurde in Abhängigkeit von der Betriebstemperatur und der Gaspartialdrücke untersucht. Die Zusammensetzung der aktiven Metalloxid-Schicht und die Mikrostruktur der sensitiven Gateelektrode sind die entscheidenden Parameter mit Einfluss auf den Messmechanismus und somit die entscheidenden Leistungsparameter des Sensors: Empfindlichkeit, Selektivität und Reaktionszeit. Durch die Optimierung der Temperatur und des richtigen Materials des Katalysators können Sensoren mit sehr hoher Empfindlichkeit gegenüber relevanten Gasen realisiert werden. Wird auch der Katalysator sorgfältig ausgewählt, können diese Erkenntnisse für eine Erhöhung der Selektivität des Sensors genutzt werden.

In **Kapitel 5:** Polykristalle von 200 nm Dicke und 10 nm nanostrukturierten Dünnschichten aus  $\text{In}_2\text{O}_3$ , die durch MOCVD (metallorganische Gasphasenabscheidung) gewachsen sind, wurden untersucht, um Informationen über ihre Eigenschaften hinsichtlich der Detektion von  $\text{NO}_x$ - and  $\text{O}_2$ -Gasen zu erhalten. Die Reaktion auf diese Gase wurde in Abhängigkeit von der Betriebstemperatur und der Gaspartialdrücke untersucht. Die Experimente in Anwesenheit verschiedener Partialdrücke des  $\text{NO}_x$  haben gezeigt, dass beide Dünnschichten in der Lage sind, Stickoxide zu detektieren. Es wurde festgestellt, dass besonders die nanostrukturierte  $\text{In}_2\text{O}_3$ -Dünnschicht stärker auf  $\text{NO}_x$  reagiert. Dieser Effekt wird durch das hohe Oberflächen-zu-Volumenverhältnis infolge der niedrigen Korngröße verbessert, so dass der relative interaktive Oberflächenbereich größer und die Dichte der Ladungsträger höher ist. Wir haben ermittelt, dass die Reduzierung der Korngröße des messenden Materials auf unter 10 nm erhebliche Auswirkung auf die Empfindlichkeit des Sensors hat. Die hinsichtlich der Empfindlichkeit und Reaktion optimalen Temperaturen des nanostrukturierten  $\text{In}_2\text{O}_3$  für den Nachweis von  $\text{NO}_x$  treten im Bereich von 100-175°C auf. In diesem Temperaturbereich ist die Reaktion auf  $\text{O}_2$  sehr schwach, was darauf hinweist, dass

der Sensor für die selektive Erkennung von  $\text{NO}_x$  bei niedrigen Temperaturen sehr gut geeignet ist. Zudem wurde festgestellt, dass die nanostrukturierte  $\text{In}_2\text{O}_3$ -Dünnschicht für den Einsatz in der Erkennung niedriger Partialdrücke die optimale ist.

**Kapitel 6** enthält Schlussfolgerungen aus den gegenwärtigen Arbeiten. In diesem Kapitel vergleichen wir alle untersuchten Gassensoren in Bezug auf deren Empfindlichkeit, Selektivität und Reaktionszeit und stellen diese anschließend den entsprechenden Ergebnissen anderer, in der wissenschaftlichen Literatur zu findenden Autoren gegenüber.





## Acknowledgement

The research for this thesis was carried out at the Laboratory of the Institute for Micro- and Nanoelectronic, Department of Nanotechnology at the Technical University Ilmenau during the years 2003-2007, under the supervision of Prof. Dr. rer. nat. Dr. habil. Oliver Ambacher and Dr.-Ing. Volker Cimalla.

First of all, I would like to thank my two supervisors Prof. Oliver Ambacher and Dr.-Ing. Volker Cimalla for the invaluable help and advice and their continuous guidance those I have received during this work.

I am thankful to Dr.-Ing. Gernot Ecke for AES measurements. To Dr.-Ing. Thomas Stauden for his technical assistance during the gas sensing measurements. Dr.-Ing. Henry Romanus from the Department of Werkstoffe der Elektrotechnik is thanked for the SEM measurements.

I would like to express my deep thankfulness to all members of the Nanotechnology group for fruitful collaboration especially, Dr. Vadim Lebedev, Dr. Jörg Pezold, Dipl.-Ing. Gabriel Kittler, Dipl.-Ing. Chunyu Wang, Dipl.-Ing. Benedikt Lübbers, Dipl.-Ing. Claus-Christian Röhlig, Dipl.-Ing. Merten Niebelschütz, Dipl.-Ing. Ulrich Liebold, Ms. Silvia Probst, Ms. Ilona Marquardt, and Dr.-Ing. Christian Förster.

I also want to give my thanks to Dr. Peter Sandvik, and Dr. Vinayak Tilak from General Electric (GE) for supplying samples to be studied.

I am grateful to Dipl.-Ing. Ingo Hörselmann, Dipl.-Ing. Andrej Herasimovich and Ms. Gundis Bauer from the Department of Festkörperelektronik who had helped me effectively by providing experimental set up for sensor characterization.

My hearty thanks go to Dr. Abdallah Ghandour from Department of electronics, Faculty of mechanical and electrical engineering at Al-Baath University in Homs, Syria for the effective help and support.

Finally, I want to express my deep thanks to my parents, my wife, and my sisters and brothers for their unconditional love and support, their constant encouragement and persistent confidence in me.



**List of Publications:**

This thesis based on the following papers:

- [1] V. Tilak, **M. Ali**, V. Cimalla, V. Manivannan, P. Sandvik, J. Fedison, O. Ambacher, D. Merfeld, "Influence of metal thickness to sensitivity of Pt/GaN Schottky diodes for gas sensing applications", in: Proceedings of the MRS Fall Meeting, 798 (2003) Y.11.5.1.
- [2] **M. Ali**, V. Cimalla, V. Tilak, P. Sandvik, D. Merfeld, and O. Ambacher, "Pt-GaN based Schottky diodes for gas sensing applications", in Proc. IEEE Sensors, 2004, pp. 959-962.
- [3] **M. Ali**, V. Cimalla, V. Lebedev, H. Romanus, V. Tilak, D. Merfeld, P. Sandvik, O. Ambacher, "Pt/GaN Schottky diodes for hydrogen gas sensors", Sensors and Actuators B 113 (2006) 797-804.
- [4] **M. Ali**, V. Cimalla, V. Lebedev, V. Tilak, P. M. Sandvik, D. W. Merfeld, and O. Ambacher: "A study of hydrogen sensing performance of Pt-GaN Schottky diodes", IEEE Sensors Journal 6 (2006) 1115-1119.
- [5] **M. Ali**, G. Ecke, V. Cimalla, Th. Stauden, V. Tilak, P. Sandvik, and O. Ambacher: "SiC-based FET for NO<sub>x</sub> gas sensing applications using InVO<sub>x</sub> metal oxides as a gate material", 51st Internationales Wissenschaftliches Kolloquium Technische Universität Ilmenau, September 11-15, (2006) 245-246.
- [6] P. Sandvik, **M. Ali**, V. Tilak, K. Matocha, Th. Stauden, J. Tucker, J. Deluca, and O. Ambacher, "SiC-based MOSFETS for harsh environment emissions sensors", Materials Science Forum 527-529 (2006) 1457-1460.
- [7] Ch. Y. Wang, V. Cimalla, H. Romanus, Th. Kups, G. Ecke, Th. Stauden, **M. Ali**, V. Lebedev, J. Pezoldt, and O. Ambacher, "Phase selective growth and properties of rhombohedral and cubic indium oxide", Appl. Phys. Lett. 89 (2006) 011904.
- [8] **M. Ali**, V. Cimalla, V. Lebedev, Th. Stauden, G. Ecke, V. Tilak, P. Sandvik and O. Ambacher, "SiC-based FET for detection of NO<sub>x</sub> and O<sub>2</sub> using InSnO<sub>x</sub> as a gate material", Sensors and Actuators B 122 (2007) 182-186.
- [9] Ch. Y. Wang, V. Cimalla, G. Cherkashinin, H. Romanus, **M. Ali**, and O. Ambacher: "Transparent conducting indium oxide thin films grown by low-temperature metal organic chemical vapor deposition", Thin Solid Films 515 (2007) 2921-2925.

[10] **M. Ali**, V. Cimalla, V. Lebedev, Th. Stauden, Ch. Y. Wang, G. Ecke, V. Tilak, P. Sandvik and O. Ambacher, "Reactively sputtered  $\text{In}_x\text{V}_y\text{O}_z$  films for detection of  $\text{NO}_x$ ,  $\text{D}_2$ , and  $\text{O}_2$ ", Sensors and Actuators B 123 (2007) 779-783.

[11] **M. Ali**, Ch. Y. Wang, C.-C. Röhlig, V. Cimalla, Th. Stauden, and O. Ambacher, " $\text{NO}_x$  sensing properties of  $\text{In}_2\text{O}_3$  thin films grown by MOCVD", Sensors and actuators B 129 (2008) 467-472.

[12] Ch. Y. Wang, **M. Ali**, C.-C. Röhling, V. Cimalla, and O. Ambacher, " $\text{NO}_x$  sensing properties of  $\text{In}_2\text{O}_3$  nanoparticles prepared by metal organic chemical vapor deposition", Sensors and actuators B accepted (2008).

**List of Acronyms:**

<b>2DEG</b>	Two Dimensional Electron Gas
<b>AC</b>	Alternating Current
<b>AES</b>	Auger Electron Spectroscopy
<b>AFM</b>	Atomic Force Microscopy
<b>BAW</b>	Bulk Acoustic Wave
<b>BH</b>	Barrier Height
<b>BOE</b>	Buffered Oxide Etch
<b>CCFET</b>	Capacitively Coupled Field Effect Transistor
<b>ChemFET</b>	Chemical Field Effect Transistor
<b>CMOS</b>	Complementary Metal Oxide Semiconductor
<b>CP</b>	Conducting Polymer
<b>CRR</b>	Constant Retard Ratio
<b>CVD</b>	Chemical Vapour Deposition
<b>ECR</b>	Electron-Cyclotron Resonance
<b>FCC</b>	Face Centered Cubic
<b>FET</b>	Field Effect Transistor
<b>GasFET</b>	Gas Sensitive Field Effect Transistor
<b>HCP</b>	Hexagonal Closed Packed
<b>HEMT</b>	High Electron Mobility Transistor
<b>HR-SEM</b>	High Resolution- Scanning Electron Microscopy
<b>HR-TEM</b>	High Resolution-Transmission Electron Microscopy
<b>HSGFET</b>	Hybrid Suspended Gate Field Effect Transistor
<b>IR</b>	Infrared
<b>ISFET</b>	Ion Selective Field Effect Transistor
<b>ITO</b>	Indium Tin Oxide
<b>LD</b>	Laser Diode
<b>LED</b>	Light Emitting Diode
<b>LEL</b>	Lower Explosive Limit
<b>LPCVD</b>	Low Pressure Chemical Vapour Deposition
<b>MBE</b>	Molecular Beam Epitaxy
<b>MFC</b>	Mass Flow Controller
<b>MIM</b>	Metal-Insulator-Metal

---

<b>MIS</b>	Metal-Insulator-Semiconductor
<b>MISFET</b>	Metal-Oxide-Semiconductor Field Effect Transistor
<b>MMOOS</b>	Metal-Metal Oxide-Oxide-Semiconductor
<b>MOCVD</b>	Metal Organic Chemical Vapor Deposition
<b>MOMBE</b>	Metal Organic Molecular Beam Epitaxy
<b>MOS</b>	Metal-Oxide-Semiconductor
<b>MOSFET</b>	Metal-Oxide-Semiconductor Field Effect Transistor
<b>nc</b>	Nanocrystalline
<b>PIMBE</b>	Plasma-Induced Molecular Beam Epitaxy
<b>PLD</b>	Pulsed Laser Deposition
<b>QCM</b>	Quartz Crystal Microbalance
<b>QMS</b>	Quadrupole Mass Spectrometer
<b>RF</b>	Radio-Frequency
<b>SAW</b>	Surface Acoustic Wave
<b>SBH</b>	Schottky Barrier Height
<b>SEM</b>	Scanning Electron Microscopy
<b>SGFET</b>	suspended gate field effect transistors
<b>TDS</b>	Thermal Desorption Spectroscopy
<b>TEM</b>	Transmission Electron Microscopy
<b>TMA</b>	Trimethylamine
<b>TMIn</b>	Trimethylindium
<b>TPD</b>	Temperature-Programmed Desorption
<b>TWC</b>	Three-Way Catalyst
<b>UHV</b>	Ultra-High Vacuum
<b>UV</b>	Ultraviolet
<b>VOC</b>	Volatile Organic Compound
<b>XRD</b>	X-ray Diffraction

## Table of Contents

<b>Abstract</b>	<b>III</b>
<b>Zusammenfassung</b>	<b>VII</b>
<b>Acknowledgement</b>	<b>XI</b>
<b>List of Publications</b>	<b>XIII</b>
<b>List of Acronyms</b>	<b>XV</b>
<b>Table of Contents</b>	<b>XVII</b>
<b>Introduction and Motivation</b>	<b>1</b>
<b>Chapter 1: Solid State Gas Sensors: State of the Art and Fundamentals</b>	<b>7</b>
1.1 Chemical gas sensors	7
1.2 The electronic nose (e-nose)	9
1.2.1 Principle of operation of e-nose systems	9
1.2.2 E-nose sensor response to odorants	10
1.2.3 Sensors employed in e-nose systems	12
1.2.3.1 Metal oxide sensors	13
1.2.3.2 Metal-oxide-semiconductor field-effect transistor sensors	15
1.3 Sorption processes	17
1.3.1 Adsorption	17
1.3.2 Adsorption isotherms	19
1.3.3 Langmuir isotherm	21
1.4 Introduction to catalysis	23
1.5 Properties of wide band gap semiconductors	25
1.5.1 The properties of SiC	25
1.5.2 The properties of GaN	29
References	33
<b>Chapter 2: Study of Hydrogen-Sensing Performances of Pt/GaN Based Schotky Diodes</b>	<b>39</b>
2.1 Introduction	39
2.2 Hydrogen sensing mechanism of Pt/GaN Schottky diodes	40
2.3 Theory of Schottky diode	42
2.3.1 Metal-semiconductor contact	42
2.3.2 Current-Voltage characteristics	46
2.3.3 Other methods to determine the barrier height $\Phi_B$	49
2.4 Device structure and fabrication	51



2.5 Experiments	53
2.5.1 AES and SEM (surface and interface measurements)	53
2.5.2 Electrical measurements without gas	54
2.5.3 Experimental set-up for gas-sensing characterization	54
2.6 Results and Discussion	57
2.6.1 Chemical characterization of the Pt/GaN Schottky diodes	57
2.6.2 Electrical characterization in air	58
2.6.3 Hydrogen sensing performances	64
2.7 Temperature-programmed desorption (TPD) measurements	86
2.7.1 TPD background and fundamentals	86
2.7.2 Experimental	88
2.7.3 Results	91
2.8 Conclusion	101
2.9 Outlook and future work	102
References	102
<b>Chapter 3: Study of Gas-Sensing Performances of SiC-Based Metal oxide-Semiconductor (MOS) and Metal-Metal Oxide-Oxide- Semiconductor (MMOOS) Capacitors</b>	<b>107</b>
3.1 Introduction	107
3.2 Gas sensing principle	108
3.3 The MIS SiC capacitor	110
3.4 Device structure and fabrication	113
3.4.1 Sample A	114
3.4.2 Sample B	114
3.5 Experiments	115
3.5.1 AES Measurements	115
3.5.2 Gas-sensing measurements (set-up and procedure)	116
3.6 Results	118
3.6.1 Sample A4	118
3.6.1.1 Chemical characterization (AES results)	118
3.6.1.2 NO <sub>x</sub> detection	119
3.6.1.3 O <sub>2</sub> detection	122
3.6.1.4 D <sub>2</sub> detection	123
3.6.1.5 Conclusion	126

3.6.2 Sample A1	127
3.6.2.1 Chemical characterization (AES results)	127
3.6.2.2 NO <sub>x</sub> detection	127
3.6.2.3 D <sub>2</sub> detection	128
3.6.2.4 Conclusion	128
3.6.3 Sample B4	130
3.6.3.1 Chemical characterization (AES results)	130
3.6.3.2 NO <sub>x</sub> detection	131
3.6.3.3 O <sub>2</sub> detection	132
3.6.3.4 D <sub>2</sub> detection	133
3.6.3.5 Conclusion	134
3.6.4 Comparisons and discussion	135
3.6.4.1 D <sub>2</sub> detection	135
3.6.4.2 NO <sub>x</sub> and O <sub>2</sub>	136
3.6.4.3 Comparison	138
3.7 Conclusion	140
3.8 Outlook and future work	140
References	141
<b>Chapter 4: Study of Gas-Sensing Performances of SiC-Based FET     using Mixtures of Metal oxides as Gate Materials</b>	<b>143</b>
4.1 Introduction	143
4.2 Theory of field-effect-transistor (FET)	144
4.2.1 Principles of a MOSFET	144
4.2.2 The GasFET	147
4.3 Principle of gas sensing via work function	148
4.4 Device structure and fabrication	150
4.4.1 Devices with In <sub>x</sub> Sn <sub>y</sub> O <sub>z</sub> and In <sub>x</sub> V <sub>y</sub> O <sub>z</sub> gate	150
4.4.2 Devices with Pt-In <sub>x</sub> Sn <sub>y</sub> O <sub>z</sub> gate	151
4.5 Experiments	153
4.5.1 AES measurements (surface and interface measurements)	153
4.5.2 Gas sensing measurements	153
4.6 Results and discussion	155
4.6.1 Sensor with In <sub>x</sub> Sn <sub>y</sub> O <sub>z</sub> gate	155
4.6.1.1 Chemical characterization of the gate electrode	155

4.6.1.2 NO <sub>x</sub> detection	156
4.6.1.3 O <sub>2</sub> detection	160
4.6.1.4 Conclusion	162
4.6.2 Sensor with In <sub>x</sub> V <sub>y</sub> O <sub>z</sub> gate	164
4.6.2.1 Chemical characterization of the gate electrode	164
4.6.2.2 NO <sub>x</sub> detection	165
4.6.2.3 Deuterium detection	168
4.6.2.4 O <sub>2</sub> detection	171
4.6.2.5 Conclusion	173
4.6.3 Sensor with Pt-In <sub>x</sub> Sn <sub>y</sub> O <sub>z</sub> gate (sample EN17)	174
4.6.3.1 SEM and AES of the sample	174
4.6.3.2 NO <sub>x</sub> detection	175
4.6.3.3 O <sub>2</sub> detection	179
4.6.3.4 Conclusion	180
4.6.4 Sensor with Pt-In <sub>x</sub> Sn <sub>y</sub> O <sub>z</sub> gate (sample EN16)	181
4.6.4.1 SEM and AES of the sample	181
4.6.4.2 NO <sub>x</sub> detection	182
4.6.4.3 O <sub>2</sub> detection	186
4.6.4.4 Conclusion	189
4.7 Comparison	190
4.8 Conclusion	191
4.9 Outlook and future work	192
References	192
<b>Chapter 5: NO<sub>x</sub> and O<sub>2</sub> Sensing Properties of In<sub>2</sub>O<sub>3</sub> Thin Films grown by MOCVD</b>	<b>197</b>
5.1 Introduction	197
5.2 Fundamentals of metal oxide gas sensors	198
5.2.1 Electrical conductivity of metal oxide semiconductor	199
5.2.2 Structure and equivalent circuit models	200
5.2.3 Sensing mechanism of metal oxide semiconductor gas sensor	201
5.2.4 Effects of grain size and the geometry of grain connections	204
5.3 In <sub>2</sub> O <sub>3</sub> properties	206
5.4 Nanocrystalline materials	207

---

5.5 Film deposition and sensor structure	208
5.6 Experiments	209
5.6.1 Film characterization	209
5.6.2 Gas sensing measurements	209
5.7 Results and discussion	211
5.7.1 Characterization of the In <sub>2</sub> O <sub>3</sub> thin films	211
5.7.2 Gas sensitivity	213
5.7.2.1 Sample A	213
5.7.2.1.1 NO <sub>x</sub> detection	213
5.7.2.1.2 O <sub>2</sub> detection	217
5.7.2.1.3 Conclusion	219
5.7.2.2 Sample B	219
5.7.2.2.1 NO <sub>x</sub> detection	219
5.7.2.2.2 O <sub>2</sub> detection	223
5.7.2.2.3 Conclusion	224
5.7.2.3 Comparison between polycrystalline and nano-structured In <sub>2</sub> O <sub>3</sub> thin films	225
5.8 Conclusion	227
5.9 Outlook and future work	228
Reference	228
<b>Chapter 6: Comparison and conclusion</b>	<b>233</b>
6.1. Comparison of all sensors studied	234
6.2. Comparison with other results present in the literature	235
6.3. Conclusion	241
References	241
<b>Appendix A</b>	<b>245</b>
<b>Appendix B</b>	<b>247</b>

## Introduction and Motivation

The high advance in the technology and industry has been accompanied by a variety of serious environmental problems, for example, the release of various chemical pollutants, including  $\text{NO}_x$ ,  $\text{SO}_x$ ,  $\text{CO}_2$ , volatile organic compounds (VOCs) and fluorocarbon, from industry and homes, into the atmosphere, resulting in global environmental issues, such as acid rain, the greenhouse effect, and ozone depletion. The atmospheric pollution can cause major disasters within a short period of time, since this type of pollution can diffuse rapidly over large areas. The emitting sources of the atmospheric pollution can be a stationary or mobile source. Stationary sources include houses, workplaces, thermal power stations, whereas mobile sources include automobiles, trains, ships, and so forth. Stationary emitting sources also cover many diverse fields, such as oil refineries, chemical plants, metal refineries, and grocery plants. In particular, with the tremendous increase in automobiles and consumption of fossil fuel, the atmospheric environment has deteriorated significantly.

Automobiles and combustion facilities are the two major contaminants of the atmosphere. In the case of automobiles, for example, new legislation in the European Union and the United States will force that the future automotive exhaust emission must drop substantially from its actual levels. In a car, the less complete the combustion of fuel in the working cylinder, the higher is the emission of toxic substances in the exhaust gas. Of the exhaust gas, about 1% is harmful to the environment. This harmful part of the exhaust consists of carbon monoxide (CO) oxides of nitrogen ( $\text{NO}_x$ ) and hydrocarbons (HC). Concentration of these components in the exhaust strongly depends on the type of engines and operating conditions, but could be in the order of several % for CO, ~1000ppm of HCs, and ~100ppm of  $\text{NO}_x$  [1]. To see the importance of car emissions, it is interesting to note that more than the 40% of the  $\text{NO}_x$  emissions are produced in Europe by automobiles. The importance becomes obvious in this particular case.

To prevent or minimize the damage caused by atmospheric pollution, monitoring and controlling systems are needed that can rapidly and reliably detect and quantify pollution sources within the range of the regulating standard values. Analytic instruments using optical spectroscopy or gas chromatography/mass spectrometry (CG/MS) (Fig.1) have been used for air pollutant measurements. These instruments can give a precise analysis, they are time-consuming, expensive, and can seldom be used in real-time in the field. A gas sensor that is compact, robust, with versatile

applications and a low cost could be an equally effective alternative. Tab. 1 presents several feature comparisons between gas sensors and analytical instruments. A lot of recent research and development has been focused on the development of solid-state gas sensors; consequently, their performances have improved dramatically.



**Fig. 1: (a)** Standard analytical instrument (chromatography/mass spectrometry). **(b)** Semiconductor based gas sensor.

Solid-state gas sensors based on semiconductor (Si) structures have been intensively developed since 1975 after the first reports of Lundstöm [2-3]. The family of electronic devices based on the semiconductor structure is applied to detect hydrogen [2-3], oxygen [4-5], carbon monoxide [4-5], and hydrogen sulphide [6], and as active element of smoke detectors [7]. However, high temperature operation of Si-based solid-state gas sensors is limited to the range below 150°C. Wide-band gap semiconductor materials such as silicon carbide (SiC) and gallium nitride (GaN), were proposed to extend this range to improve the sensing properties such as sensitivity and the response time. GaN and SiC are capable of operating at much higher temperatures than more conventional semiconductors such as Si because of their large band gap (3.4 eV for GaN, 3.26 eV for the 4H-SiC poly-type vs. 1.1 eV for Si). One additional attractive attribute of GaN and SiC is the fact that gas sensors based on these materials could be integrated with high-temperature electronic devices on the same chip.

In addition, many automotive sensor applications require sensor operation in harsh, i.e. in hot and/or corrosive environments. Examples are power train or exhaust gas sensors which require sensor operation in high-temperature or chemically

reactive environments in which silicon devices cannot successfully be operated. In this latter area SiC and GaN are likely to make useful contributions [8-13].

**Tab. 1:** Comparison between analytical instruments and solid state gas sensors [14].

	Analytical methods (CG, MS)	Solid-state gas sensor
<b>Data acquisition</b>	Long	Real time
<b>Size</b>	Large	Compact
<b>Cost</b>	High	Low
<b>Resolution</b>	Excellent	Comparable
<b>Process control</b>	Difficult	Easy
<b>Mass production</b>	Difficult	Easy
<b>Application</b>	Environmental monitoring stationary state	Process control monitoring stationary state, mobile state

The aim of this thesis is to develop field effect gas sensors (Schottky diodes, MOS capacitors, and MOSFET transistors) based on wide band gap semiconductors, silicon carbide (SiC) and gallium nitride (GaN), as well as resistive gas sensors based on indium oxide ( $\text{In}_2\text{O}_3$ ) grown by metal organic chemical vapor deposition (MOCVD), for the detection of reducing gases ( $\text{H}_2$ ) and oxidising gases ( $\text{NO}_x$ ,  $\text{O}_2$ ).

### Why $\text{H}_2$ gas sensors?

With the increasing concern about the global climate change, more attention is paid to hydrogen as a clean energy source. Since hydrogen is a renewable, abundant, efficient energy source and provides zero emission, it is the near-future fuel. Hydrogen has also many potential applications as an energy carrier. It is possible that in the future hydrogen will be used more widely as a city gas and to power cars in the same way as natural gas is used. Moreover, hydrogen is an important raw material for the aerospace, chemical, medical, semiconductor and other sectors. In all these applications some precautions are required for the safe use of hydrogen.

Hydrogen has a large diffusion coefficient ( $0.61 \text{ cm}^2/\text{s}$ ) and wide combustion range (4-75%) and small ignition energy (0.02 mJ in air, methane's value is 0.3 mJ). Continuous monitoring of hydrogen leak at storage or usage sites is indispensable for safe operation. The demand for using hydrogen as a next generation, clean and renewable energy source has stimulated considerable efforts towards developing

sensitive, reliable, and cost effective hydrogen sensors for the fast detection of hydrogen leaks below the lower explosive limit (LEL) of 4.65% by volume ratio of hydrogen to air. The sensor must be able to survive exposure to 100% hydrogen without damage or change in calibration. Further, the sensor may be exposed to gases emerging from cryogenic sources. Thus, sensor temperature control is necessary.

### **Why NO<sub>x</sub> gas sensors?**

In recent years much attention has been focused on the role of NO<sub>x</sub> containing gases and their detection and measurement in urban air quality due to automotive and industrial emissions. Nitrogen oxide NO which is found in the combustion exhaust of automobiles and oil-burning power plants is a poisonous, odourless, colorless gas. Once is mixed with air, it quickly forms NO<sub>2</sub>, which is a highly toxic, reddish brown gas with a very pungent odour. NO<sub>x</sub> (mixture of NO and NO<sub>2</sub>) cause also problems such as acid rain, and the formation of photochemical smog. Hence, detection and emission control of toxic NO<sub>x</sub> using gas sensors specifically selective to NO<sub>x</sub> is of great importance.

### **References:**

- [1] H. Nakagawa, S. Okazaki, S. Asakura, K. Fukuda, H. Akimoto, S. Takahashi, and T. Shigemori, "An automated car ventilation system", Techn. Digest of the 7th international meeting of Chemical Sensors, Beijing, July 27-30 (1998) 187-189.
- [2] I. Lundström, M. S. Shivaraman, C. M. Svensson, and L. Lundkvist, "A hydrogen-sensitive MOS field-effect transistor", Appl. Phys. Lett. 26 (1975) 55-57.
- [3] K. I. Lundström, M. S. Shivaraman, and C. M. Svensson, "A hydrogen-sensitive Pd-gate MOS transistor", J. Appl. Phys. 46 (1975) 3876-3881.
- [4] W. P. Kang, and C. K. Kim, "Novel platinum-tin-oxide-silicon nitride-silicon dioxide-silicon gas sensing component for oxygen and carbon monoxide gases at low temperature", Appl. Phys. Lett. 63 (1993) 421-423.
- [5] W. P. Kang, and C. K. Kim, "Performance and detection mechanism of a new class of catalyt (Pd, Pt, or Ag)-adsorptive oxide (SnO<sub>x</sub> or ZnO)-insulator-semiconductor gas sensors", Sensors and Actuators B 22 (1994) 47-55.



- [6] S. Shivaraman, "Detection of H<sub>2</sub>S with pd gate MOSFETs", J. Appl. Phys. 47 (1976) 3592-3593.
- [7] I. Lundström, S. Shivaraman, L. Stibler, and C. Svenson, "Hydrogen in Smoke detected by the palladium-gate-field-effect transistor", Rev. Sci. Instrum. 47 (1976) 738-740.
- [8] J. Schalwig, G. Müller, M. Eickhoff, O. Ambacher, and M. Stutzmann, "Group III-nitride-based gas sensors for combustion monitoring", Mater. Sci. Eng. B 93 (2002) 207-214.
- [9] J. Schalwig, P. Kreisl, S. Ahlers, and G. Müller, "Response mechanism of SiC-based MOS field-effect gas sensors", IEEE Sensors J. 2 (2002) 394-402.
- [10] H. Wingbrant, L. Uneus, M. Andersson, J. Cerda, S. Savage, H. Svenningstorp, P. Salomonsson, P. Ljung, M. Mattsson, Salomonsson, J. H. Visser, D. Kubinski, R. Soltis, S. G. Ejakov, M. Löfdahl, M. Einehag, M. Persson, and A. Lloyd Spetz, "MISiCFET chemical sensors for applications in exhaust gases and flue gases", Material Science Forum 433-436 (2003) 953-956.
- [11] M. Andersson, P. Ljung, M. Mattsson, M. Löfdahl, A. Lloyd Spetz, "Investigations on the possibilities of a MISiCFET sensor system for OBD and combustion control utilizing different catalytic gate materials", Springer Verlag, Berlin, 30-31 (2004), 365-368.
- [12] I. Belov, H. Wingbrant, A. Lloyd Spetz, H. Sundgren, B. Thuner, H. Svenningstorp, and P. Leisner, "Thermal and flow analysis of SiC-based gas sensors for automotive applications", Proc. of 5th IEEE conference EuroSimE 2004, Brussels, May 9-12 (2004) 475-482.
- [13] H. Wingbrant, H. Svenningstorp, P. Salomonsson, D. Kubinski, J. H. Visser, M. Löfdahl, A. Lloyd Spetz, "Using a MISiC-FET sensor for detecting NH<sub>3</sub> in SCR systems", IEEE Sensors J. 5 (2005) 1099-1105.
- [14] N. Yamazoe and N. Miura, "Environmental gas sensing", Sensors and Actuators B 20 (1994) 95-102.



## Chapter 1

### 1 Solid-State Gas Sensors: State of the Art and Fundamentals

#### 1.1 Chemical gas sensors:

Sensors are important components in quality control as well as for online control of different processes in industry. Physical sensors, measuring parameters like temperature, pressure, and flow, have been used very long. For some parameters, like gas molecules in odours, chemical sensors are needed. A chemical gas sensor can be described as a device, which upon exposure to a gaseous chemical compound or a mixture of chemical compounds, alters one or more of its physical properties (e.g. mass, electrical conductivity, or capacitance) in a way that can be measured and quantified directly or indirectly. The most common types of changes utilised in chemical gas sensors are shown in Tab. 1.1 along with the classes of sensor devices used to detect these changes.

**Tab. 1.1:** Physical changes in the sensor active film and the sensor devices used to transduce them into electrical signals.

Physical changes	Type of devices
Electrical conductivity/resistivity, $\Delta\sigma/\Delta R$	Conductivity sensors (metal oxide gas sensors, conducting polymers)
Work function, $\Delta\Phi$	Field effect gas sensors: diodes, transistors, capacitors
Mass, $\Delta m$	Piezoelectric sensors: Quartz crystal microbalances (QMB), surface acoustic wave (SAW), microcantilevers
Optical parameters: reflection, absorption interferometry, fluorescence, refractive index or optical path length	Optical sensors (fibre optic or thin film)
Heat of temperature, $\Delta T$	Catalytic gas sensors: Seebeck effect, pellistors, semistors
Electromotive force or electrical current in a solid state electrochemical cell	Electrochemical gas sensors (potentiometric or amperometric)

Single gas sensors can, for examples, be used as fire detectors, leakage detectors, controllers of ventilation in cars and planes, alarm devices warning the overcoming of threshold concentration values of hazardous gases in the work places. The detection of volatile organic compounds (VOCs) or smells generated from food or household products has also become increasingly important in food industry and in indoor air

quality, and multisensor systems (often referred to as *electronic noses*) are the modern gas sensing devices designed to analyse such complex environmental mixtures [1.1-1.3]. In Tab. 2.2 examples of application for gas sensors and electronic noses are reported.

**Tab. 2.2:** Example of applications for gas sensors and electronic noses [1.4].

<b>Applications</b>
<b>Automobiles</b> <ul style="list-style-type: none"> <li>• Car ventilation control</li> <li>• Filter control</li> <li>• Gas-online vapour detection</li> <li>• Alcohol breath tests</li> </ul>
<b>Safety</b> <ul style="list-style-type: none"> <li>• Fire detection</li> <li>• Leak detection</li> <li>• Toxic/flammable/explosive gas detectors</li> <li>• Boiler control</li> <li>• Personal gas monitor</li> </ul>
<b>Indoor air quality</b> <ul style="list-style-type: none"> <li>• Air purifiers</li> <li>• Ventilation control</li> <li>• Cooking control</li> </ul>
<b>Environmental control</b> <ul style="list-style-type: none"> <li>• Weather stations</li> <li>• Pollution monitoring</li> </ul>
<b>Food</b> <ul style="list-style-type: none"> <li>• Food quality control</li> <li>• Process control</li> <li>• Packaging quality control (off-odours)</li> </ul>
<b>Industrial production</b> <ul style="list-style-type: none"> <li>• Fermentation control</li> <li>• Process control</li> </ul>
<b>Medicine</b> <ul style="list-style-type: none"> <li>• Breath analysis</li> <li>• Disease detection</li> </ul>

Solid-state gas sensors, based on a variety of principles and materials, are the best candidates to the development of commercial gas sensors for a wide range of such applications [1.5-1.8]. The great interest of industrial and scientific world on solid state gas sensors comes from their numerous advantages, like small sizes, high sensitivities in detecting very low concentrations (at level of ppm or even ppb) of a wide range of gaseous chemical compounds, possibility of on-line operation and, due to possible bench production, low cost. On the contrary, traditional analytical instruments such as mass spectrometer and chromatography are expensive, complex, and large in size. In addition, most analysis requires sample preparation, so

that on-line, real-time analysis is difficult. Solid-state chemical sensors have been widely used, but they also suffer from limited measurement accuracy and problems of long-time stability. However, recent advances in nanotechnology, i.e. in the cluster of technologies related to the synthesis of materials with new properties by means of the controlled manipulation of their microstructure on a nanometer scale, produce novel classes of nanostructured materials with enhanced gas sensing properties providing in such a way the opportunity to dramatically increase the performances of solid state gas sensors.

## **1.2 The electronic nose (e-nose):**

An electronic nose is an instrument comprised of an array of different gas sensors and signal multiplexing electronics, capable of recognizing individual or mixtures of analytes through pattern recognition [1.9-1.11]. It is based on the multi-sensing principle in which the distributed response of an array is used to identify the constituents of a gaseous environment, emulating the olfactory sense. Individual sensor elements may or may not be selective to any one gas. But by using an array of different sensors, gases can be distinguished and identified by a distinct “fingerprint” each gas produces in the form of a pattern of measured electrical responses. The e-nose is a cost-effective solution to the problems associated with sensory panels and with chromatographic and mass-spectrometric techniques and can accommodate real time performance in the field when implemented in portable form.

### **1.2.1 Principle of operation of e-nose systems:**

The e-nose attempts to emulate the mammalian nose by using an array of sensors that can simulate mammalian olfactory responses to aromas. The odour molecules are drawn into the e-nose using sampling techniques such as headspace sampling, diffusion methods, bubblers or pre-concentrators [1.12]. The odour sample is drawn across the sensor array and induces a reversible physical and/or chemical change in the sensing material, which causes an associated change in electrical properties. Each “cell” in the array can behave like a receptor by responding to different odours to varying degrees [1.13]. These changes are transduced into electrical signals,

which are pre-processed and conditioned before identification by a pattern recognition system as shown in Fig. 1.1.

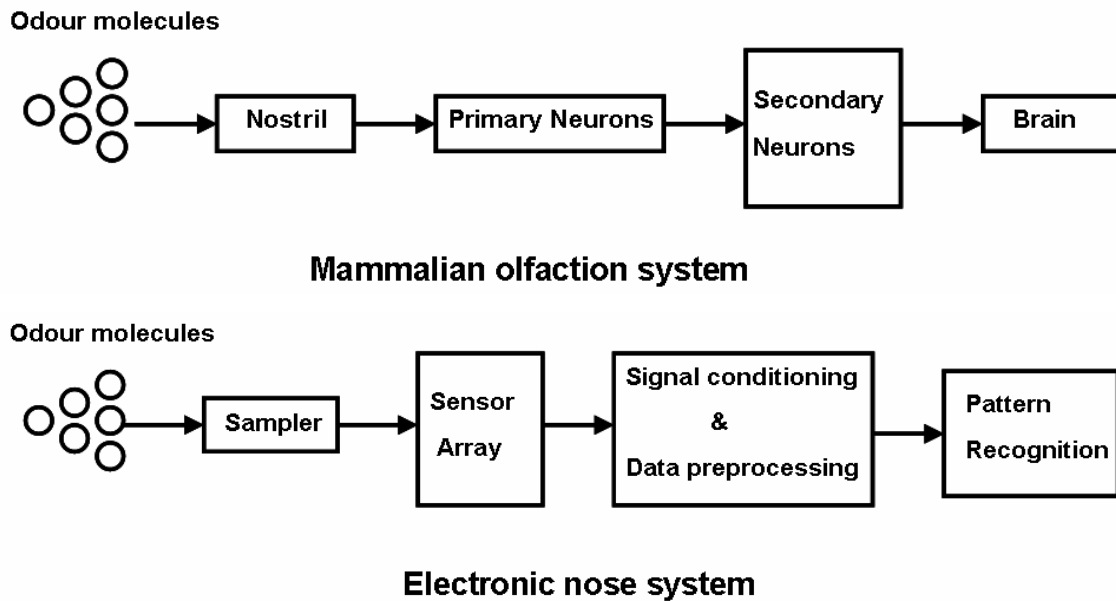


Fig. 1.1: Comparison of the mammalian olfactory system and the e-nose system [1.13].

### 1.2.2 E-nose sensor response to odorants:

The response of e-nose sensors to odorants is generally regarded as a first order time response. The first stage in odour analysis is to flush a reference gas through the sensor to obtain a baseline [1.13]. The sensor is exposed to the odorant, which causes changes in its output signal until the sensor reaches steady-state.

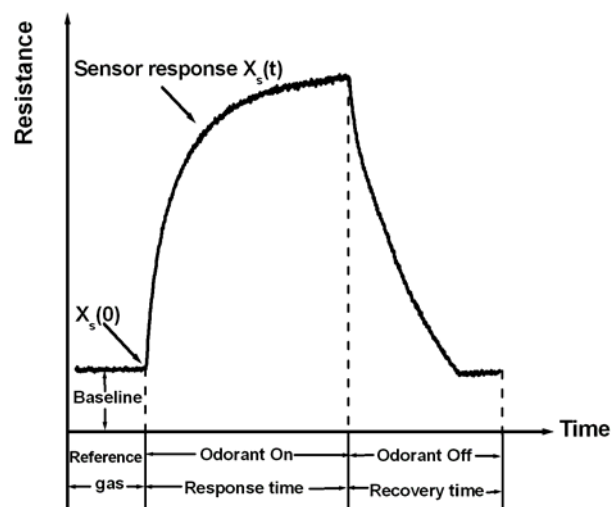


Fig. 1.2: E-nose sensor response to an odorant (adapted from [1.13]).

The odorant is finally flushed out of the sensor using the reference gas and the sensor returns back to its baseline as shown in Fig. 1.2. The time during which the sensor is exposed to the odorant is referred to as the response time while the time it takes the sensor to return to its baseline resistance is called the recovery time [1.13].

The next stage in analysing the odour is sensor response manipulation with respect to the baseline. This process compensates for noise, drift and also for inherently large or small signals. The three most commonly used methods as defined by Pearce *et al.* [1.12] are as follows.

**(1) Differential:** the baseline  $x_s(0)$  is subtracted from the sensor response  $x_s(t)$  to remove any noise or drift  $\delta_A$  present. The baseline manipulated response  $y_s(t)$  is determined by:

$$y_s(t) = (x_s(t) + \delta_A) - (x_s(0) + \delta_A) = x_s(t) - x_s(0). \quad (1.1)$$

**(2) Relative:** the sensor response is divided by the baseline. This process eliminates multiplicative drift  $\delta_M$  and a dimensionless response  $y_s(t)$  is obtained.

$$y_s(t) = \frac{x_s(t)(1 + \delta_M)}{x_s(0)(1 + \delta_M)} = \frac{x_s(t)}{x_s(0)}. \quad (1.2)$$

**(3) Fractional:** the baseline is subtracted from the response  $x_s(t)$  and then divided by the baseline  $x_s(0)$  from the sensor response which provides a dimensionless, normalised response  $y_s(t)$  that can compensate for inherently large or small signals.

$$y_s(t) = \frac{x_s(t) - x_s(0)}{x_s(0)}. \quad (1.3)$$

The choice of baseline manipulation depends on the sensor type being used, the sensor applications and also the researcher's preference. However, certain manipulation techniques have been shown to be more suitable to certain sensor types and also variations in the manipulation techniques can occur in the literature.

Sensitivity is the measure of the change in output of a sensor for a change in the input. This is the standard definition given for the sensitivity of a sensor in several texts on sensor related topics [1.14, 1.15]. In the case of e-nose sensors, the sensitivity of the sensor ( $S$ ) to the odorant is the change in the sensor output parameter ( $y$ ) for a change in the concentration of the odorant ( $x$ ) as shown in equation (1.4).

$$S = \frac{\Delta y}{\Delta x}. \quad (1.4)$$

However, in the literature several authors use different values to measure sensitivity, usually calculated from baseline-manipulated data.

### 1.2.3 Sensors employed in e-nose systems:

The ideal sensors to be integrated in an electronic nose should fulfil the following criteria [1.16-1.18]:

- high sensitivity toward chemical compounds, i.e. similar to that of the human nose (down to  $10^{-12}$  g/mL),
- low sensitivity towards humidity and temperature,
- medium selectivity, i.e. must respond to different compounds present in the headspace of the sample,
- high stability,
- high reproducibility and reliability,
- short reaction and recovery time,
- robust and durable,
- easy calibration,
- easily processable data output and
- small dimensions.

As the sensors are designed for industrial purposes, especially as on-line systems, a minimal working temperature with low power consumption, a high safety level, and low manufacturing costs present valuable advantages.

Most manufacturers are looking for highly selective sensors. In the case of an “electronic nose”, every compound present in the gaseous phase should be detected by at least one sensor. If a new compound is added to a mixture, at least one sensor must detect this addition. The use of too many sensors leads to an over complex system with a large amount of unnecessary data. Various kinds of gas sensors are available, but only four technologies are currently used in commercialised “electronic noses”

- Metal oxide gas sensors
- Metal oxide semiconductor field effect transistors (MOSFET)
- Conducting organic polymers (CP)
- Piezoelectric crystals (bulk acoustic wave (BAW)).

The metal oxide and MOSFETs gas sensors will be discussed in the following:



### 1.2.3.1 Metal oxide gas sensors:

Metal oxide gas sensors were first commercialised in the 1960s as household gas alarms in Japan with the names Taguchi (the inventor) or Figaro (the company's name). These sensors, also called oxide or ceramic gas sensors [1.19].

The principle of operation of metal oxide sensors is based on the change in conductance of the oxide on interaction with a gas and the change is usually proportional to the concentration of the gas [1.13]. There are two types of metal oxide sensors; *n*-type (zinc oxide (ZnO), tin dioxide (SnO<sub>2</sub>), titanium dioxide (TiO<sub>2</sub>), indium oxide (In<sub>2</sub>O<sub>3</sub>) or iron (III) oxide (Fe<sub>2</sub>O<sub>3</sub>)) which respond to oxidising gases and *p*-type (nickel oxide (NiO), cobalt oxide (CoO)) which respond to reducing gases [1.12]. Thermal or photolytic excitation of an *n*-type (*n* = negative electron) or donor semiconductor results in an excess of electrons in its conduction band which increases the reactivity with oxidising molecules. An excited *p*-type (*p* = positive hole) or acceptor semiconductor shows an electron deficiency in its valence band which promotes reactions with reducing compounds [1.20].

The *n*-type sensor operates as follows: oxygen in the air reacts with the surface of the sensor and traps any free electrons on the surface or at the grain boundaries of the oxide grains. This produces large resistance in these areas due to the lack of carriers and the resulting potential barriers produced between the grains inhibit the carrier mobility. However, if the sensor is introduced to a reducing gas like H<sub>2</sub>, CH<sub>4</sub>, CO, C<sub>2</sub>H<sub>5</sub> or H<sub>2</sub>S the resistance drops because the gas reacts with the oxygen and releases an electron [1.13].

This lowers the potential barrier and allows the electrons to flow, thereby increasing the conductivity. *p*-type sensors respond to oxidising gases like O<sub>2</sub>, NO<sub>2</sub>, and Cl<sub>2</sub> as these gases remove electrons and produce holes, i.e. producing charge carriers [1.13]. Equations (1.5) and (1.6) describe the reactions occurring at the surface:



where *e* is an electron from the oxide. *R(g)* is the reducing gas and *g* and *s* are the surface and gas, respectively [1.12,1.21].

The film deposition technique further divides each sensor type into thin (5 to 1000 nm) or thick (1 to 300 μm) film metal oxide sensors [1.22]. Film deposition includes screen printing [1.23], spin coating [1.24], RF sputtering [1.25] physical or

chemical vapour deposition [1.26]. The metal oxide films are deposited onto a flat or tube type substrate made of alumina, glass, silicon or some other ceramic. Gold, platinum, silver or aluminium electrodes are deposited onto the substrate using the same methods. There are various electrode designs but the interdigitated structure appears to be the most common approach. A heating element is printed onto the back of the substrate to provide the high temperatures required for metal oxides to operate as gas sensors, typically 200-500°C.

The main advantages of metal oxide sensors are fast response and recovery times, which mainly depend on the temperature and the level of interaction between the sensor and gas [1.26]. Thin film metal oxide sensors are small, and relatively inexpensive to fabricate, have lower power consumption than thick film sensors and can be integrated directly into the measurement circuitry [1.26]. However, they have many disadvantages due to their high operating temperatures, which results in increased power consumption over sensors fabricated from materials other than metal oxides. As a result, no handheld e-nose system has been fabricated utilising sensors prepared from metal oxides [1.12].

Other important disadvantages are the sensitivity to water vapour and the lack of selectivity. Metal oxide-based gas sensors are normally sensitive to more than one chemical species in air and usually show cross-sensitivities. This non-specificity of the response to chemical species whose presence, identity and concentration in air have to be determined is by now considered an intrinsic property of metal oxide-based gas sensors. It's easy to understand how this disadvantage represents a real problem when different reactive gases are present simultaneously in the same atmosphere and interference effects between them can occur. Unselectivity cannot be eliminated completely but it can be improved in different ways, like:

- The use of filters [1.27] or chromatographic columns to discriminate between gases on the basis of their molecular size or other physical properties [1.28].
- The use of catalysts and promoters or more specific surface additives [1.29, 1.30].
- The selection of the material for the sensing layer [1.31] and its physical preparation.
- The analysis of the transient sensor response [1.32].
- The selection of a fixed temperature to maximize sensitivity to a particular analyte gas [1.33].

- The use of temperature modulated operation mode [1.34].

A different approach to the problem of unselectivity is based on the development of the above mentioned electronic nose, that consists in an array of different sensing elements with partially overlapping sensitivity and a pattern recognition system. Basically the idea of an electronic nose is to exploit the unavoidable cross-sensitivity of the sensors instead of trying to eliminate it, by linking the sensors in an array configuration and by analyzing the responses of the sensors in a subsequent data processing step in order to perform a qualitative and/or quantitative analysis of the ambient under examination.

### 1.2.3.2 Metal-oxide-semiconductor field-effect transistor sensor (MOSFET):

The metal-oxide-semiconductor field-effect transistor (MOSFET) used in gas sensing is a device in which conduction between the source and drain of the transistor (Fig. 1.3) is controlled by charge or potential on the gate electrode. The device performs as a capacitor with one electrode the gate and the other the channel between source and drain. Charge present at the gate gives rise to a reflected charge induced in the channel and this modifies the conductance between source and drain. Any process that alters either the charge on the gate or its potential will alter the conduction of the channel and this can be detected as a useful electrical signal.

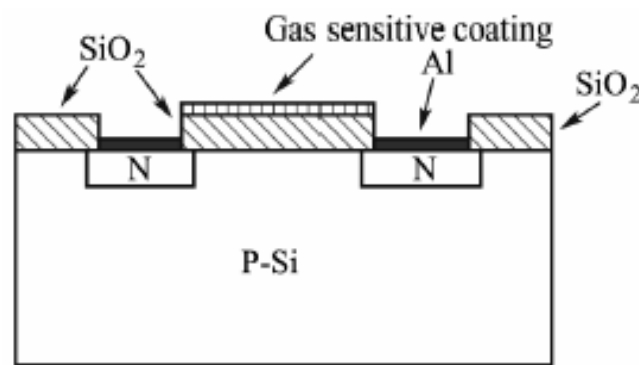


Fig. 1.3: MOSFET gas sensor with gas sensitive membrane deposited on top of SiO<sub>2</sub> [1.35].

This particular sensor works on the principle that the threshold voltage of the MOSFET sensor changes on interaction of the gate material [1.13], usually a catalytic metal, with certain gases, such as hydrogen, due to corresponding changes in the work functions of the metal and the oxide layers [1.12]. The changes in the

work functions occur due to the polarization of the surface and interface of the catalytic metal and oxide layer when the gas interacts with the catalytically active surface [1.36]. In order for the physical changes in the sensor to occur, the metal-insulator interface has to be accessible to the gas. Therefore, a porous gas sensitive gate material is used to facilitate diffusion of gas into the material [1.35]. It has been observed that the change in the threshold voltage is proportional to the concentration of the analyte and is used as the response mechanism for the gas. Changes in the drain-source current and the gate voltage have also been used as the response mechanisms for the MOSFET gas sensors as they are also affected by changes in the work function [1.21, 1.37].

Gas sensing MOSFETs are produced by standard microfabrication techniques, which incorporate the deposition of gas sensitive catalytic metals onto the silicon dioxide gate layer. In the case of catalytic metals, such as platinum (Pt), palladium (Pd), rhodium (Rh) and iridium (Ir), the gate material is thermally evaporated onto the gate oxide surface through a mask forming 100-400 nm thick films or 3-30 nm thin films depending on the application [1.21].

Polymers have also been used as the gate material for MOSFET gas sensors [1.38] Covington et al. used three polymers (poly(ethylene-co-vinylacetate), poly(styrene co-butadiene), poly(9-vinylcarbazole)) mixed with 20 per cent carbon black, which were deposited onto the FETs using a spray system. The polymer thickness was between 1.9 and 3.7  $\mu\text{m}$ , respectively [1.39]. These MOSFETs, which use polymers can operate at room temperature. A part from the standard MOSFET gas sensor architecture, a hybrid suspended gate FET (HSGFET) gas sensor can also be fabricated by micromachining (Fig. 1.4).

The HSGFET is a metal air-gap insulator (MAIS) device. The air-gap allows easy access to both the gate material and the insulator, so diffusion is not necessary and therefore a wider choice of gas sensitive materials can be used [1.12,1.35].

The selectivity and sensitivity of MOSFET sensors may be influenced by the operating temperature (50-200°C), the composition of the metal gate, and the microstructure of the catalytic metal [1.37].

MOSFET sensors have a number of advantages and disadvantages when used in e-nose arrays. Gas sensing MOSFETs are produced by microfabrication, therefore reproducibility is quite good and the sensor can be incorporated into CMOS technology resulting in small, low cost sensors [1.12, 1.37]. The sensors can suffer

from baseline drift and instability depending on the sensing material used. If CMOS is used, the electronic components of the chip have to be sealed because the sensor needs a gas inlet so it can penetrate the gate [1.37].

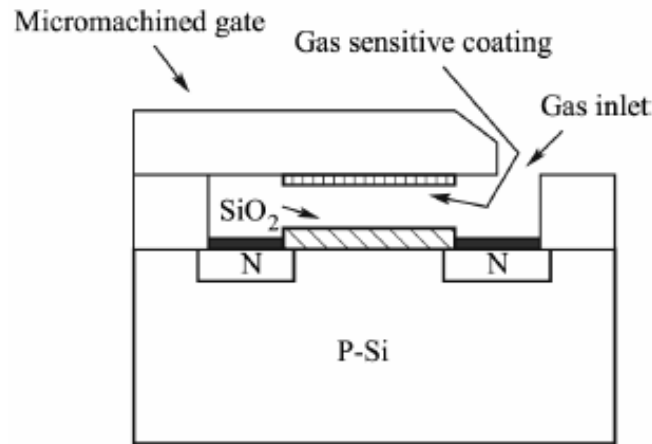


Fig. 1.4: Hybrid suspended gate field effect transistor [1.35].

### 1.3 Sorption processes:

When a gas or vapour is brought into contact with a solid, it will be partly taken up by the solid until equilibrium of the concentrations in the two phases is reached. The molecules either enter the inside of the solid, called absorption or dissolution, or remain on the outside attached to the surface, named adsorption. The general term for all possible processes is sorption.

It concludes adsorption, absorption, clustering of sorbate molecules, and incorporation into microvoids of the sorbent. Several modes of sorption may occur simultaneously depending on the nature of the sorbate and sorbent, the ambient conditions, namely pressure and temperature, and the concentration of the sorbate in the gas phase. The amount of sorbed molecules as a function of the partial pressure in the gas phase at a fixed temperature is modelled by a sorption isotherm.

#### 1.3.1 Adsorption:

A solid material usually exhibits a heterogeneous distribution of surface energy. Gas, vapor, or liquid molecules may become bound to the surface if they approach sufficiently close to interact. The solid is called the adsorbent; the gas or vapor molecule prior to being adsorbed is called the adsorptive and while bound to the solid

surface, the adsorbate. The adsorbed amount depends on the pressure of the adsorbate, the temperature and the properties of the adsorbent.

The phenomenon of adsorption plays an important role in both heterogeneous catalysis and in adsorption and membrane applications. Two main types of adsorption processes exist; **physisorption** and **chemisorption**.

Chemisorption involves the creation of bonds between the adsorbent and the adsorbate and resembles chemical reactions. Most of the reactions being catalysed by a solid are believed to involve an intermediate step with chemisorption of at least one of the reactants.

Physisorption is caused by weak intermolecular forces such as van-der-Waals, induced dipoles and dipole-dipole interactions and adsorption energy usually not exceeding 80 kJ/mole, with typical energies being considerably less. Physisorption resembles condensation of vapours rather than actual chemical reactions as in chemisorption. Physisorption is the main phenomenon used in adsorptive separation processes. Further, physisorption is used to determine the specific surface area as well as pore sizes and pore size distributions of the adsorbent.

Chemical bonds involving chemical reactions are stronger than the ones involving van-der-Waal forces. The heat of adsorption is a direct measure of the bond strength between the surface and the adsorbate. This parameter will yield information on which adsorption process is taking place. For physisorption the heat of adsorption is approximately 2-3 times smaller than the heat of vaporization [1.40]. Physisorption from gas phase is always an exothermic process.

Physisorption is an equilibrium process, which is fully reversible. Equilibrium is quickly achieved unless the process is restricted by slow diffusion of the adsorbate. Physisorption is usually nonspecific in contrast to chemisorption, which is highly specific taking place on certain specific sites on the surface. As a consequence chemisorption is restricted to forming a monolayer, whilst in physisorption both monolayers as well as multilayers may form. At low partial pressures monolayer adsorption is dominating whilst at higher partial pressures multilayers may form.

Chemisorption is usually explained using the Lennard-Jones-Model [1.41]. Fig. 1.5 details the potential energies in case of physisorption ( $E_{\text{phys}}$ ) and chemisorption ( $E_{\text{chem}}$ ) as a function of the distance  $r$  from the surface.

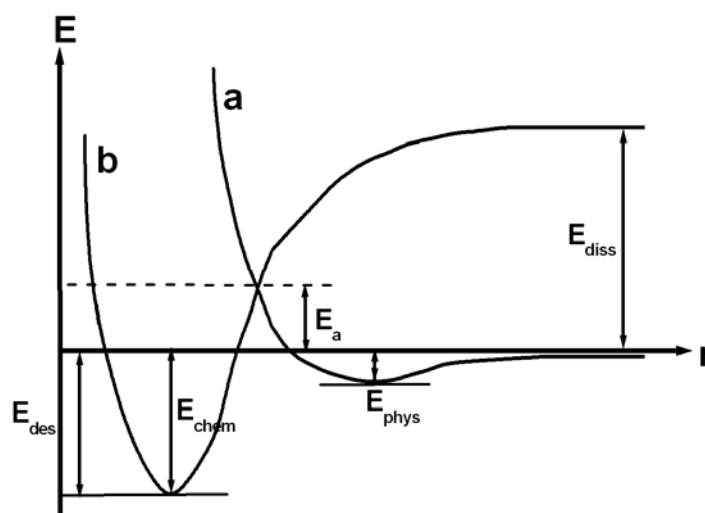


**Fig. 1.5:** Lennard-Jones model of physisorption and chemisorption: **(a)** physisorption of a molecule; **(b)** chemisorption of a molecule. Activation energy  $E_a$ , dissociation energy  $E_{\text{diss}}$ , desorption energy  $E_{\text{des}}$  (adapted from [1.41]).

If a gaseous molecule approaches the surface it will first be physisorbed, gaining  $\Delta E$  equal to  $E_{\text{phys}}$ . Upon a further approach towards the surface the molecule encounters a growing energy barrier, tending towards an infinite energy for a finite distance  $r$ . By spending the activation energy  $E_a$  the gaseous molecule can dissociate, thereby allowing a further approach to the surface. This stronger interaction with the surface (chemisorption) results in a higher energy gain  $\Delta E$  equal to  $E_{\text{chem}}$  than during physisorption. This energy gain  $E_{\text{chem}}$  depends strongly on the individual surface sites available and their reactivity. The most reactive sites will therefore be occupied with gaseous molecules during thermodynamic equilibration. However, the chemisorption energy not only depends on the number of reactive sites (high potential gain in  $\Delta E_{\text{chem}}$ ) but also on the ambient gas concentration  $p_{\text{gas}}$  and temperature  $T$  (probability of molecules overcoming the energy barrier  $E_a$ ).

As for chemisorption, desorption also requires the molecule to overcome an energy barrier  $E_{\text{des}} = E_{\text{chem}} + E_a$ . Therefore chemisorption and desorption are both activated processes requiring an activation energy supplied either thermally or by photoexcitation, contrary to physisorption which is a slightly exothermic process.

### 1.3.2 Adsorption isotherms:

Adsorption isotherms are usually classified according to Brunauer [1.42], see Fig. 1.6. Microporous materials usually shows type I behaviour. The type I isotherm is

also referred to as a Langmuir type of isotherm, with a steep increase in surface coverage at low partial pressures. At higher partial pressures the isotherms starts to level off towards a distinct saturation limit when the pore system is completely filled with the adsorbate. Type II isotherms represent multilayer adsorption on non-porous solids. Type IV isotherms are typical for porous materials containing mesopores where capillary condensation occurs in the mesopores. Types III and V are rare and occurs in systems where the forces of adsorption are relatively weak.

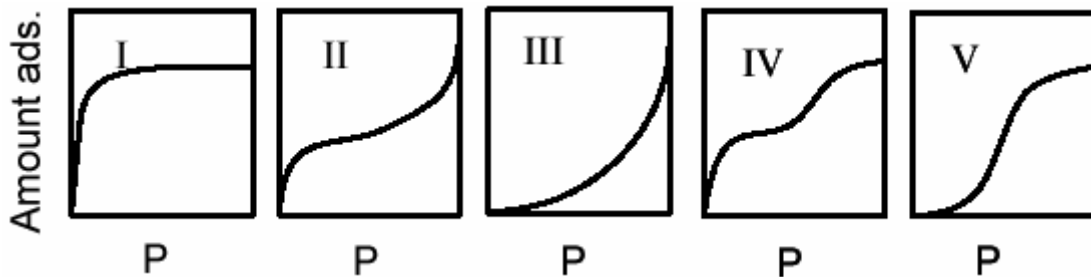


Fig. 1.6: Brunauer's five types of adsorption isotherms [1.43].

At low partial pressures of the adsorbate there will be a low surface coverage, and the adsorbed molecules may be regarded as isolated from the neighbours. Assuming that the surface is uniform, the relationship between the partial pressure and the amount adsorbed on the surface will be linear.

This relationship is often referred to as Henry's law because of the similarity to the limiting behaviour of gases dissolved in liquids. For a Henry constant expressed in pressure the Henry law is written as:

$$q = K_H P . \quad (1.7)$$

The loading of the adsorbate is  $q$  ( $\text{mol kg}^{-1}$ ),  $K_H$  is the Henry constant ( $\text{mol kg}^{-1} \text{Pa}^{-1}$ ) and  $P$  is the partial pressure of the adsorbate in gas phase.

At higher partial pressures molecules adsorbed at adjoining sites will interact with each other. The surface will begin to reach monolayer coverage alt. These factors will affect the amount adsorbed so that the linear relationship between the partial pressure and the surface coverage according to Eq. 1.7 is no longer valid. To model this behavior a number of adsorption models have been proposed, a common model is the so-called Langmuir model or the Langmuir isotherm.



### 1.3.3 Langmuir isotherm:

This simplest physically plausible isotherm is based on three assumptions:

- Adsorption cannot proceed beyond the point at which the adsorbates are one layer thick on the surface (monolayer).
- All adsorption sites are equivalent.
- The ability of a molecule to adsorb at a given site is independent of the occupation of neighboring sites.

The Langmuir isotherm describes the surface coverage ( $\theta$ ) of an adsorbed gas and is dependent upon the pressure ( $P$ ) at a fixed temperature [1.44]. It can easily be derived by assuming that the rate of adsorption is proportional to the rate of molecular collisions with vacant sites:

$$R_{ads} = k_A P(1 - \theta). \quad (1.8)$$

In the expression,  $k_A$  is the adsorption constant;  $P$  is the partial pressure of the adsorbate. Further, if  $q_s$  is the saturation capacity of the surface and by letting  $\theta$  be the fractional surface coverage,  $\theta = q/q_s$ , this implies that  $1-\theta$  is the fraction of vacant sites.

The disengagement of an atom or molecule from a surface is termed "desorption". At low temperatures a molecule adsorbed on a surface could remain for an indefinite time. However, as the surface temperature increases the molecule will receive energy, and so one of the following processes can occur:

- the molecules can react with the surface,
- the molecules can break down to two or more other molecules (either in gaseous or solid state),
- the molecules can desorb.

The last option is the desorption process, which could also occur in the second option if one of the products is a gas. The rate constant of the desorption process with respects to the change of the surface coverage by desorption is given by:

$$R_{des} = k_D \theta. \quad (1.9)$$

In the expression, the desorption constant is denoted  $k_D$ . At equilibrium the rate of adsorption and desorption rates in equations (1.8) and (1.9) are equal, so that:

$$k_A P(1 - \theta) = k_D \theta. \quad (1.10)$$

By setting  $b = k_A/k_D$  and by solving for  $\theta$  the following expression is obtained:

$$\theta = \frac{q}{q_s} = \frac{bP}{1+bP}. \quad (1.11)$$

At high partial pressures  $q \rightarrow q_s$  and  $\theta \rightarrow 1$  while at low partial pressures  $bP \ll 1$ . As a consequence, at low partial pressures, Henry's law is valid. The adsorption equilibrium constant,  $b$ , is easily obtained from experimental data Eq. (1.11) is linearised to:

$$\frac{P}{q} = \frac{P}{q_s} + \frac{1}{q_s b}. \quad (1.12)$$

A plot of  $P/q$  as a function of  $P$  should yield a straight line with slope equal to  $1/q_s$  and the intercept with the y-axis equal to  $1/(q_s b)$ .

Fig. 1.7 shows the characteristics of several Langmuir isotherms for different values of  $b(T)$ . A surface with high desorption relative to the adsorption rate has a small surface coverage ( $b(T)$  is small). With an increase in desorption rate (and thus  $b(T)$ ) the surface coverage will rise.

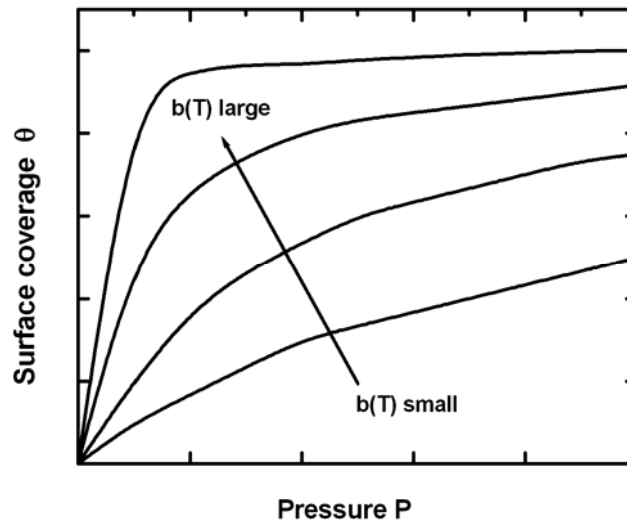


Fig. 1.7: Characteristics of several Langmuir isotherms for different  $b(T)$  [1.45].

When considering an adsorption process of two gases (gas A and gas B) on a surface it is necessary to modify Eq. (1.11) to:

$$\theta_A = \frac{b_A P_A}{1 + b_A P_A + b_B P_B}. \quad (1.13)$$

and

$$\theta_B = \frac{b_B P_B}{1 + b_A P_A + b_B P_B}. \quad (1.14)$$

These equations allow to express the surface coverage of two gases, which react with each other on the surface in the following way:



This model suitably describes the surface coverage of oxygen in terms of oxygen partial pressure and the concentration of gaseous co-reactants. Examples of such reactions are:



and



#### 1.4 Introduction to catalysis:

Catalytic effects play an important role in the field of gas detection. Solid-state gas sensors are directly related to the phenomenon of catalysis. Catalytic processes not only control the rate at which a chemical reaction approaches equilibrium (this affects the response time in the case of gas detection) but also affect the sensitivity and selectivity. The ideal catalyst is one which increases the rate of the gas-surface reaction without itself becoming permanently affected by the reaction. Thus the response time will be fast and the process will be reversible.

Fig. 1.8 shows schematically the energetic of the reaction (both catalyzed and uncatalyzed):



The uncatalyzed reaction is characterized by extremely high activation energy,  $E_g$ . In the catalyzed reaction the gaseous species A and B adsorb on the surface with an exothermic heat of adsorption  $\Delta H$  (state I). The state I is followed by state II toward the reaction products C and D (state II) characterized by the activation energy  $E_c$ , which is much lower than  $E_g$ . It can be seen from Fig 1.8 that if the heats of adsorption ( $\Delta H$ ) are too large, that is if the species are too strongly adsorbed, the activation energy  $E_c$  may become too high for the reaction to be accelerated. However, the value of the activation energy alone does not define the activity of the catalyst, for example, as the heat of adsorption, and hence the activation energy, falls, so does the surface concentration of the reactants. Consequently, although the reaction becomes energetically easier, fewer species are available for reaction.

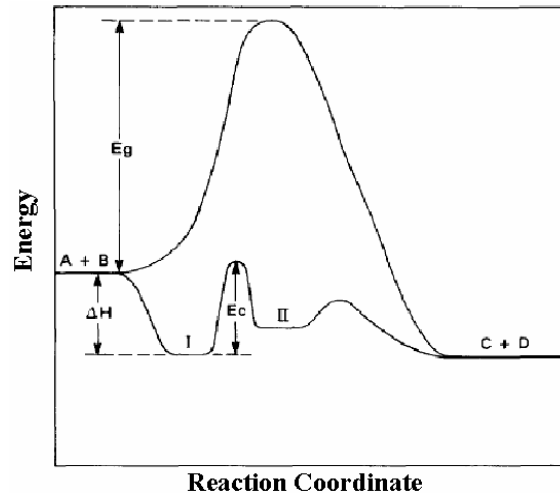


**Fig 1.8:** Energy barriers for reaction of Eq. (1.18). Activation energies:  $E_g$ , homogeneous gas phase reaction;  $E_c$ , heterogeneous catalyzed reaction [1.46].

The activation energy is not the only factor determining the activity of the catalyst. The following five factors play a role in affecting catalytic reaction [1.46]:

- Transport of gases to the solid surface.
- Adsorption of the gases on the solid surface.
- Reaction between the adsorbed species and/or with the solid surface.
- Desorption of the surface species and products of surface reactions.
- Transport of the gaseous reactants and products away from the surface.

In sensor technology two types of catalytic materials are mostly used: metals and semiconducting metal oxides [1.46]. In metals, the electrons involved in chemisorption are the free electrons, or in simple chemical terms the d-band electrons. Thus, one can understand why the noble metals (Pt, Pd, Rh, Ir) are the most active catalysts [1.47], since they possess a partially filled d-band.

The semiconductor metal oxides are those with lattice defects arising from an excess or deficit of oxygen in the lattice. The association of electrons with these defects following chemisorption allows a certain change of the electrical conductivity of the oxide. In the case of metals there is also a certain change of electrical conductivity, but the relative change is very small owing to the high concentration of conduction electrons and is therefore difficult to measure. In a successful gas sensor utilizing electrical conductivity changes, the changes in conductivity must be proportional to the concentration of the detecting gas.

## **1.5 Properties of wide bandgap semiconductors:**

The substrate materials chosen for the sensors described in this thesis are wide bandgap semiconductor materials SiC and GaN, which are capable of operating at much higher temperatures than more conventional semiconductors such as Si. This, as well as other properties of the material, will be treated in the following.

### **1.5.1 The properties of SiC:**

Silicon carbide (SiC) is a very promising material for semiconductor devices which have to work under extreme conditions, such as high temperature, high power, and high frequency. Because of the good thermal conductivity, the high radiation resistance, and the high breakdown voltages, SiC is well suited for demanding applications in harsh environments. These properties make SiC a suitable material for use in exhaust gas applications. The atmosphere inside the exhaust pipe of an engine is very warm (up to 1000°C in the case with a gasoline engine) and contain many different gases and particles, which altogether creates a very harsh environment. It is necessary to use a material that is chemically inert so that it does not degrade in this atmosphere.

#### **1.5.1.1 Crystallography-Polytypes:**

Silicon carbide occurs in many different crystal structures, called polytypes. Despite the fact that all SiC polytypes chemically consist of 50% carbon atoms covalently bonded with 50% silicon atoms, each SiC polytype has its own distinct set of electrical and physical properties. While there are over 200 known polytypes of SiC, only a few are commonly grown in a reproducible form acceptable for use as an electronic semiconductor. The most common polytypes of SiC presently being developed for electronics are 3C-SiC, 4H-SiC, and 6H-SiC, due to the ability to synthesize these poly types in thin films and/or wafer forms using conventional methods.

3C-SiC, also referred to as  $\beta$ -SiC, is the only form of SiC with a cubic crystal lattice structure. The non-cubic polytypes of SiC are sometimes ambiguously referred to as  $\alpha$ -SiC. 4H-SiC and 6H-SiC are only two of many possible SiC polytypes with hexagonal crystal structure. Similarly, 15R-SiC is the most common of many possible

SiC polytypes with a rhombohedral crystal structure. 4H-SiC and 6H-SiC are the far superior forms of semiconductor device quality SiC commercially available in mass-produced wafer form. Different polytypes of SiC are actually composed of different stacking sequences of Si-C bilayers (also called Si-C double layers), where each single Si-C bilayer can simplistically be viewed as a planar sheet of silicon atoms coupled with a planar sheet of carbon atoms [1.48]. The plane formed by a bilayer sheet of silicon and carbon atoms is known as the basal plane, while the crystallographic *c*-axis direction, also known as the stacking direction or the [0001] direction, is defined normal to Si-C bilayer plane. Fig. 1.9 depicts schematically the stacking sequence of the 6H-SiC polytype, which requires six Si-C bilayers to define the unit cell repeat distance along the *c*-axis [0001] direction.

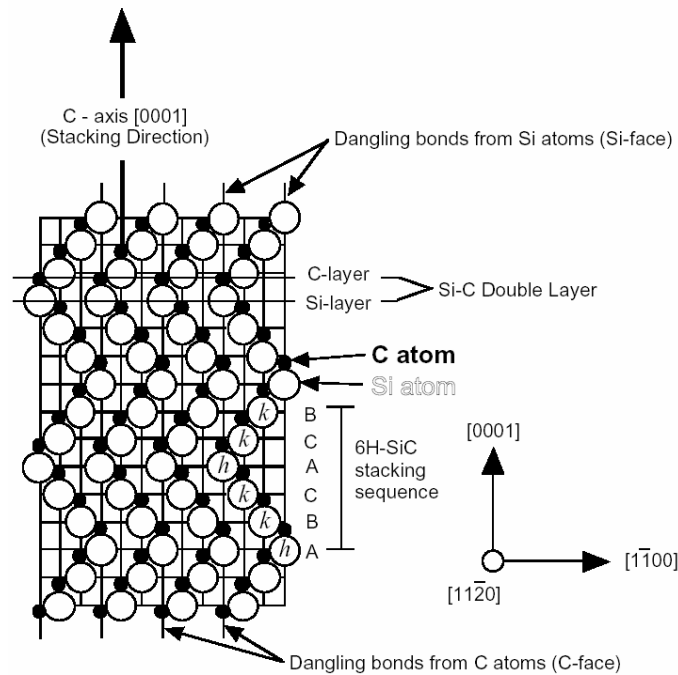


**Fig. 1.9:** Schematic cross-section  $\{(11\bar{2}0) \text{ plane}\}$  of the 6H-SiC polytype [1.48]

The [1100] direction depicted in Fig. 1.9 is often referred to as the *a*-axis direction. The silicon atoms labeled “h” or “k” in Fig. 1.9 denote Si-C double layers that reside in “quasi-hexagonal” or “quasi-cubic” environments with respect to their immediately neighboring above and below bilayers. SiC is a polar semiconductor across the *c*-axis, in that one surface normal to the *c*-axis is terminated with silicon atoms while the opposite normal *c*-axis surface is terminated with carbon atoms. As shown in Fig. 1.9, these surfaces are referred to as the “silicon face” and “carbon face,” respectively.

### 1.5.1.2 Electrical properties:

Owing to the differing arrangement of Si and C atoms within the SiC crystal lattice, each SiC polytype exhibits unique fundamental electrical and optical properties. Some of the more important semiconductor electrical properties of the 3C-, 4H-, and 6H-SiC are summarized in Tab. 1.3. Physical properties of Si and GaAs are shown for comparison. As can be seen, SiC has large band gap (2.3 ~ 3.3 eV), high break down field ( $\sim 3 \times 10^6$  V/cm), high saturation electron velocity ( $\sim 2.7 \times 10^7$  cm/s), and high thermal conductivity ( $\sim 5$  W/cm°C).

**Tab. 1.3:** Physical properties of 3C-, 4H-, 6H-SiC, Si and GaAs at 300 K [1.49].

Property	Si	GaAs	6H-SiC	4H-SiC	3C-SiC
Crystal structure	diamond	zinc blende	hexagonal	hexagonal	zinc blende
Lattice constant (Å)	5.43	5.65	a = 3.9 c = 15.1	a = 3.9 c = 10.1	4.36
Band structure	indirect	direct	indirect	indirect	indirect
Band gap (eV)	1.11	1.43	3	3.3	2.2
Maximum operating temperature (K)	300	460	1240	1240	1240
Electron Mobility (cm <sup>2</sup> /V.s)	1400	8500	600	1000	1000
Hole Mobility (cm <sup>2</sup> /V.s)	600	400	50	100	40
Breakdown Voltage E <sub>b</sub> , (V/cm) × 10 <sup>6</sup>	0.3	0.4	3	3	4
Thermal conductivity c <sub>T</sub> , (W/cm °C)	1.5	0.5	5	5	5
Saturation drift velocity V (sat), × 10 <sup>7</sup> (cm/s)	1	2	2	2.7	2
Relative dielectric constant	11.8	12.8	9.7	9.7	9.7

### 1.5.1.3 SiC epilayer doping:

In-situ doping during CVD epitaxial growth is primarily accomplished through the introduction of nitrogen (usually N<sub>2</sub>) for *n*-type and aluminum (usually trimethyl- or triethylaluminum) for *p*-type epilayers [1.50]. Some alternative dopants such as

phosphorous, boron, and vanadium have also been investigated for *n*-type, *p*-type, and semi-insulating epilayers, respectively. While some variation in epilayer doping can be carried out strictly by varying the flow of dopant gasses, the site-competition doping methodology [1.51] has enabled a much broader range of SiC doping to be accomplished. In addition, site competition epitaxy has also made moderate epilayer dopings more reliable and repeatable. The site-competition dopant-control technique is based on the fact that many dopants of SiC preferentially incorporate into either Si lattice sites or C lattice sites. As an example, nitrogen preferentially incorporates into lattice sites normally occupied by carbon atoms. By epitaxially growing SiC under carbon-rich conditions, most of the nitrogen present in the CVD system (whether it is a residual contaminant or intentionally introduced) can be excluded from incorporating into the growing SiC crystal. Conversely by growing in a carbon-deficient environment, the incorporation of nitrogen can be enhanced to form very heavily-doped epilayers for ohmic contacts. Aluminum, which is opposite to nitrogen, prefers the Si-site of SiC, and other dopants have also been controlled through sitecompetition by properly varying the Si/C ratio during crystal growth. SiC epilayer dopings ranging from  $9 \times 10^{14}$  to  $1 \times 10^{19} \text{ cm}^{-3}$  are commercially available, and researchers have reported obtaining dopings nearly a factor of 10 larger and smaller than this range for *n*-type and *p*-type dopings.

#### 1.5.1.4 Properties of SiO<sub>2</sub> on SiC:

If there is a singular property of silicon that has contributed to its success as a semiconductor material, it is the native oxide, SiO<sub>2</sub>. This oxide can be thermally grown to form an effective insulating layer as part of the gate in a metal-oxide-semiconductor field-effect-transistor (MOSFET) structure. SiC also has the ability to grow a similar oxide, and when combined with the bulk properties of wide bandgap, high thermal conductivity and extremely low intrinsic free carrier concentrations, will lead to an enormous number of applications. This means that so far as the gate oxide is concerned SiC can be processed in much the same way as Si, the exception being that the processing temperature is generally higher.

A major obstacle to the formation of a high quality oxide on SiC is the role that the carbon plays during the oxide growth. Thermal oxidation in a wet or dry atmosphere results in residual carbon in the oxide layer and carbon clusters at the oxide-SiC interface. It has been found that oxidation or post oxidation annealing in a



nitrogen-containing atmosphere has two beneficial effects-enhanced removal of carbon, and pasivation of silicon dangling bonds [1.52]. The most effective gases in achieving this effect have been nitric oxide (NO) and nitrogen oxide (N<sub>2</sub>O).

### 1.5.2 The properties of GaN:

The group III-nitrides represent an important class of material with applications in high temperature electronics, optoelectronic devices operating in the visible and UV region of the spectrum, high temperature gas sensors, and cold cathodes. Owing to their combination of wide band gap, high thermal conductivity, high thermal stability and physical robustness they offer, in principle, an attractive route to such devices. As members of the III-nitrides family, AlN, GaN, InN and their alloys are all wide band gap materials, and can crystallize in both wurtzite and zinc blende polytypes. Wurtzite GaN, AlN and InN have direct room temperature bandgaps of 3.4 eV, 6.2 eV and 0.7 eV, respectively (Fig. 1.10). In cubic form, GaN and InN have direct bandgaps, while AlN is indirect. In view of the available wide range of direct bandgaps, GaN alloyed with AlN and InN may span a continuous range of direct bandgap energies throughout much of the visible spectrum well into the ultraviolet wavelengths. This makes the nitride system attractive for optoelectronic device applications, such as light emitting diodes (LEDs), laser diodes (LDs), and detectors, which are active in the green, blue or UV wavelengths [1.53].

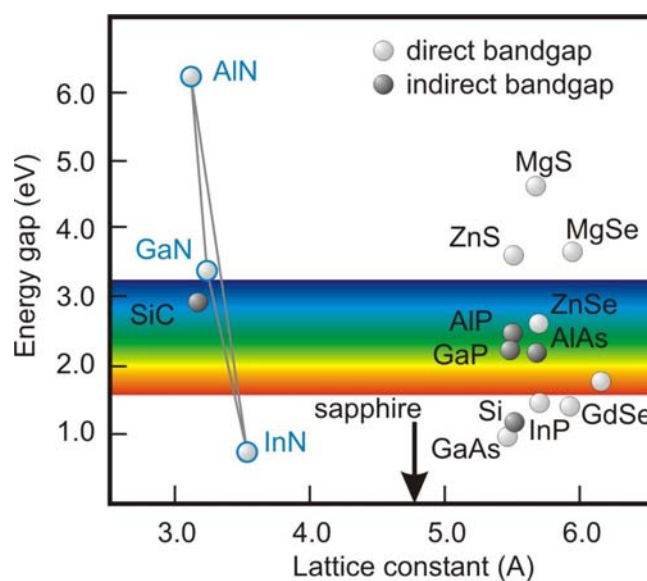


**Fig. 1.10:** Bandgap vs. lattice constant plot for the group III-nitrides and selected semiconductors.

Some of the more important properties of GaN are summarized in Tab. 1.4. GaN's large bandgap, large field strength, high thermal conductivity, high breakdown field, and good electron transport properties (as listed in Tab. 1.4) make GaN based electronic devices very promising in high voltage, high power, and high frequency applications. Furthermore, GaN is able to withstand temperatures as high as 800°C, which implies the possibility of use in harsh environments.

**Tab. 1.4:** Properties of GaN, sources [1.53-1.55].

Crystal structure	Unit	Wurtzite	Zinc blende
Density	g/cm <sup>3</sup>	6.15	
Static dielectric constant		8.9-9.5	9.7
High frequency dielectric constant		5.35	5.3
Lattice constant, a	Å	3.189	4.52
Lattice constant, c	Å	5.185	4.5
Energy gap	eV	3.51	3.3
Effective electron mass	m <sub>0</sub>	0.2-0.22	0.15
Breakdown field	V/cm	~5 × 10 <sup>6</sup>	~5 × 10 <sup>6</sup>
Electron mobility	cm <sup>2</sup> /Vs	~1000	≤1000
Hole mobility	cm <sup>2</sup> /Vs	≤200	≤350
Electron saturation velocity	cm/s	2-2.5 × 10 <sup>7</sup>	2 × 10 <sup>7</sup>
Peak velocity	cm/s	2.5-3 × 10 <sup>7</sup>	2.5 × 10 <sup>7</sup>
Peak velocity field	kV/cm	150-180	100-150
Thermal Conductivity	W/cm°C	>2.1	
Melting temperature	°C	>1700	
Polar Optical Phonon Energy	meV	91.8	91.9

### 1.5.2.1 Crystal Structure:

There are three common crystal structures shared by the group III-nitrides: wurtzite, zinc blende, and rocksalt [1.53]. At ambient conditions, at her modynamically stable structure is wurtzite or bulk AlN and GaN. The wurtzite structure has a hexagonal unit cell and thus two lattice constants, c and a shown in Fig. 1.11. The hexagonal unit cell contains 6 atoms of each type. The wurtzite structure consists of two interpenetrating hexagonal closed packed (HCP) sub lattices, each of one type of atom, offset along the c-axis by 5/8 of the cell height c.

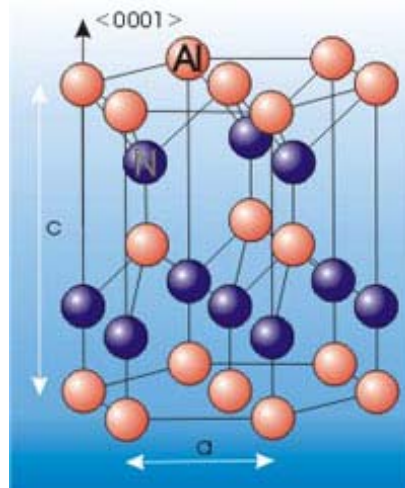


**Fig. 1.11:** Crystal structure of Wurtzite GaN. Note that, for WZ-GaN lattice parameters ( $a$  and  $c$ ) are 3.189 Å, and 5.1850 Å, respectively [1.53].

The zinc blende structure has a unit cell, containing four group III elements and four nitrogen elements Fig. 1.12a. The position of atoms within the unit cell is identical to the diamond crystal structure. Both structures consist of two interpenetrating face centered cubic (FCC) sub lattices, offset by one quarter of distance along a body diagonal. Each atom in the structure may be viewed as positioned at the center of a tetrahedron with its four neighbors defining the four corners of a tetrahedron (Fig. 1.12b).

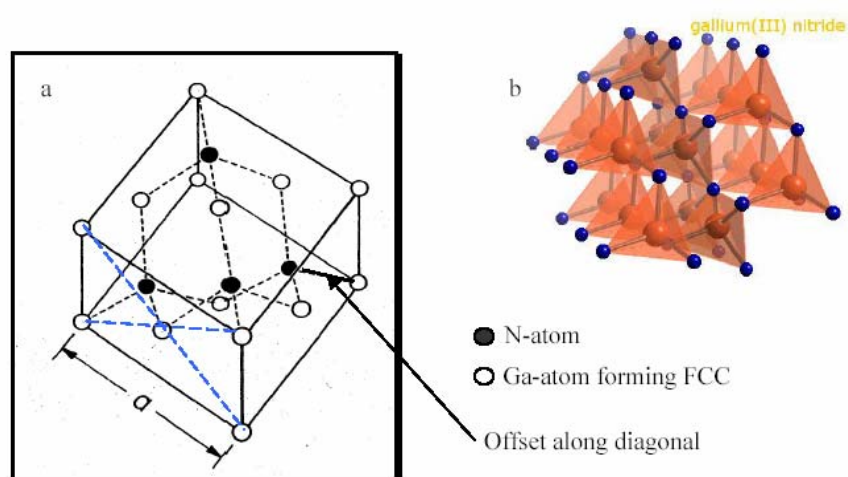


**Fig. 1.12:** Crystal structure of a zinc blende configuration of GaN. **(a)** FCC unit cell. **(b)** View of tetrahedron structures of GaN in which each fourth atom (Ga) is shared with the second tetrahedron [1.56].

### 1.5.2.2 Growth of GaN layers:

The high melting temperatures and dissociation pressures are the main obstacles in obtaining large single crystals of III-N compounds, which can serve as substrates for the homoepitaxial growth (when a material is grown epitaxial on a substrate of the same material). Therefore, III-V films have been grown heteroepitaxially (if the layer and the substrate are different materials, like GaN on SiC, GaN on Sapphire, GaN on Si) on a number of substrates which match more or less close to the lattice constants and thermal expansion coefficient of III-V nitrides. Remarkable progress in the growth of high-quality epitaxial layers of III-nitrides by a variety of methods has been recently achieved.

The most successful among them are metal organic chemical vapor deposition (MOCVD) and molecular beam epitaxy (MBE). MBE plays an important role in the development of modern quantum devices because it is able to prepare compositionally sharp interfaces with atomic layer precision of the designed device over a large substrate area. Typical MBE growth rate is approximately 0.1-1 mkm/h, although much higher growth rates can be attained. The MOCVD technique for the growth of III-nitrides had become mature by the mid of 1990s. Until recently, most nitride-based devices were fabricated using MOCVD. The development of MBE as a growth technique for the III-nitrides has been slow enough. This has happened because the MBE growth is usually performed at relatively low temperatures of 600-800°C. The molecular nitrogen is inert and does not chemisorb on the III-N surface below 950°C due to the strong N-N bond of the nitrogen molecule. Therefore, atomic nitrogen or nitrogen containing molecule with weaker bonds should be provided for the III-nitride epitaxy. Several modifications to conventional MBE method have been implemented for III-nitride growth: growth with ammonia or hydrazine, plasma-assisted MBE (PAMBE), metalorganic MBE (MOMBE), pulsed laser deposition (PLD), etc. Among other methods, radio-frequency (RF) and electron-cyclotron resonance (ECR) plasma sources are the most commonly employed devices to activate the neutral nitrogen species in the MBE environment.

### 1.5.2.3 GaN doping:

Conductivity modulation can be achieved in GaN by doping with donors such as Si, O and Ge or with acceptor such as Mg, Zn, and Be. Si and Mg are primarily the *n*-

type and *p*-type dopands of choice, respectively. Si-doping has been successfully used to produce films with electron concentration from low  $10^{17}$  to the mid  $10^{19}$   $\text{cm}^{-3}$  with almost complete room temperature donor activation. For example, catalytic/GaN Schottky diodes used as gas sensors use GaN doped with Si where the electron concentration is usually in the range from  $10^{16}$  to  $10^{18}$   $\text{cm}^{-3}$ . It will be seen that Pt/GaN gas sensors based on Schottky diodes discussed in the second chapter use Si-doping with concentration of  $\sim 1 \times 10^{17}$   $\text{cm}^{-3}$ .

The ionization energy of the Si level (temperature dependent) in GaN was reported approx. 27 meV [1.57], and 12-17 meV as measured by Hall effect [1.58]. The solubility of Si in GaN is high, of the order of  $10^{20}$   $\text{cm}^{-3}$ . Therefore, Si is suitable for III-Nitrides doping and most frequently used.

### References:

- [1.1] J. W. Gardner, P. N. Bartlett, "Electronic noses-Principles and Applications", Oxford University Press 1999.
- [1.2] J. W. Gardner, K. C. Persaud (eds.), "Electronic noses and olfaction 2000", Proceedings of 7<sup>th</sup> Symposium on Olfaction and Electronic Noses, Brighton, UK, July 2000, IOP Publishing (2001).
- [2.3] P. Mielle, F. Marquis, C. Latrasse, "Electronic noses: specify or disappear", Sensors and Actuators B 69 (2000) 287-294.
- [1.4] S. Capone, A. Forleo, L. Francioso, R. Rella, P. Siciliano, J. Spadavecchia, D. S. Presicce, A. M. Taurino, "Solid state gas sensors: state of the art and future activities", Journal of Optoelectronics and Advanced Materials 5 (2003) 1335-1348.
- [1.5] M. J. Madou, S. R. Morrison (eds.), "Chemical sensing with solid state devices", Academic Press, New York, 1989.
- [2.6] A. Mandelis, C. Christofides (eds.), "Physics, Chemistry and technology of solid state gas sensor devices", Wiley (1993).
- [1.7] P. T. Moseley, "Solid state gas sensors", Meas. Sci. Technol. 8 (1997) 223-237.
- [1.8] I. Lundström, "Approaches and mechanisms to solid state based sensing", Sensors and Actuators B 35-36 (1996) 11-19.
- [1.9] J. Tiffany, R. E. Cavicchi, and S. Semancik, "Microarray study of temperature dependent sensitivity and selectivity of metal/oxide sensing interfaces", Proc. SPIE 4205 (2000) 240-247.

- [1.10] J. W. Gardner and P. N. Barlett, "A brief history of electronic noses", *Sensors and Actuators B* 18 (1994) 210-211.
- [1.11] M. C. Horrillo, J. Getino, L. Ares, J. I. Robla, I. Sayago, and F. J. Gutierrez, "Measurements of VOCs with a Semiconductor Electronic Nose", *J. Electrochem. Soc.* 145 (1998) 2486-2489.
- [1.12] T. C. Pearce, S. S. Schiffman, H. T. Nagle, and J. W. Gardner, *Handbook of Machine Olfaction*, Wiley-VCH, Weinheim (2003).
- [1.13] K. Arshak, E. Moore, G.M. Lyons, J. Harris and S. Clifford, "A review of gas sensors employed in electronic nose applications", *Sensor Review* 24 (2004) 181-198.
- [1.14] W. Göpel, J. Hesse, and J. N. Zemel (eds.), "Magnetic Sensors", VCH, Weinheim, 1989.
- [1.15] J. Fraden. "AIP handbook of modern sensors", American Institute of Physics, New York, 1993.
- [1.16] V. Demarne and R. Sanjin, "Thin film semiconducting metal oxide gas sensors". In: G. Sberveglieri. (Ed), "Gas Sensors", Kluwer Academic Publishers, Dordrecht, NL, (1992) 89-116.
- [1.17] D. Hodgins, "The electronic nose: Sensor array-based instruments that emulate the human nose". In: R. Marsili (Ed), "Techniques for analyzing food aroma. New York", Marcel Dekker Inc., New York, US, (1997) 331-371.
- [1.18] C. M. Mari and G. B. Barbi, "Electrochemical gas sensors". In: G. Sberveglieri (Ed), *Gas Sensors*, Kluwer Academic Publishers, Dordrecht, NL, (1992) 29-364.
- [1.19] N. Tagushi, *Jpn. Patent* 45-38200 (1962).
- [1.20] N. N. Greenwood and A. Earnshaw, *Silicium*. In: N. N. Greenwood and A. Earnshaw (Eds), *Chemie der Elemente*. Weinheim: VCH Verlag, pp. 424-426 (1988).
- [1.21] K. J. Albert and N. S. Lewis, "Cross-reactive chemical sensor arrays", *Chem. Rev.* 100 (2000) 2595-2626.
- [1.22] E. Schaller, J. O. Bosset, and F. Escher, "'Electronic noses' and their application to food", *Lebensmittel-Wissenschaft und-Technologie* 31 (1998) 305-316.
- [1.23] W. Schmid, N. Barsan and U. Weimar, "Sensing of hydrocarbons with tin oxide sensors: possible reaction path as revealed by consumption measurements", *Sensors and Actuators B* 89 (2003) 232-236.

- [1.24] S. Hamakawa, L. Li, A. Li and E. Iglesia, "Synthesis and hydrogen permeation properties of membranes based on dense  $\text{SrCe}_{0.95}\text{Yb}_{0.05}\text{O}_{3-\alpha}$  thin films", *Solid State Ionics* 148 (2002) 71-81.
- [1.25] W-H. Tao and C-H. Tsai, " $\text{H}_2\text{S}$  sensing properties of noble metal doped  $\text{WO}_3$  thin film sensor fabricated by micromachining", *Sensors and Actuators B* 81 (2002) 237-247.
- [1.26] G. Dai, "A study of the sensing properties of thin film sensor to trimethylamine", *Sensors and Actuators B* 53 (1998) 8-12.
- [1.27] C. O. Park, S. A. Akbar, J. Hwang, "Selective gas detection with catalytic filter", *Mater. Chem. Phys.* 75, (2002) 56-60.
- [1.28] I. Heberle, A. Liebminger, U. Weimar, W. Göpel, "Optimised sensor arrays with chromatographic pre-separation: characterisation of alcoholic beverages", *Sensors and Actuators B* 68, (2000) 53-57.
- [1.29] M. Penza, G. Cassano, F. Tortorella, and G. Zaccaria, "Classification of food, beverages and perfumes by  $\text{WO}_3$  thin-film sensors array and pattern recognition techniques", *Sensors and Actuators B* 73 (2001) 76-87.
- [1.30] D. S. Vlachos, C. A. Papadopolos, and J. A. Avaritsiotis, "Characterisation of the catalyst-semiconductor interaction mechanism in metal-oxide gas sensors", *Sensors and Actuators B* 44 (1997) 458-461.
- [1.31] P. T. Moseley, "Materials selection for semiconductor gas sensors", *Sensors and Actuators B* 6 (1992) 149-156.
- [1.32] C. Distanto, M. Leo, P. Siciliano, K. Persaud, "On the study of feature extraction methods for an electronic nose", *Sensors and Actuators B* 87 (2002) 274-288.
- [1.33] S. Capone, Ph.D. Thesis, University of Lecce, (2001).
- [1.34] Andrew P. Lee, Brian J. Reedy, "Temperature modulation in semiconductor gas sensing", *Sensors and Actuators B* 60 (1999) 35-42.
- [1.35] I. Eisele, T. Doll and M. Burgmair, "Low power gas detection with FET sensors", *Sensors and Actuators B* 78 (2001) 9-25.
- [1.36] E-L. Kalman, A. Lofvendahl, F. Winquist and I. Lundström, "Classification of complex gas mixtures from automotive leather using an electronic nose", *Analytica Chimica Acta* 403 (2000) 31-38.
- [1.37] H. T. Nagle, R. Gutierrez-Osuna and S. S. Schiffman, "The how and why of electronic noses", *IEEE Spectrum* 35 (1998) 22-31.

- [1.38] J. V. Hatfield, J. A. Covington and J. W. Gardner, "GasFETs incorporating conducting polymers as gate materials", *Sensors and Actuators B* 65 (2000) 253-256.
- [1.39] J. A. Covington, J. W. Gardner, D. Briand and N. F. de Rooij, "A polymer gate FET sensor array for detecting organic vapours", *Sensors and Actuators B* 77 (2001) 155-62.
- [1.40] D. Rutven, "Principles of adsorption and adsorption processes", Wiley-Interscience, New York, (1984).
- [1.41] W. Göpel, "Solid state chemical sensors: Atomistic models and research trends", *Sensors and Actuators* 16 (1989) 167-193.
- [1.42] D. Shaw, "Introduction to colloid & surface chemistry", Butterworth-Heinemann, Oxford, (1992).
- [1.43] R. I. Mase, "Principles of adsorption and reaction on solid surfaces", Wiley, New York (1996).
- [1.44] I. Langmuir, "The Adsorption of gases on plane surface of glass, mica and platinum", *Journal of the American Chemical Society* 40 (1918) 1361-1403.
- [1.45] [http://www.chem.qmul.ac.uk/surfaces/scc/scat3\\_4.htm](http://www.chem.qmul.ac.uk/surfaces/scc/scat3_4.htm).
- [1.46] S. J. Gentry, and T. A. Jones, "The role of catalysis in solid-state gas sensors", *Sensors and Actuators* 16 (1986) 141-163.
- [1.47] D. Kohl, "The role of noble metals in the chemistry of solid-state gas sensors", *Sensors and Actuators B* 1 (1990) 158-165.
- [1.48] J. A. Powell, P. Pirouz, and W. J. Choyke, "Growth and characterization of silicon carbide polytypes for electronic applications", *Semiconductor Interfaces, Microstructures, and Devices: Properties and Applications*, Z. C. Feng, Eds., Institute of Physics Publishing, Bristol, United Kingdom, 1993, 257.
- [1.49] A. Itoh, and H. Matsunami, "Single crystal growth of SiC and electronic devices", *Critical reviews in solid state and Material Science* 22 (1997) 111-197.
- [1.50] W. J. Choyke, H. Matsunami, and G. Pensl, "Silicon Carbide - A Review of fundamental questions and applications to current device technology", Wiley-VCH, Berlin, 1997.
- [1.51] D. J. Larkin, "SiC dopant incorporation control using site-competition CVD", *phys. stat. sol. (b)* 202 (1997) 305-320.
- [1.52] P. Jamet, S. Dimitrijevic, and P. Tanner. "Effects of nitridation in gate oxides grown on 4H-SiC", *J. Appl. Phys.* 90 (2001) 5058-5063.



- [1.53] O. Ambacher, "Growth and applications of group III-nitrides", J. Phys. D: Appl. Phys. 31 (1998) 2653-2710.
- [1.54] H. Harima, "Properties of GaN and related compounds studied by means of Raman scattering", Journal of physics: Cond. Matter 14 (2002) R967-R993.
- [1.55] J. G. Kim, A. C. Frenkel, T. Liu, and R. M. Park, "Growth of molecular beam epitaxy and electrical characteristics of Si-doped zinc blende and wurtzite GaN films deposited on beta-SiC coated (001) Si substrates", Appl. Phys. Lett. 65 (1994) 91-93.
- [1.56] A. M. Malik, "Technology and physics of gate recessed GaN/AlGaN FETs", Masters thesis, Stuttgart University, Stuttgart, Germany, 2003.
- [1.57] D. K. Gaskill, A. E. Wickenden, K. Doverspike, B. Tadayon, and L. B. Rowland, "The effect of organometallic vapor phase epitaxial growth conditions on wurtzite GaN electron transport properties", J. Electron. Mater. 24 (1995) 1525-1530.
- [1.58] W. Götz, N. M. Johnson, C. Chen, H. Liu, C. Kuo, and w. Imler, "Activation energies of Si donors in GaN", Appl. Phys. Lett. 68 (1994) 3144-3146.



## Chapter 2

### 2. Study of Hydrogen-Sensing Performances of Pt/GaN Based Schottky Diodes

#### 2.1 Introduction:

Recently, the use of molecular hydrogen has gained a considerable attention in industrial fabrication processes, medical installations, laboratories and fuelled motor vehicles. For safety reasons, the determination of hazardous hydrogen concentration in air (4.65-74.5%) is an important issue in many areas of human activity. Hence, it is encouraging and interesting to fabricate a hydrogen sensor having high sensitivity, high accuracy, chemical selectivity, small size, short response times, reproducibility, wide operating temperature regimes, simple operation, ease to fabrication, and, finally, low cost.

Lundström *et al.* [2.1] reported on the hydrogen detector fabricated using a Si-based Pd gate field-effect transistor (FET). However, high-temperature operation of silicon-based FETs is limited to the range below 150°C. High band gap semiconductors, especially GaN, were proposed to extend this range to improve the sensitivity and the response time. GaN-based wide band gap semiconductors have become one of the most extensively studied materials and rapid progress has been demonstrated in both optical and electrical devices. Due to their wide band gap and good thermal and chemical stability, GaN based semiconductor materials are also very promising for high temperature gas sensor devices. In addition the small Fermi level pinning characteristics of GaN are also important features that may lead in high gas sensitivity.

Moreover, it was recently demonstrated that a Pt/GaN Schottky contact is very sensitive to the hydrogen exposure. Pt/GaN Schottky diodes [2.2] and AlGaIn/GaN transistors [2.3] have been shown to detect hydrogen and hydrocarbon molecules. These devices have the same principles of operation as the hydrogen-sensitive FET sensors based on Si [2.1] and SiC [2.4-2.6]. On the Pt surface, molecular hydrogen is dissociated into the atomic hydrogen, which diffuses through the Pt contact and is adsorbed at the metal-semiconductor interface. Hydrogen accumulation at the interface changes the work function of the metal gate and therefore the barrier height of the Schottky contact. This effect can be proven by measuring current-voltage (I-V)

curves and has previously been reported for a number of metals [2.7]. Recent elastic recoil detection measurements on Pt/GaN Schottky diodes confirm the presence of hydrogen at the metal-semiconductor interface after exposure to molecular hydrogen at 400°C [2.3].

In this chapter, we show the response of Pt/GaN Schottky diodes to molecular hydrogen. We will prove that the sensitivity of the diode towards hydrogen is affected by the thickness and the microstructure of the Pt. We investigate the microstructure by a combination of electron microscopy and image processing to correlate microstructure and sensitivity.

## 2.2 Hydrogen sensing mechanism of Pt/GaN Schottky diodes:

Pt/GaN Schottky diode hydrogen gas sensors have the same principle of operation as the hydrogen-sensitive FET sensors based on Si [2.1] and SiC [2.4-2.6]. The hydrogen response mechanism of Pt/GaN sensors with a thick, homogeneous Pt gate is illustrated in Fig. 2.1a.

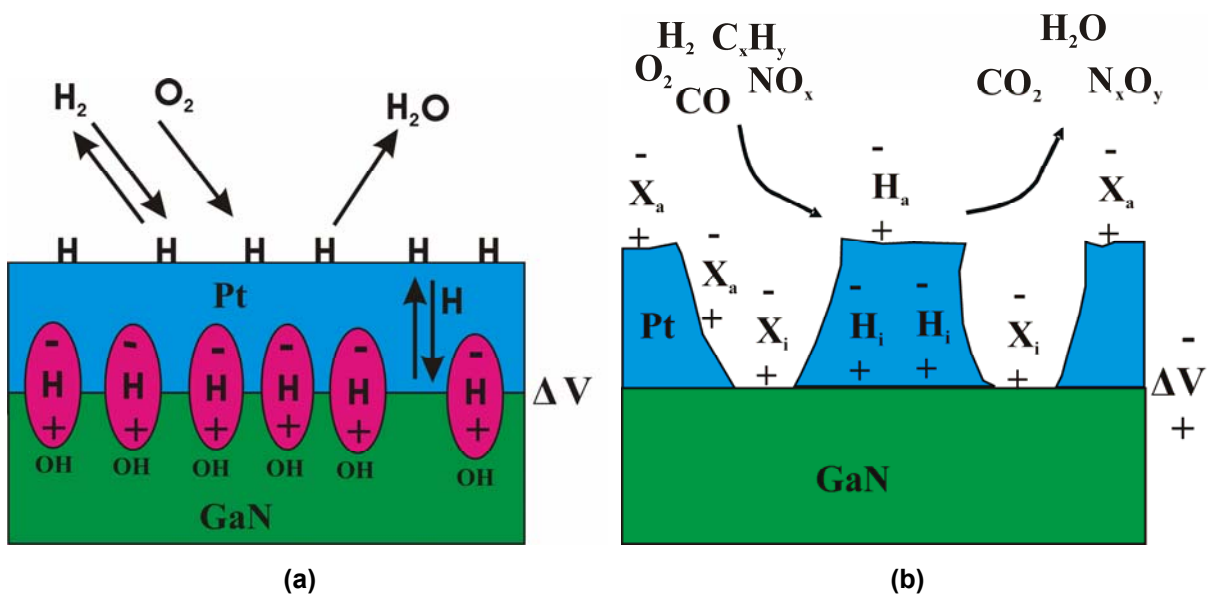


**Fig. 2.1:** Schematic representation of the sensing mechanism of a Pt/GaN Schottky diode. **(a)** With a thick, homogeneous Pt gate, hydrogen atoms formed by dissociation on the Pt surface, rapidly diffuse through the metal gate and become trapped at the Pt/GaN interface, forming a polarization layer. **(b)** With a porous gate the gas response may have contribution from hydrogen atoms or other polarized species both on the (oxidized) GaN surface and on the catalyst ( $H_a$ ,  $H_i$ : adsorbed and interfacial hydrogen metal,  $X_a$ ,  $X_i$ : adsorbed and interfacial molecules).

On the Pt surface, molecular hydrogen is dissociated into atomic hydrogen, which diffuses rapidly, within microseconds, through the metal and is adsorbed at the metal/GaN interface. Hydrogen atoms adsorbed at the interface are polarized and form a dipole layer. This dipole layer is effectively created by O-H-bonds and consequently strongly dependent on the presence of oxygen on the GaN surface [2.3, 2.8]. The exposure of the GaN surface to air prior to the catalyst deposition is sufficient to accumulate oxygen for effective sensor operation. In contrast, complete *in-situ* processing resulted in decreased sensing performance [2.8]. The dipole layer will change the effective work function of the metal gate, and therefore the barrier height of the Schottky contact. This shifts the current-voltage (I-V) curve of a Schottky diode toward a lower voltage (Fig. 2.2). The gas response of the sensor measured as the voltage shift,  $\Delta V$ , at a constant current is also indicated in Fig. 2.2.

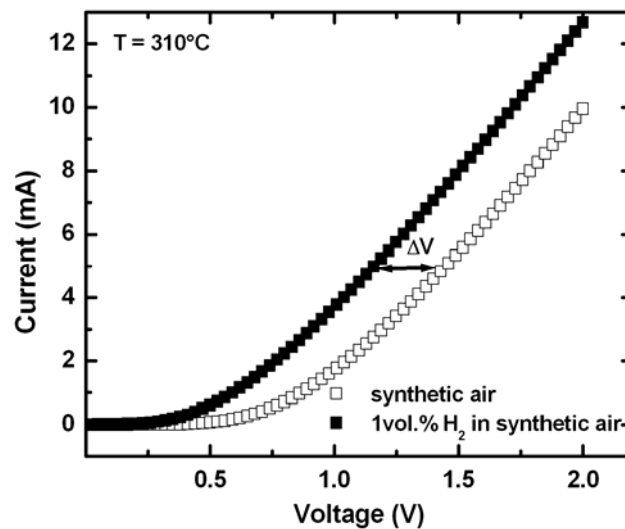


**Fig. 2.2:** I-V curve of a Pt/GaN Schottky diode with Pt thickness  $d_{\text{Pt}} = 8 \text{ nm}$  and area  $A_{\text{Pt}} = 250 \times 250 \mu\text{m}^2$  operated at  $310^\circ\text{C}$ , in synthetic air (open symbols) as well as 1 vol.% hydrogen in synthetic air (closed symbols). The sensor response is indicated by an arrow.

If oxygen is present in the ambient, water formation will occur on the catalytic surface, which affects the hydrogen response. The formation of water is assumed to follow the scheme:





If the device is operated at an elevated temperature ( $>100^\circ\text{C}$ ), which desorbs the formed water from the surface.

However, Pt/GaN sensors exhibit sensitivity to both oxidizing and reducing gases [2-9, 2-10]. Since hydrogen is the only specie that can diffuse through the catalyst, an alternating transport mechanism was proposed [2-10] taken the porosity of Pt into account (Fig. 2.1b). At porous Pt gates, patches of GaN are directly exposed to the gas ambient thus allowing a direct interaction of the test gases with the polar (oxidized) GaN surface leading to polarized adsorbates. This model was confirmed by the investigation of the CO sensitivity of Pt/GaN Schottky diodes [2.11]. By decreasing the catalyst thickness and thermal annealing, the response on CO was increased due to the surface restructuring of the Pt film, which opens channels (pores) for gas transports towards a free GaN surface.

### 2.3 Theory of Schottky diode:

Before the investigation of the hydrogen sensing performance of the Schottky diode, a theoretical understanding of its functionality is necessary. It is also necessary to know how its parameters can be calculated (extracted) from I-V and C-V curves. The most important parameters of the Schottky diodes used as  $H_2$  gas sensors are: the barrier height  $q\Phi_B$ , ideality factor  $n$ , saturation current density  $J_s$ , and the series resistance  $R_s$  since the exposure to  $H_2$  influence them.

#### 2.3.1 Metal-semiconductor contact:

In 1874, i.e., 133 years ago Braun [2.12] first reported on rectifying metal-semiconductor contacts. Schottky et al. explained this behavior by space-charge layers on the semiconductor side of the interface that are depleted of mobile majority carriers [2.13]. The most characteristic parameter of such a Schottky contact is its barrier height, i.e., the energy separation between the Fermi level and the edge of the majority carrier band right at the interface. Fig. 2.3a shows the energy band diagram of a metal adjacent to  $n$ -type semiconductor.

The metal work function is generally different from the semiconductor work function. The work function is the energy difference between the Fermi level  $E_F$  and the vacuum level  $E_{\text{vacuum}}$  ( $q\Phi_m$  for the metal and  $q\Phi_s$  for the semiconductor).

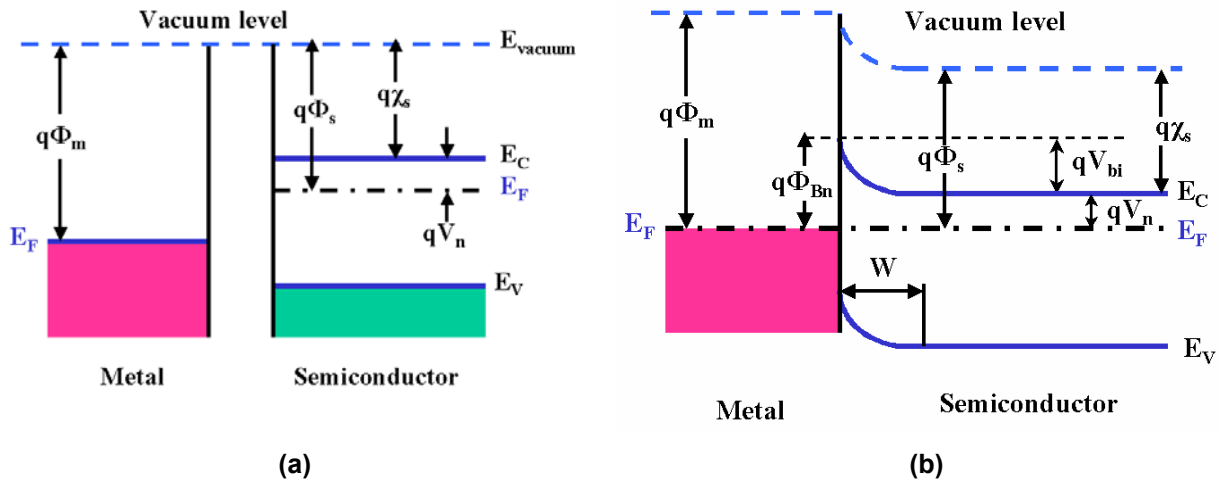


**Fig. 2.3:** Energy band diagram of metal contact to  $n$ -type semiconductor. **(a)** Neutral materials separated from each other. **(b)** Thermal equilibrium situation after contact has been made.

Work functions of metals that are commonly used for fabrication of metal-semiconductor contacts are listed in the Tab. 2.1. From these elements Pt, Ni, Pd, and Au are commonly used for Schottky contact processing. Pd and Pt have very large work functions which makes them ideal for use as Schottky contacts on most  $n$ -type semiconductors, including  $n$ -type GaN. They are also useful for contacts because of their resistance to oxidation and corrosion. In this work Pt was selected to serve as a catalytic metal due to its high work function and stability during the exposure to hydrogen.

**Tab. 2.1:** Work functions of metals commonly used for fabrication of metal-semiconductor contacts.

Metal	Work function (eV)	Metal	Work function (eV)
Pt	5.65	Zn	4.33
Ni	5.15	Al	4.28
Pd	5.12	Ag	4.26
Au	4.65	Pb	4.25
Cu	4.65	Ta	4.25
W	4.55	Cd	4.22
Cr	4.5	Ga	4.2
Hg	4.49	In	4.12
Sn	4.42	Zr	4.05
Ti	4.33	Cs	2.14

The electron affinity  $q\chi_s$  is the energy difference between the conduction band edge and the vacuum level. When metal is making intimate contact with a semiconductor, the Fermi levels in the two materials must be coincident at thermal equilibrium. In addition, the vacuum level must be continuous. These two requirements determine a unique energy band diagram for the ideal metal-semiconductor contact as shown in Fig.2.3b. For this ideal case the *Barrier height*  $q\Phi_{Bn}$  is simply the difference between the metal work function and the electron affinity of the semiconductor:

$$q\Phi_{Bn} = q(\Phi_m - \chi). \quad (2.5)$$

Elemental Pt Schottky diodes exhibit ideal Schottky behaviour and have a reasonably high barrier height of  $\sim 1$  eV on n-GaN [2.14, 2.15]. For an ideal contact between a metal and a  $p$ -type semiconductor, the Barrier height  $q\Phi_{Bp}$  can be determined using a similar procedure:

$$q\Phi_{Bp} = E_g - q(\Phi_m - \chi). \quad (2.6)$$

where  $E_g$  is the bandgap of the semiconductor, Therefore, for a given semiconductor and for any metal, the sum of the barrier heights on  $n$ -type and  $p$ -type substrates is expected to be equal to the bandgap:

$$q(\Phi_{Bn} + \Phi_{Bp}) = E_g. \quad (2.7)$$

The energy band diagrams for metal on  $n$ -type semiconductor are shown in Fig. 2.4 for different biasing conditions. The built-in potential  $V_{bi}$  for the  $n$ -type semiconductor is given by:

$$V_{bi} = \Phi_{Bn} - V_n, \quad (2.8)$$

where  $V_n$  is the potential difference between the Fermi level and conduction band edge  $E_C$ .

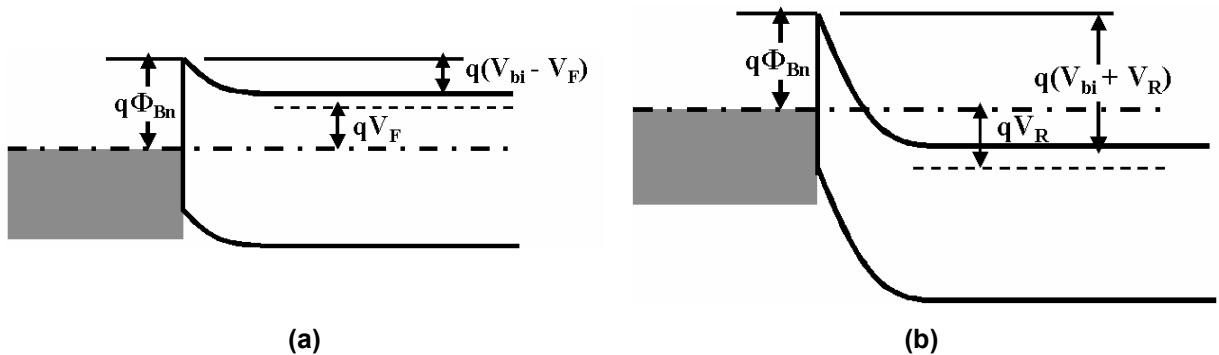


**Fig. 2.4:** Energy band diagram of metal contact to  $n$ -type semiconductor under different biasing conditions. **(a)** Forward bias. **(b)** Reverse bias.



Under the abrupt approximation, the carrier density (electron in  $n$ -type semiconductor) is  $\rho(x) = qN_D$  for  $x < W$ , and  $\rho(x) = 0$  and  $dV(x)/dx = 0$  for  $x > W$ , where  $W$  is the depletion layer width, We then obtain:

$$W = \sqrt{\frac{2\epsilon_s}{qN_D}(V_{bi} - V)}. \quad (2.9)$$

The space charge  $Q_{sc}$  per unit area of the semiconductor and the depletion layer capacitance  $C$  per unit area are given by:

$$Q_{sc} = qN_D W = \sqrt{2q\epsilon_s N_D (V_{bi} - V)}, \quad (2.10)$$

$$C = \left| \frac{\partial Q_{sc}}{\partial V} \right| = \sqrt{\frac{q\epsilon_s N_D}{2(V_{bi} - V)}} = \frac{\epsilon_s}{W}. \quad (2.11)$$

Equation (2.11) can be written in the form:

$$\frac{1}{C^2} = \frac{2(V_{bi} - V)}{q\epsilon_s N_D}, \quad (2.12)$$

or:

$$\frac{-d(1/C^2)}{dV} = \frac{2}{q\epsilon_s N_D}, \quad (2.13)$$

$$N_D = \frac{2}{q\epsilon_s} \left[ \frac{-1}{d(1/C^2)/dV} \right]. \quad (2.14)$$

Thus, measurements of the capacitance per unit area as a function of voltage can provide the impurity distribution directly from Eq. (2.14). If  $N_D$  is constant throughout region, we should obtain a straight line by plotting  $1/C^2$  versus  $V$ . Fig. 2.5 is a plot of  $1/C^2$  versus  $V$  for Pt/GaN Schottky diode with Pt thickness ( $d_{Pt} = 24$  nm) and area ( $A_{Pt} = 250 \times 250 \mu\text{m}^2$ ) at room temperature.

The voltage intercept at  $1/C^2 = 0$  gives the built-in voltage  $V_{bi}$  of 1.7 V. The built-in voltage is related to the barrier height by the relationship:

$$\Phi_B = V_{bi} + V_n = \left( V_{bi} + \left( \frac{kT}{q} \right) \ln \left( \frac{N_C}{N_D} \right) \right), \quad (2.15)$$

where  $N_C$  is the effective density of states in the conduction band. For GaN  $N_C = 4.3 \times 10^{14} \text{ T}^{3/2} \text{ cm}^{-3}$ , at 300 K,  $N_C = 2.21 \times 10^{18} \text{ cm}^{-3}$ . The room temperature barrier height calculated using Eq. (2.15) is 1.75 eV. While the barrier height  $\Phi_B$  is the parameter that is changed during the exposure to hydrogen and  $\Phi_B$  can be extracted from the plot  $1/C^2$  versus  $V$ , the C-V characteristics is an important method that can be used to study the Pt/GaN Schottky diodes used as  $\text{H}_2$  gas sensors.

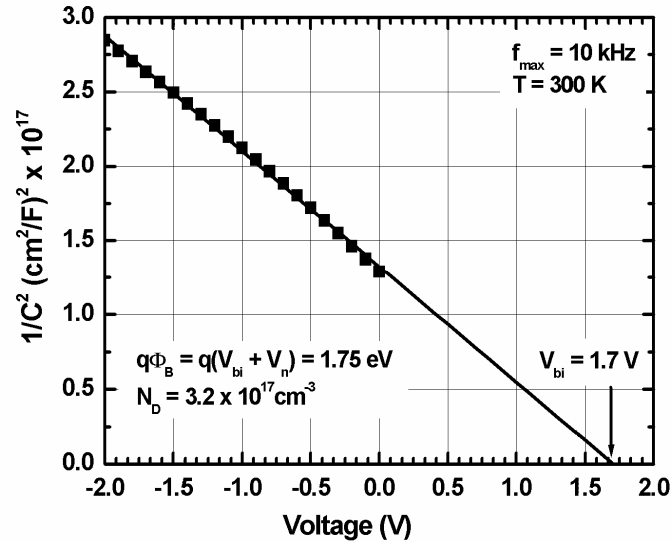


**Fig. 2.5:** Plot of  $1/C^2$  versus applied voltage for a Pt/GaN Schottky diode with  $d_{Pt} = 40$  nm and  $A_{Pt} = 250 \times 250 \mu\text{m}^2$ .

### 2.3.2 Current-Voltage Characteristics:

The current transport in metal-semiconductor contacts is due mainly to majority carriers, in contrast to  $p-n$  junctions, where current transport is due mainly to minority carriers. The current can be transported in various ways under forward bias conditions as shown in Fig. 2.6. The four processes are [2.16]:

(a) emission of electrons from the semiconductor over the top of the barrier into the metal. This is the dominant process for Schottky diodes with moderately doped semiconductors operating at or near room temperature); (b) quantum mechanical tunneling through the barrier in heavily doped semiconductors; (c) electron-hole recombination in the space-charge region; and (d) recombination in the neutral region (equivalent hole injection from the metal to the semiconductor).

The transport of electrons over the potential barrier have been discussed in terms of thermionic emission diffusion by Crowell and Sze [2.17], who have shown that the complete expression of the current density-voltage ( $J$ - $V$ ) characteristics for the Schottky diode is:

$$J_{ideal} = J_s \left[ \exp\left(\frac{qV}{kT} - 1\right) \right], \quad (2.16)$$

where the saturation current  $I_s$  and the saturation current density  $J_s$  are defined by:

$$J_s = \left( \frac{I_s}{A_d} \right) = A^{**} T^2 \exp\left( -\frac{q\Phi_B}{kT} \right), \quad (2.17)$$

The quantities  $A_d$ ,  $A^{**}$ ,  $T$ ,  $q$ ,  $k$  and  $\Phi_B$  are the diode area, the effective Richardson constant, temperature in Kelvin, the electronic charge, Boltzmann's constant and the barrier height, respectively.

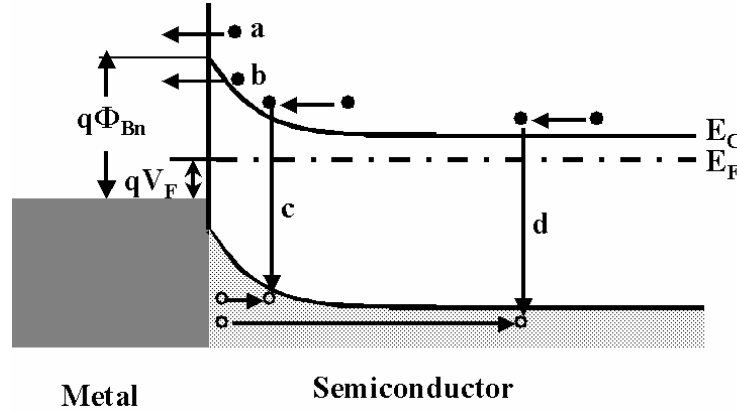


**Fig. 2.6:** Four basic transport processes in forward-biased Schottky barrier on an  $n$ -type semiconductor [2.16].

The barrier height is commonly calculated from the saturation current  $I_s$ , determined by the extrapolation of the  $\log(I)$  versus  $V$  to  $V = 0$ . The current axis intercept for the straight-line portion of this semi-logarithmic plot at  $V = 0$  is given by  $I_s$ . The barrier height  $\Phi_B$  is calculated from  $I_s$  in Eq. (2.17) according to

$$\Phi_B = \frac{kT}{q} \ln\left( \frac{A_d A^{**} T^2}{I_s} \right) = \frac{kT}{q} \ln\left( \frac{J_s}{A^{**} T^2} \right). \quad (2.18)$$

The ideality factor  $n$  is introduced to describe the deviation of the experimental I-V data from the ideal TE model using the definition:

$$n = \frac{q}{kT} \left( \frac{d \ln I}{dV} \right)^{-1}. \quad (2.19)$$

However, a deviation from the ideal behaviour is frequently observed and the I-V curves cannot be fitted by Eq. (2.16). The Schottky effect, series and parallel resistance, the presence of other mechanisms and inhomogeneous Schottky barrier heights (SBHs) have been established by several authors as the most important causes of non-ideal behaviour. Regarding the linear increase of barrier height with

forward bias ( $V \geq 3kT/q$ ) and series resistance ( $R_s$ ), Eq. (2.16) is modified and can be rewritten as:

$$J = J_s \exp\left(\frac{qV_d}{nkT}\right) \left[ 1 - \exp\left(-\frac{qV_d}{kT}\right) \right], \quad (2.20)$$

where  $V_d = (V - IR_s)$  is the diode voltage. When the parallel resistance ( $R_p$ ) is introduced into Eq. (2.20), the total current can be written as [2.18]:

$$I_T = I + \frac{V_d}{R_p}. \quad (2.21)$$

The effects of the  $R_s$  and  $R_p$  are to deviate the  $\ln(I)$  versus  $V$  plot from a straight line at higher and lower forward bias, respectively.

Semi-logarithmic forward-bias I-V characteristics of a Pt/GaN Schottky diode with Pt thickness ( $d_{Pt} = 8$  nm) and area ( $A_{Pt} = 250 \times 250 \mu\text{m}^2$ ) at room temperature are presented in Fig. 2.7.

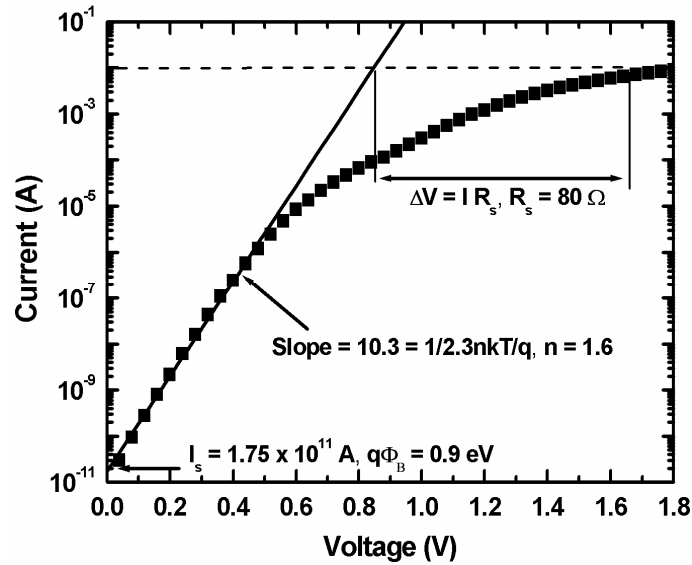


**Fig. 2.7:** Log( $I$ ) versus applied voltage ( $V$ ) at room temperature for a Pt/GaN Schottky diode with  $d_{Pt} = 8$  nm and  $A_{Pt} = 250 \times 250 \mu\text{m}^2$ .

From the slope  $n = 1.6$  and from the  $V = 0$  intercept, we find  $I_s = 1.75 \times 10^{-11}$  A. The barrier height calculated from Eq. (2.18) is  $q\Phi_B = 0.9 \pm 0.003$  eV (for  $A^{**} = 26$  A  $\text{cm}^{-2}$   $\text{K}^{-2}$  and n-GaN). The derivation of the log( $I$ )- $V$  curve from linearity is  $\Delta V = IR_s$ , allowing the series resistance  $R_s$  to be determined according to  $R_s = \Delta V/I = 80 \Omega$ .

The series resistance  $R_s$  can be also extracted from the slope of the  $I(dV/dI)$  versus  $I$  curve as per the following equation, at a current value where the experimental I–V data begin to display current saturation (Fig. 2.8):

$$I\left(\frac{dV}{dI}\right) = IR_s + \frac{kT}{q}. \quad (2.22)$$

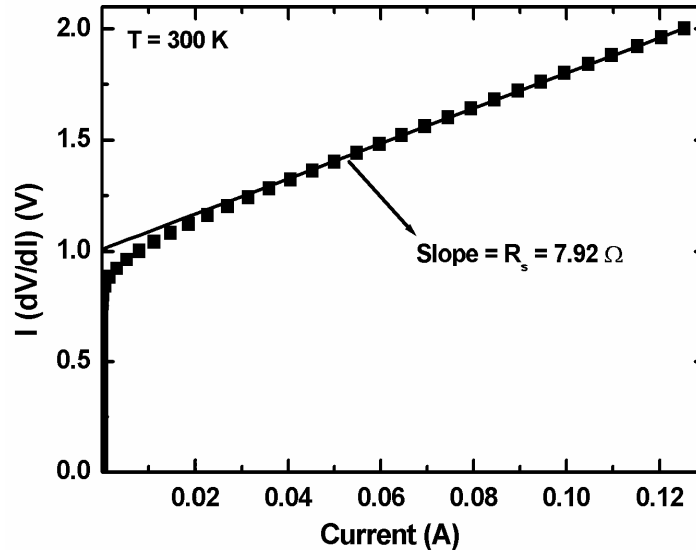


**Fig. 2.8:** Variation of  $I(dV/dI)$  with the current  $I$  at room temperature for Pt/GaN Schottky diode with  $d_{Pt} = 40$  nm and  $A_{Pt} = 1000 \times 1000 \mu\text{m}^2$ .

### 2.3.3 Other methods to determine the barrier height $\Phi_B$ :

For the evaluation of the barrier height, one may also make use of the Richardson plot of the saturation current density. Eq. (2.17) can be rewritten as:

$$\ln\left(\frac{J_s}{T^2}\right) = \ln(A^{**}) - \frac{q\Phi_B}{k}\left(\frac{1}{T}\right). \quad (2.23)$$

Therefore, the  $\ln(J_s/T^2)$  versus  $1/T$  plot should correspond to a straight line with a slope giving barrier height  $\Phi_B$  ( $T = 0$ ) at 0 K and the intercept at the ordinate, the Richardson constant ( $A^{**}$ ).

The  $\ln(J_s/T^2)$  versus  $1000/T$  plot for a Pt/GaN Schottky diode with  $d_{Pt} = 24$  nm and  $A_{Pt} = 1000 \times 1000 \mu\text{m}^2$  is shown in Fig. 2.9. The value of the Richardson constant for Pt-GaN diodes was found from the intercept of the  $\ln(J_s/T^2)$  vs.  $1000/T$  plot to be  $0.18 \text{ A cm}^{-2} \text{ K}^{-2}$ , respectively. The average value of Schottky barrier height was found from the slope of the plot to be 1 eV. The measured value of  $A^{**}$  is much smaller than the theoretical value ( $26 \text{ A cm}^{-2} \text{ K}^{-2}$ ). In the literature, there is a large

scattering in the measured value of the Richardson constant. Values of  $A^{**}$  of 0.006 [2.19] and 14.68  $\text{A cm}^{-2} \text{K}^{-2}$  [2.20] for Au/GaN, 0.04 [2.15] and 3.2  $\text{A cm}^{-2} \text{K}^{-2}$  [2.21] for Pd/GaN, 6.61 [2.14] and 64.61  $\text{A cm}^{-2} \text{K}^{-2}$  [2.21] for Pt/GaN have been reported. Almost all published values of  $A^{**}$  are far from the theoretical Richardson constant of GaN (26  $\text{A cm}^{-2} \text{K}^{-2}$ ).

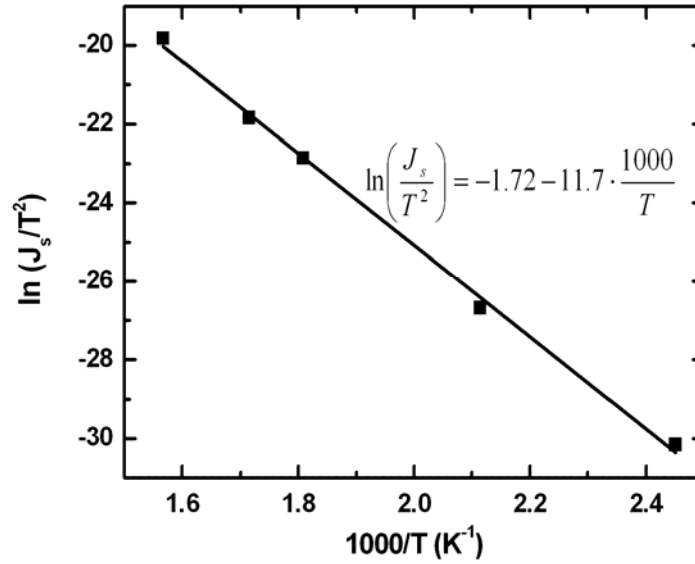


**Fig. 2.9:** Richardson plot  $\ln(J_s/T^2)$  versus  $1000/T$  with linear fit  $\ln(J_s/T^2) = -1.72 - 11.7 \times (1000/T)$  for a Pt/GaN Schottky diode with  $d_{\text{Pt}} = 24 \text{ nm}$  and  $A_{\text{Pt}} = 1000 \times 1000 \mu\text{m}^2$ ,  $\Phi_B = 1 \text{ eV}$  and  $A^{**} = 0.18 \text{ A cm}^{-2} \text{K}^{-2}$ .

The barrier height,  $\Phi_B$ , of the Schottky junction can be also calculated using the Norde method. The method involves a Norde function,  $F(V)$ , being plotted against  $V$ .  $F(V)$  is given by [2.22]:

$$F(V) = \frac{V}{2} - \frac{kT}{q} \ln \left[ \frac{I(V)}{A_d A^{**} T^2} \right], \quad (2.24)$$

where the symbols bear the same significance as mentioned above.

The slope of the graph of  $F(V)$  vs.  $V$  changes from  $-1/2$  to  $+1/2$  and passes through a minimum within these two limits. The barrier height of the Schottky junction is then calculated as:

$$\Phi_B = F(V_{\min}) + \frac{V_{\min}}{2} - \frac{kT}{q}, \quad (2.25)$$

where  $F(V_{\min})$  is the minimum value of  $F(V)$  and  $V_{\min}$  is the corresponding voltage.

Fig.2.10 shows a plot of  $F(V)$  versus  $V$  at different temperatures for a Pt/GaN Schottky diode with  $d_{Pt} = 24 \text{ nm}$  and  $A_{Pt} = 1000 \times 1000 \mu\text{m}^2$ .

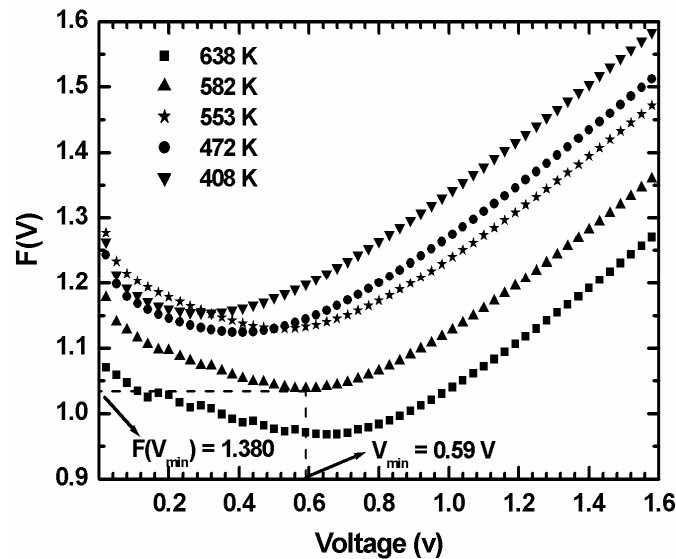


**Fig. 2.10:** Plot of  $F(V)$  versus  $V$  (Norde method) at different temperatures for a Pt/GaN Schottky diode with  $d_{Pt} = 40 \text{ nm}$  and  $A_{Pt} = 250 \times 250 \mu\text{m}^2$ .

## 2.4 Device Structure and Fabrication:

The basic device structure consisted of GaN ( $n$ -type, Si-doped) as a semiconductor with an ohmic contact and a Pt gate as the Schottky barrier (Fig. 2.11). Material with Ga-face polarity was obtained by depositing a thin AlN nucleation layer prior to starting the actual GaN growth.

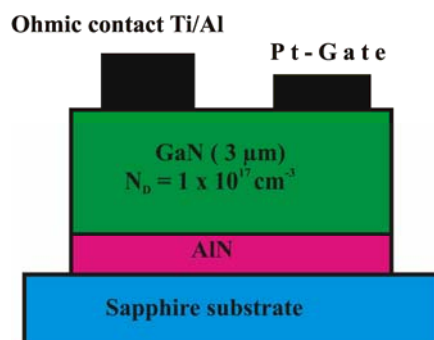


**Fig. 2.11:** Device cross section of the studied Pt/GaN Schottky diode.

Three microns of GaN were grown on  $c$ -plane sapphire by metal organic chemical vapor deposition (MOCVD). The free electron concentration of GaN was determined

to  $\sim 1 \times 10^{17} \text{ cm}^{-3}$  by capacitance-voltage (C-V) measurements. Leighton sheet measurements were also performed on the wafers and an average sheet resistance of  $1300 \text{ } \Omega/\square$  was measured on all three wafers. The devices were initially deposited with 200 nm silicon dioxide ( $\text{SiO}_2$ ) layer grown at  $425^\circ\text{C}$  as a passivation layer. This 200 nm thick layer was then patterned in order to realize an ohmic contact to the  $n$ -type GaN. This was done by patterning photoresist over the oxide, wet etching the oxide in the opened areas, then depositing Ti/Al with 30/70 nm, followed by a lift-off step.

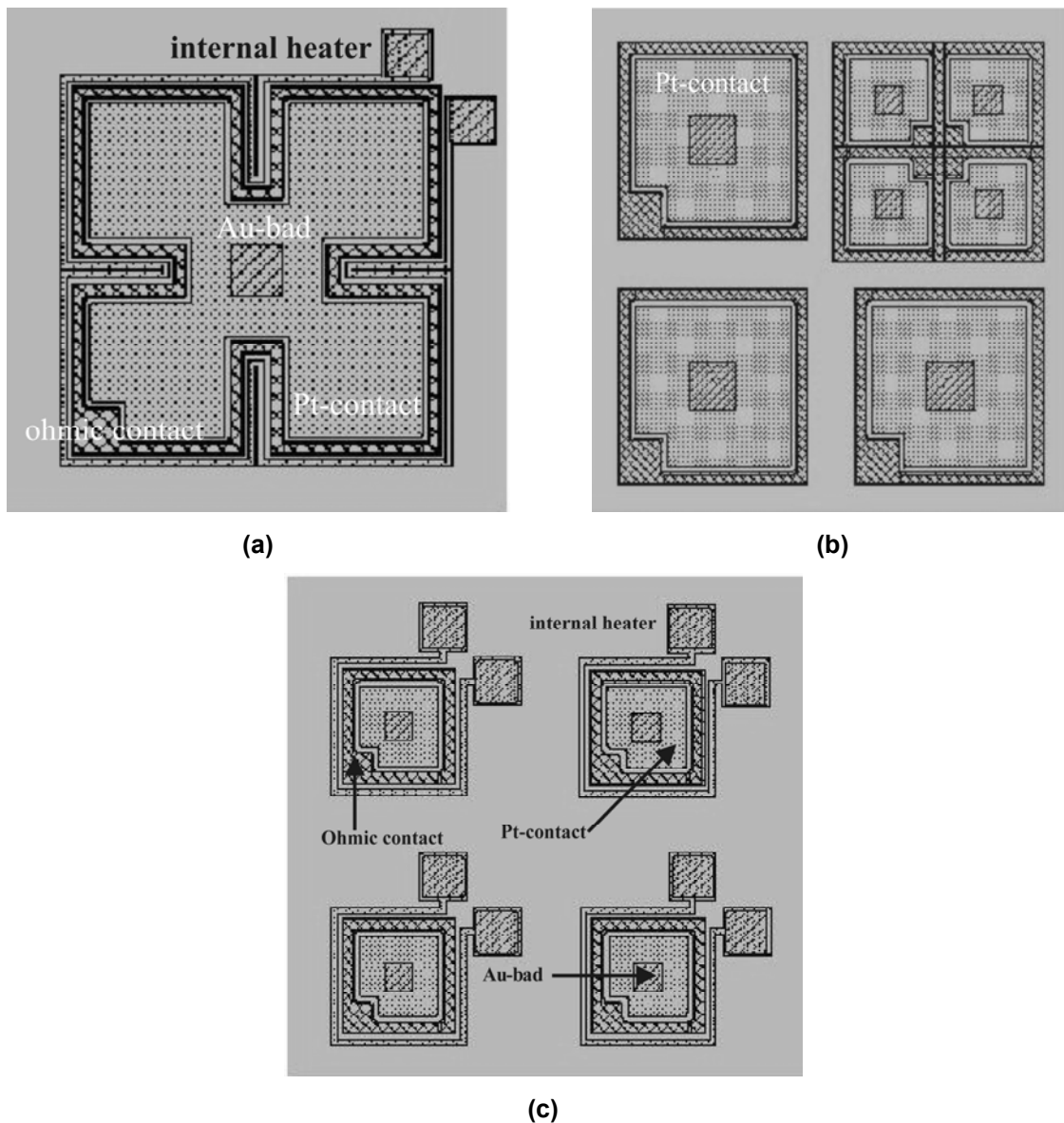


**Fig. 2.12:** Optical micrographs of the investigated sensors (a)  $1000 \times 1000 \text{ } \mu\text{m}^2$ ; (b)  $500 \times 500 \text{ } \mu\text{m}^2$ ; (c)  $250 \times 250 \text{ } \mu\text{m}^2$ .



The ohmic contact was annealed at 800°C for 1 min in nitrogen atmosphere to reduce contact resistance. Next, the Schottky contact was made in the same fashion. Three different sets Schottky diodes were processed with either 8, 24, or 40 nm thick continuous layer of platinum as Schottky contacts evaporated using e-beam evaporation. The GaN surface was treated with buffered oxide etch (BOE) (7:1) to remove the surface oxide before evaporation. An internal heater consisting of Ti/Al/Ti with 20/100/80 nm was fabricated around the device to facilitate resistive heating. Finally, gold bond pads were evaporated on the ohmic and Schottky contacts, then the devices were wire bonded to a 16 pin TO-8 header package. An external heating element was presented in this package to increase the temperature of the device up to 365°C during operation. The active gate area was varied between  $250 \times 250 \mu\text{m}^2$  and  $1000 \times 1000 \mu\text{m}^2$ . The optical micrographs of the investigated sensors are shown in Fig. 2.12.

## **2.5. Experiments:**

### **2.5.1 AES and SEM measurements (surface and interface measurements):**

The surface and interface properties of Pt/GaN Schottky diode gas sensors studied in this chapter are investigated using Auger Electron Spectroscopy (AES), Scanning Electron Microscopy (SEM). The AES system used for this work was a Riber ASC 2000 (Fig. 2.13) equipped with a differential pumped ion gun VG X5.

The Auger sputter depth profiling procedures were carried out in the Auger spectrometer Riber ASC 2000 (Fig.2.13) equipped with differential pumped ion gun VG X5. The electron gun was operated at 3 keV with the current 1  $\mu\text{A}$ . The spot size was approximately 20  $\mu\text{m}$ . The emitted electrons were analysed by cylindrical mirror analyser with coaxially placed electron gun working with resolution 0.3%. The Auger transition were recorded in the differentiated mode. The ion gun was operated at 1 keV, argon was used as the sputtering gas. The ion beam was rastered over an area of some  $\text{mm}^2$ . The ion beam current density was approximately 42  $\mu\text{A}/\text{cm}^2$  measured perpendicular to the ion beam direction. The angle between the electron and ion gun was fixed in the spectrometer. For sputtering under 60° with respect to the surface normal the angle between surface normal and the electron beam was 22°.

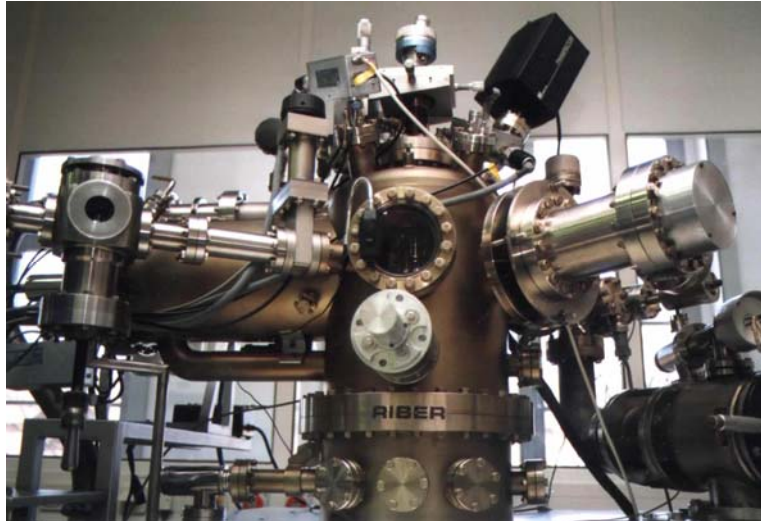


**Fig. 2.13:** AES system (Riber ASC 2000).

High-resolution SEM images of the surfaces were taken and processed using Clemex Vision image processing and analysis software. The images were comprised of 1024 by 768 pixels with 256 gray levels from black to white. The images were then imported into the image analysis program and processed to obtain the grain boundaries and any observed porosity. The mechanism for analysis is the contrast difference between features of interest and the remainder of the image. The grain boundaries were enhanced and thresholded in order to reduce the gray level image to a binary image so that the program could measure the porosity has a much darker to black gray level range. The segmented binary image containing grain boundaries was supplemented with manual image editing to complete and delineate the grain boundaries. The image analysis software quantified the grain sizes and determined the number of grain boundaries automatically.

### **2.5.2 Electrical measurements without gas:**

An Agilent 4142B Modulator DC Source was used for the current-voltage (I-V) measurements. The capacitance-voltage (C-V) measurements were carried out at a test frequency of 10 kHz using an Impedance analyzer (Solartron 1296)

### **2.5.3. Measurements set-up for gas-sensing characterization:**

Fig. 2.14 shows an overall view of the gas-sensing measurement system.

The important features, such as the measurement chamber, gas delivery system, and control units are indicated in the picture.

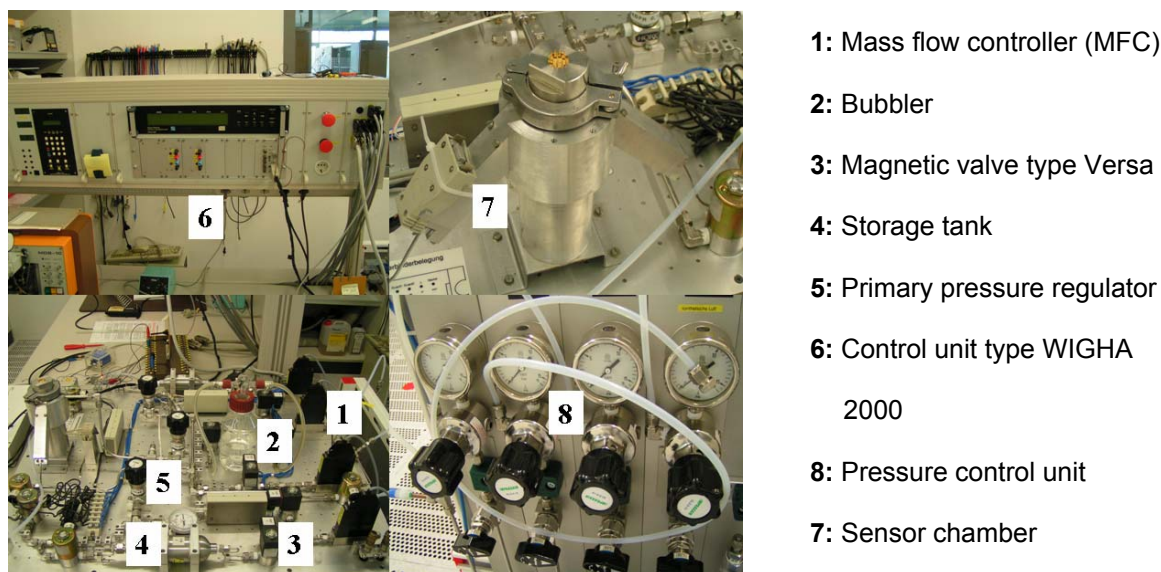


**Fig. 2.14:** Overall view of the measurement set-up for the gas-sensing characterization of Pt/GaN gas sensors.

### 2.5.3.1 Gas delivery system:

The schematic details of the gas delivery system, including the magnetic valves (MV), two mass flow controllers (MFC), the first (maximum flow rate: 1l/min) for dry synthetic air (20% O<sub>2</sub> and 80% N<sub>2</sub>) and the other (maximum flow rate: 50 ml/min) for the analysing gas (1%H<sub>2</sub> in synthetic air) is presented in Fig. 2.15. The control unit (type WIGHA 2000) controls the MFCs and magnetic valves; the gas concentration can be adjusted within the range of 1 to 10000 ppm depending on the initial gas concentration supplied. All gases used were of 99.999% purity or better.

### 2.5.3.2 Gas-sensing measurement chamber:

Gas-sensing measurements require defined atmospheres. Consequently, the gas must be introduced into a defined reaction volume. This volume is assured by a closed measurement chamber. The measurement chamber, with a reaction volume of 1 cm<sup>3</sup> (1 ml), is fabricated out of stainless steel (Fig. 2.14). The gases were supplied to the gas chamber through tubes with a diameter of 2 mm.

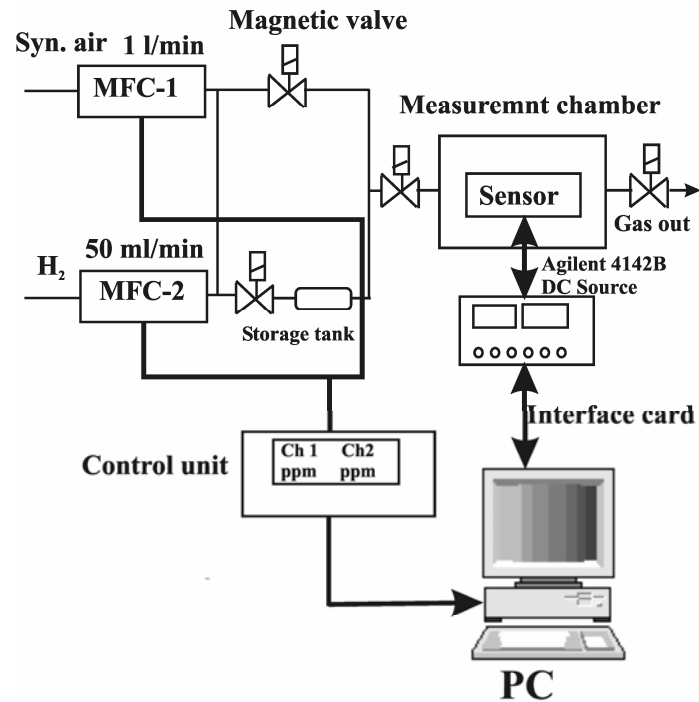


Fig. 2.15: Schematic drawing of the gas delivery system.

### 2.5.3.3 Electrical measurements procedure:

After injecting the hydrogen gas into the testing chamber of the gas sensor characterization system through the mass flow controller, the forward and reverse current-voltage characteristics of the sensor were measured separately at different temperatures and then compared to the results obtained in absent of hydrogen gas (in synthetic air). I-V characteristics were measured, generally 10 min after introducing the test gas into the test chamber. For I-V, an Agilent 4142B modulator DC source (Fig. 2.16) was used.

For measurements of the response and recovery times (dynamic behaviour) of the sensors, a source-measure-unit (model 2000, Keithley Instr.) with an external voltage source was used (Fig. 2.16). The instruments were connected via an IEEE-488 bus to the computer. During the measurements, the sensor was held at a constant voltage (1 V) and exposed to different concentration of the test gas at different operation temperatures.

Heating the sensors was provided by a patterned platinum resistive element on a sapphire substrate. The heater was placed beneath the sensor and controlled by a regulated DC power supply (Fig. 2.16). A thermocouple type S (Pt10%Rh-Pt) (see **Appendix A**) was placed near the sensor to determine its temperature.

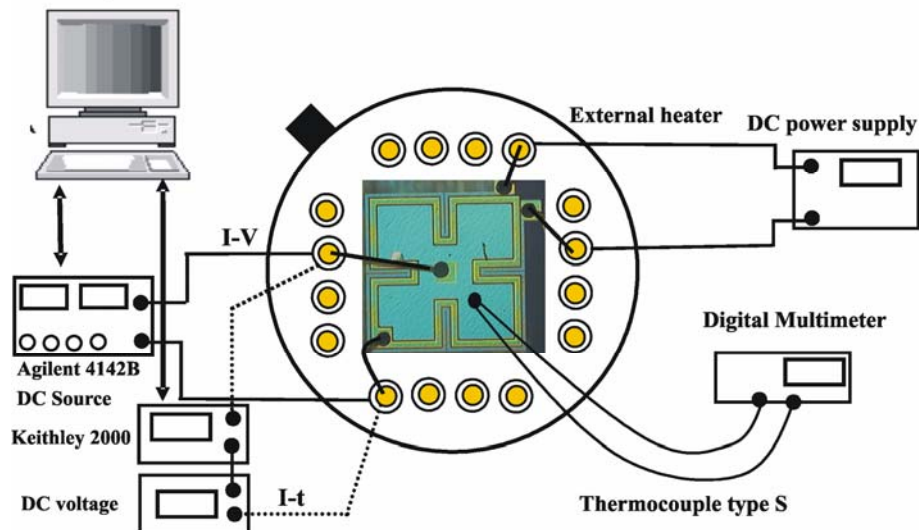


Fig. 2.16: Schematic presentation of the electrical (I-V and I-t) gas sensing measurements.

## 2.6 Results and Discussion:

### 2.6.1 Chemical characterization of the Pt/GaN Schottky diodes:

Fig. 2.17 shows the Auger signal pph (peak-to-peak height) versus sputter time for Pt/GaN sensors with area  $A_{Pt} = 250 \times 250 \mu\text{m}^2$  and three different Pt thickness.

As can be seen from Fig. 2.17, a number of oxygen atoms at the interface between Pt layer and GaN are observed, indicating the existence of a very thin native oxide layer. In addition, no significant reaction between Pt metal and GaN semiconductor is observed. This thin native oxide layer has been found to play an important role in the effectiveness in sensing hydrogen for similar devices [2.8].

Oxygen and carbon observed within the Pt layer as shown in Fig. 2.17 were considered to originate mainly from the atmosphere during the evaporation process or handling the film in air after the deposition.

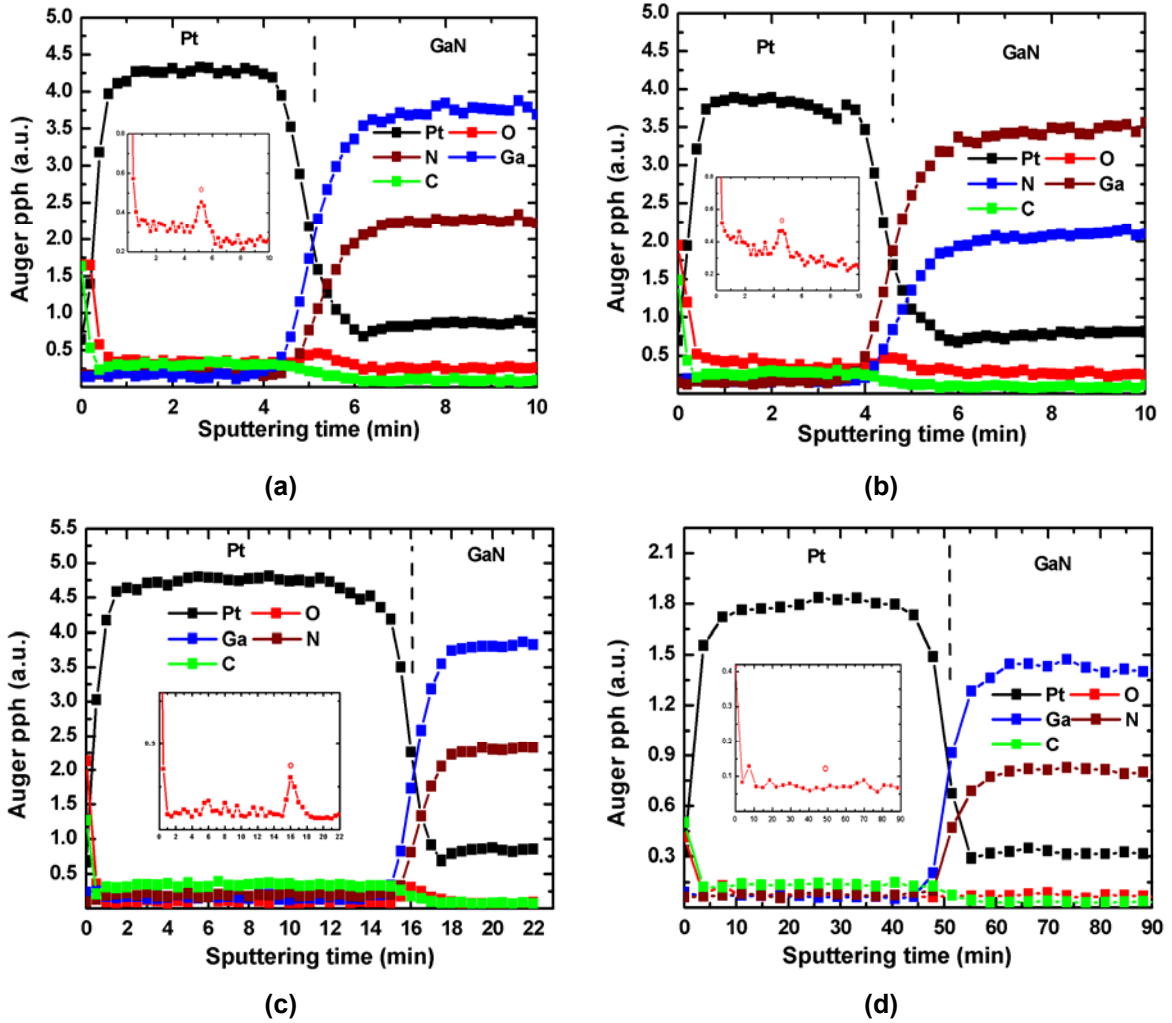


**Fig. 2.17:** AES depth profiles of the Pt/GaN sensors with area  $A_{Pt} = 250 \times 250 \mu\text{m}^2$  and three different Pt thickness. (a) and (b): 8 nm, (c): 24 nm, and (d): 40 nm.

## 2.6.2 Electrical characterization in air:

### 2.6.2.1 Room temperature measurements:

The Pt/GaN Schottky diodes characterized by (I-V) measurements exhibited at room temperature ideality factors between  $n = 1.2$  and  $3.15$  as well as saturation current densities between  $1 \times 10^{-9}$  and  $8 \times 10^{-6}$  ( $\text{A}/\text{cm}^2$ ), respectively. A series and parallel resistance of  $0.35\text{-}1$  ( $\Omega \text{ cm}^2$ ) and  $0.0005\text{-}2.88$  ( $\text{M}\Omega \text{ cm}^2$ ) can be extracted. The barrier heights (BHs) were calculated from the thermionic emission theory yielding an effective barrier height of  $\Phi_B = 0.95$  eV. This value is in agreement with results reported in the literature [2.15]. Schalwig *et al.* [2.9] reported a Pt/GaN Schottky barrier height of  $1.15$  eV as determined by (I-V) measurements, whereas Schmitz *et al.* [2.21] obtained a value of  $1.08$  eV. The observed disparities in the measured

barrier heights between the different authors may be attributed to variations in material characteristics and measurement techniques used.

Capacitance-voltage (C-V) measurements at 10 kHz showed higher values for the (BHs) between 1.27 and 2.2 eV at room temperature and doping concentrations  $N_d$  between  $4.8 \times 10^{16}$  and  $3.4 \times 10^{17} \text{ cm}^{-3}$ . Our data clearly show that the diodes have ideality factors that are considerably large. The high values of  $n$  can be attributed to the presence of a wide distribution of low Schottky barrier height (low-SBH) patches as a consequence of the quality of the GaN used.

The experimental effective (BHs) and ideality factors obtained from the (I-V) and (C-V) characteristics differ from diode to diode even if they are identically prepared (on the same sample). It has been reported theoretically by Tung and co-worker [2.23, 2.24] and experimentally by Mönch and co-worker [2.25-2.28] that the linear relationship between effective BHs and ideality factor may be explained by the BH inhomogeneity, that is, the BHs become smaller as the ideality factors increase. This finding may be attributed to lateral inhomogeneities of the BH [2.23-2.28].

Fig. 2.18 shows a plot of the experimentally determined BHs of 24 diodes as a function of their ideality factors at room temperature. As can be seen from Fig. 2.18, there is a linear relationship between the experimental effective BHs and the ideality factors of the Schottky contacts. That is, the BHs become smaller as the ideality factors increase.

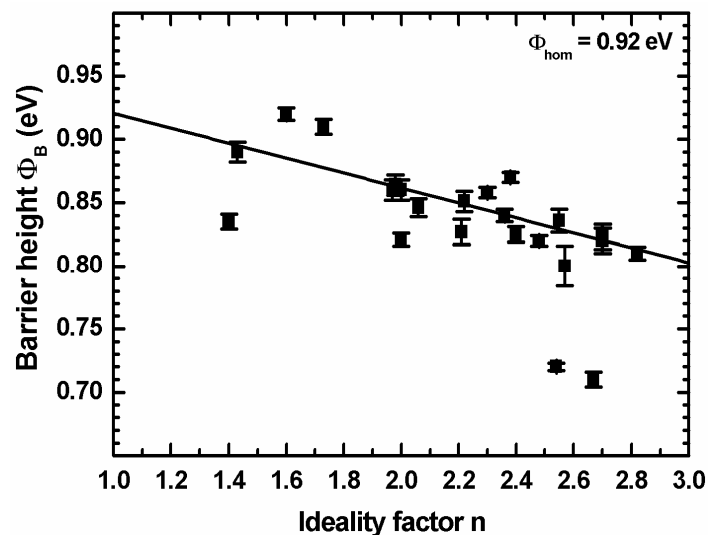


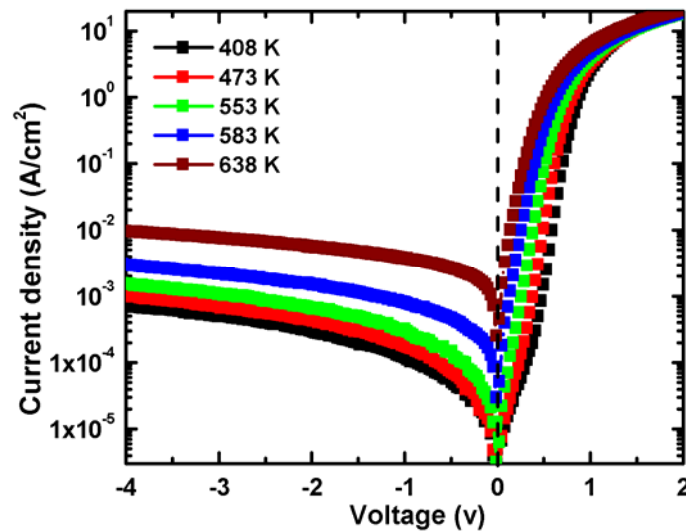
**Fig. 2.18:** Plot of experimental BH versus ideality factor of the Pt/GaN Schottky diodes. The extrapolation of the effective barrier height to ideality factors of 1.02 provides the zero bias barrier height.

For homogeneous metal-semiconductor contacts, the effective barrier height is lowered due to the image force and becomes voltage dependent. The extrapolation to  $n = 1.02$  for the plot in Fig. 2.18 result in a laterally homogeneous BH of 0.92 eV [2.29].

### 2.6.2.2 Measurements as a function of temperature:

#### 2.6.2.2.1 Temperature dependent (I-V) characteristics:

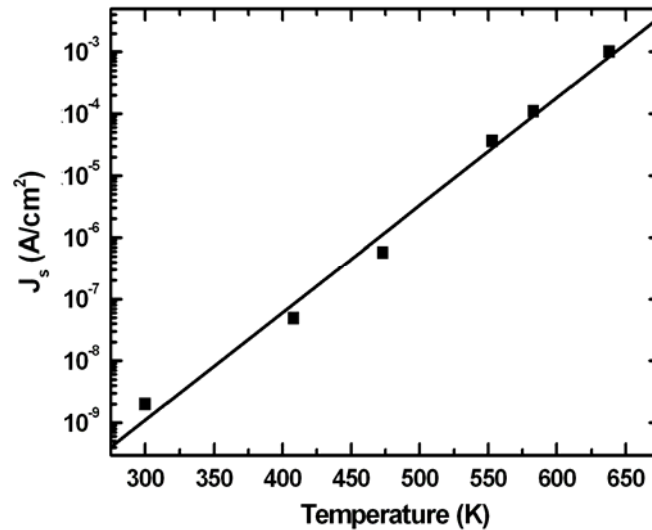
Fig. 2.19 shows (I-V) characteristics from the Pt/GaN Schottky diodes with  $d_{Pt} = 40$  nm and  $A_{Pt} = 250 \times 250 \mu\text{m}^2$ , as a function of measurement temperature. The forward current increases with increasing temperature. The extracted values of saturation current density  $J_s$  were  $2 \times 10^{-9} \text{ A cm}^{-2}$  at 300 K, and  $10^{-3} \text{ A cm}^{-2}$  at about 640 K (Fig. 2.20).



**Fig. 2.19:** I-V characteristics of a Pt/GaN Schottky diode with  $d_{Pt} = 40$  nm and  $A_{Pt} = 250 \times 250 \mu\text{m}^2$ , for temperatures varying from 300 to 638 K.

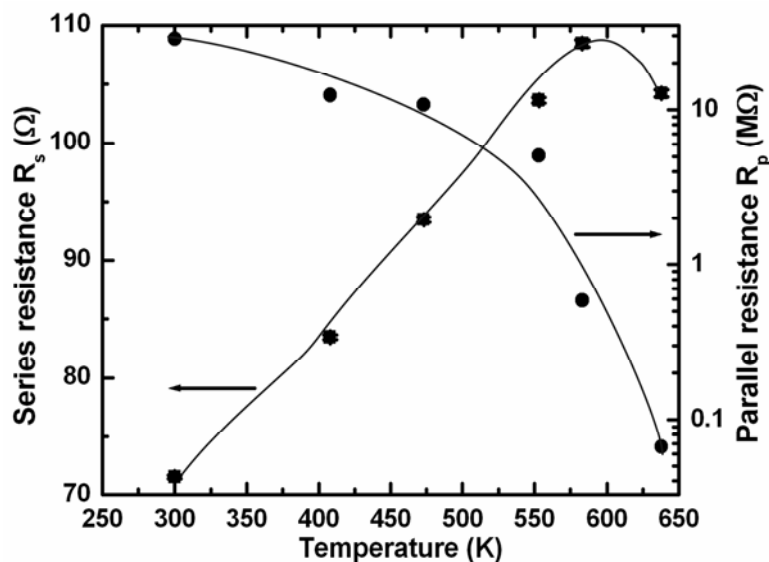
The value of  $R_s$  determined from Eq. (2.22) increases with increasing temperature and  $R_p$  decreases with increasing temperature (Fig. 2.21). However, as  $R_p$  dominates in the lower bias region, a significant contribution from the parallel resistance on  $n$  and  $J_s$  was not observed.



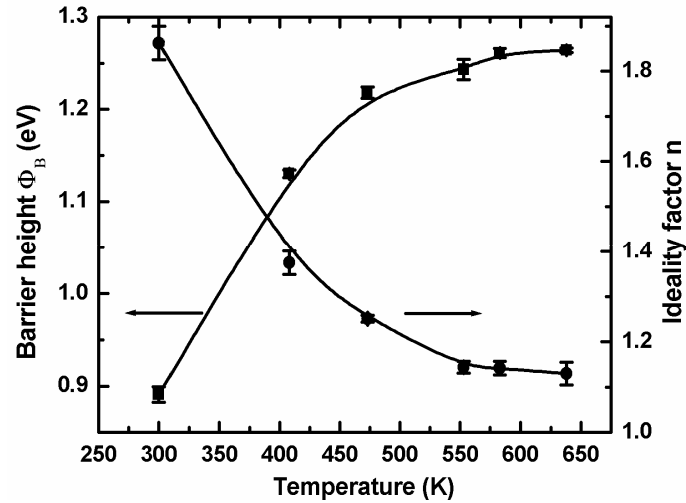


**Fig. 2.20:** Experimental variations of the saturation current extracted from forward I-V curves, as a function of temperature, for a Pt/GaN Schottky diode with  $d_{Pt} = 40$  nm and  $A_{Pt} = 250 \times 250 \mu\text{m}^2$ , for temperatures varying from 300 to 638 K.

The experimental values of  $n$  (denoted by closed circles) and  $\Phi_B$  (denoted by closed squares) are plotted as a function of temperature in Fig. 2.22. As seen in this figure, the ideality factor decreases with increasing temperature and the change is more pronounced at  $T > 300$  K, whereas the barrier height  $\Phi_B$  increases with increasing temperature.



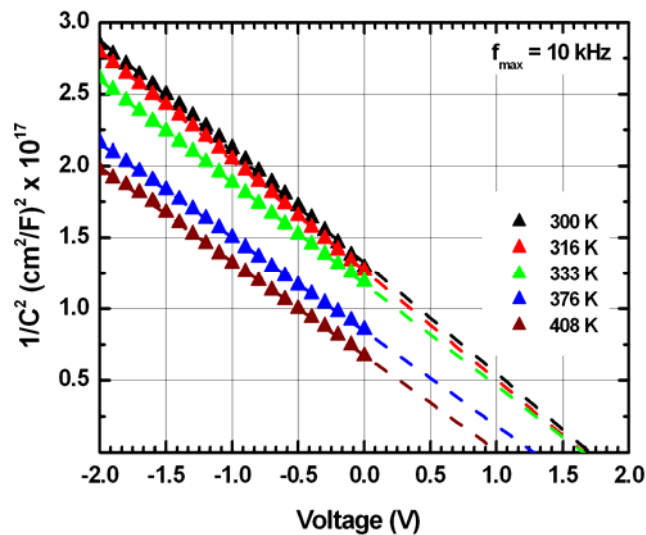
**Fig. 2.21:** Experimental variation of the series and parallel resistance extracted from forward I-V curves, as a function of temperature, for a Pt/GaN Schottky diode with  $d_{Pt} = 40$  nm and  $A_{Pt} = 250 \times 250 \mu\text{m}^2$ , for temperatures varying from 300 to 638 K.



**Fig. 2.22:** Barrier height  $\Phi_B$  and ideality factor  $n$  extracted from I-V measurements, as a function of temperature, for a Pt/GaN Schottky diode with  $d_{Pt} = 40$  nm and  $A_{Pt} = 250 \times 250 \mu\text{m}^2$ , for temperatures varying from 300 to 638 K.

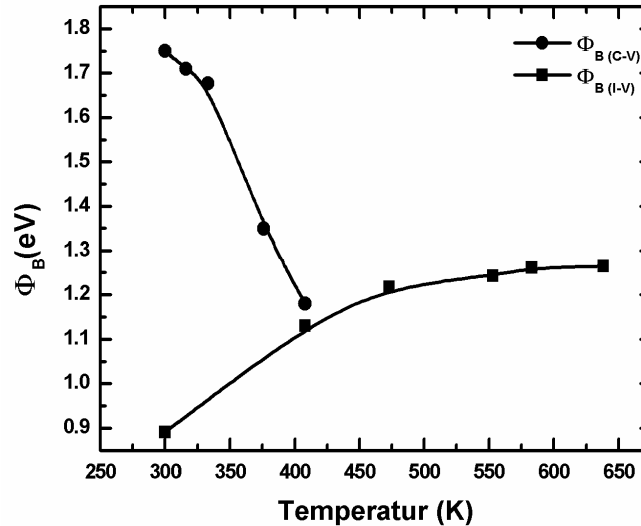
#### 2.6.2.2.2 Temperature dependent (C-V) characteristics:

Fig. 2.23 shows the plot of the square of the inverse of the capacitance per unit area ( $1/C^2$ ) as a function of applied voltage for a Pt/GaN Schottky diode with  $d_{Pt} = 40$  nm and  $A_{Pt} = 250 \times 250 \mu\text{m}^2$ , for temperatures varying from 300 to 408 K. The room temperature barrier height calculated using Eq. (2.15) is 1.75 eV.



**Fig. 2.23:**  $1/C^2$  versus the applied gate bias measured for a Pt/GaN Schottky diode with  $d_{Pt} = 24$  nm and  $A_{Pt} = 1000 \times 1000 \mu\text{m}^2$ , at 10 kHz, for temperatures varying from 300 to 408 K.

The  $\Phi_{B(C-V)}$  decreases with temperature from 1.75 at room temperature to 1.18 eV at 408 K (135°C). The  $(1/C^2-V)$  plots at different temperatures were parallel to one another to a good approximation, thus indicating that the net carrier concentration remains unaffected up to 135°C.



**Fig. 2.24:** Schottky barrier height of a Pt/GaN Schottky diode with  $d_{Pt} = 24$  nm and  $A_{Pt} = 1000 \times 1000$   $\mu\text{m}^2$  determined from I-V and C-V methods as function of temperature.

Fig. 2.24 reveals a drastic difference between the barriers  $\Phi_{B(I-V)}$ , and  $\Phi_{B(C-V)}$ .  $\Phi_{B(C-V)}$  values were higher than the  $\Phi_{B(I-V)}$  values for Pt/GaN Schottky contacts. The difference between  $\Phi_{B(I-V)}$  and  $\Phi_{B(C-V)}$  was about 0.86 eV at room temperature. The large difference in  $\Phi_{B(I-V)}$  and  $\Phi_{B(C-V)}$  values may be due to the presence of oxide interfacial layer at Pt/GaN interface [2.30]. Itoh *et al.* have also compared the I-V and C-V method to evaluate the barrier height of metal contacts to 6H-SiC [2.31]. It has been pointed out that the intersect voltage  $V_{bi}$  obtained by the C-V method divided by the ideality factor is related to the barrier height determined from the I-V curve [2.32]. By dividing  $V_{bi}$  (1.70) by the  $n$  value (1.863) obtained from I-V characteristics at room temperature, we obtain a value of 0.91 eV in agreement with the value (0.892 eV) determined from the I-V curve.

## 2.6.3 Hydrogen sensing performances:

### 2.6.3.1 Temperature-dependent J-V characteristics in synthetic air and 1 vol.% H<sub>2</sub> in synthetic air:

In the first step three devices with different Pt thicknesses were tested for the response to hydrogen in dependence on the operation temperature in synthetic air as well in 1 vol.% H<sub>2</sub> in synthetic air. The temperature was varied in the range between room temperature and 365°C.

Fig. 2.25 and Fig. 2.26 show the J-V characteristics for a Pt/GaN Schottky diode with an area  $A_{Pt} = 250 \times 250 \mu\text{m}^2$  and two different Pt thicknesses in two different atmospheres that contain oxygen (synthetic air) and hydrogen (1 vol.% H<sub>2</sub> in synthetic air) at various temperatures. It is obvious that the exposure of a Pt/GaN Schottky diode to molecular hydrogen causes an increase of both forward and reverse current, which can be attributed to a decrease in the Schottky barrier height. In a constant current operation mode, this reduction of the Schottky barrier height results in a shift to lower bias voltages, which constitutes the sensor signal.

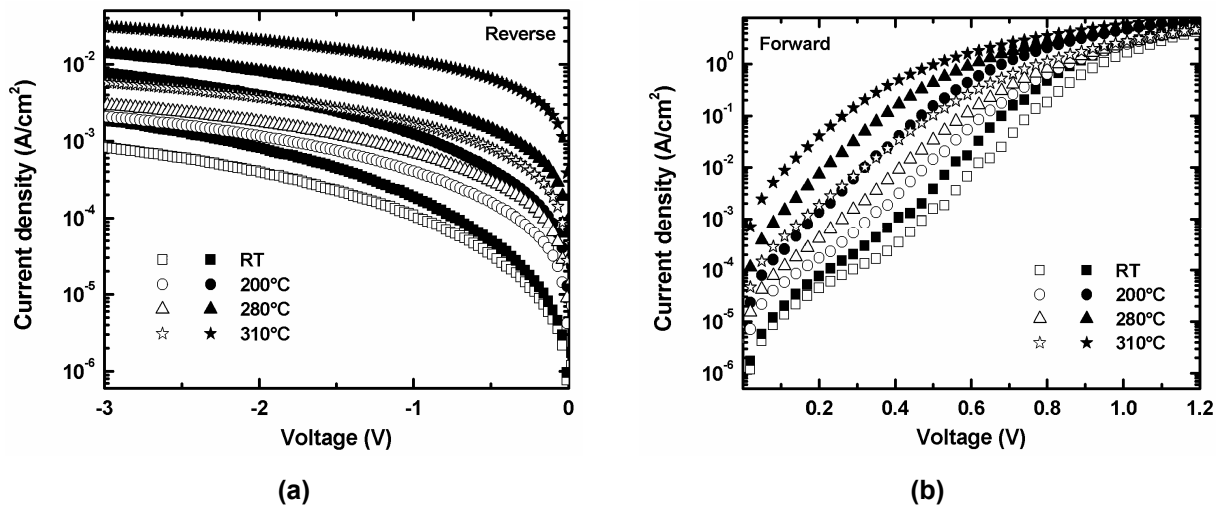


**Fig. 2.25:** Reverse (a) and forward (b) characteristics of a Pt/GaN Schottky diode with  $d_{Pt} = 8 \text{ nm}$  and  $A_{Pt} = 250 \times 250 \mu\text{m}^2$  operated at different temperatures, in synthetic air (open symbols) as well as in synthetic air with 1 vol.% hydrogen (closed symbols).

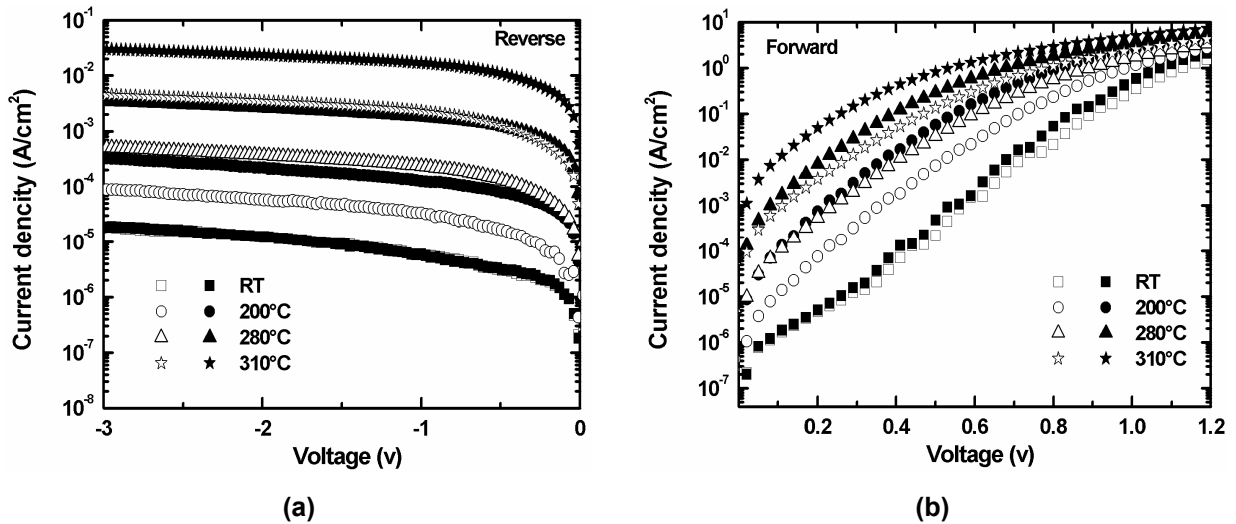


**Fig. 2.26:** Reverse (a) and forward (b) characteristics of a Pt/GaN Schottky diode with  $d_{Pt} = 24$  nm and  $A_{Pt} = 250 \times 250 \mu m^2$  operated at different temperatures, in synthetic air (open symbols) as well as in 1 vol.% hydrogen in synthetic air (closed symbols).

The variation of series resistance, saturation current density, ideality factor and barrier height in synthetic air as well as in synthetic air with 1 vol.% hydrogen in synthetic air as a function of operating temperature for Pt/GaN Schottky diodes with ( $d_{Pt} = 8$  nm,  $A_{Pt} = 250 \times 250 \mu m^2$ ) and ( $d_{Pt} = 24$  nm,  $A_{Pt} = 1000 \times 1000 \mu m^2$ ) are shown in Fig. 2.27 and Fig. 2.28, respectively.

The series resistance increases as the temperature increases. The increase of the resistance with temperature is due to the decrease of the electron mobility because the resistance increases approximately in proportion to  $T^{-3/2}$ , and it is known that the scattering by optical phonons is dominant above room temperature in GaN [2.33]. In addition, the change in the series resistance upon exposure of 1 vol.%  $H_2$  in synthetic air can be found insignificant as can be seen in Fig. 2.27a and Fig. 2.28a.

The increase in the saturation current density with temperature (Fig. 2.27b, Fig. 2.28b) is an expected phenomenon. However, hydrogen decreased the barrier height of Pt/GaN Schottky diodes, whereas oxygen increased it. The temperature dependence of change in barrier height ( $\Delta\Phi_B$ ) when the ambient gas was changed from synthetic air to 1 vol.%  $H_2$  in synthetic is presented in Fig. 2.27d and Fig. 2.28d.

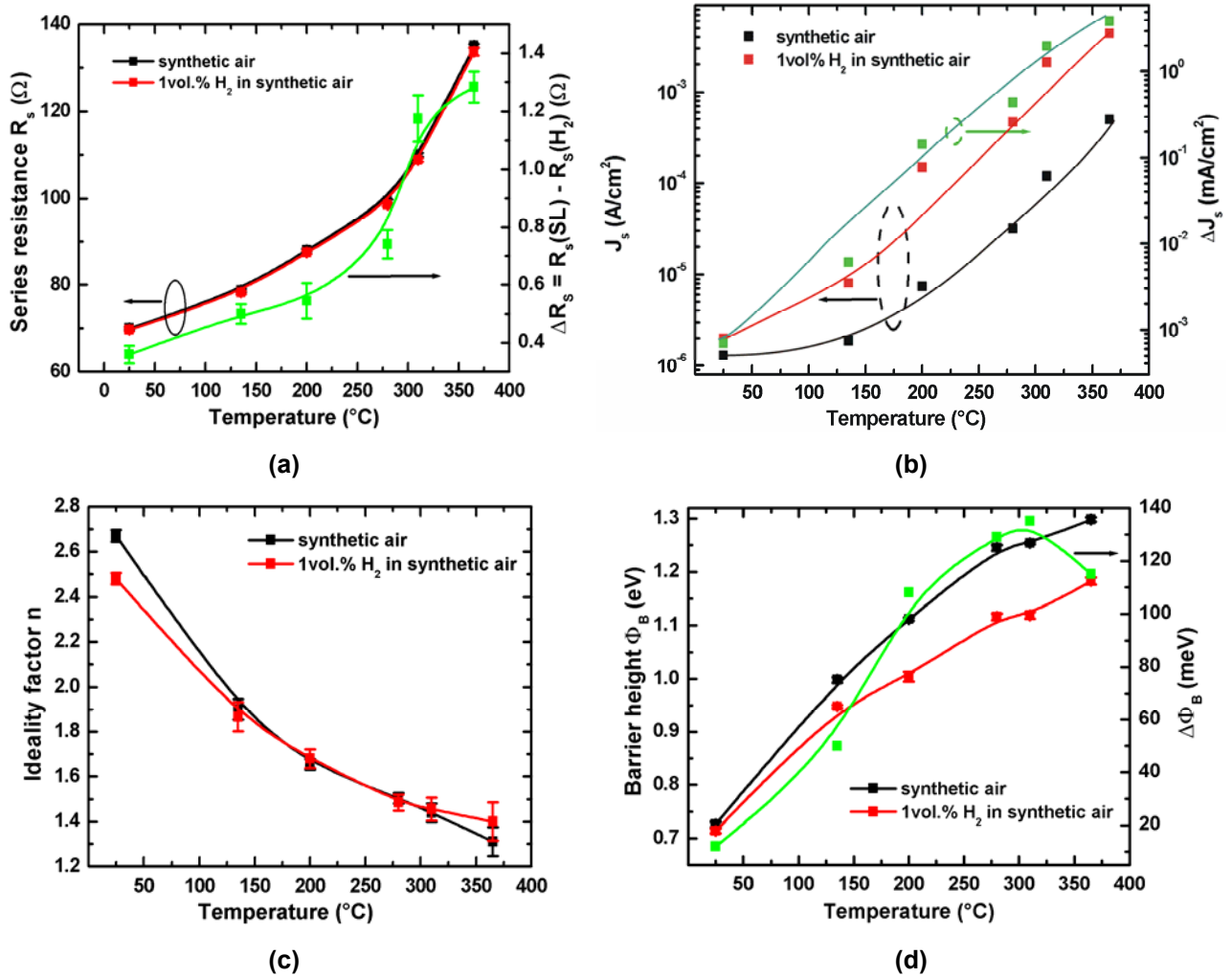


**Fig. 2.27:** Variation of (a) series resistance, (b) saturation current density, (c) ideality factor, and (d) barrier height, with temperature for a Pt/GaN Schottky diode with  $d_{\text{Pt}} = 8$  nm,  $A_{\text{Pt}} = 250 \times 250 \mu\text{m}^2$  in synthetic air (black squares) as well as 1 vol.% hydrogen in synthetic air (red squares).

The barrier height changed significantly in the temperature range from 100 to 365°C. These results suggest that Pt/GaN Schottky diodes are promising for use in gas sensors operating at high temperatures. Experimentally, the  $\Delta \Phi_B$  values of the Pt/GaN Schottky diode with ( $d_{\text{Pt}} = 24$  nm,  $A_{\text{Pt}} = 1000 \times 1000 \mu\text{m}^2$ ) are increased from 8 at room temperature to 124 meV at 365°C.

The change in the ideality factor upon exposure of 1 vol.%  $\text{H}_2$  in synthetic air can be found insignificant (0.1-0.2) as seen in Fig. 2.27c and Fig. 2.28c. From room temperature to 200°C the change in ideality factor is positive and after 200°C becomes negative.

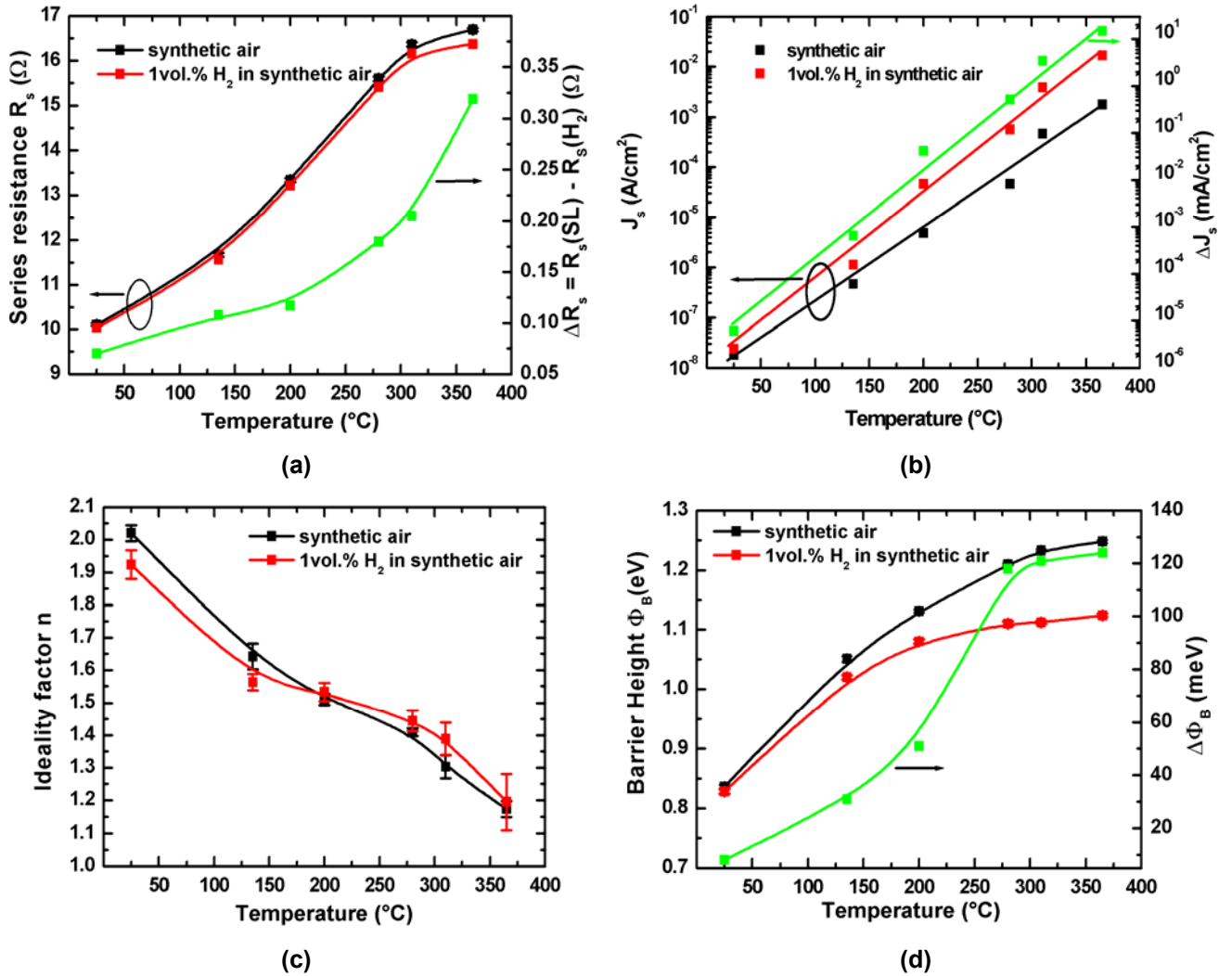


**Fig. 2.28:** Variation of (a) series resistance, (b) saturation current density, (c) ideality factor, and (d) barrier height, with temperature for a Pt/GaN Schottky diode with  $d_{Pt} = 24$  nm,  $A_{Pt} = 1000 \times 1000 \mu m^2$  in synthetic air (black squares) as well as 1 vol.% hydrogen in synthetic air (red squares).

### 2.6.3.2 The gas response (R) and the sensitivity (S):

For Schottky diode based gas sensors the response can be defined in the following ways (Fig. 2.29):

#### A. In forward direction:

In forward direction we can define the following responses:

$$R = \Delta V = |V_0 - V_{gas}|, J_F = const., \quad (2.26)$$

where  $V_{gas}$  and  $V_0$  are the voltages of the sensor in presence of gas and in synthetic air, respectively.

$$R_1 = \Delta I = |I_{gas} - I_0|, V_F = const. , \quad (2.27)$$

$$R_2 = \frac{\Delta I}{I_0} = \frac{|I_{gas} - I_0|}{I_0}, V_F = const. , \quad (2.28)$$

$$R_3 = \frac{I_{gas}}{I_0}, V_F = const. , \quad (2.29)$$

where  $I_{gas}$  and  $I_0$  are the currents of the sensor in presence of gas and in synthetic air, respectively.

$$R_4 = \Delta I_s = |I_{s_{gas}} - I_{s_0}|, \quad (2.30)$$

$$R_5 = \frac{\Delta I_s}{I_{s_0}} = \frac{|I_{s_{gas}} - I_{s_0}|}{I_{s_0}}, \quad (2.31)$$

$$R_6 = \frac{I_{s_{gas}}}{I_{s_0}}, \quad (2.32)$$

where  $I_{s_{gas}}$  and  $I_{s_0}$  are the currents of the sensor in presence of gas and in synthetic air, respectively.

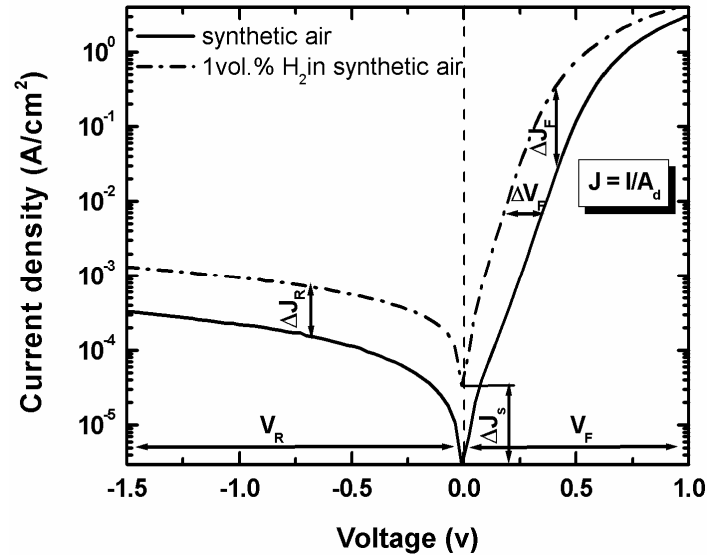


Fig 2.29: Responses of a Pt/GaN Schottky diode gas sensors.

### B. In reverse direction:

In reverse direction different responses can be given:

$$R_7 = \Delta I_R = |I_{gas} - I_0|, V_R = const. , \quad (2.33)$$



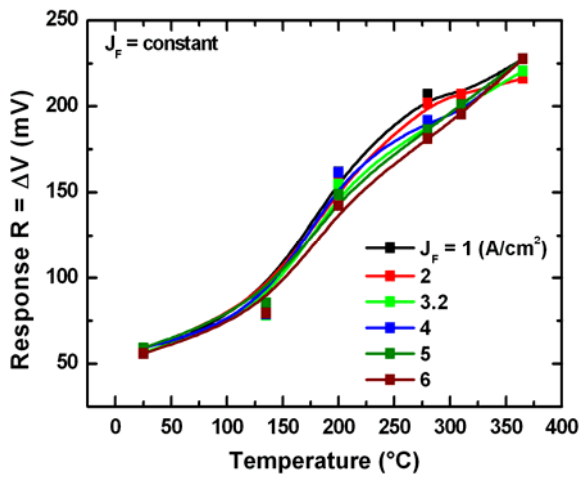
$$R_8 = \frac{\Delta I_R}{I_0} = \frac{|I_{gas} - I_0|}{I_0}, V_R = const., \quad (2.34)$$

$$R_9 = \frac{I_{gas}}{I_0}, V_R = const., \quad (2.35)$$

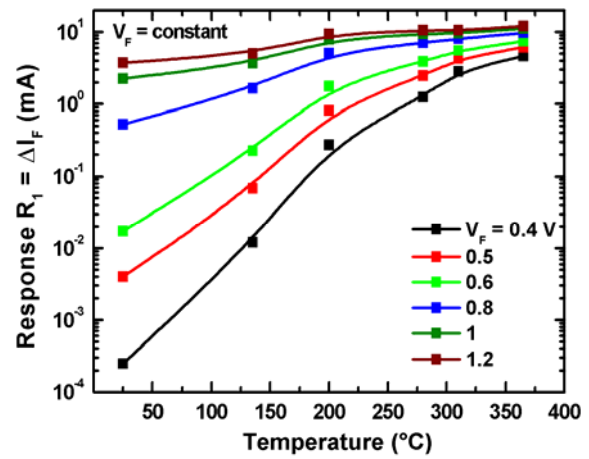
The sensitivity (S) is given by:

$$S = \frac{\text{response}}{\text{concentration}} = \frac{R}{C_{gas} [ppm]}. \quad (2.36)$$

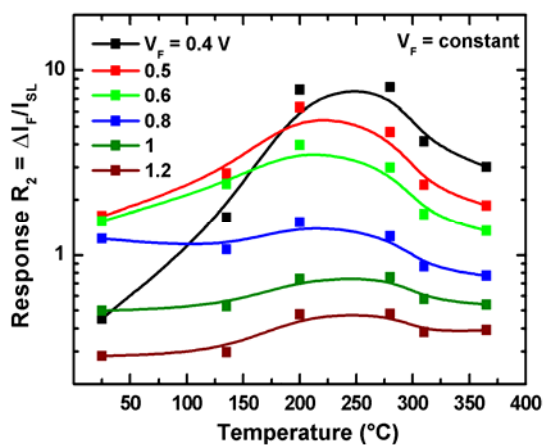
For example, Fig 2.30 shows the response to 1 vol.%H<sub>2</sub> in synthetic air of a Pt/GaN Schottky diode with ( $d_{Pt} = 24$  nm,  $A_{Pt} = 1000 \times 1000 \mu\text{m}^2$ ) as function of operation temperature.



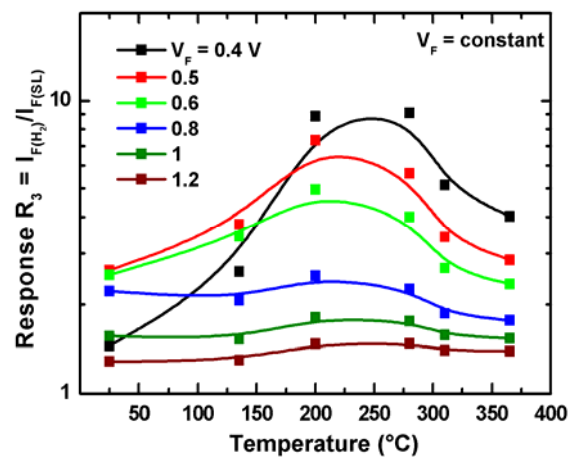
(a)



(b)



(c)



(d)

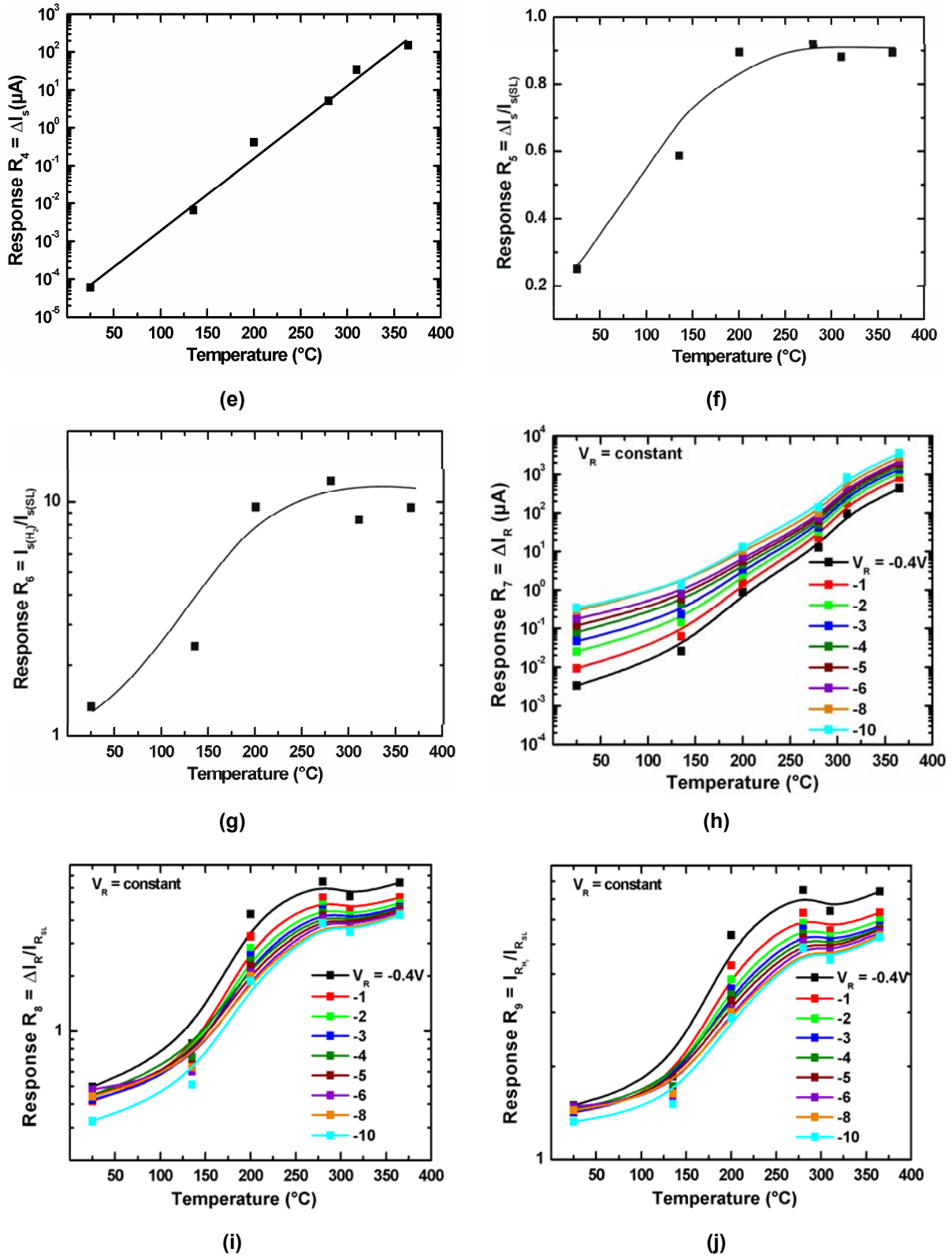


**Fig. 2.30:** The response (a)  $R$ , (b)  $R_1$ , (c)  $R_2$ , (d)  $R_3$ , (e)  $R_4$ , (f)  $R_5$ , (g)  $R_6$ , (h)  $R_7$ , (i)  $R_8$ , and (j)  $R_9$  to 1 vol.%  $H_2$  in synthetic air of Pt/GaN Schottky diodes with ( $d_{Pt} = 24$  nm,  $A_{Pt} = 1000 \times 1000 \mu m^2$ ) as function of operation temperature.

It becomes obvious that the responses can be enhanced by increasing the operation temperature. At 310°C and above a general decrease of the responses  $R_2$ ,  $R_3$ ,  $R_5$ ,  $R_6$ ,  $R_8$ , and  $R_9$  were observed, very likely due to an increased thermal desorption of the test gas species from the sensor surface. In order to study this effect temperature-programmed desorption (TPD) measurements were performed (section 2.7). In this thesis we focus on the sensor response  $R$  (Eq. 2.26) but we consider also the other responses to compare our results with the results present in the literature.

The response  $R$  to  $H_2$  was investigated in dependence on the active area, Pt thickness and the operating temperature. The change in the voltage of the diode at a fixed current density was monitored as the diode was exposed to 1 vol.%  $H_2$  in synthetic air and for comparison to dry synthetic air in order to determine the voltage difference as a measure for the response toward hydrogen. In this work we have defined the response as the signal level after exposure to hydrogen for 10 minutes at various temperatures. Fig. 2.31 plots the response  $R$  at different temperatures of the three set of the Schottky diodes. During this measurement, we held the device at a constant current density level of  $3.2 \text{ A/cm}^2$  and monitored the voltage.

A response to hydrogen was observed already at room temperature for all three kinds of sensors. The data in Fig.2.31a can be explained as follows. At lower temperatures, the diffusion of hydrogen through platinum to reach the semiconductor surface is faster through thinner in comparison to thicker Pt. This explains the nearly 20% higher signal we observe in the 8 nm in comparison to the 24 nm device. As we go higher in temperature the difference in response between the 8 nm and 24 nm device is decreasing. This is because at elevated temperatures, the diffusion rate through the 24 nm metal is much higher than at room temperature. The 40 nm device also shows enhanced sensitivity once the temperature crosses 280°C. Thus at 310°C, we determine the sensitivity of all three devices with different metal thickness to be very similar. This could be due to the fact that at this temperature the time constant of hydrogen diffusion for all three Schottky contacts is of the same order of magnitude and negligible in comparison to the time needed to detect the signal. At 310°C and above a general decrease of the response was observed, very likely due to an increased thermal desorption of the test gas species from the sensor surface. A significant increase of response has been observed by increasing the temperature of

operation to  $\sim 310^\circ\text{C}$  and by decreasing the Pt thickness down to 8 nm for all three set of Schottky diodes.

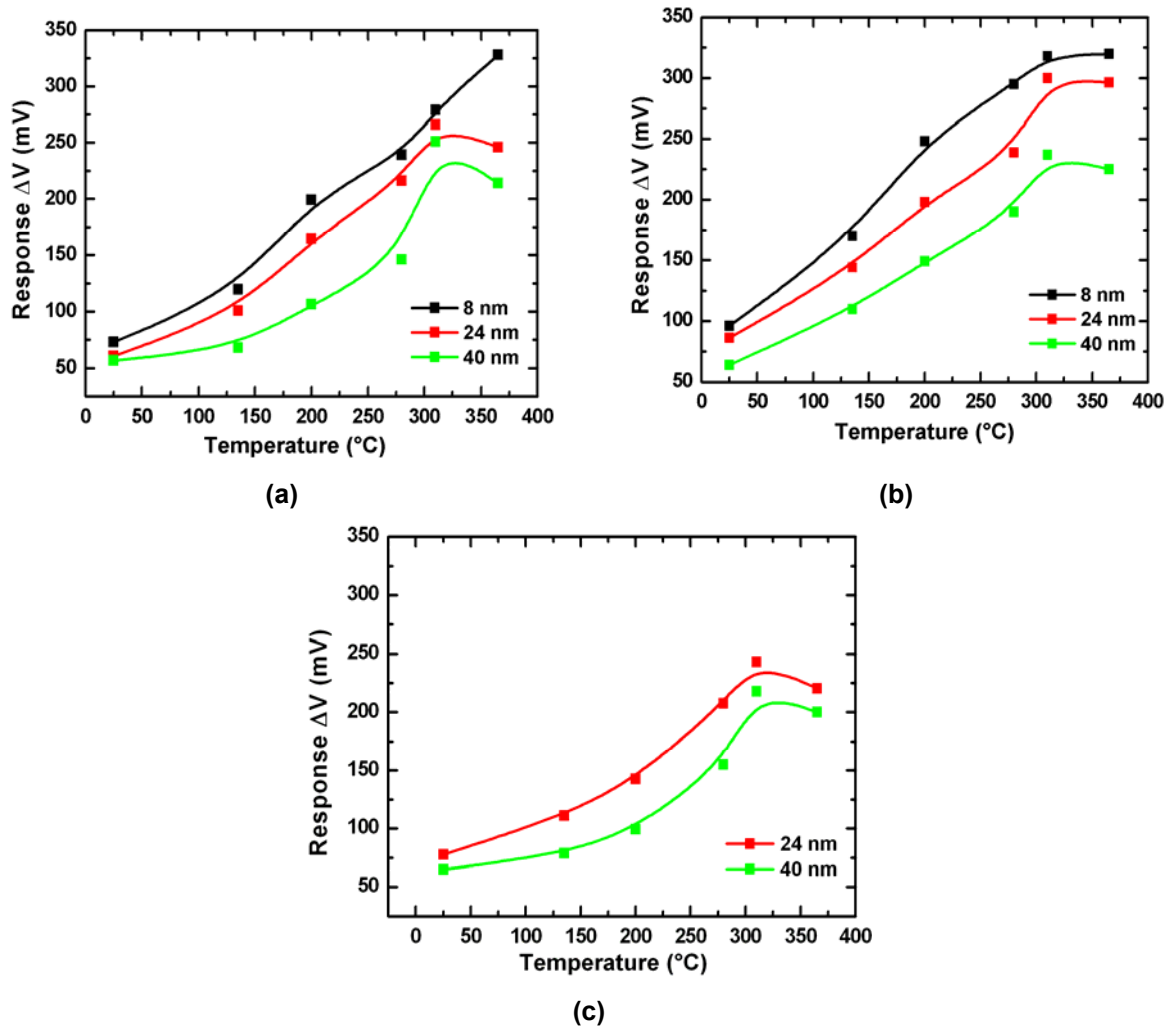


**Fig. 2.31:** The response to 1 vol.%  $\text{H}_2$  in synthetic air at different temperatures for different Pt thicknesses and different Pt areas. **(a)**  $A_{\text{Pt}} = 250 \times 250 \mu\text{m}^2$ , **(b)**  $A_{\text{Pt}} = 500 \times 500 \mu\text{m}^2$ , and **(c)**  $A_{\text{Pt}} = 1000 \times 1000 \mu\text{m}^2$ . The measurements were performed at a constant current density of  $3.2 \text{ mA/cm}^2$ .

Fig. 2.32 provides the influence of the effective sensor area (Pt area) on the sensitivity towards to 1 vol.% hydrogen in synthetic air at different temperatures. The sensitivity is given by Eq. (2.36).

As one can see, a significant increase of sensitivity has been observed by increasing the temperature of operation to  $\sim 310^\circ\text{C}$  and by decreasing the Pt thickness down to 8 nm for all Pt areas. In addition, the sensor with the Pt area of  $500 \times 500 \mu\text{m}^2$  was the more sensitive one for all three thicknesses of Pt. The best sensitivity of the sensors with the Pt area of  $500 \times 500 \mu\text{m}^2$  may be due to high

quality of the Pt film. As well known, the atomic structure of the catalytic metal surface will affect the surface reactions and thus affect the sensitivity of the sensor [2.34].

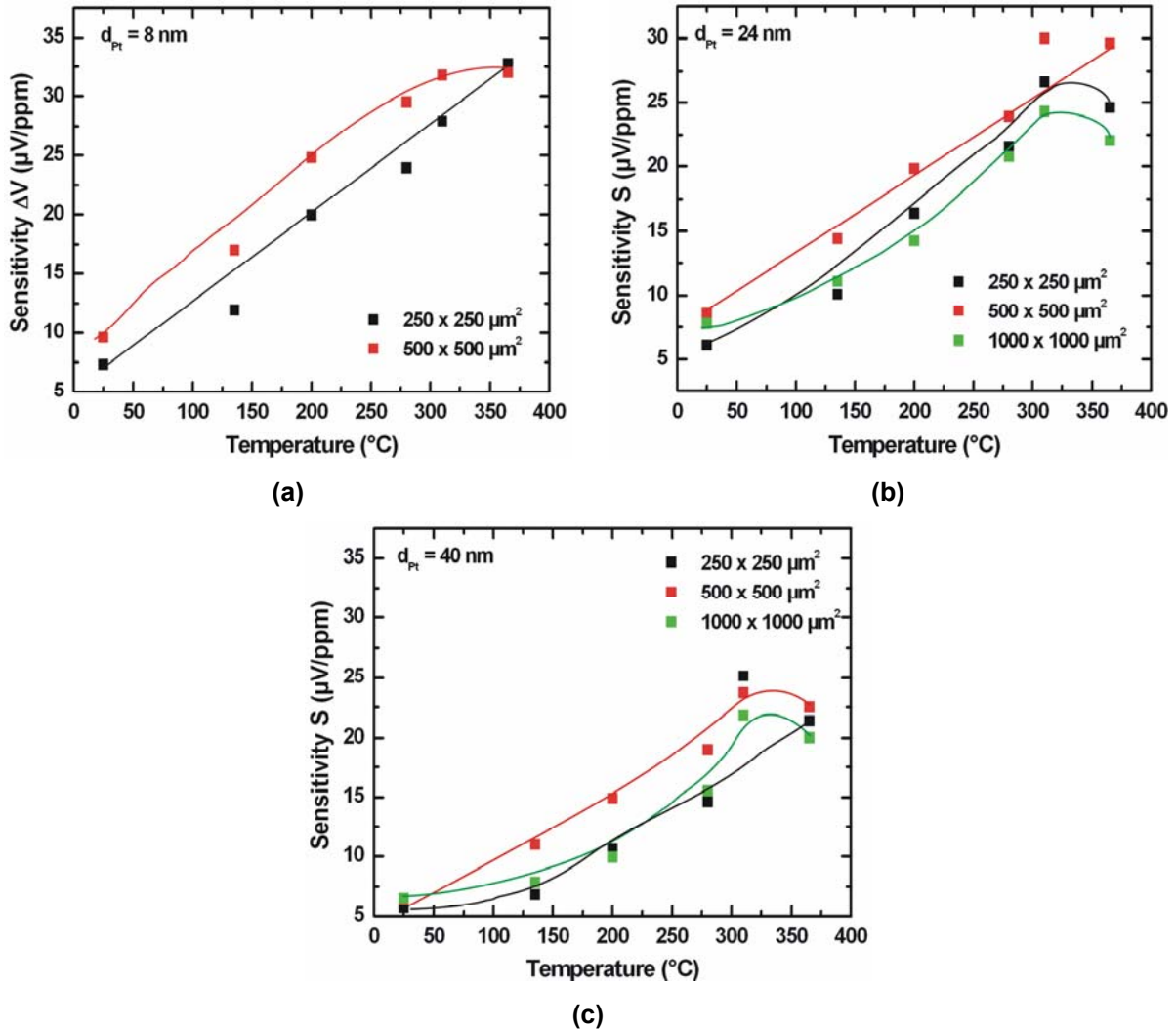


**Fig. 2.32:** The sensitivity to 1 vol.% H<sub>2</sub> in synthetic air at different temperatures for different Pt thicknesses and different Pt areas. (a) d<sub>Pt</sub> = 8 nm, (b) d<sub>Pt</sub> = 24 nm, and (c) d<sub>Pt</sub> = 40 nm. The measurements were performed at a constant current density of 3.2 mA/cm<sup>2</sup>.

### 2.6.3.3 H<sub>2</sub>-concentration-dependent J-V characteristics at T = 310°C:

In a second step the response of Pt/GaN Schottky diodes operating at 310°C for different concentrations of H<sub>2</sub> admixed to a background of synthetic air, was tested.

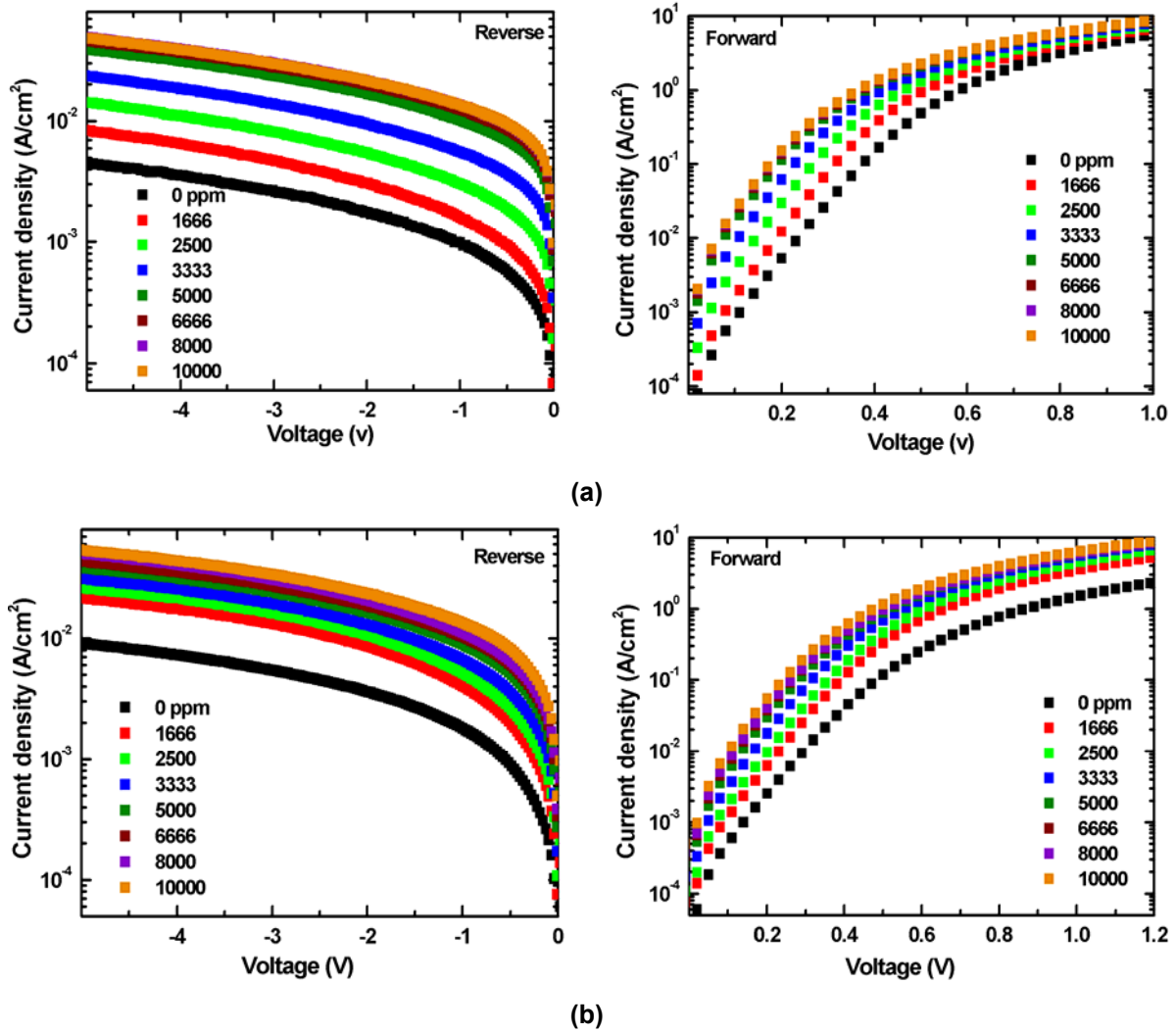


**Fig. 2.33:** The change in J-V characteristics of a Pt/GaN Schottky diode with two different Pt thicknesses (a) 40 nm and (b) 8 nm upon exposure to different concentrations of  $H_2$  diluted in synthetic air at  $310^\circ C$  ( $A_{Pt} = 250 \times 250 \mu m^2$ ).

In Fig. 2.33 the change in the J-V characteristics of sensors  $A_{Pt} = 250 \times 250 \mu m^2$  and different Pt thickness are shown in response to different concentrations of  $H_2$  in synthetic air. A pronounced decrease in the rectifying behaviour was determined indicating a reduction of the barrier height in the presence of hydrogen, since upon exposure to  $H_2$  the I-V characteristics become more ohmic. Under the hydrogen-containing ambient, both of the forward and reverse currents are increased obviously with increasing the hydrogen concentrations. A gas response can be measured both in the reverse and in the forward direction.

Fig. 2.34 shows the dependence of series resistance, saturation current density, Ideality factor, barrier height, and the change in barrier height ( $\Delta\Phi_B$ ) estimated from J-V measurements in Fig. 2.33b on the hydrogen concentrations at  $310^\circ C$ .

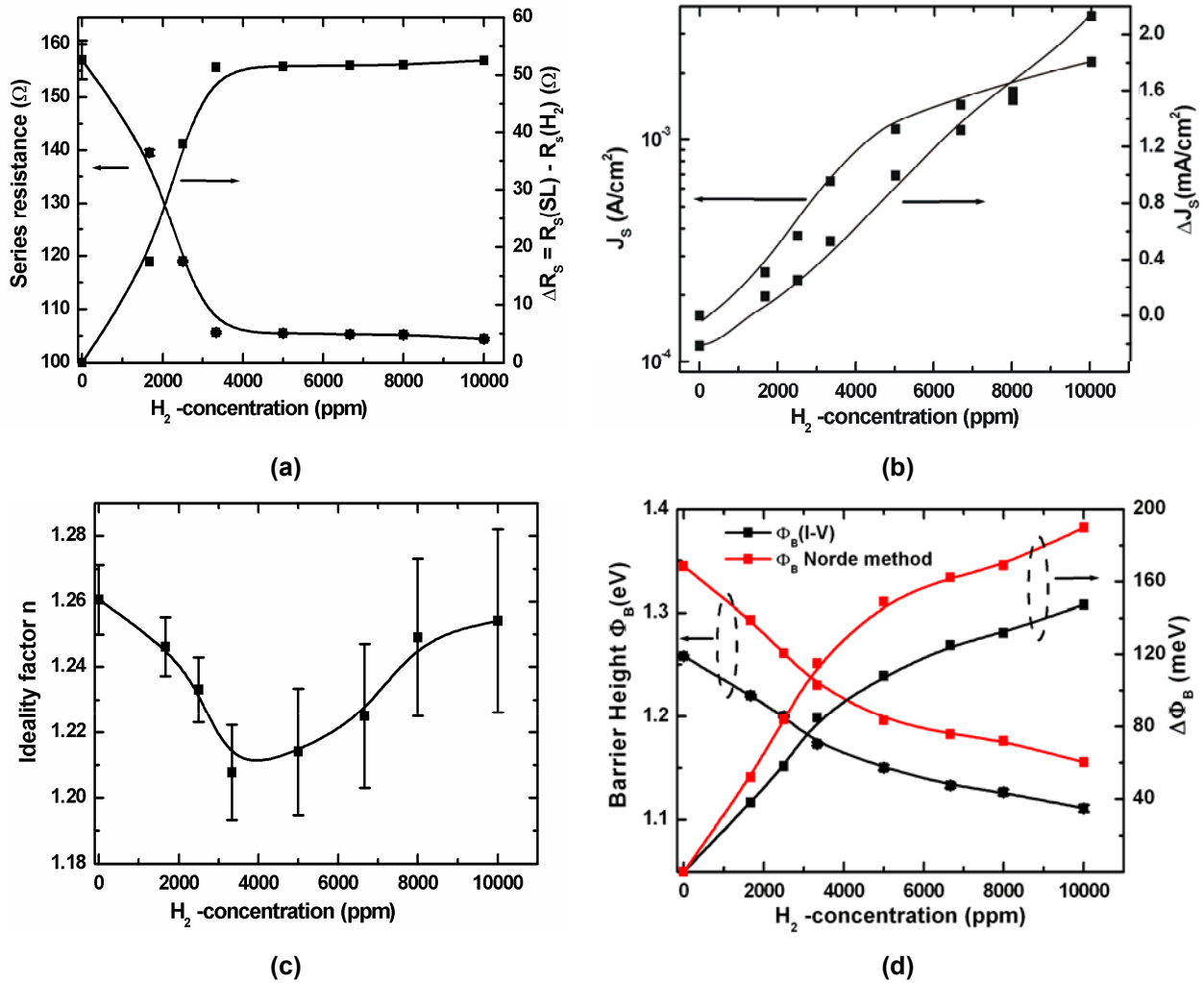


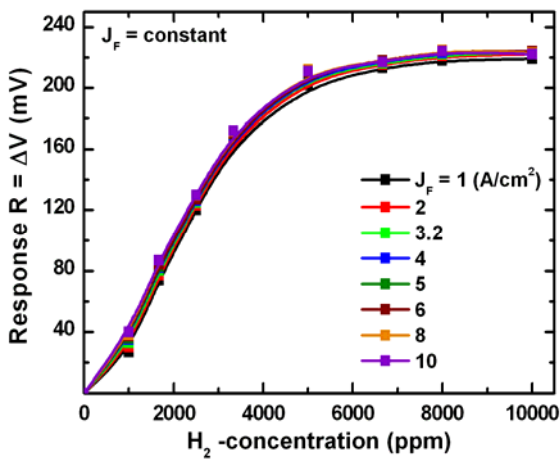
**Fig. 2.34:** The dependence of (a) series resistance, (b) saturation current density, (c) ideality factor, and (d) barrier height on hydrogen concentration at 310°C for a Pt/GaN Schottky diode with  $d_{Pt} = 8$  nm,  $A_{Pt} = 250 \times 250 \mu m^2$ .

The series resistance decreases as the  $H_2$  concentration increases, since I-V characteristics become more ohmic with increasing the  $H_2$  concentration. In addition, the change in the series resistance upon exposure to different concentrations of  $H_2$  in synthetic air can be found significant as seen in Fig. 2.34a. It can be seen from the Fig. 2.34c that the ideality factor of Pt/GaN is almost independent of  $H_2$  concentrations at 310°C.

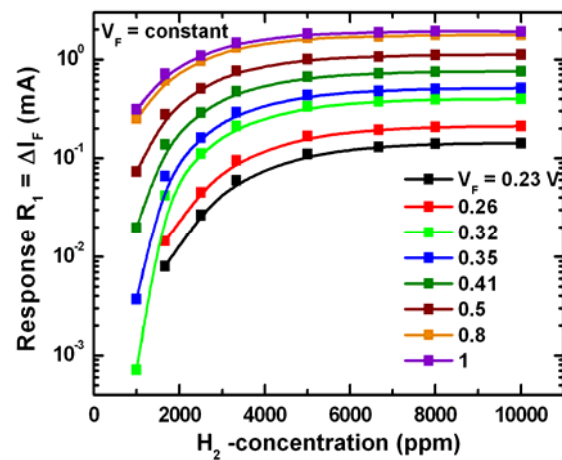
It becomes obvious from Fig. 2.34d that upon exposing to hydrogen-containing ambient, the Schottky barrier height of the devices studied is decreased with increasing hydrogen concentration. With increasing hydrogen concentration, the Pt-GaN Schottky diode shows also a rapid increase in  $\Delta\Phi_B$  followed by a saturation trend at hydrogen concentrations higher than 5000 ppm. The large change in barrier

height ( $\Delta\Phi_B$ ) is responsible for the high hydrogen sensitivity of Pt/GaN Schottky diodes. Experimentally, the  $\Delta\Phi_B$  values of the studied Pt/GaN Schottky diodes are increased from 38 (1666 ppm  $H_2$  in synthetic air) to 147 meV (1 vol.%  $H_2$  in synthetic air).

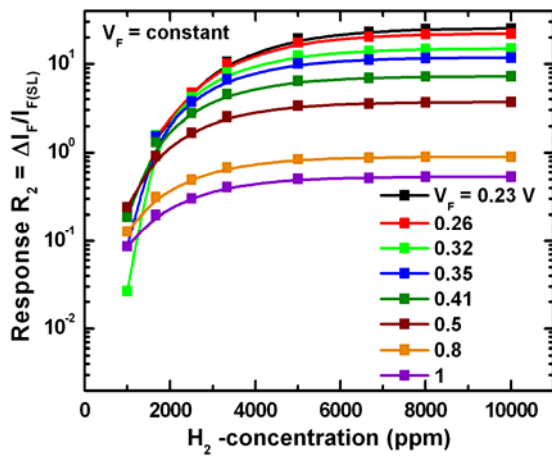
Fig 2.35 shows the all responses of Pt/GaN Schottky diodes with ( $d_{Pt} = 40$  nm,  $A_{Pt} = 250 \times 250 \mu m^2$ ) as function of  $H_2$  concentration at a temperature of  $310^\circ C$ . As can be seen in Fig. 2.35, all responses increase non-linearly and complete saturation is observed at concentrations above 8000 ppm.



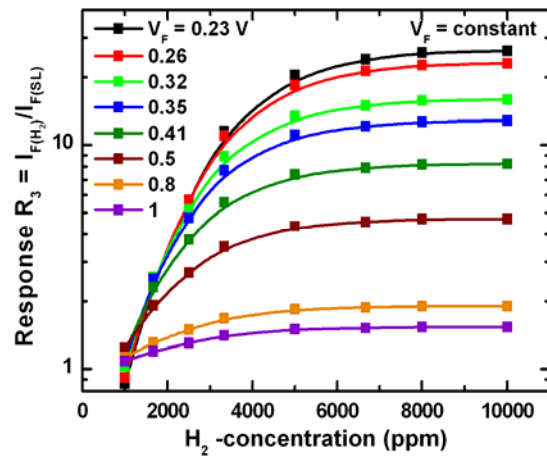
(a)



(b)



(c)



(d)



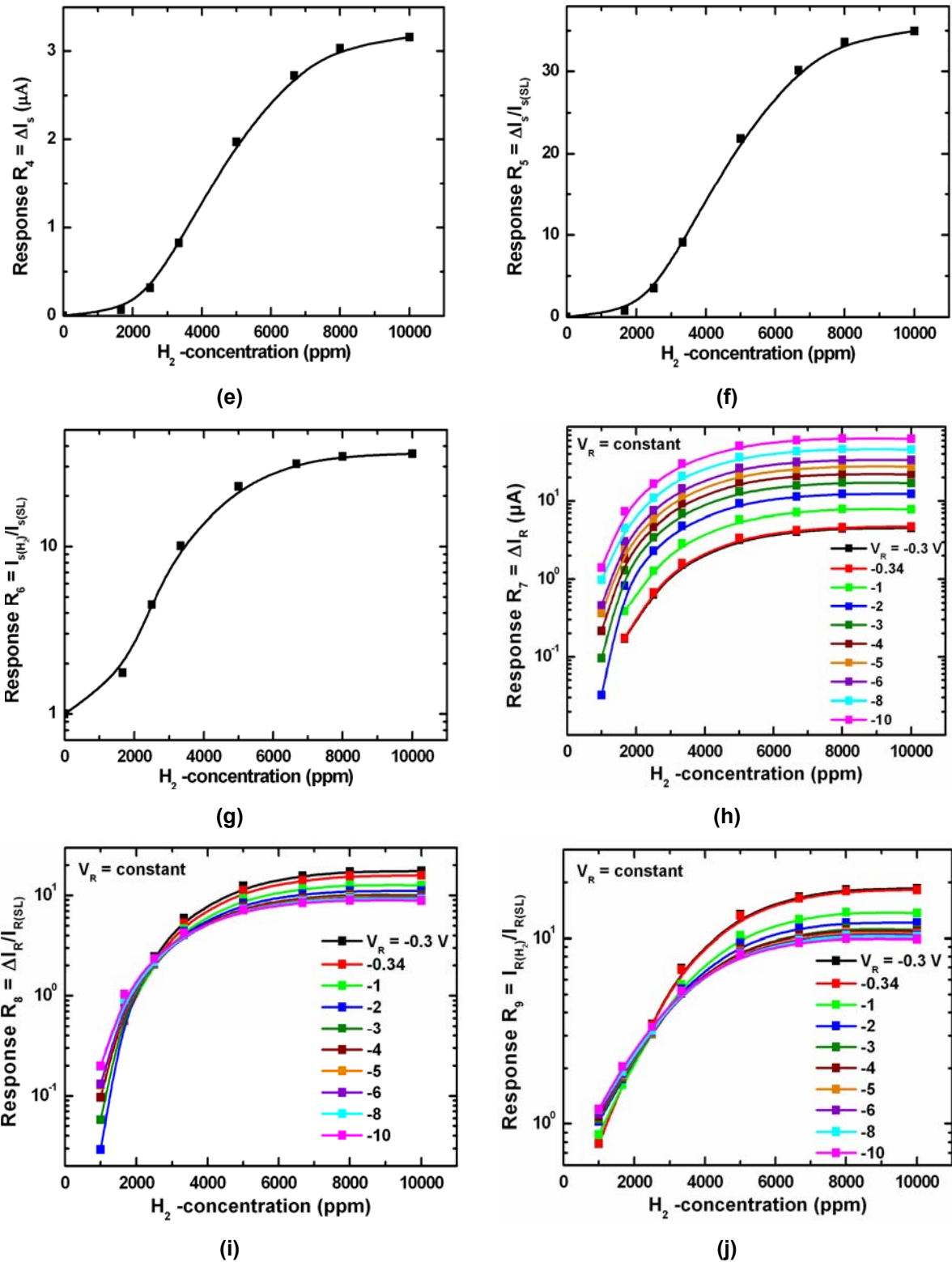


**Fig. 2.35:** The dependence of the responses (a)  $R$ , (b)  $R_1$ , (c)  $R_2$ , (d)  $R_3$ , (e)  $R_4$ , (f)  $R_5$ , (g)  $R_6$ , (h)  $R_7$ , (i)  $R_8$ , and (j)  $R_9$  on the  $H_2$  concentration at  $310^\circ C$  for Pt/GaN Schottky diodes with ( $d_{Pt} = 40 \text{ nm}$ ,  $A_{Pt} = 250 \times 250 \mu m^2$ ).

Concerning on the response  $R$ , Fig. 2.36 shows the dependence of the response  $R$  on  $H_2$  concentration for Pt/GaN Schottky diodes with a Pt area  $A_{Pt} = 250 \times 250 \mu m^2$

and different Pt thicknesses at two different temperatures: 310°C (Fig. 2.36a) and room temperature (Fig. 2.36b). We have found that the response  $R$  increases non-linear with an increasing concentration of  $H_2$  in air starting from 0.1 to 1 vol.% for all Pt contact thicknesses.

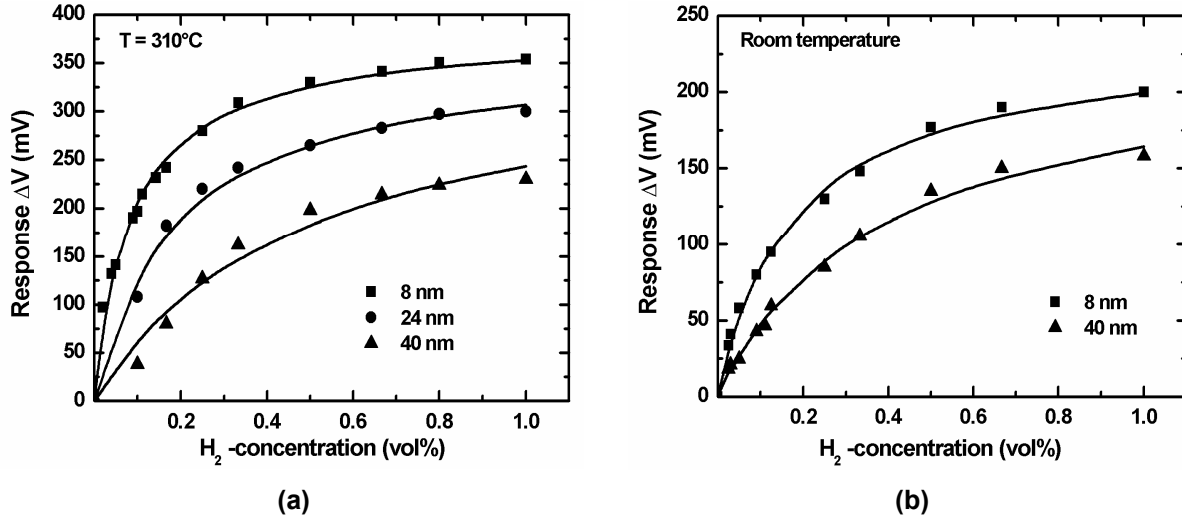


**Fig. 2.36:** The dependence of the response  $R$  on  $H_2$  concentration for Pt/GaN Schottky diodes with a Pt area  $A_{Pt} = 250 \times 250 \mu m^2$  and different Pt-layer thickness at (a) 310°C and (b) room temperature. The measurements were performed at a constant current density of  $3.2 A/cm^2$ .

This dependence of response  $R$  on  $H_2$  concentration can be described with the function (RectHyperbola):

$$R = a \frac{bC_{H_2}}{1 + bC_{H_2}}, \quad (2.37)$$

where  $a$  and  $b$  are constants. Different fits, with this function, were made and optimized values for the coefficients  $a$  and  $b$  as well as  $R^2$  are summarized in Tab.2.2 and Tab. 2.3 for 310°C and room temperature, respectively.

**Tab. 2.2:** Fitting parameter of the response  $R$  curves at 310°C.

Thickness (nm)	a	b	$R^2$
8	$383.49 \pm 6.51$	$11.52 \pm 0.68$	0.992
24	$362.18 \pm 12.47$	$5.54 \pm 0.63$	0.991
40	$359.78 \pm 38.95$	$2.09 \pm 0.49$	0.975

**Tab. 2.3:** Fitting parameter of the response R curves at room temperature.

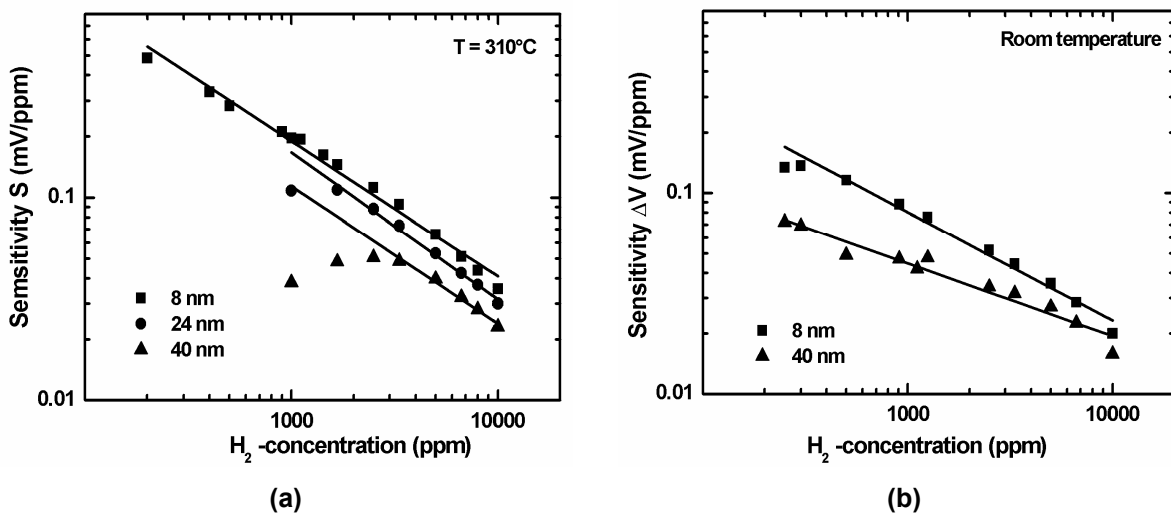
Thickness (nm)	a	b	R <sup>2</sup>
8	234.37 ± 6.12	5.70 ± 0.43	0.995
40	226.43 ± 9.51	2.638 ± 0.24	0.994

Fig. 2.37 shows the dependence of the sensitivity  $S$  on  $H_2$  concentration for Pt/GaN Schottky diodes with a Pt area  $A_{Pt} = 250 \times 250 \mu m^2$  and different Pt thicknesses at two different temperatures  $310^\circ C$  and room temperature is presented. We have found that the sensitivity  $S$  decreases non-linearly with an increasing concentration of  $H_2$  in air starting from 1000 to 10000 ppm for all Pt contact thicknesses. This effect is likely due to a reduction in the number of adsorption sites as the gas concentration is increased leading to a lower sensitivity for higher concentration of  $H_2$ .

One can see in Fig. 2.37 that the log/log trend fits perfectly the observed data in the range (1000-10000 ppm) of the  $H_2$  concentration. From the curve fitting, we can recover the equation of the sensitivity vs. the concentration:

$$S = 10^{(a+b \log C)}, \quad (2.38)$$

Where  $C$  is the  $H_2$  concentration expressed in ppm,  $a$  and  $b$  are constants. Different fits, with this equation were made and the values for the coefficient  $a$ ,  $b$ , and  $R^2$  are summarized in Tab. 2.4 and Tab. 2.5 at  $310^\circ C$  and room temperature, respectively.



**Fig. 2.37:** The dependence of the sensitivity  $S$  on  $H_2$  concentration for Pt/GaN Schottky diodes with Pt area ( $A_{Pt} = 250 \times 250 \mu m^2$ ) and different Pt-layer thickness at (a)  $310^\circ C$  and (b) room temperature. The measurements were done at a constant current density of  $3.2 A/cm^2$ .

**Tab. 2.4:** Fitting parameter of the sensitivity S curves at 310°C.

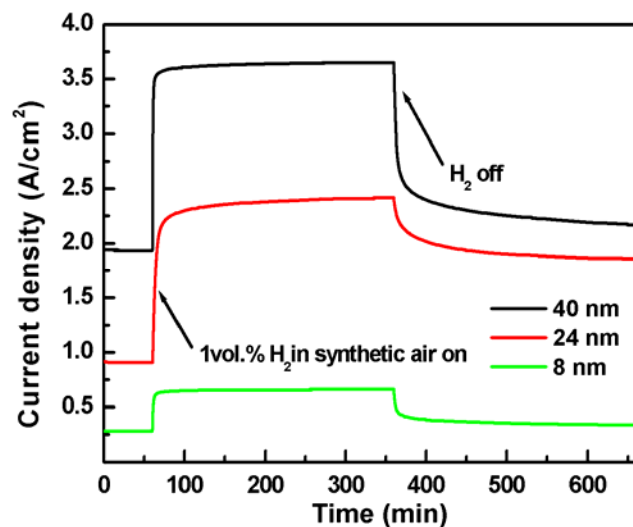
Thickness (nm)	a	b	R <sup>2</sup>
8	1.274 ± 0.06	-0.665 ± 0.02	0.994
24	1.4 ± 0.09	-0.726 ± 0.02	0.997
40	1.094 ± 1.69	-0.679 ± 0.04	0.993

**Tab. 2.5:** Fitting parameter of the sensitivity S curves at room temperature.

Thickness (nm)	a	b	R <sup>2</sup>
8	0.521 ± 0.09	-0.539 ± 0.02	0.992
40	-0.265 ± 0.06	-0.3619 ± 0.03	0.974

#### 2.6.3.4 Dynamic behaviour (I-t characteristics):

In order to clarify, if thinner Pt layers result in faster diffusion of hydrogen towards the Pt/GaN interface and therefore faster response of the sensor, time-resolved measurements were performed. Fig. 2.38 shows the response in A/cm<sup>2</sup> of a sensor held at a constant voltage (1 V) and exposed to 1 vol.% hydrogen in synthetic air for different thickness of Pt. The measurements were realized at room temperature. The response (diffusion) times were more than 1 hour and the recovery times were also very long, typically several hours.

**Fig. 2.38:** The change in current density of 500 x 500 µm<sup>2</sup> sensor in constant voltage mode (U = 1 V) at room temperature.

The long recovery time of Pt/GaN Schottky contacts after exposure to hydrogen at room temperature indicates storage of hydrogen atoms at electronically active adsorption sites. We observed a significant decrease of response and recovery time by decreasing the Pt thickness down to 8 nm.

An important aspect of sensor performance is stability and repeatability. Fig. 2.39 shows the response of a Pt/GaN Schottky diode with  $d_{\text{Pt}} = 24$  nm,  $A_{\text{Pt}} = 500 \times 500 \mu\text{m}^2$  to a repeated cycling of synthetic air to 1 vol.%  $\text{H}_2$  in synthetic air at an operating temperature of 200 and 310°C, respectively. It is observed that the responses are stable and reproducible.

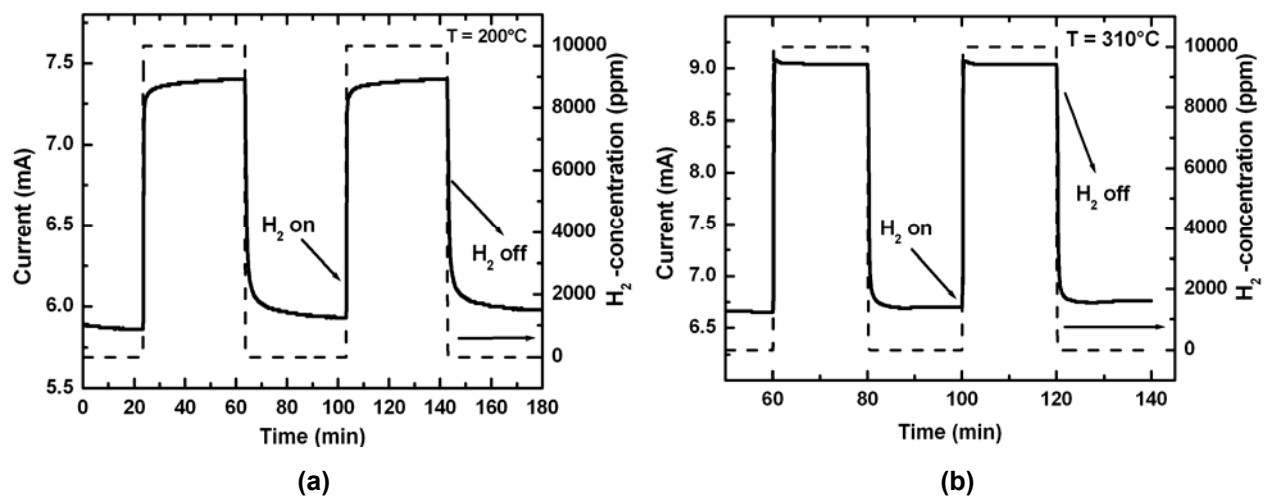


**Fig. 2.39:** Transient behaviour of the electrical response of a sensor with  $d_{\text{Pt}} = 24$  nm,  $A_{\text{Pt}} = 500 \times 500 \mu\text{m}^2$  in constant voltage mode ( $U = 1$  V) for device temperatures of (a) 200°C and (b) 310°C.

In Fig. 2.40, the response and recovery times are presented which are affected by increasing the operation temperature to about 350°C. In this work we have defined the response time as the time in which the output current reaches 90% of its final value. The recovery time is defined as the time in which the output current reaches 90% of its final value. The current variations are increased in proportion to the temperature. Again this effect can be attributed to the change of the Schottky barrier height.

We observed a significant decrease of the response and recovery times by increasing the operation temperature. As the temperature is increased from room temperature to 310°C the response time and recovery time are decreased from 13 min to 13 s and from 111 min to 35 s respectively (Fig. 2.41).

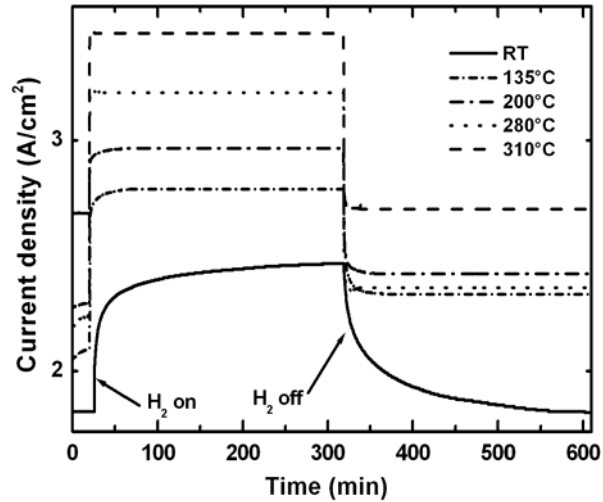


**Fig. 2.40:** Transient behaviour of the electrical response of a  $500 \times 500 \mu\text{m}^2$  sensor in constant voltage mode ( $U = 1 \text{ V}$ ) for different device temperatures. The thickness of Pt layer is 24 nm.

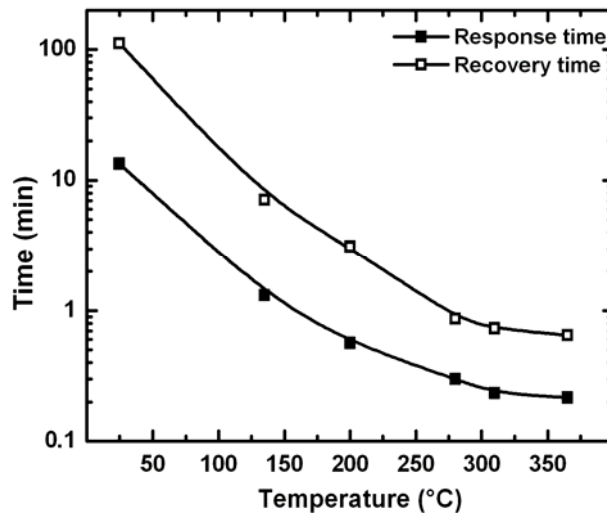


**Fig. 2.41:** Response and recovery times as a function of the operation temperature.

To investigate the nature of hydrogen response, we took the change in forward current at a fixed time of 1 min after switching of the gas and plotted this change in Arrhenius format in Fig. 2.42.

The data in Fig. 2.42 does not show a single slope, i.e., there are two different mechanisms at work. At high temperatures ( $\geq 135^\circ\text{C}$ ), the activation energy is 7.52 kJ/mol (0.078 eV). This value is in the range of the diffusion-limited processes. This suggests that the time needed for the atomic hydrogen to diffuse through the Pt to the Pt/GaN interface is the rate-limiting step under these conditions. As the temperature is lowered below  $135^\circ\text{C}$ , there is obviously an other mechanism at work

and it is plausible that under these conditions the initial dissociation of the  $H_2$  is one of the rate-limiting steps, along with competing processes such as recombination of atomic hydrogen to form  $H_2$  molecules.

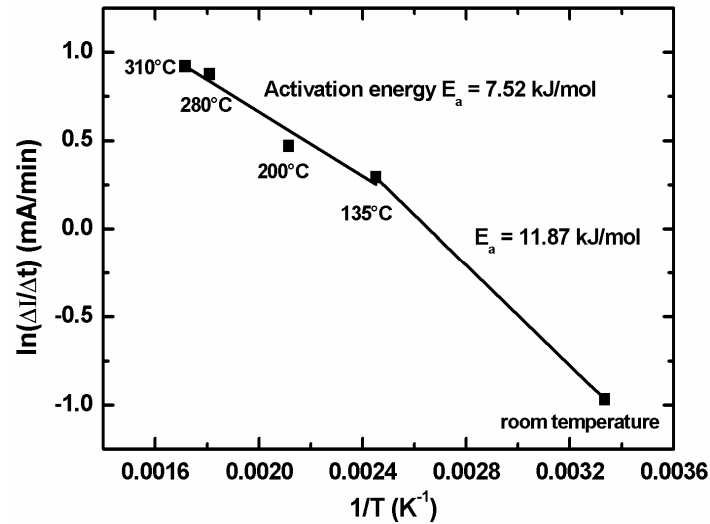
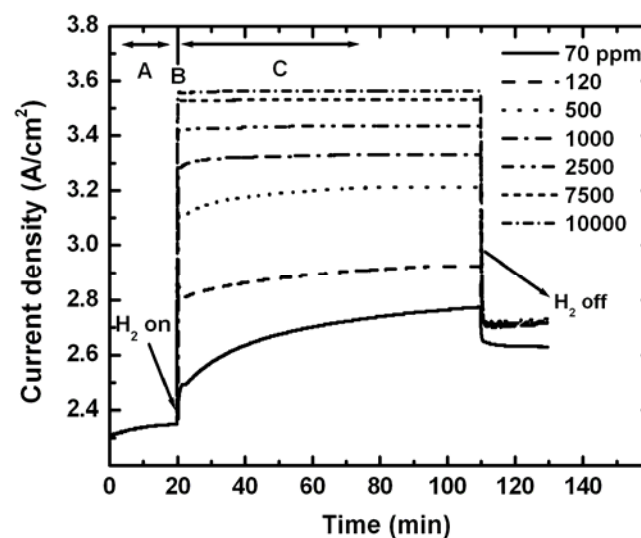


Fig. 2.42: Arrhenius plot of change in forward current of Pt/GaN diodes at a fixed time of 1 min after switching from synthetic air to 1 vol.%  $H_2$  in synthetic air.

Fig. 2.43 shows the transient response on the introduction and removal of 70, 120, 500, 1000, 2500, 7500 and 10000 ppm hydrogen gas at 280°C. The applied voltage is kept at 1 V.



**Fig. 2.43:** Transient behaviour of the electrical response of a Pt/GaN sensor ( $d_{Pt} = 24$  nm,  $A_{Pt} = 500 \times 500 \mu m^2$ ) sensor in constant voltage mode for different concentrations of  $H_2$  at an operating temperature  $T = 310^\circ C$ .

Obviously, the current variations are increased in proportion to the hydrogen concentration. When the catalytic metal, e.g. Pd or Pt, is exposed to hydrogen gas, hydrogen molecules are separated into hydrogen atoms and part of them permeate into the catalytic metal. These hydrogen atoms trapped at the interface between the metal and the semiconductor cause an electrical polarization given by [2.35]:

$$\Delta V = \frac{\mu N_i \theta_i}{\epsilon}, \quad (2.39)$$

where  $\mu$  is the effective dipole moment,  $N_i$  is the number of sites per area at the interface,  $\theta_i$  is the coverage of hydrogen atoms at the interface and  $\epsilon$  is the dielectric constant. The higher the hydrogen concentration causes a larger value of  $\Delta V$ . In order to study the transient response characteristics in more detail, the transient response curves are divided into A, B and C regions (see Fig. 2.43).

In region A, the studied device is exposed to synthetic air and the measured current is considered as a reference current. In region B, the hydrogen gas is introduced. As the hydrogen concentration is increased from 70 ppm to 10000 ppm, the response time constant is decreased from 30 min to 3 sec as shown in Fig. 2.44. This positive hydrogen concentration dependence can be attributed to the increased collision among hydrogen atoms that induce a higher reaction rate and more hydrogen atoms trapped at the Pt/GaN interface. In region C, the transient response curves approach a dynamic equilibrium. In this region, the curves exhibit saturation trends.

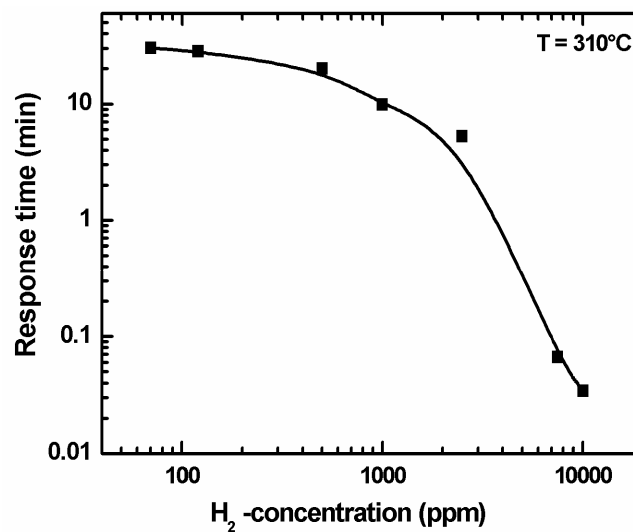


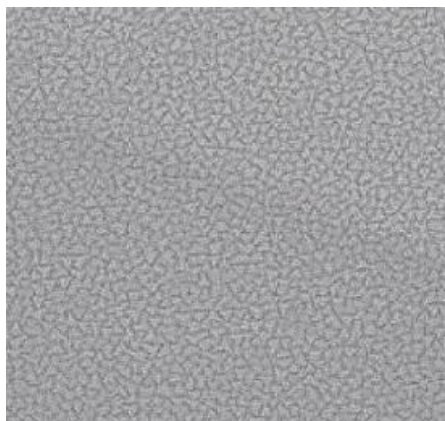
**Fig. 2.44:** The response time measured for different concentrations of H<sub>2</sub>. The operating temperature is T = 310°C.



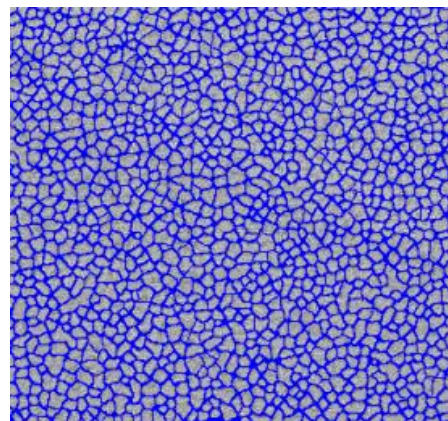
In a last step, the microstructure of Pt contacts was studied by means of high resolution SEM (HR-SEM) image analysis in order to investigate the differences observed in the diffusion of hydrogen through Platinum. Tab. 2.6 describes the microstructure of the three thicknesses of Pt in terms of the grain boundary density and the average grain size.

**Tab. 2.6:** Microstructure of Schottky contacts with three thickness of Pt. The response of a 250 x 250  $\mu\text{m}^2$  device is measured in constant mode with current density of 3.2 A/cm<sup>2</sup> [2.36].

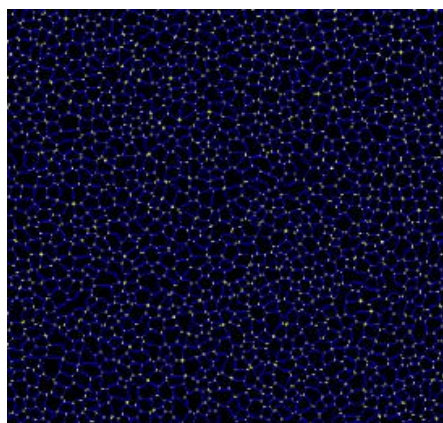
Thickness (nm)	Triple phase boundaries (TPB) (#/ $\mu\text{m}^2$ )	Mean grain size (nm)	Response at 25°C (mV)
8	19210	9.1	73
24	10825	12.9	60.7
40	7144	15.5	56.8



(a)



(b)



(c)

**Fig. 2.45.** (a) an SEM image of the 8 nm Pt surface; (b) the processed image showing the cell boundaries; (c) the processed image showing the grain boundaries [2.36].

As expected, the higher response film also has the higher grain boundary density proving that hydrogen molecules dissociate on the Pt surface and diffuse along the grain boundaries reaching the Pt/GaN interface (Fig. 2.45).

## 2.7 Temperature-programmed desorption (TPD) measurements:

### 2.7.1 TPD background and fundamentals:

Temperature-programmed desorption (TPD) techniques are important methods for the determination of kinetic and thermodynamic parameters of desorption processes or decomposition reactions. A sample is heated with a temperature ramp  $\beta(t) = dT/dt$  (with the temperature  $T$  usually being a linear function of the time  $t$ ) and the partial pressures of atoms and molecules evolving from the sample are measured, e.g. by quadrupole mass spectrometer (QMS). When experiments are performed using well-defined surfaces of single-crystalline samples in a continuously pumped ultra-high vacuum (UHV) chamber then this experimental technique is often also referred to as thermal desorption spectroscopy (TDS).

#### 2.7.1.1 Kinetics of desorption:

The disengagement of an atom or molecule from a surface is termed "desorption". At low temperatures a molecule adsorbed on a surface could remain for an indefinite time. However, as the surface temperature increases the molecule will receive energy, and so one of the following processes can occur:

- the molecules can react with the surface,
- the molecules can break down to two or more other molecules (either in gaseous or solid state),
- the molecules can desorb.

The last option is the desorption process, which could also occur in the second option if one of the products is a gas.

##### 2.7.1.1.1 Polanyi-Wigner Equation:

The desorption rate is usually expressed by a rate law of  $n^{\text{th}}$  order [2.37]:

$$r_{des} = -\frac{d\theta}{dt} = k_n \theta^n, \quad (2.40)$$

If the rate constant  $k_n$  is described by the *Arrhenius* equation:

$$k_n = \nu \exp\left(-\frac{E_{des}}{RT}\right), \quad (2.41)$$

then the rate law is usually referred to as the *Polanyi-Wigner* equation:

$$r_{des} = -\frac{d\theta}{dt} = \nu \theta^n \exp\left(-\frac{E_{des}}{RT}\right), \quad (2.42)$$

where  $\nu$  is the rate constant ( $s^{-1}$ ),  $\theta$  is the instantaneous coverage (the areal density of molecules in molecules/cm<sup>2</sup>),  $n$  is the kinetic or desorption order,  $R$  is the universal gas constant (8.31 J/mol), and  $E_{des}$  is the activation energy of desorption (J/mol).

Most terms in the Polanyi-Wigner equation are:

- factors affecting peak desorption temperature:  $E_{des}$ ,  $\nu$ ,  $\theta$  ( $n \neq 1$ ),
- factors affecting peak desorption temperature:  $\nu$ ,  $n$  and
- factors affecting peak desorption temperature:  $\theta$ .

Eq. 2.42 can be rewritten:

$$\ln\left(\frac{d\theta}{dt}\right) = \ln \nu + n \ln \theta + \frac{-E_{des}}{RT}. \quad (2.43)$$

A graph of  $\ln(d\theta/dt)$  versus  $1/T$  will produce a straight line of slope  $-E_{des}/R$  and intercept  $\ln \nu + n \ln \theta$ .

### 2.7.1.1.2 Analysis according to Reahead:

Redhead *et al.* [2.37] derived a simple relation between  $E_{des}$ ,  $\nu$ , and  $T_{max}$ . He assumed that activation parameters are independent of surface coverage and that desorption followed 1<sup>st</sup> order kinetics. During TPD the sample is heated with a linear ramp:

$$T(t) = T_0 + \frac{dT}{dt}t = T_0 + \beta t. \quad (2.44)$$

where  $\beta$  is the heating rate (K/s). Substituting the time  $t$  in the *Polanyi-Wigner* Eq. 2.42 by  $dt = (1/\beta)dT$ :

$$\frac{d\theta}{dT} = -\frac{1}{\beta} \nu \theta^n \exp\left(-\frac{E_{des}}{RT}\right). \quad (2.45)$$

For the maximum at  $T = T_{max}$  the condition:

$$\left.\frac{dr_{des}}{dT}\right|_{T_{max}} = 0, \quad (2.46)$$

must be fulfilled, or, because of  $r_{des} = -\frac{d\theta}{dt} = -\beta \frac{d\theta}{dT}$ :

$$\left. \frac{d^2\theta}{dT^2} \right|_{T_{max}} = n\theta \frac{d\theta}{dT} + \theta^n \frac{E_{des}}{RT_{max}^2}. \quad (2.47)$$

Inserting (2.45) for  $d\theta/dT$  and solving for  $\frac{E_{des}}{RT_{max}^2}$  provides

$$\frac{E_{des}}{RT_{max}^2} = \frac{1}{\beta} \nu n \theta^{n-1} \exp\left(-\frac{E_{des}}{RT_{max}}\right). \quad (2.48)$$

If 1<sup>st</sup> order desorption ( $n = 1$ ) takes place then  $T_{max}$  is independent of the coverage  $\theta$ , but dependent on the heating rate  $\beta$ :

$$\frac{E_{des}}{RT_{max}^2} = \frac{1}{\beta} \nu \exp\left(-\frac{E_{des}}{RT_{max}}\right). \quad (2.49)$$

Solving (2.49) for  $E_{des}$  provides

$$E_{des} = RT_{max} \left[ \ln \frac{\nu T_{max}}{\beta} - \ln \frac{E_{des}}{RT_{max}} \right], \quad (2.50)$$

where the second part in brackets is small relative to the first and is estimated as  $\ln(E_{des}/RT_{max}) = 3.64$ . The error introduced through this estimate is less than 1.5% for  $10^8 < \nu / \beta < 10^{13} \text{ K}^{-1}$ .

Eq (2.50) becomes:

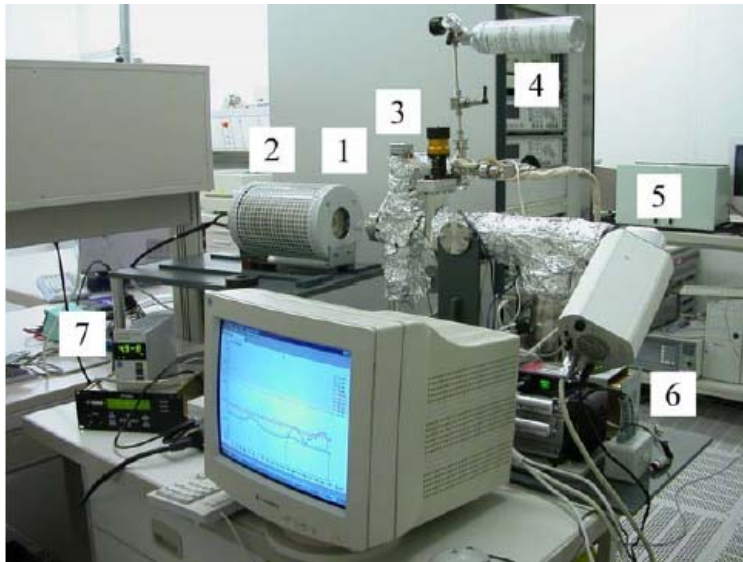
$$E_{des} = RT_{max} \left[ \ln \frac{\nu T_{max}}{\beta} - 3.64 \right]. \quad (2.51)$$

The Redhead method is often employed to extract activation energies from a single desorption spectrum. This requires that an approximate value for  $\nu$  is known ( $\nu = 10^{13} \text{ s}^{-1}$  is a commonly chosen value).

## 2.7.2 Experimental:

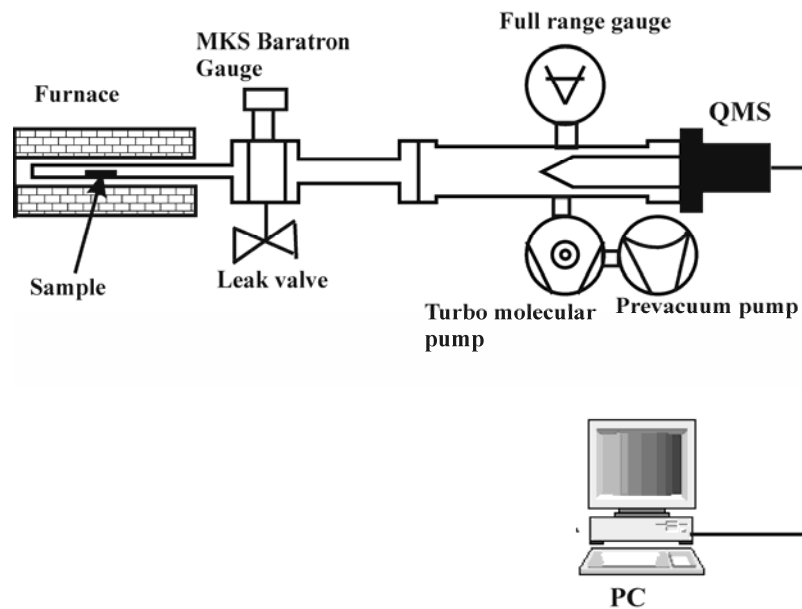
### 2.7.2.1 UHV system:

TPD experiments were performed in an ultra-high vacuum (UHV) system consisting of a pumping system and the vacuum chamber. The chamber consists of a closed quartz tube of about 25 cm in length and 1 cm in diameter. A photograph and schematic drawing of the UHV apparatus for this experiment and all devices mounted in it is shown in Fig. 2.46.



- 1: Chamber
- 2: Programmable heater (furnace)
- 3: Leak valve (needle valve)
- 4: Deuterium- reservoir
- 5: Quadrupole mass spectrometer (QMS 200).
- 6: Pump Station
- 7: Pressure measurements

(a)



(b)

**Fig. 2.46:** UHV system. (a) Photograph (b) Schematic drawing.

All parts of the vacuum vessel are made from high-grade steel. Besides the pressure gauges, the following equipment is attached to the chamber and will be utilised for the experiment:

- a leak valve (needle valve), allowing the controlled dosing of gases into the UHV chamber and
- a quadrupole mass spectrometer (QMS) type (Balzers QMS 200).

Vacuum is maintained by a turbomolecular pump with pumping speed of 60 l/s backed by a membrane vacuum pump as prevacuum pump. Dosing of gases into the

chamber is achieved by use of a leak valve. The final pressure  $P_f$  measured during dosing is the sum of the base pressure  $P_0$  and the partial pressure  $P_i$  of the gas flowing into the system, i.e.,  $P_f - P_0 = P_i$  (or  $P_i = P_f$  for  $P_0 \ll P_f$ ).

### 2.7.2.2 Sample preparation for TPD measurements:

High-purity platinum (99.995%) was evaporated with an electron-beam evaporator (Ardeene LA 440 S) with areas of  $0.6 \times 2.1 \text{ cm}^2$  on Si-doped GaN layers grown on the c-plane of sapphire substrates by (MBE) molecular-beam epitaxy. The thickness of Pt metal was of about 24 nm as determined by profilometer. The GaN surface was treated 1min with BOE (7:1) to remove the surface oxide before Pt evaporation.

The deposition conditions were as follows:

- base pressure  $\sim 2 \times 10^{-6}$  mbar,
- deposition pressure  $\sim 10^{-5}$  mbar and
- substrate temperature: room temperature.

### 2.7.2.3 Measurements procedure:

The Pt/GaN sample with Pt thickness of 24 nm and area of  $1.26 \text{ cm}^2$  was put in the quartz tube which was placed in an electrical furnace. The sample was exposed at different temperatures to different partial pressures of deuterium ( $D_2$ ) for different times, and then the sample was heated with a linear temperature ramp ( $24^\circ\text{C}/\text{min}$ ) from  $100^\circ\text{C}$  up to  $800^\circ\text{C}$ . Four procedures were performed:

- The sample was exposed to  $D_2$  of 4 mbar for different times (from 10 min to 20 h) at room temperature and then  $D_2$  was pumped away and the quartz tube was evacuated to less than  $2 \times 10^{-8}$  mbar before starting the measurement **(Procedure I)**.
- The sample was exposed to  $D_2$  of 40 mbar for 3 min at different temperatures (from room temperature to  $300^\circ\text{C}$ ) and then  $D_2$  was pumped away and the quartz tube was evacuated to less than  $2 \times 10^{-8}$  mbar before starting the measurement **(Procedure II)**.
- The sample was exposed to  $D_2$  of 40 mbar for different times (from 1/2 min to 10 min) at  $100^\circ\text{C}$  and then  $D_2$  was pumped away and the quartz tube was evacuated to less than  $2 \times 10^{-8}$  mbar before starting the measurement **(Procedure III)**.

- The sample was exposed to D<sub>2</sub> of different partial pressures (from 0.5 to 50 mbar) for 3 min at 15°C and then D<sub>2</sub> was pumped away and the quartz tube was evacuated to less than  $2 \times 10^{-8}$  mbar before starting the measurement **(Procedure IV)**.

The products of desorption were measured using a Balzers QMS 200 type quadrupole mass spectrometer with a detection limit of  $10^{-14}$  mbar and the ability to detect 9 masses in one cycle (cycletime  $\approx$  30 s). During the experiment the total pressure was always below  $10^{-7}$  mbar to ensure that the mean free path of the effused radicals and molecules is longer than the distance between the sample and the entrance of the mass spectrometer. The partial pressures of D<sub>2</sub>, H<sub>2</sub>O, CO, N<sub>2</sub>, and O<sub>2</sub> in the quartz tube were determined at the same time. To calculate the concentration of the desorbed species or the deuterium flux from the sample surface, the effective pumping speed at the position of the quadrupole mass spectrometer (QMS) was determined for deuterium [ $S_{\text{eff}}(\text{D}_2) = 41.66$  l/s].

Because of the turbomolecular pumping system used, the pumping rate is constant over the whole measurement range so that the partial pressure values allow the calculation of the flux or desorption rate  $F(x)$  of molecules  $x$  evolved at the temperature  $T$  from the measured partial pressure  $p(x)$  (mbar) and effective constant pumping rate  $S(x)$  [mbar l/s]. Under the assumption that the desorbed gases can be treated as ideal gases ( $N_A$  Avogadro's number,  $p_0$  pressure under normal conditions) one obtains:

$$F(x) = \frac{N_A}{22.4l} \cdot \frac{p(x)S(x)}{p_0 A} (\text{cm}^{-2}\text{s}^{-1}). \quad (2.52)$$

By integrating the molecular flux over the measured time, it is possible to determine the total amount ( $x$ ) of desorbed molecules.

### 2.7.3 Results:

Fig. 2.47 shows the residual gas spectrum of the quartz tube at 100°C. As it can be seen, the peaks are observed at mass of 2, 16, 18, 28 and 32. This is exactly the composition of air with water, hydrogen, nitrogen and oxygen. A further peak is to be recognized on mass 44. This is with large probability carbon dioxide.

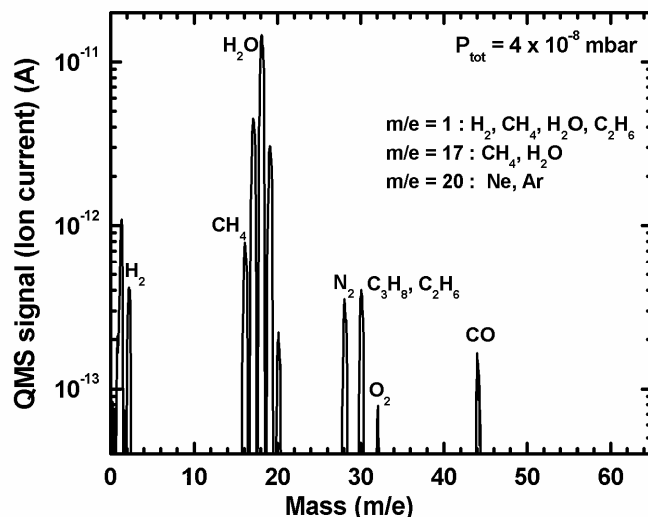


Fig. 2.47: The residual gas spectrum of the quartz tube at 100°C.

The partial pressures of  $D_2$ , CO,  $O_2$ ,  $H_2O$ , and  $H_2$  desorbed from the fresh sample versus time, as well as versus desorption temperature are shown in Fig. 2.48a and Fig. 2.48b, respectively. The sample was exposed to  $D_2$  of 4 mbar for 30 min at room temperature and then  $D_2$  was pumped away and the quartz tube was evacuated to less than  $2 \times 10^{-8}$  mbar before the desorption from the sample was measured.

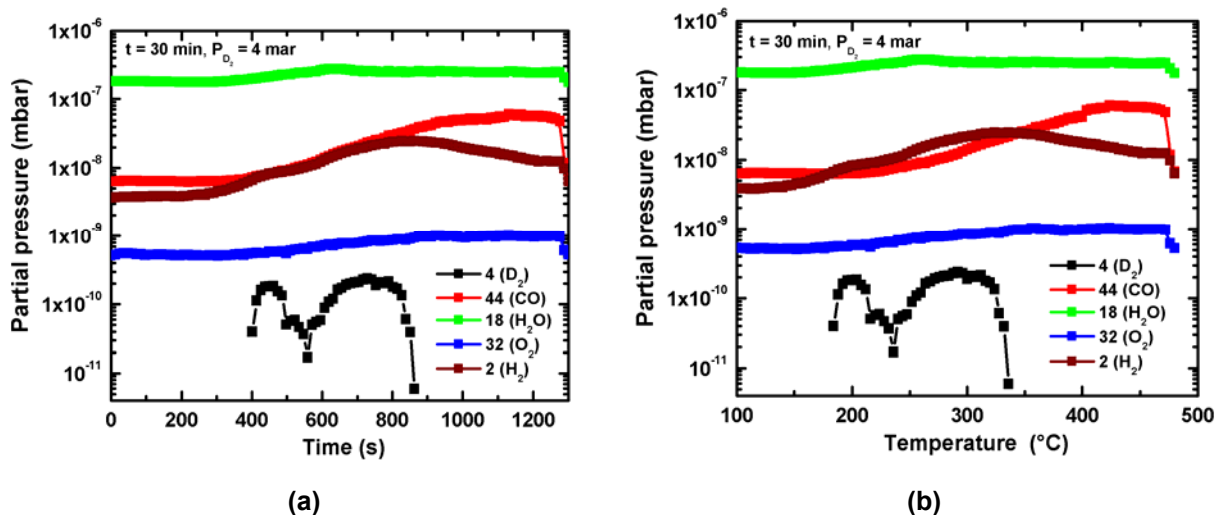
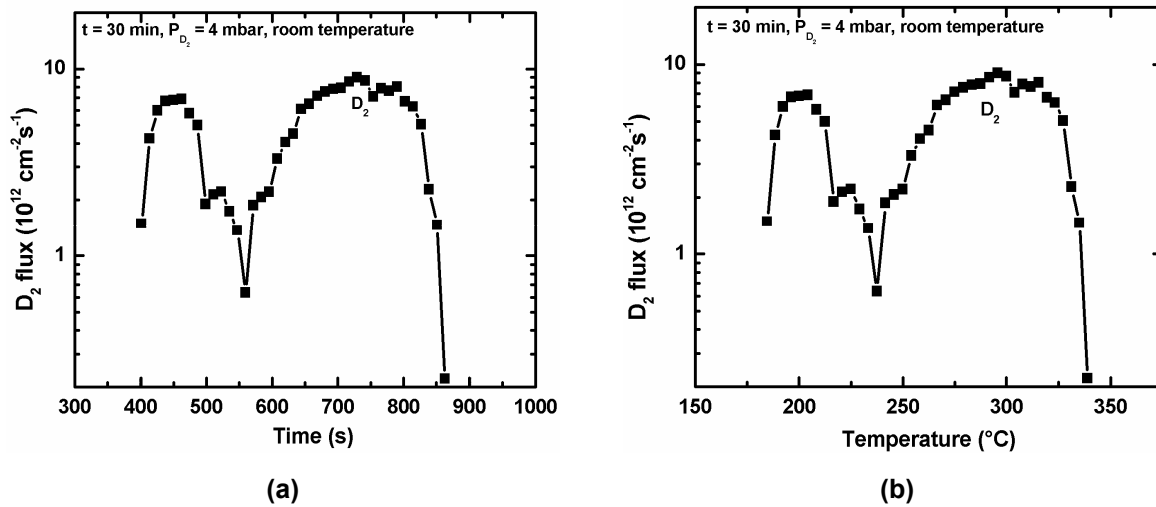


Fig 2.48: The partial pressures of  $D_2$ , CO,  $O_2$ ,  $H_2O$ , and  $H_2$  desorbed from the fresh sample versus time (a), as well as versus desorption temperature (b). The sample was exposed to  $D_2$  of 4 mbar for 30 min at room temperature.

As can be seen in Fig. 2.49, four peaks are found in the case of  $D_2$ . These peaks are centred on 200, 250, 290 and 310°C, respectively.





**Fig. 2.49:** Deuterium flux from the sample (a) versus time and (b) versus desorption temperature.

The peak 1 and 2 is due to  $D_2$  desorption from the Pt-surface and the other peaks is due to desorption from the Pt-bulk and Pt/GaN interface. The peak of  $H_2O$  observed at  $260^\circ\text{C}$  and the increase of the partial pressure of mass 32, and 44 starting at  $T > 200^\circ\text{C}$  indicate to the existence of oxygen at the interface between Pt layer and GaN.

The  $D_2$  flux versus time, and versus desorption temperature are shown in Fig. 2.49a and Fig. 2.49b, respectively. By integrating the molecular flux over the measured time, it is possible to determine the total amount of desorbed molecules of  $D_2$ . The total amounts of  $D_2$  desorbed from the Pt-surface (peak 1 and 2) and from Pt bulk as well as Pt-GaN interface (peaks 2 and 3) are  $6.3 \times 10^{14} \text{ cm}^{-2}$  and  $1.7 \times 10^{15} \text{ cm}^{-2}$ , respectively. Our results indicate an interfacial effect with a coverage approximately monolayer to occur in the case of Pt/GaN contacts. The low hydrogen (deuterium) amount of  $1.7 \times 10^{15} \text{ cm}^{-2}$  let us believe that the hydrogen adsorption takes place at the semiconductor side [2.3].

### 2.7.3.1 Procedure I:

The influence of exposure time to  $D_2$  at room temperature on the  $D_2$  flux is presented in Fig. 2.50. The sample was exposed to  $D_2$  of 4 mbar for different times at room temperature and then  $D_2$  was pumped away and the quartz tube was evacuated to less than  $2 \times 10^{-8}$  mbar and then the desorption from the sample was measured. As one can see the main  $D_2$  desorption peaks occurred in the range  $192\text{--}232^\circ\text{C}$  (Fig. 2.51).

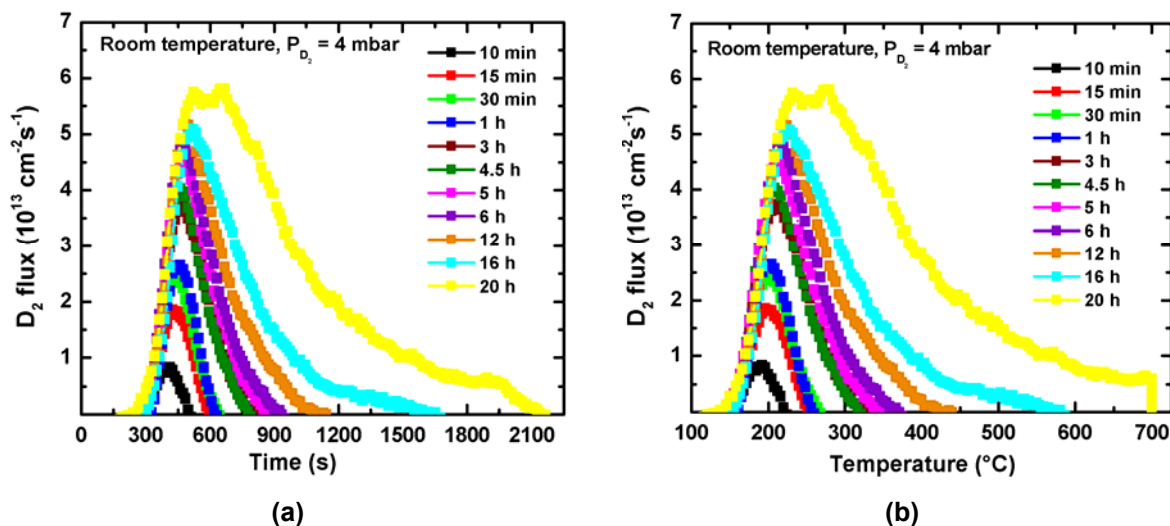


**Fig. 2.50:** Deuterium flux from the sample versus time (a) and versus desorption temperature (b). The sample was exposed to  $D_2$  of 4 mbar for different times at room temperature.

The shape of the desorption spectra shown in Fig. 2.50 exhibit the characteristics of zero-order desorption. In the zero-order case, the TPD curves are asymmetric, with coincident rinsing edges, and the peak temperature,  $T_m$ , increases with exposure. This is typical of multiplayer desorption, where the intensity of the TPD spectrum increases as more and more material is condensed on the surface. The shift in  $T_m$  (the peak position) occurs because the desorption rate increases exponentially with temperature, so the rate can increase indefinitely until all the layers have been stripped away, and the TPD signal falls rapidly to zero.

Fig. 2.51 presents the influence of the exposure time on the total amount of  $D_2$  desorbed from the sample and on the peak temperature  $T_m$ .

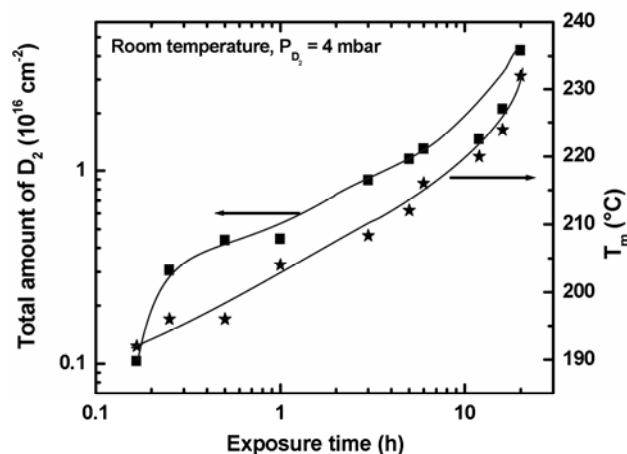


**Fig. 2.51:** The influence of the exposure time on the total amount of  $D_2$  desorbed from the sample and on the peak temperature  $T_m$ .

We have found that the total amount of  $D_2$  desorbed from the sample increases by increasing the exposure time and no saturation was observed even at long exposure time of 20 h.

The activation energy  $E_{des}$  for  $D_2$  desorption is extracted from the linear part of the Arrhenius plot (Fig. 2.52a). The activation energy expressed in kJ/mol as well as eV versus the exposure time (adsorption time) presented in Fig 2.52b. Clearly, the activation energy increases linearly with increasing exposure time.

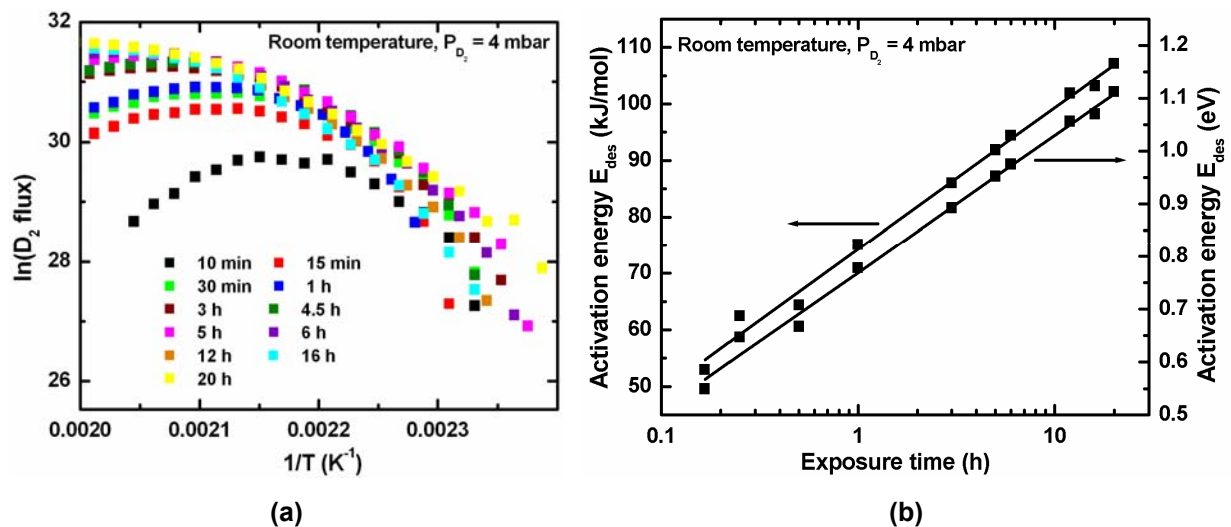
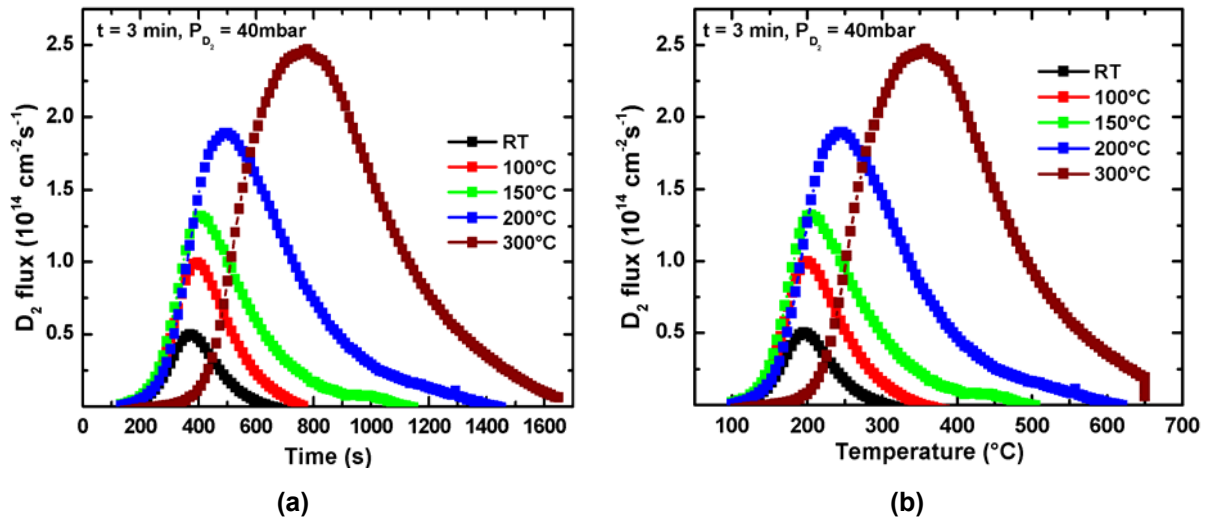


**Fig. 2.52:** (a) Arrhenius plot ( $\ln(D_2 \text{ flux})$  versus  $1/T$ ); (b) The dependence of the activation energy of desorption  $E_{des}$  on the exposure time (adsorption time).

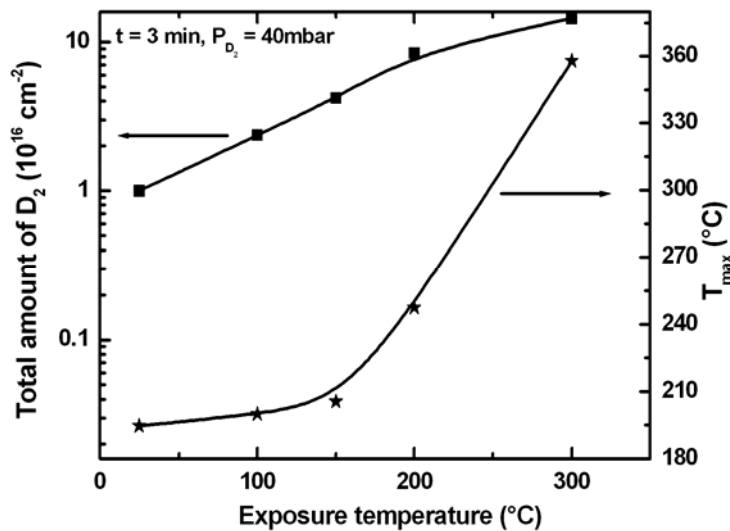
### 2.7.3.2 Procedure II:

Fig. 2.53 shows the influence of exposure temperature (adsorption temperature) on the  $D_2$  flux is. The sample was exposed to  $D_2$  of 40 mbar for 3 min at different temperatures and then  $D_2$  was pumped away and the quartz tube was evacuated to less than  $2 \times 10^{-8}$  mbar and then the desorption from the sample was measured.

One desorption peak was found for all adsorption temperatures. With increasing the exposure temperature (adsorption temperature), the desorption peak grows and the desorption temperature shifts to higher temperature (from  $195^\circ\text{C}$  for room temperature exposure to  $358^\circ\text{C}$  for exposure at  $300^\circ$ ) as shown in Fig. 2.54.



**Fig. 2.53:** Deuterium flux from the sample versus time (a) and versus desorption temperature (b). The sample was exposed to  $D_2$  of 40 mbar for 3 min at different temperatures.



**Fig. 2.54:** The influence of the exposure temperature on the total amount of  $D_2$  desorbed from the sample and on the peak temperature  $T_m$ .

In addition, the total amounts of  $D_2$  desorbed from the sample increases with increasing exposure temperatures and no saturation was observed even at high temperature of  $300^{\circ}\text{C}$  (Fig. 2.54). This observation agrees with the results presented in Fig. 2.31. The higher the exposure temperature, the higher amount of  $D_2$  desorbed from the sample (Pt/GaN) and thus higher response of the Pt/GaN Schottky diode sensors.

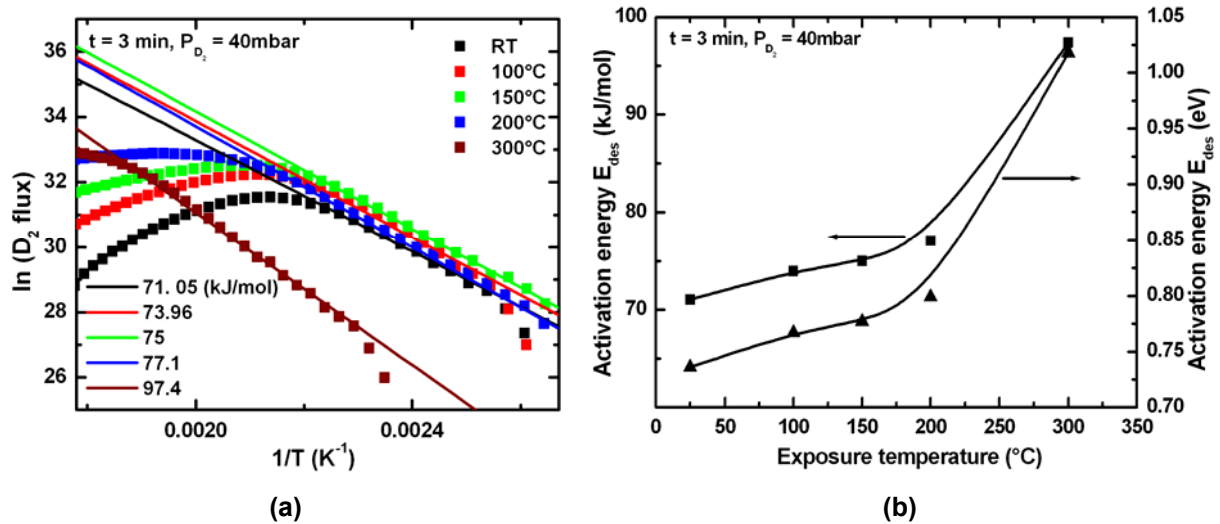


**Fig. 2.55:** (a) Arrhenius plot ( $\ln(D_2 \text{ flux})$  versus  $1/T$ ); (b) The dependence of the activation energy of desorption  $E_{\text{des}}$  on the exposure temperature (adsorption temperature).

The activation energy  $E_{\text{des}}$  of D<sub>2</sub> desorption is extracted from the linear part of the Arrhenius plot that slopes down indicating to that the deuterium have completely desorbed from the sample (Fig. 2.55a). The activation energy expressed in kJ/mol and eV versus the exposure temperature (adsorption temperature) is shown in Fig. 2.55b. We have found that the activation energy increases non-linearly with increasing exposure temperature.

### 2.7.3.3 Procedure III:

The influence of exposure time to D<sub>2</sub> at 100°C temperature on the D<sub>2</sub> flux is presented in Fig. 2.56. The sample was exposed to D<sub>2</sub> of 40 mbar for different times at 100°C and then D<sub>2</sub> was pumped away and the quartz tube was evacuated to less than  $2 \times 10^{-8}$  mbar and then the desorption from the sample was measured.

The shape of the desorption spectra shown in Fig. 2.56 exhibits the characteristics of first order desorption: constant peak temperature and asymmetric desorption curves about a single  $T_m$  value of 200°C. A first order analysis of the leading edges of these spectra reveals an activation energy for desorption of about 70 kJ/mol (0.732 eV) (Fig. 2.57).

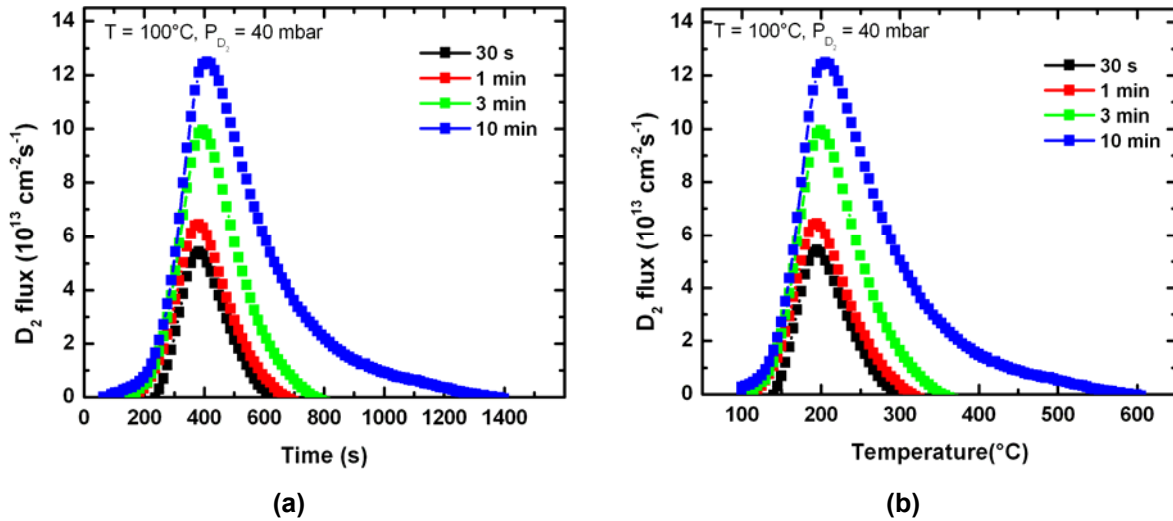


**Fig. 2.56:** Deuterium flux from the sample versus time (a) and versus desorption temperature (b). The sample was exposed to  $\text{D}_2$  of 40 mbar for different times at  $100^\circ\text{C}$ .

The total amount of  $\text{D}_2$  desorbed from the sample versus the exposure time is shown in Fig. 2.58. The longer the exposure time, the wider the desorption peak (Fig. 2.56) and the higher amount of  $\text{D}_2$  desorbed from the sample. We have found that the total amount of  $\text{D}_2$  desorbed from the sample increases non-linearly with increasing exposure time and saturation trend was observed at exposure time longer than 3 min.

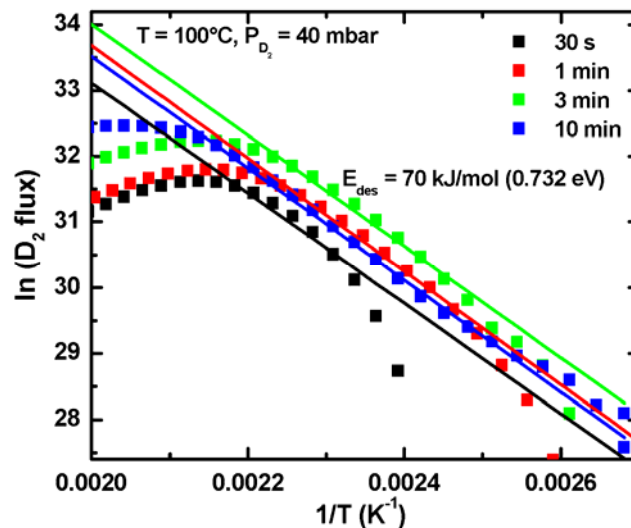


**Fig. 2.57:** (a) Arrhenius plot ( $\ln(\text{D}_2 \text{ flux})$  versus  $1/T$ ). The sample was exposed to  $\text{D}_2$  of 40 mbar for different times at  $100^\circ\text{C}$ .

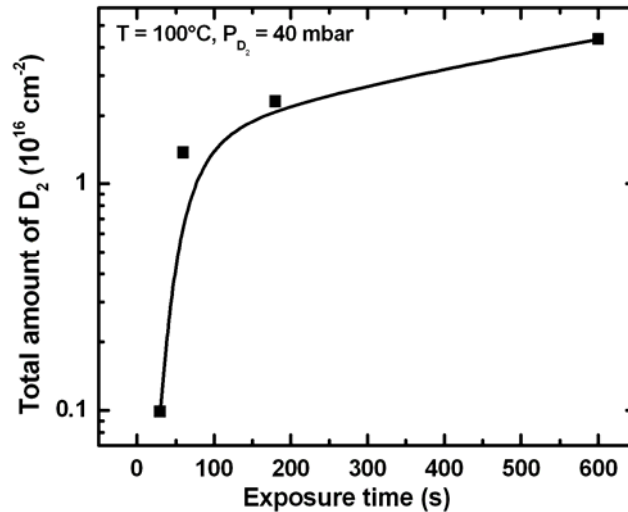


**Fig. 2.58:** The influence of the exposure time on the total amount of  $D_2$  desorbed from the sample. The sample was exposed to  $D_2$  of 40 mbar for different times at  $100^\circ\text{C}$ .

#### 2.7.3.4 Procedure IV:

The influence of exposure dose on the  $D_2$  flux is shown in Fig. 2.59. The sample was exposed to various partial pressures of  $D_2$  for 3 min at  $150^\circ\text{C}$  and then  $D_2$  was pumped away and the quartz tube was evacuated to less than  $2 \times 10^{-8}$  mbar and then the desorption from the sample was measured.

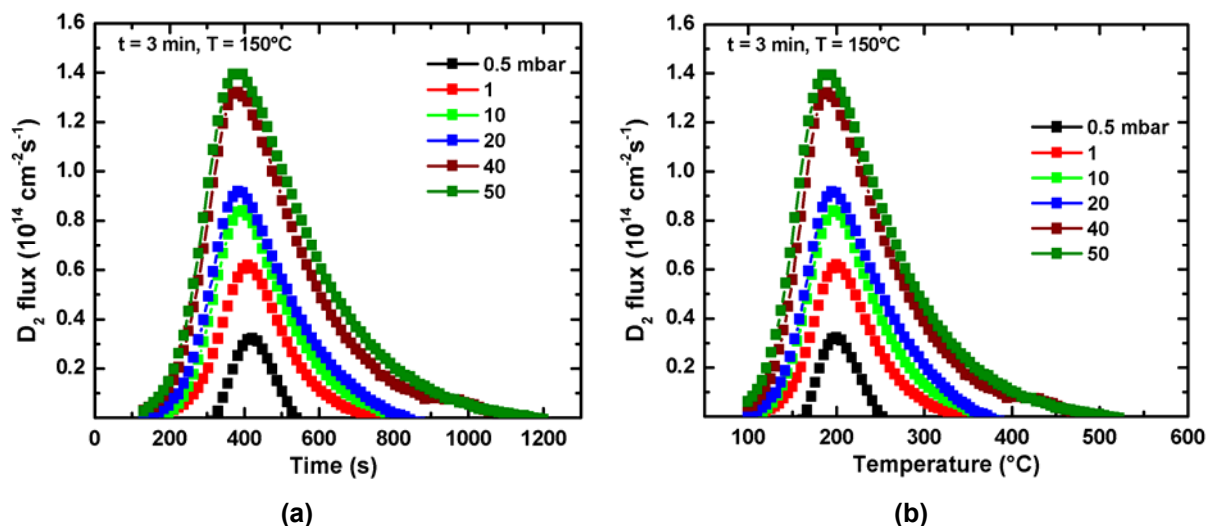


**Fig. 2.59:** Deuterium flux from the sample versus time (a) and versus desorption temperature (b). The sample was exposed to various partial pressures of  $D_2$  of 40 mbar for 3 min at  $150^\circ\text{C}$ .

After exposure to 0.5 mbar of  $D_2$ , the TPD gives a single symmetric peak at  $200^\circ\text{C}$ ; with increasing the  $D_2$  exposure, the desorption peak grows and the desorption

temperature shifts to lower temperature. These observation demonstrate a typical two-order desorption kinetics, proving that  $D_2$  dissociatively chemisorbs on Pt surface to form surface  $H_{ad}$  species that, upon heating, recombines to form  $H_2$  desorbing from the surface [2.38]. The surface  $H_{ad}$  species tends to saturate after a dose of 50 mbar, and the corresponding TPD spectrum gives a single desorption peak at  $190^\circ\text{C}$  (Fig. 2.60).

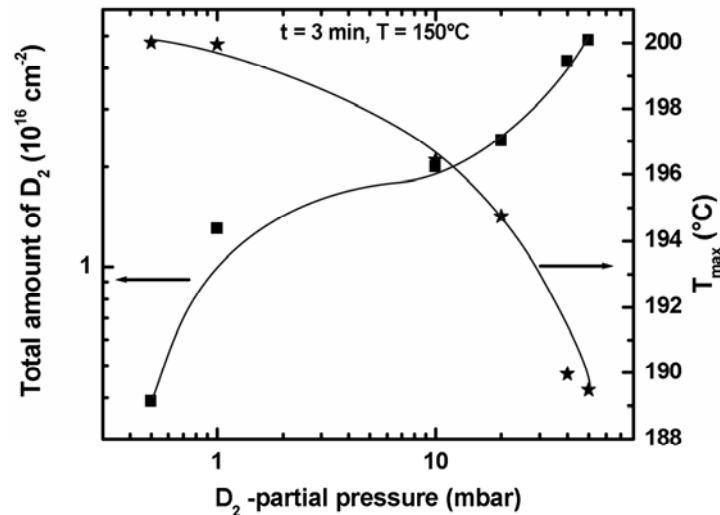


**Fig. 2.60:** The influence of the exposure dose on the total amount of  $D_2$  desorbed from the sample and on the peak temperature  $T_m$ .

Fig. 2.60 presents the total amount of  $D_2$  desorbed from the sample versus the  $D_2$  partial pressure (exposure dose). The higher the exposure dose, the wider the desorption peak (Fig. 2.59) and the higher the amount of  $D_2$  desorbed from the sample. This observation agrees with the results presented in Fig. 2.36. The higher the exposure dose, the higher the amount of  $D_2$  desorbed from the sample (Pt/GaN) and thus the response of the Pt/GaN Schottky diode increases.

As one can see in Fig. 2.60, the total amounts of  $D_2$  desorbed from the sample increases non-linearly with increasing exposure times and no saturation was observed even at high exposure dose of 40 mbar. The activation energy  $E_{des}$  of  $D_2$  desorption is extracted from the linear part of the Arrhenius plot (Fig. 2.61a). The activation energy expressed in kJ/mol and eV versus the exposure dose ( $D_2$  partial pressures) is shown in Fig. 2.61b. We have found that the activation energy of desorption  $E_{des}$  decreases continuously with increasing partial pressure of  $D_2$ .



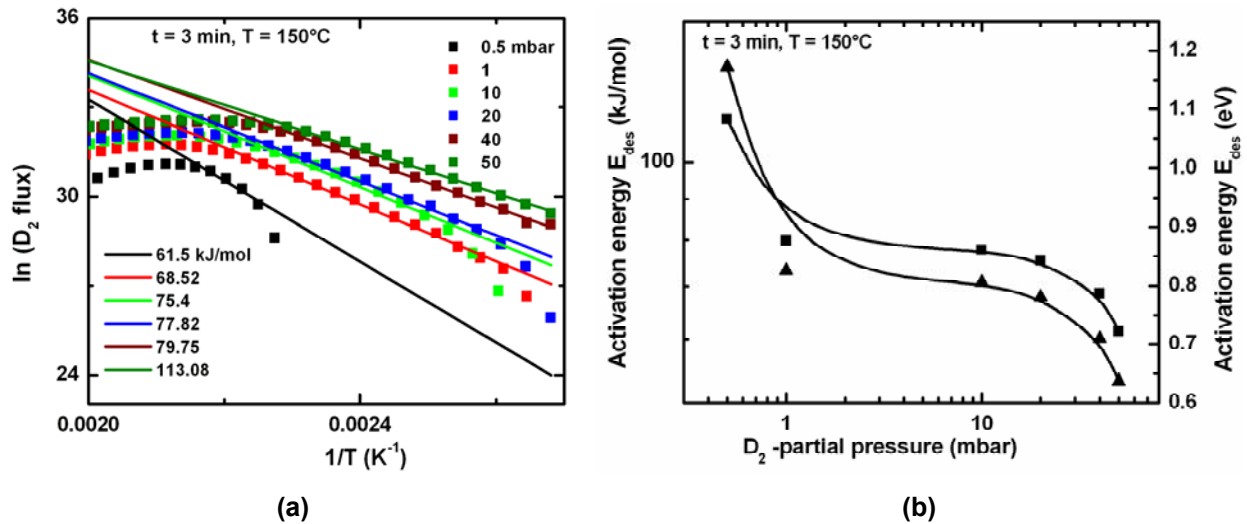


**Fig. 2.61:** (a) Arrhenius plot ( $\ln(D_2 \text{ flux})$  versus  $1/T$ ); (b) The dependence of the activation energy of desorption  $E_{\text{des}}$  on the D<sub>2</sub> partial pressure (exposure dose).

## 2.8. Conclusion:

The performance of Pt/GaN Schottky diodes with different thickness of the catalytic metal were investigated as hydrogen gas detectors. The area as well as the thickness of the Pt was varied between  $250 \times 250 \mu\text{m}^2$  and  $1000 \times 1000 \mu\text{m}^2$ , 8 and 40 nm, respectively.

The response to hydrogen gas was investigated in dependence on the active area, the Pt thickness and the operating temperature for 1 vol.% hydrogen in synthetic air. We observed a significant increase of the sensitivity and a decrease of the response and recovery times by increasing the temperature of operation to about 350°C and by decreasing the Pt thickness down to 8 nm. The sensors with the thinnest Pt layer showed the maximum sensitivity at room temperature indicating that an effective sensor operation at room temperature is possible.

Electron microscopy of the microstructure showed that the thinner platinum had a higher grain boundary density. The increase in sensitivity with decreasing Pt thickness points to the dissociation of molecular hydrogen on the surface, the diffusion of atomic hydrogen along the platinum grain boundaries and the adsorption of hydrogen at the Pt/GaN interface as From TPD measurements we could prove that the hydrogen adsorbs mainly at the Pt surface and at the Pt/GaN interface.

## 2.9 Outlook and future work:

For further investigation in this field of study, the followings are suggested:

- The oxidation of the GaN surface before the Pt deposition will enhance the H<sub>2</sub> sensing properties of catalyst-GaN Schottky diode gas sensors.
- With regard to sensor properties a further study of the selectivity against other reducing gases such as CO and oxidizing gases such as NO<sub>x</sub> is needed.
- The influence of the relative humidity on the performance of the Pt/GaN Schottky diode gas sensors at different operation temperatures must be studied.
- We observed a significant increase of the response and a decrease of the response and recovery times by decreasing the Pt thickness from 24 to 8 nm. What is the optimal thickness of Pt for the maximum response? Is the thickness thinner than 8 nm or in the range 8-24 nm?
- Analogous Pt/GaN Schottky diodes, adsorption of gas species on the Pt gate of AlGaIn/GaN high electron mobility transistors (HEMTs) leads to changes in the effective barrier height and thus either to enhancement or depletion effects in the two dimensional electron gas (2DEG). However, the HEMT devices are more sensitive to the exhaust gases leading to an earlier onset of signal saturation.

## 2.11 References:

- [2.1] I. Lundström, M. S. Shivaraman, C. M. Svensson, and L. Lundqvist, "A hydrogen-sensitive MOS field-effect transistor", *Appl. Phys. Lett.* 26 (1975) 55-57.
- [2.2] B. P. Luther, S. D. Wolter, and S. E. Mohny, "High temperature Pt Schottky diode gas sensors on n-type GaN", *Sensors and Actuators B* 56 (1999) 164-168.
- [2.3] J. Schalwig, G. Müller, U. Karrer, M. Eickhoff, O. Ambacher, M. Stutzmann, L. Görgens, and G. Dollinger, "Hydrogen response mechanism of Pt-GaN Schottky diodes", *Appl. Phys. Lett.* 80 (2002) 1222-1224.
- [2.4] I. Lundström, M. Armgrath, and L. Petterson, "Physics with catalytic metal gate chemical sensors", *CRC Crit. Rev. Solid State Mater. Sci.* 15 (1989) 201-278.
- [2.5] A. Baranzahi, A. Lloyd Spetz, B. Andersson, and I. Lundström, "Gas sensitive field effect devices for high temperatures", *Sensors and Actuators B* 26 (1985) 165-169.
- [2.6] A. Lloyd Spetz, L. Uneus, H. Sveningstorp, P. Tobias, L.-G. Ekedahl, O. Larsson, A. Göras, S. Savage, C. Harris, P. Martensson, R. Wigren, P. Salmonsson,

- B. Hägghendahl, P. Ljung, M. Marttsson, and I. Lundström, "SiC based field effect gas sensors for industrial applications", *phys. stat. sol. A* 185 (2001) 15-25.
- [2.7] R. Dus, "Hydrogen adsorption and absorption on evaporated palladium films study by surface potential measurements", *Surf. Sci.* 42 (1973) 324-328.
- [2.8] O. Weidemann, M. Hermann, G. Steinhoff, H. Wingbrant, A. Lloyd Spetz, M. Stutzmann, and M. Eickhoff, "Influence of surface oxides on the hydrogen-sensitive of Pd:GaN Schottky diodes", *Appl. Phys. Lett.* 83 (2003) 773-775.
- [2.9] J. Schalwig, G. Müller, O. Ambacher, and M. Stutzmann, "Group-III Nitride based gas sensing devices", *phys. stat. sol. A* 185 (2001) 39-45.
- [2.10] J. Schalwig, G. Müller, M. Eickhoff, O. Ambacher, and M. Stutzmann, "Group III-nitride-based gas sensors for combustion monitoring", *Mater. Sci. Eng. B* 93 (2002) 207-214.
- [2.11] E. J. Cho, D. Pavlidis, G. Y. Zhao, S. M. Hubbard, and J. Schwank, "Improvement of CO sensitivity in GaN-based gas sensors", *IEICE Trans. Electron.* E89C (2006) 1047-1051.
- [2.12] F. Braun, *Pogg. Ann. Phys.* 153 (1874) 556.
- [2.13] W. Schottky, "Halbleiterteorie der Sperrschicht", *Naturwissenschaften* 26 (1938) 843.
- [2.14] J. D. Guo, M. S. Feng, R. J. Guo, F. M. Pan, and C. Y. Chang, "Study of Schottky barriers on n-type GaN grown by low-pressure metalorganic chemical vapor deposition", *Appl. Phys. Lett.* 67 (1995) 2657-2659.
- [2.15] L. Wang, M. I. Nathan, T. H. Lim, M. A. Khan, and Q. Chen, "High barrier height GaN Schottky diodes: Pt/GaN and Pd/GaN", *Appl. Phys. Lett.* 68 (1996) 1267-1269.
- [2.16] E. R. Rhoderick, "Metal semiconductor contacts", *IEE Proc.* 129 (1982) 1-14.
- [2.17] C. R. Crowell and S. M. Sze, "Current transport in metal-semiconductor barriers". *Solid-State Electron.* 9 (1966) 1035-1048.
- [2.18] M. P. Hernandez, C. F. Alonso and J. L. Pena, "Barrier height determination in homogeneous nonideal Schottky contacts". *J. Phys. D: Appl. Phys.* 34 (2001) 1157-1161.
- [2.19] P. Hacke, T. Detchprohm, K. Hiramatsu, and N. Sawaki, "Schottky barrier on n-type GaN grown by hydride vapor phase epitaxy", *Appl. Phys. Lett.* 63 (1993) 2676-2678.

- [2.20] A. T. Ping, A. C. Schmitz, M. A. Khan, and I. Adesida, "Characterisation of Pd Schottky barrier on n-type GaN", *Electron. Lett.* 32 (1996) 68-70.
- [2.21] A. C. Schmitz, A. T. Ping, M. Asif Khan, Q. Chen, J. W. Yang, and I. Adesida, "Schottky barrier properties of various metals on n-type GaN", *Semicond. Sci. Technol.* 11 (1996) 1464-1967.
- [2.22] H. Norde, "A modified forward I-V plot for Schottky diodes with high series resistance", *J. Appl. Phys.* 50 (1979) 5052-5053.
- [2.23] R. T. Tung, "Recent advances in Schottky barrier concepts", *Mater. Sci. Eng. R* 35 (2001) 1-138
- [2.24] J. P. Sullivan, M. R. Pinto, and W. R. Graham, "Electron transport of inhomogeneous Schottky barriers: A numerical study", *J. Appl. Phys.* 70 (1991) 7403-7424.
- [2.25] T. U. Kampen and W. Mönch, "Lead contacts on Si(111):H-1 × 1 surfaces", *Surf. Sci.* 331-333 (1995) 490-495.
- [2.26] W. Mönch, "Chemical trends in Schottky barriers: Charge transfer into adsorbate-induced gap states and defects", *Phys. Rev. B* 37 (1988) 7129-7132.
- [2.27] R. F. Schmitsdorf, T. U. Kampen, and W. Mönch, "Explanation of the linear correlation between barrier heights and ideality factors of real metal-semiconductor contacts by laterally non uniform Schottky barriers", *J. Vac. Sci. Technol. B* 15 (1997) 1221-1226.
- [2.28] W. Mönch, "Barrier heights of real Schottky contacts explained by metal-induced gap states and lateral inhomogeneities," *J. Vac. Sci. Technol. B* 17 (1999) 1867-1876.
- [2.29] R. T. Tung, "Electron transport at metal-semiconductor interfaces: General theory," *Phys. Rev. B* 45 (1992) 13509-13523
- [2.30] V. M. Bremudez, "Simple interpretation of metal/wurtzite-GaN barrier heights", *J. Appl. Phys.* 86 (1999) 1170-1171.
- [2.31] A. Itoh and H. Malsunami, "Schottky barrier heights of Metal/SiC contacts", *phys. stat. sol. (a)* 162 (1997) 389-408.
- [2.32] S. S. Cohen, "VLSI electronics-Micromstructure Science, vol. 13. Metal-Semiconductor Contacts and Devices", New York. Academic Press (1986) p. 269.
- [2.33] M. Shur, B. Geimont and M. A. Khan, "Electron mobility in two-dimensional electron gas in AlGaIn/GaN heterostructures and in bulk GaN", *J. Electron. Mater.* 25 (1996) 777-785.

[2.34] A. E. Abom, R. T. Haasch, N. Hellgren, N. Finnegan, L. Hultman, and M. Eriksson, "Characterization of the metal-insulator interface of field-effect chemical sensors", *J. Appl. Phys.* 93 (2003) 9760-9768.

[2.35] M. Johansson, I. Lundström, and L.-G. Ekedahl, "Bridging the pressure gap for palladium metal-insulator-semiconductor hydrogen sensors in oxygen containing environments", *J. Appl. Phys.* 84 (1998) 44-51.

[2.36] V. Tilak, M. Ali, V. Cimalla, V. Manivannan, P. Sandvik, J. Fedison, O. Ambacher, and D. Merfeld, "Influence of metal thickness to sensitivity of Pt/GaN Schottky diodes for gas sensing applications", in: *Proceedings of the MRS Fall Meeting*, 798 (2003) Y.11.5.1.

[2.37] P. A. Redhead, "Thermal desorption of gases", *Vacuum* 12 (1962) 203-211.

[2.38] K. Christmann and G. Ertl, "Interaction of hydrogen with Pt(111): The role of atomic steps", *Surf. Sci.* 60 (1976) 365-384.



## Chapter 3

### 3. Study of Gas-Sensing Performance of SiC-Based Metal-Oxide-Semiconductor (MOS) and Metal-Metal Oxide-Oxide-Semiconductor (MMOOS) Capacitors

#### 3.1 Introduction:

Gas-sensitive silicon metal-oxide-semiconductor (MOS) devices with catalytically active palladium (Pd) Gates were first reported by Lundström *et al.* in 1975 [3.1]. In the case of a thick, continuous gate, such devices work as selective hydrogen sensors. Intensive research led to a model which attributes the sensing mechanism to the formation of a H-induced dipole layer at the Pd-SiO<sub>2</sub> interface [3.2].

In order to allow continuous operation of field-effect gas sensors even at temperatures higher than 300°C, the Lundström group later introduced MOS sensors based on silicon carbide (SiC) with platinum (Pt) gates [3.3, 3.4]. A natural extension of the work on SiC-based hydrogen and hydrocarbon sensors is the development of a NO<sub>x</sub> sensor using the same baseline structures. Lunström *et al.* have demonstrated the use of capacitive structure for NO<sub>x</sub> detection [3.3].

In this chapter, we focus on fabrication of SiC capacitors for NO<sub>x</sub>, O<sub>2</sub>, and D<sub>2</sub> sensing applications. The capacitors were fabricated using either silicon dioxide or silicon dioxide-silicon nitride stack as the dielectric. This stack is potentially more stable than a silicon dioxide dielectric as the silicon nitride can act as a good barrier layer to prevent the diffusion of mobile ions to the oxide-carbide interface and thereby reducing drifts. In addition, we change the catalytic gate to a material more sensitive to the presence of NO<sub>x</sub>. A prime candidate material is rhodium Rh. Changes in the Rh upon exposure to NO<sub>x</sub> is thought to change the electronic properties of the capacitor. These changes can be correlated to changes in the NO<sub>x</sub> concentration in the ambient and thus be used to quantitatively measure the NO<sub>x</sub> concentration. The most important property of the sensors studied in this chapter is that the sensors can be used as NO<sub>x</sub> gas sensor at room temperature.

### 3.2 Gas sensing principle:

The sensing principle is based upon the change in C-V (capacitance-voltage) characteristics of the device that is induced by the presence of different gases. The simplest case to study is when  $H_2$  gas is detected. The hydrogen sensitivity of palladium-oxide-semiconductor, Pd-MOS, structures was first reported by Lundström *et al.* in 1975 [3.1]. A model was suggested for the gas sensitivity according to which hydrogen atoms from the hydrogen molecules that are dissociated on the catalytic metal surface, diffuse through the metal film and form an electrically polarised layer at the metal-insulator interface [3.5] (Fig. 3.1a). Recent results suggest the polarized layer to be located in the surface layer of the insulator rather than in the metal [3.6], further supported by results from Infrared Spectroscopy measurements [3.7].

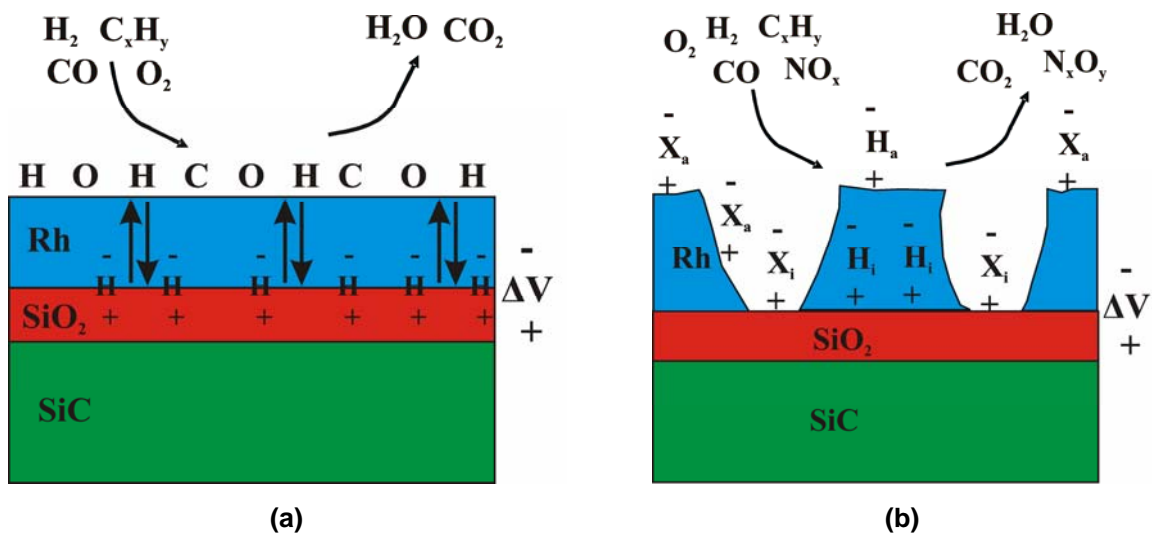


**Fig. 3.1:** Schematic illustration of the principle of gas sensitive MOS capacitors. **(a)** Thick nonporous gates can detect all molecules which deliver hydrogen atoms to the catalytic metal film. **(b)** Thin, discontinuous or porous metal gates detect several types of chemically induced polarization phenomena at the surface and interface of the catalytic metal and on the insulator ( $X_a$ ,  $X_i$ : adsorbed and interfacial molecules). Some possible chemical reactions are also shown.

The hydrogen atoms at the metal insulator interface decrease the flat band voltage of the capacitor (the voltage at which there is no band bending in the semiconductor), which gives a voltage drop,  $\Delta V$ , resulting in a shift,  $\Delta V$  along the voltage axis, of the C-V curve of a capacitor (Fig. 3.2). The field effect devices also respond to other hydrogen-containing molecules like hydrocarbons, which deliver hydrogen atoms to the metal-oxide interface provided that the molecules are



dissociated on the metal surface [3.8, 3.9]. Oxygen molecules are also dissociated on the catalytic metal surface, (Fig. 3.1a). Oxygen, hydrogen, and carbon atoms forms water and carbon dioxide which leaves the surface. The water formation consumes hydrogen and thus decreases the sensor signal.

The sensitivity of field-effect gas sensors to non-hydrogen containing gases such as CO is normally explained in terms of porosity-related effects of the sensing electrodes. A thin porous metal gate on the MISiC sensor introduces more possibilities to detect gases. Beside the decomposed hydrogen atoms, even reaction species or just adsorbed charged or polarized species, on the metal surface along the borders of the cracks and/or on the oxide, exposed in the cracks in the porous film, give rise to a shift of the C-V curve (Fig.3.1b, Fig. 3.2).

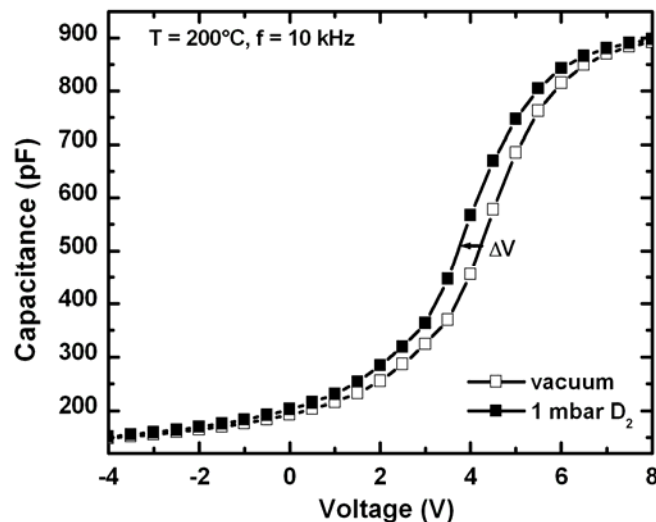


**Fig. 3.2:** C-V curve of a Rh-SiO<sub>2</sub>-SiC capacitor with Rh thickness  $d_{Rh} = 30$  nm and area  $A_{Rh} = 0.0128$  cm<sup>2</sup> operated at 200°C, in vacuum (open symbols) as well as 1 mbar pure deuterium (closed symbols). The sensor response is indicated by an arrow.

Schalwig *et al.* investigated the porosity-related effect using multi-layer stacks consisting of Pt/Au/Pt (30/55/15 nm) as catalytic layer in SiC-based MOS gas sensors [3.10]. An artificial porosity was introduced into these electrodes by photolithography and Ar sputter etching. The pores had a diameter of around 3 μm and were spaced from each other by distances ranging from 9 to 23 μm, which results in open-area fractions ranging from 2 to 11%. A nearly constant hydrogen response was observed, independent of the open SiO<sub>x</sub> area. In the case of CO and butane, on the other hand, an almost vanishing signal was observed in the absence

of artificial porosity ( $A = 0$ ). A linear increase in the CO response, however, was observed as  $A$  was increased. This result agrees well with  $\text{NH}_3$  sensing experiments performed on Si-based MOS capacitors with Pt electrodes [3.11]. There, a strong correlation between  $\text{NH}_3$  response and crack density in the Pt electrodes was observed.

### 3.3 The MOS SiC capacitor:

For investigation of MOS capacitor as gas sensor a theoretical understanding of its functionality is necessary. A theoretical understanding of functionality is also necessary for a correct interpretation of experimental data.

The SiC field effect MOS capacitor is made up of three different parts; a semiconductor, an insulator (oxide) and a catalytic metal (Fig. 3.3). The semiconductor is either  $n$ - or  $p$ -doped. The semiconductor capacitor is different from ordinary capacitors in that it has minority and majority carriers that highly influence the behavior of the component.

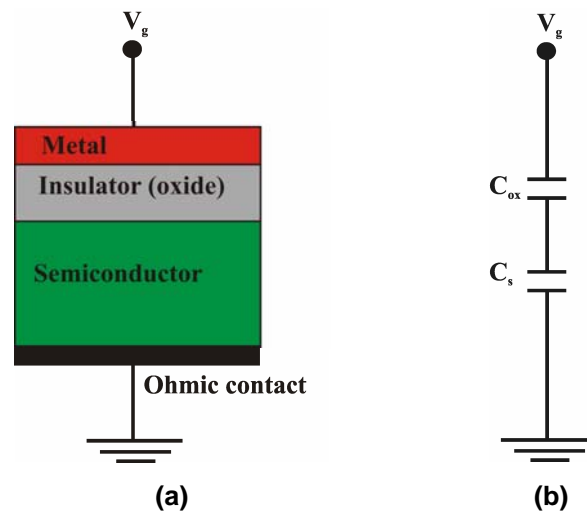


**Fig. 3.3:** (a) Schematic drawing of the SiC-based capacitor. (b) Simplified equivalent circuit of MOS capacitor (adapted from [3.12]).

The semiconductor in itself contributes to the capacitance of the entire device, which means that the total capacitance is the semiconductor capacitance,  $C_s$ , in series with the oxide capacitance,  $C_{ox}$ . This can be described according to Eq. 3.1:

$$C_{tot} = \frac{C_{ox} C_s}{C_{ox} + C_s}. \quad (3.1)$$

The capacitance of this type of device is normally studied in a C-V measurement. During such a measurement, a high-frequency voltage is applied to the device, and its capacitance is measured. The amplitude of the alternating voltage is normally about 100 mV. A bias voltage is then added to the high-frequency signal and varied over time, which gives the dependence of the capacitance on the bias voltage. A plot of this dependence is called a C-V plot and is shown in Fig. 3.4 when using an n-doped semiconductor.

The shape of the C-V plot can be explained through studying the properties of the component and how they are affected by different bias voltages. If an n-doped semiconductor is used, positive voltages on the metal will attract majority carriers, which are the negatively charged electrons in an n-type material, in the semiconductor close to the insulator. This mode is called **accumulation** (Fig. 3.5a). The majority carriers easily move back and forth in the semiconductor. This means that they follow the alternating voltage closely and that the entire semiconductor is conductive. In such a case the total capacitance according to Eq. 3.1 becomes close to the capacitance of the oxide. The capacitance of the oxide is independent of the applied voltage, and thus the total capacitance is constant at high positive voltages. [3.12-3.13].

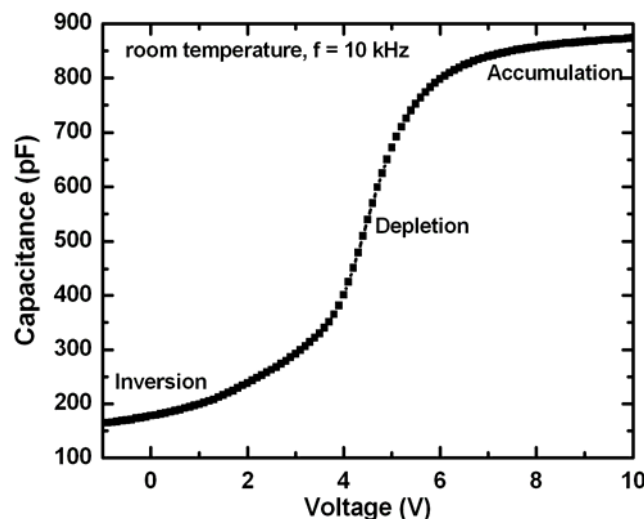


**Fig. 3.4:** The C-V characteristics of an n-doped semiconductor (Rh-ITO-SiO<sub>2</sub>-SiC) capacitor with Rh thickness  $d_{Rh} = 30$  nm and area  $A_{Rh} = 0.0128$  cm<sup>2</sup> operated at room temperature.

When the applied voltage is decreased, the density of majority carriers at the oxide-semiconductor interface will decrease as well. At a negative voltage a depletion layer

will be formed. In the depletion layer the concentration of majority carriers is lower than in the bulk. The depletion layer has the same effect on the semiconductor as introducing an insulator layer in the material, since carriers cannot move so easily across it, and the total capacitance of the MIS structure thereby decreases. In the C-V plot shown in Fig. 3.4 it is seen that **depletion** is initiated at a positive voltage rather than at a negative. The reason for this is that the discussion above assumes that the capacitor is ideal, that is, the difference in Fermi level between the metal and the semiconductor is neglected as well as oxide charges and surface states. The effect of these phenomena is to shift the C-V curve, which causes the behaviour observed in Fig. 3.4. [3.12-3.13].

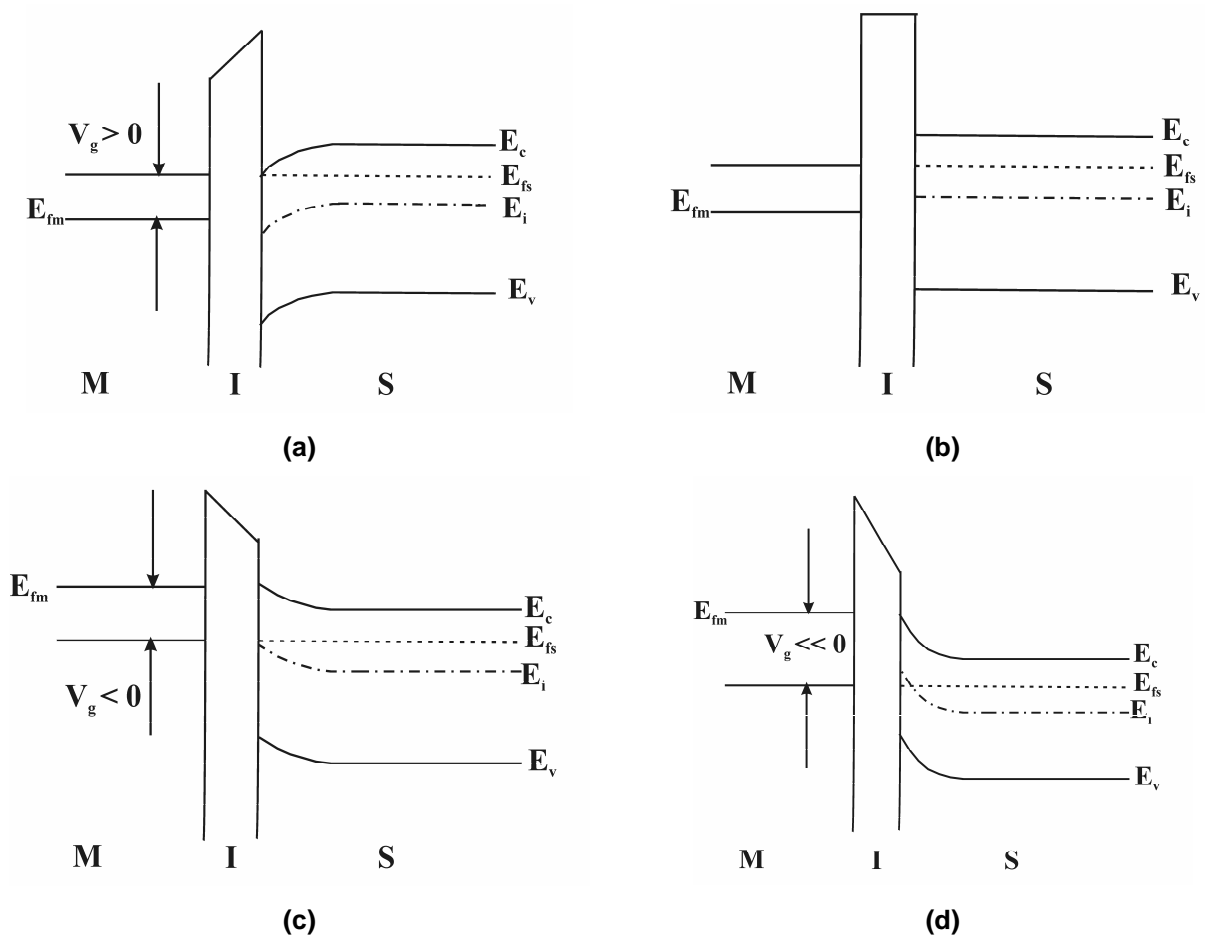


**Fig. 3.5:** Energy-band diagrams for an ideal MIS diode (*n*-type semiconductor) at (a) accumulation, (b) flat band conditions, (c) depletion and (d) inversion [3.12].

At even larger negative voltages the region closest to the insulator becomes not only depleted of majority carriers, but the negative voltage attracts so many minority carriers that a state called **weak inversion** is reached. In this state the density of

minority carriers in the region is higher than the density of majority carriers. If the voltage is decreased even further, so that the density of minority carriers in the inversion region becomes higher than the density of majority carriers in the bulk, **strong inversion** has been reached.

The size of the depletion layer is then not affected by further decreasing the bias voltage. This is due to the efficient shielding of changes in the applied electric field by a large concentration of charges in the inversion layer of the depletion region [3.12-3.13]. At strong inversion the density of carriers in the inversion region is almost the same as in the case of accumulation, although the minority carriers do not move as easily as the majority carriers did. This means that the carriers will not follow the alternating voltage, and the depletion layer will remain even for a large negative bias. Band diagrams for an ideal MIS junction at accumulation, at band conditions (no band bending), depletion and inversion are shown in Fig. 3.5. Weak inversion is reached when  $E_{fs}$  of the semiconductor is lower than  $E_i$ .

The presence of a dipole layer at the metal-insulator interface, caused by gases owing across the sensor surface, adds charge to the applied voltage, which means that there will be a shift in the C-V plot (see Fig. 3.2). The sensor signal is normally taken as the shift in voltage at a constant capacitance.

### 3.4 Device structure and fabrication:

Fig. 3.6 shows the optical micrographs of the investigated sensors. We have fabricated capacitors with different insulators ( $\text{SiO}_2$ ,  $\text{SiN/SiO}_2$ ) and different catalytic metals (Rh, Rh/ITO) deposited by e-beam evaporation or sputtering.

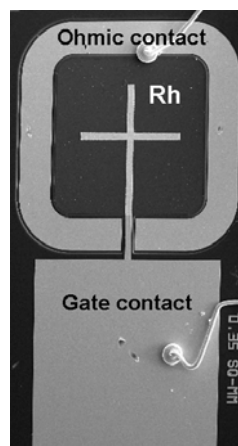


**Fig 3.6:** Optical micrographs of the investigated sensors. The active area  $A_{Rh} = 0.0128 \text{ cm}^2$ .

### 3.4.1 Sample A:

The epitaxial structure for the MOS capacitor was 3 micron of  $1 \times 10^{16} \text{ cm}^{-3}$  *n*-type SiC grown on 4H-SiC substrates. After mesa etching, a 50 nm gate oxide ( $\text{SiO}_2$ ) was thermally grown with  $\text{N}_2\text{O}$  at  $1250^\circ\text{C}$ . Nickel ohmic contacts (55 nm) were deposited by sputtering by a lift off process after patterning with photoresist and were annealed at  $975^\circ\text{C}$  for 1 min in nitrogen ambient. Finally catalysts were deposited as gate electrodes.

Two types of catalysts were deposited on the wafers: rhodium (30nm) (sample A4) and rhodium (30 nm)/Indium oxide-tin oxide (40 nm) (sample A1) stack. The indium oxide-tin oxide was deposited by co-sputtering indium oxide and tin oxide simultaneously. Rhodium was deposited by e-beam evaporation for the sample A4 and by puttering for the sample A1. Two types of capacitors were fabricated, a Metal-Insulator-Silicon Carbide (MOSiC) capacitor and a Metal-Metal Oxide-Insulator-Silicon Carbide (MMOOSiC) capacitor. The wafer were then diced and individual chips were attached to TO-8 headers with a ceramic die attach compound. The chips were then wire bonded to TO-8 heater pins. The cross section of the finished capacitors (sample A1 and A4) is shown in Fig.3.7.

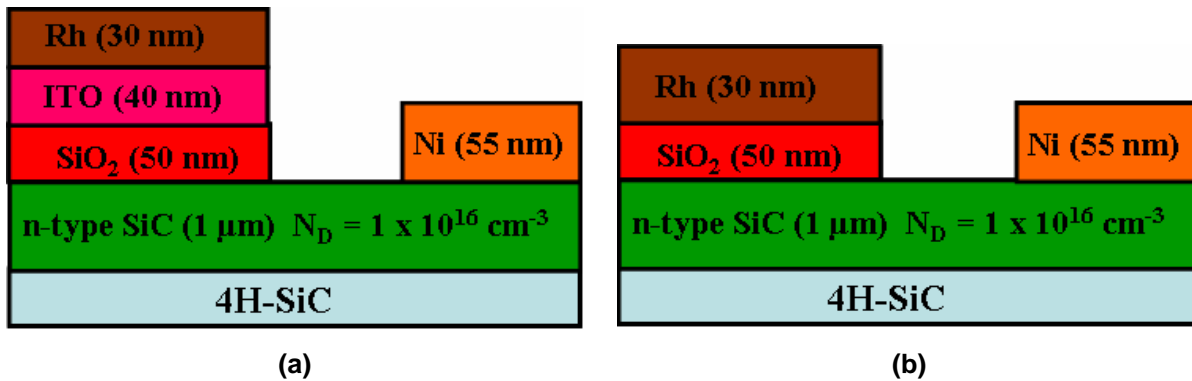


**Fig. 3.7:** Schematic cross section of (a) MMOOSiC capacitor (sample A1) and (b) MOSiC capacitor (sample A4). The active area of the sensor  $A_{\text{Rh}} = 0.0128 \text{ cm}^2$ .

### 3.4.2 Sample B:

The epitaxial structure for the MIS capacitor was 1 micron of  $2 \times 10^{16} \text{ cm}^{-3}$  *n*-type SiC grown on 4H-SiC substrates. After mesa etching, a 33 nm gate oxide ( $\text{SiO}_2$ ) was thermally grown with  $\text{N}_2\text{O}$  at  $1250^\circ\text{C}$ . Next, 33 nm silicon nitride was deposited at  $725^\circ\text{C}$  by low pressure chemical vapor deposition (LPCVD). Nickel ohmic contacts

(55 nm) were deposited by sputtering by a lift off process after patterning with photoresist and were annealed at 975°C for 1 min in nitrogen ambient. Finally catalyst (rhodium 30 nm) was deposited by e-beam evaporation as gate electrodes. The wafer were then diced and individual chips were attached to TO-8 headers with a ceramic die attach compound. The chips were then wire bonded to TO-8 heater pins. The cross section of the finished capacitors (sample B4) is shown in Fig.3.8.

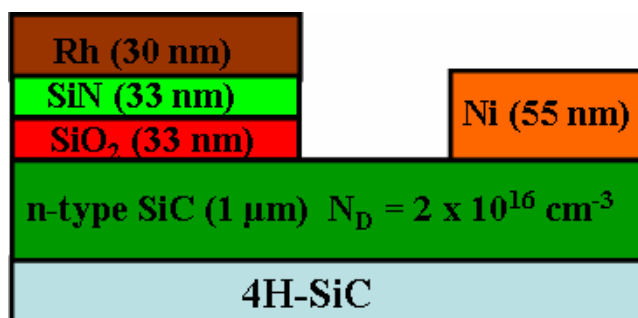


**Fig. 3.8:** Schematic cross section of the MOSiC capacitor (sample B4). The active area of the sensor  $A_{Rh} = 0.0128 \text{ cm}^2$ .

### 3.5 Experiments:

#### 3.5.1 AES Measurements:

The sensitivity of field-effect gas sensors is strongly influenced by the structure and the composition of the catalytically active electrodes. Therefore, the surface and interface properties of the MOSiC and MMOOSiC gas sensors studied in this chapter are investigated using Auger Electron Spectroscopy (AES) equipped with Scanning Electron Microscopy (SEM). The AES measurements have been carried out using a Thermo Microlab 350 (Fig. 3.9).

The primary electron beam parameters were: 5 keV and 1-5 nA, a spot diameter of approximately 30 nm under 60° irradiation with respect to the surface normal. The measurement of the kinetic energies of the Auger electrons has been carried out with a hemispherical electron energy analyzer of 0.3% energy resolution with a constant retard ratio (CRR) of 4. The angle of the analyzer axis was 0° to the surface normal. The Auger signals have been recorded in a direct mode with dwell times of 80-150 ms, a number of scans of 1-3 for each Auger peak and a step width of 0.5-1 eV. The Auger intensities are measured as the area under the Auger peaks after subtracting

a Shirley background. Sputtering for the depth profiling was performed by a 1 keV Ar scanned ion beam ( $2.25 \text{ mm}^2$ ) under  $47^\circ$  without sample rotation.



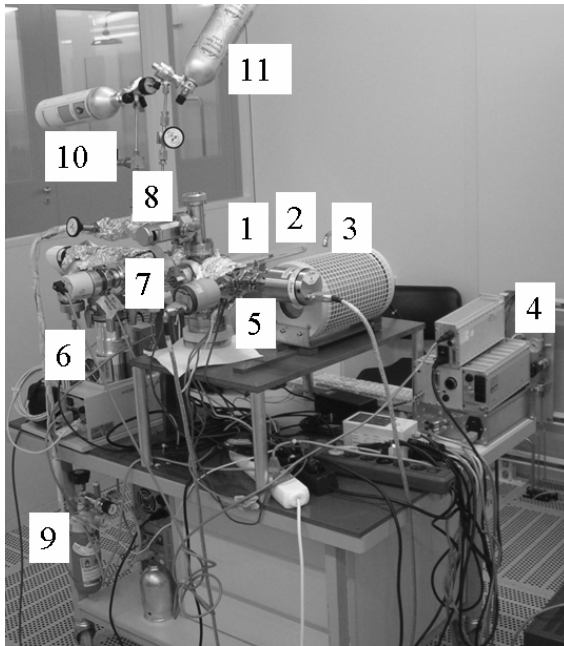
Fig. 3.9: AES system (Thermo Microlab 350).

### 3.5.2 Gas-sensing measurements (set-up and procedure):

For gas sensing tests, the sensors were mounted in an ultra high vacuum (UHV) chamber reaching a base pressure of  $4 \times 10^{-8}$  mbar. A photograph and schematic drawing of the UHV apparatus for this experiment and all devices mounted in it is shown in Fig. 3.10. The chamber consisted of a closed quartz tube about 29 cm in length and 2.5 cm in diameter. Vacuum is maintained by a turbo molecular pump backed by a membrane vacuum pump as pre-vacuum pump.

Dosing of gases into the chamber is achieved by use of a leak valve (needle valve). The final pressure  $P_f$  measured during dosing is the sum of the base pressure  $P_0$  and the partial pressure  $P_i$  of the gas flowing into the system, i.e.,  $P_f - P_0 = P_i$  (or  $P_i = P_f$  for  $P_0 \ll P_f$ ). The sensors were heated during operation at different temperatures using a furnace. The temperature was measured by a thermocouple type S (Pt10%Rh-Pt) (see **Appendix A**) placed a few millimetres above the sensor. The test gases in these measurements are pure deuterium  $D_2$ , nitrogen oxide (NO), and oxygen ( $O_2$ ). The gases used are of 99.99% purity or better. The NO gas might be partly oxidized to  $NO_2$  due to long gas tubes and is denoted  $NO_x$ .





- 1: Sensor
- 2: Quartz tube
- 3: Furnace
- 4: Pressure measurements
- 5: MKS Baratron gauge
- 6: Pump station
- 7: Sensor contacts
- 8: Needle valve
- 9: NO bottle
- 10: H<sub>2</sub> bottle
- 11: O<sub>2</sub> bottle

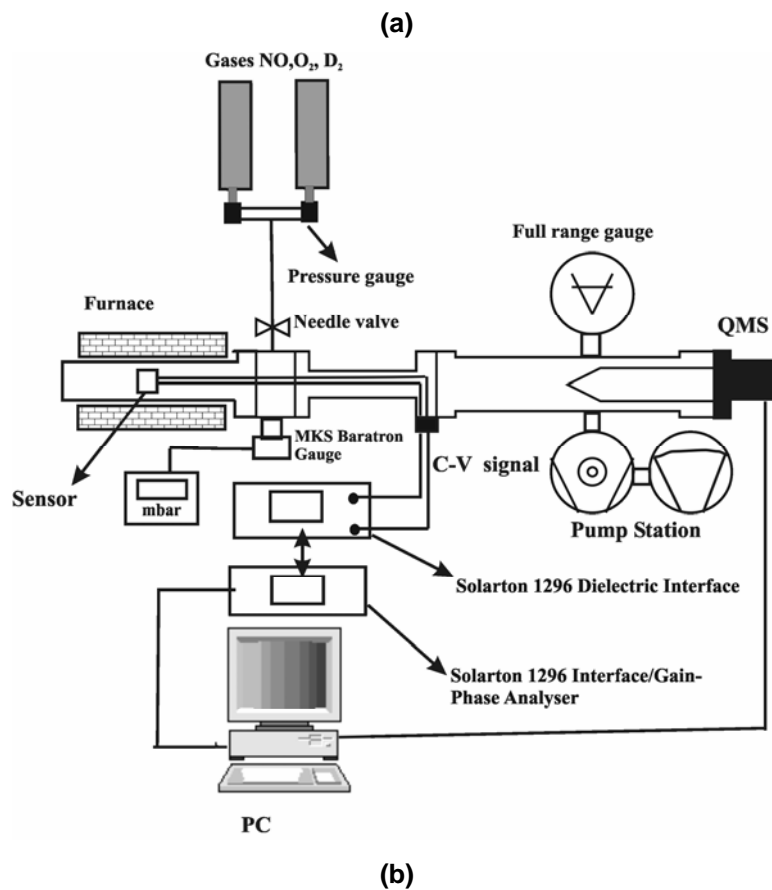


**Fig. 3.10:** Gas measurements system. (a) Photograph (b) Schematic drawing.

The electrical properties were evaluated by measuring capacitance-voltage (C-V) characteristics, obtained from an Impedance Analyzer (Solartron 1296) operated at 10 kHz. Measuring the (C-V) characteristics of MOS devices at high frequencies, a

low capacitance is observed in the case of inversion and a high capacitance in the case of accumulation. The interaction of gas molecules with MOS-SiC devices gives rise to changes in the (C-V) curves. In the case of reducing gases like D<sub>2</sub>, the C-V curve is shifted toward negative voltages, i.e., to the left and into the opposite direction in the case of oxidizing gases (NO<sub>x</sub>, O<sub>2</sub>). During exposure to gas, the capacitance was held constant by controlling the bias voltage. This bias voltage is the sensor signal.

The gas response R is the difference between the steady state voltages measured at the test gas exposure and in vacuum. We have defined the gas response R as the voltage variation at constant capacitance:

$$R = \Delta V = V_v - V_g, \quad C = \text{const.}, \quad (3.2)$$

where  $V_v$  and  $V_g$  are the voltage of the sensor in vacuum and in the presence of gas, respectively. The voltage shift obtained in the case of reducing gases was defined as positive and in the case of oxidizing gases as negative.

The sensitivity S is given by:

$$S = \frac{R}{C_{gas} [\text{mbar}]}, \quad (3.3)$$

where  $C_g$  is the gas partial pressure in mbar.

### 3.6 Results:

#### 3.6.1 Sample A4:

##### 3.6.1.1 Chemical characterization (AES results):

Fig. 3.11a shows a typical Auger spectrum taken from two different areas of the active sensor area as shown in the SEM image (Fig. 3.11b). The only impurity detected from Rh film is carbon (C), which remains even after sputtering process for 8 min. One reason we can think of is the packaging process.

The AES depth profile in Fig. 3.12 revealed shows that the sample structure includes Rh, SiO<sub>x</sub>, and SiC layers, as well as carbon or carbon containing molecules. Silicon and oxygen was detected both in the bulk and on the surface of Rh due to annealing in N<sub>2</sub>.

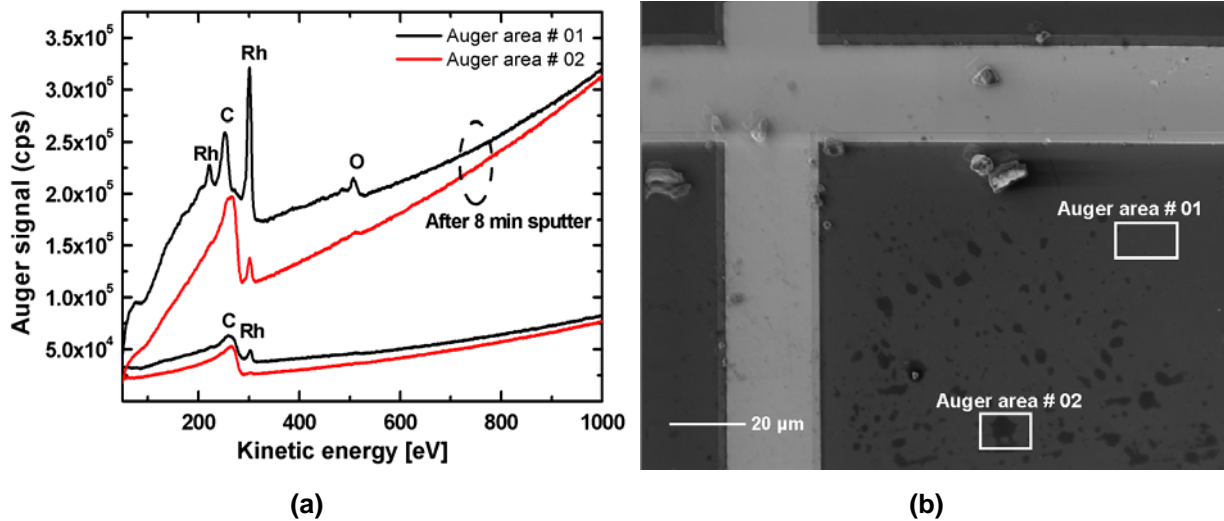


Fig. 3.11: (a) Typical Auger spectrum of the active sensor area. (b) SEM image of Rh surface.

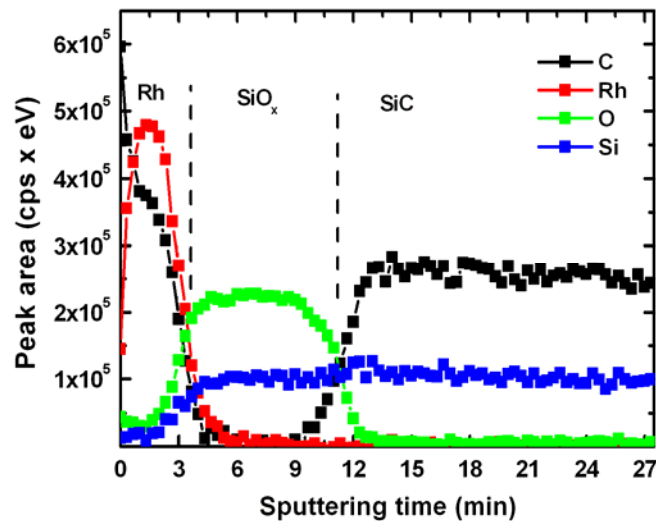
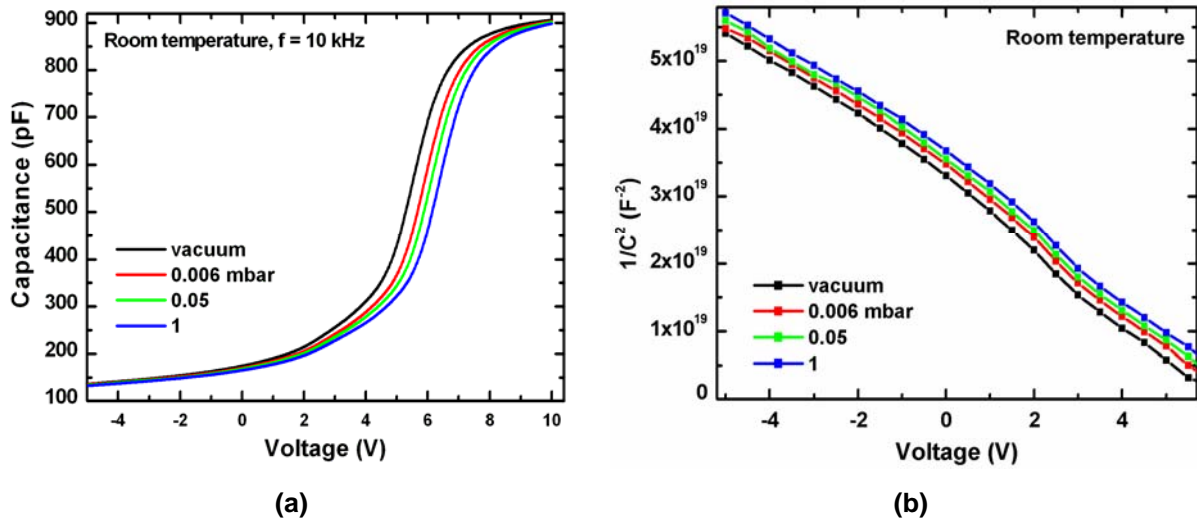


Fig. 3.12: Auger depth profiles of the active sensor area.

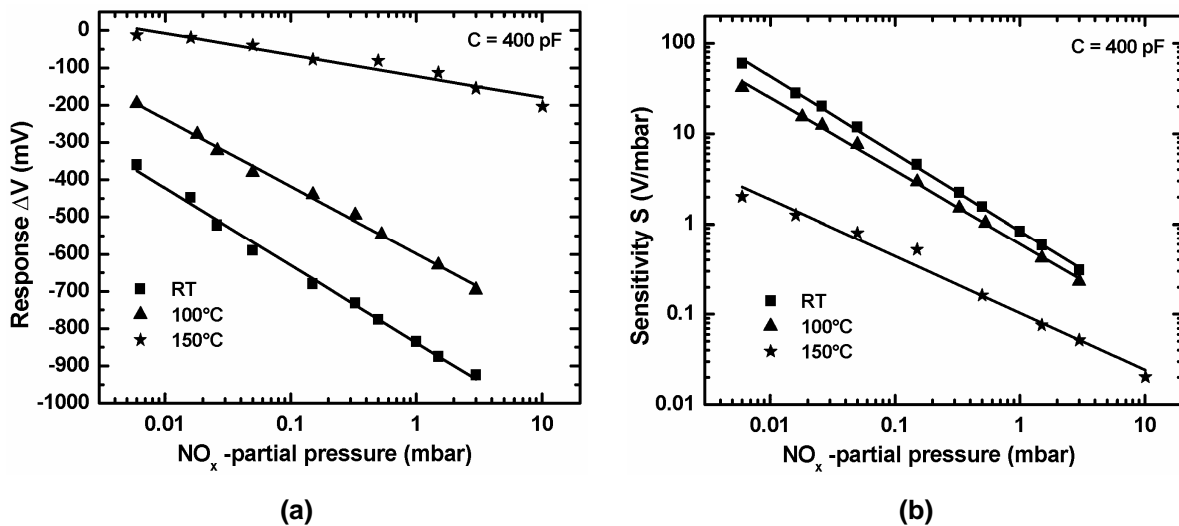
### 3.6.1.2 NO<sub>x</sub> detection:

Fig. 3.13 shows the high frequency (10 kHz) C-V and  $1/C^2$ -V characteristics of the sensor A4 at room temperature in vacuum and in the presence of different partial pressures of pure NO<sub>x</sub>. Exposure to NO<sub>x</sub> results in a flat band voltage occurring at a more positive bias than in vacuum. The shifts in the flat-band voltages due to NO<sub>x</sub> were estimated by measuring the voltage differences at a capacitance of 400 pF. This value,  $\Delta V$ , is shown in Fig. 3.14a as a function of NO<sub>x</sub> partial pressures



**Fig. 3.13:** (a) C-V and (b)  $1/C^2$ -V characteristics of the sensor A4 at room temperature in vacuum and in the presence of different partial pressures of pure NO<sub>x</sub>.

We note in Fig. 3.13b that the vacuum curve is parallel to the NO<sub>x</sub> curve. This suggests that the major effect of the NO<sub>x</sub> gas is to change the work function of the Rh gate. The dependence of the response R to NO<sub>x</sub> on the partial pressure of NO<sub>x</sub> at different temperatures is presented in Fig 3.14a.



**Fig. 3.14:** The dependence of response R (a), and sensitivity S (b) on the NO<sub>x</sub> partial pressures at different operation temperatures for the sample A4. The measurements were performed at a constant capacitance of 400 pF.

We observed a significant increase of the response by decreasing the temperature of operation and by increasing the gas partial pressure and no saturation was observed

even at high partial pressures of up to 3 mbar. The maximum response to  $\text{NO}_x$  was observed at room temperature. The dependence of the response to  $\text{NO}_x$  on the partial pressure of  $\text{NO}_x$  can be described with the equation:

$$R = a + b \log(\text{NO}_x) \quad (3.4)$$

where  $a$  and  $b$  are constants. Different fits, with this equation were made and the values for the coefficient  $a$ ,  $b$ , and  $R^2$  are presented in Tab. 3.1

**Tab. 3.1:** Fitting parameter of the response  $R$  to  $\text{NO}_x$  at several temperatures.

Temperature (°C)	$R = a + b \log(\text{NO}_x)$		$R^2$
	$a$	$b$	
25	$-837.1 \pm 6.06$	$-207.4 \pm 5.19$	0.997
100	$-598.6 \pm 5.3$	$-180.57 \pm 4.34$	0.998
150	$-122.24 \pm 7.2$	$-57.24 \pm 5.9$	0.969

Fig 3.14b shows the dependence of sensitivity on the partial pressure of  $\text{NO}_x$  at different temperatures. One can see that the log/log trend fits the sensitivity in the whole  $\text{NO}_x$  partial pressure range. From the curve fitting, we can recover the equation of the sensitivity vs. the partial pressure of  $\text{NO}_x$ :

$$S = 10^{[a+b \log(\text{NO}_x)]}, \quad (3.5)$$

where  $a$  and  $b$  are constants. Different fits, with this equation were made and the values for the coefficient  $a$ ,  $b$ , and  $R^2$  are summarized in Tab. 3.2.

**Tab. 3.2:** Fitting parameter of the sensitivity  $S$  to  $\text{NO}_x$  at several temperatures.

Temperature (°C)	$S = 10^{[a+b \log(\text{NO}_x)]}$		$R^2$
	$a$	$b$	
25	$-0.07 \pm 0.01$	$-0.85 \pm 0.01$	0.999
100	$-0.22 \pm 0.02$	$-0.81 \pm 0.01$	0.998
150	$-0.98 \pm 0.04$	$-0.63 \pm 0.03$	0.992

The dependence of the response time  $\tau_{90}$  on the operation temperature for 0.1 mbar of  $\text{NO}_x$  is shown in Fig. 3.15. In this chapter we have defined the response time  $\tau_{90}$  as the time in which the gate voltage at constant capacitance of 400 pF reaches 90% of its final value.

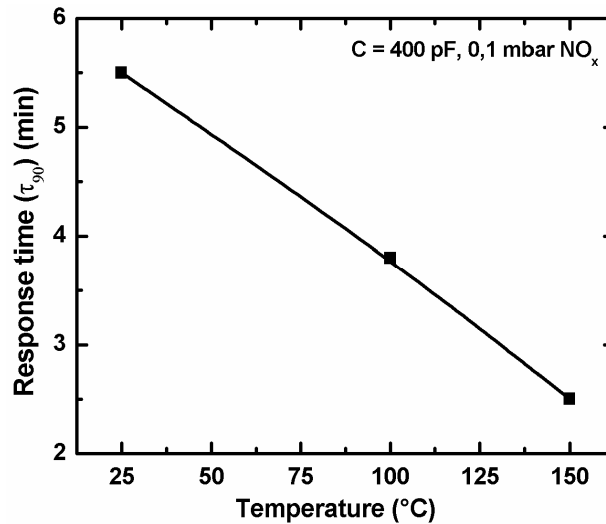


**Fig. 3.15:** The response time as a function of temperature for 0.1 mbar of NO<sub>x</sub>.

By increasing the operation temperature from room temperature to 150°C, the response time is decreasing from 5.5 to 2.5 min. Taking into account the sensitivity and the response time, the experimental results indicate that the optimal operating temperature of the sensor for NO<sub>x</sub> is in the range (25-100°C).

### 3.6.1.3 O<sub>2</sub> detection:

In the second step the sensors were tested for the response to other oxidizing gases such as O<sub>2</sub> with partial pressures starting from 0.002 going up to 10 mbar at temperatures between room temperature and 250°C.

The dependence of the response R and the sensitivity S to O<sub>2</sub> on the partial pressure of O<sub>2</sub> at different temperatures is shown in Fig. 3.16. We observed a significant increase of the response by increasing the gas partial pressure. The maximum response to O<sub>2</sub> was observed at 200°C and no significant response to O<sub>2</sub> was observed at temperatures lower than 150°. In addition, at 250°C and above a general decrease of the response was observed, very likely due to an increased thermal desorption of the test gas species from the sensor surface.

The equation of the sensitivity vs. the partial pressure of O<sub>2</sub> is given by:

$$S = 10^{[a+b \log(O_2)]}, \quad (3.6)$$

where a and b are constants. Different fits, with this equation were made for and the values for the coefficient a, b, and R<sup>2</sup> are presented in Tab. 3.3.

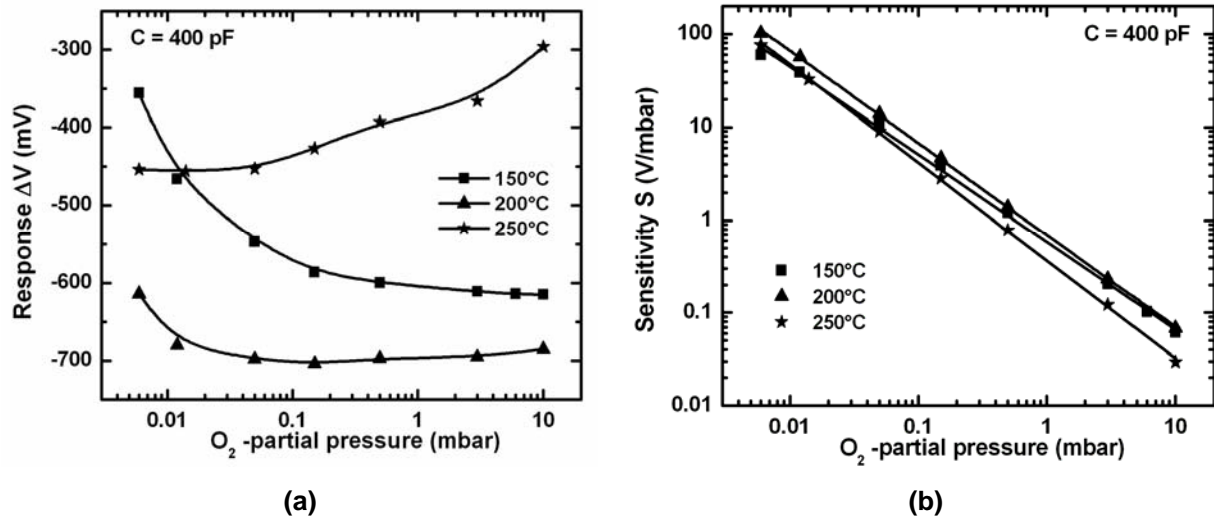


**Fig. 3.16:** The dependence of response R (a), and sensitivity S (b) to different partial pressures of pure O<sub>2</sub> on the operation temperature for the sample A4. The measurements were performed at a constant capacitance of 400 pF.

**Tab. 3.3:** Fitting parameter of the sensitivity S towards O<sub>2</sub> at several temperatures.

Temperature (°C)	$S = 10^{[a+b\log(O_2)]}$		R <sup>2</sup>
	a	b	
150	-0.23 ± 0.02	-0.94 ± 0.015	0.996
200	-0.16 ± 0.01	-0.99 ± 0.006	0.999
250	-0.43 ± 0.01	-1.05 ± 0.01	0.999

#### 3.6.1.4 D<sub>2</sub> detection:

In the third step the sensors were tested for the response to reducing gases such as D<sub>2</sub> with partial pressures starting from 0.008 going up to 10 mbar at temperatures between room temperature and 250°C. Fig. 3.17 shows the high frequency (10 kHz) C-V and 1/C<sup>2</sup>-V characteristics of the sensor A4 at 200°C in vacuum and in the presence of different partial pressures of pure D<sub>2</sub>.

Exposure to D<sub>2</sub> results in a flat band voltage occurring at a more negative bias than in vacuum. The shifts in the flat-band voltages due to D<sub>2</sub> were estimated by measuring the voltage differences at a capacitance of 400 pF. This value,  $\Delta V$ , is shown in Fig. 3.18 as a function of D<sub>2</sub> partial pressure. We note in Fig. 3.17b that the vacuum curve is parallel to the D<sub>2</sub> curve. This suggests that the major effect of the D<sub>2</sub> gas is to change the work function of the Rh gate.

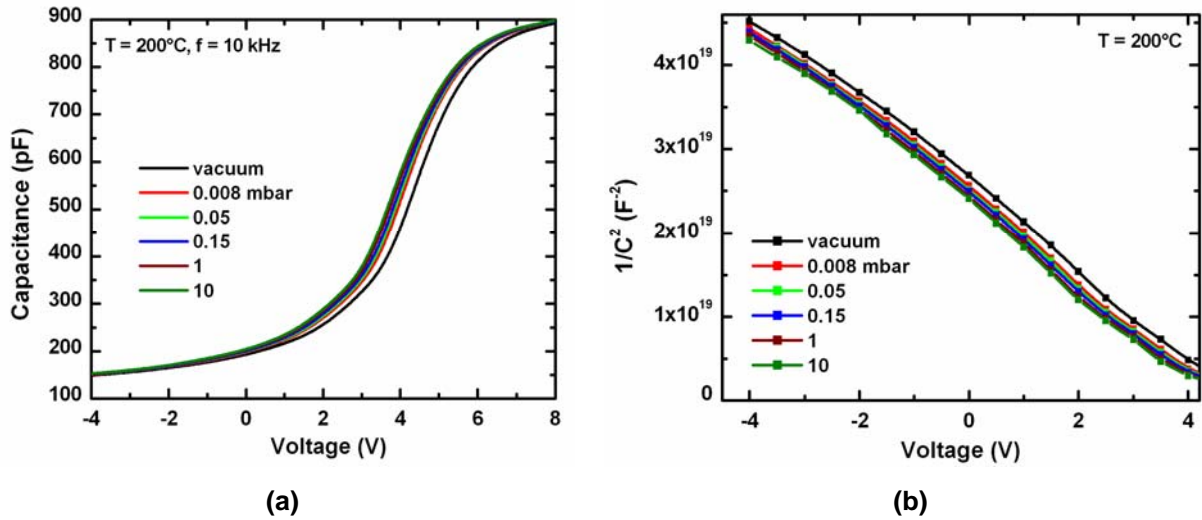


**Fig. 3.17:** (a) C-V and (b)  $1/C^2$ -V characteristics of the sensor A4 at room temperature in vacuum and in the presence of different partial pressures of pure  $\text{D}_2$ .

The dependence of the response R on the partial pressures of  $\text{D}_2$  (calibration curves) at different operating temperatures is shown in Fig. 3.18.

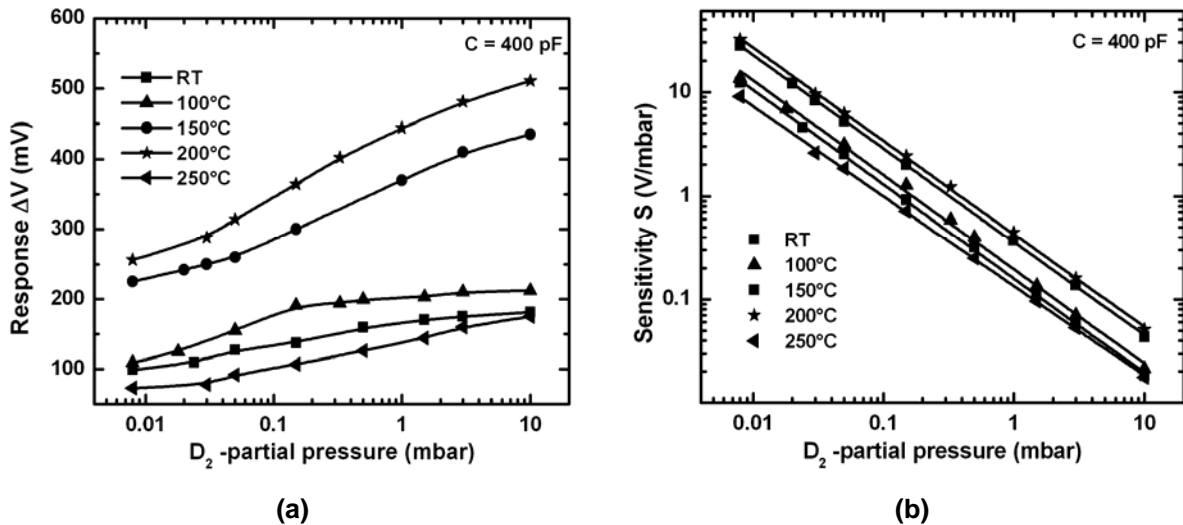


**Fig. 3.18:** The dependence of response R (a), and sensitivity S (b) to different partial pressures of pure  $\text{D}_2$  on the operation temperature for the sample A4. The measurements were performed at a constant capacitance of 400 pF.

As one can see, the responses increase non-linearly with increasing the partial pressure of  $\text{D}_2$  and no complete saturation was observed even at a high partial pressure of up to 10 mbar. The maximum response to  $\text{D}_2$  was observed at  $200^\circ\text{C}$ .



Fig 3.18b shows the dependence of the sensitivity  $S$  to several different partial pressures of pure  $D_2$  on the operating temperature. It can be seen also from Fig. 3.18b that the sensitivity can be enhanced by increasing the operating temperature.

In all cases the sensitivity decreases with increasing the partial pressure of the  $D_2$  gas. This effect is likely due to a reduction in the number of adsorption sites as the gas partial pressures are increased leading to a lower sensitivity for higher  $D_2$  partial pressures. As one can see, in the range of the partial pressures investigated, the sensitivity  $S$  is related to the gas partial pressure by:

$$S = 10^{[a+b\log(D_2)]}, \quad (3.7)$$

where  $a$  and  $b$  are constants. Fitting parameters with this equation for the sensitivity  $S$  towards  $D_2$  are presented in Tab. 3.4.

**Tab. 3.4:** Fitting parameter of the sensitivity  $S$  towards  $D_2$  at several temperatures.

Temperature (°C)	$S = 10^{[a+b\log(D_2)]}$		$R^2$
	a	b	
25	$-0.78 \pm 0.01$	$-0.91 \pm 0.01$	0.999
100	$-0.71 \pm 0.018$	$-0.90 \pm 0.01$	0.998
150	$-0.44 \pm 0.005$	$-0.9 \pm 0.003$	0.999
200	$-0.37 \pm 0.007$	$-0.89 \pm 0.006$	0.999
250	$-0.87 \pm 0.007$	$-0.9 \pm 0.006$	0.999

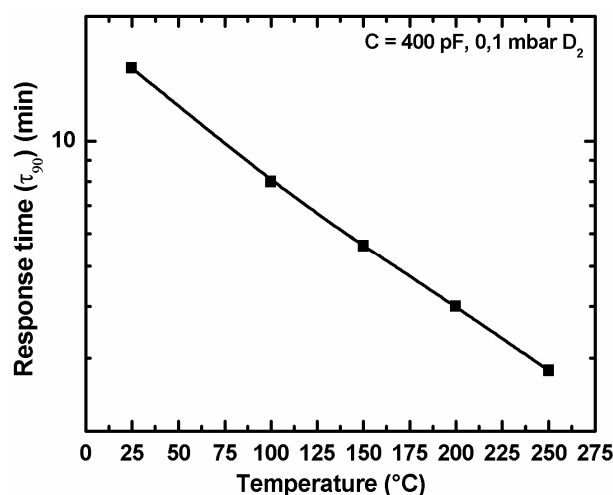


**Fig. 3.19:** The response time as a function of temperature for 0.1 mbar of  $D_2$ . The measurements were performed at a constant capacitance of 400 pF.

Fig. 3.19 reveals the response time as a function of temperature for 0.1 mbar of  $D_2$ . It becomes obvious from Fig. 3.19 that the response time can be reduced by increasing the operating temperature. The response time is decreasing from 15 to  $\sim 2$  min by increasing the temperature of operation from room temperature to  $250^\circ\text{C}$ .

### 3.6.1.5 Conclusion:

The operating temperature defines the single most effective control of sensor performance. The response of the sensors can be tailored via control of the temperature of the sensor. The dependence of the responses  $R$  to 0.05, 0.15, and 3 mbar of pure  $\text{NO}_x$ ,  $\text{O}_2$ , and  $D_2$  on the operating temperature is presented in Fig. 3.20.

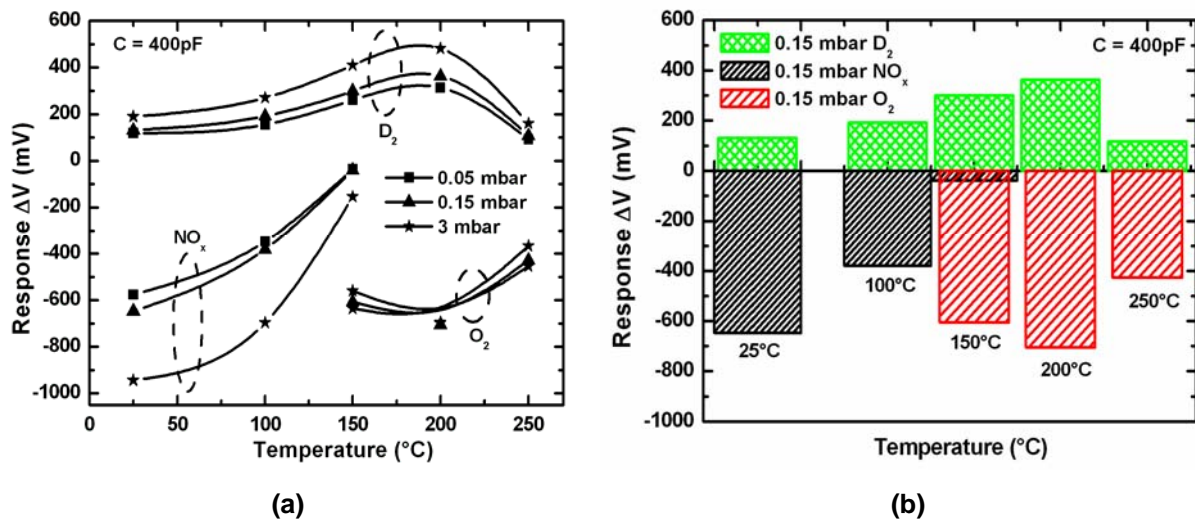


**Fig. 3.20:** (a) The dependence of the response  $R$  to 0.05, 0.15 and 3 mbar of  $\text{NO}_x$ ,  $\text{O}_2$ , and  $D_2$ , on the operating temperature. The measurements were performed at a constant capacitance of 400 pF. (b) Block presentations for 0.15 mbar of the all three gases.

As one can see, the optimum detection temperatures occur in the range of 25-75  $^\circ\text{C}$  for  $\text{NO}_x$ . In this range no response to  $\text{O}_2$  was observed and the cross response to  $D_2$  is very low indicating that the sensor is very suitable for selective detection of  $\text{NO}_x$  at low temperatures. The optimum temperature of operation for detection of deuterium is determined to be between 115-140  $^\circ\text{C}$ . In this range no significant response to  $\text{O}_2$  and  $\text{NO}_x$  is observed indicating that the sensor is very suitable for selective  $D_2$  detection at very low temperatures. In the range 225-250  $^\circ\text{C}$  the response to  $D_2$  is low and no response to  $\text{NO}_x$  was observed, therefore, the sensor A4 can be used as  $\text{O}_2$  gas sensor in this range.

### 3.6.2 Sample A1:

#### 3.6.2.1 Chemical characterization (AES results):

Fig. 3.21 shows a typical Auger spectrum and AES depth profile of the active sensor area. We can see in Fig. 3.21a that the only impurity detected from Rh film is carbon (C) (at 270 eV) and the indium, tin, oxygen, Rh peaks appear at energies of 402, 426, 510, and 300 eV, respectively.

Fig 3.21b shows that the sample structure includes  $\text{In}_x\text{Sn}_y\text{O}_z$ ,  $\text{SiO}_x$ , and SiC layers (Rh is not measured), as well as carbon, which exist in the sample with large amounts. The interfaces between the layers are relatively narrow and sharp.

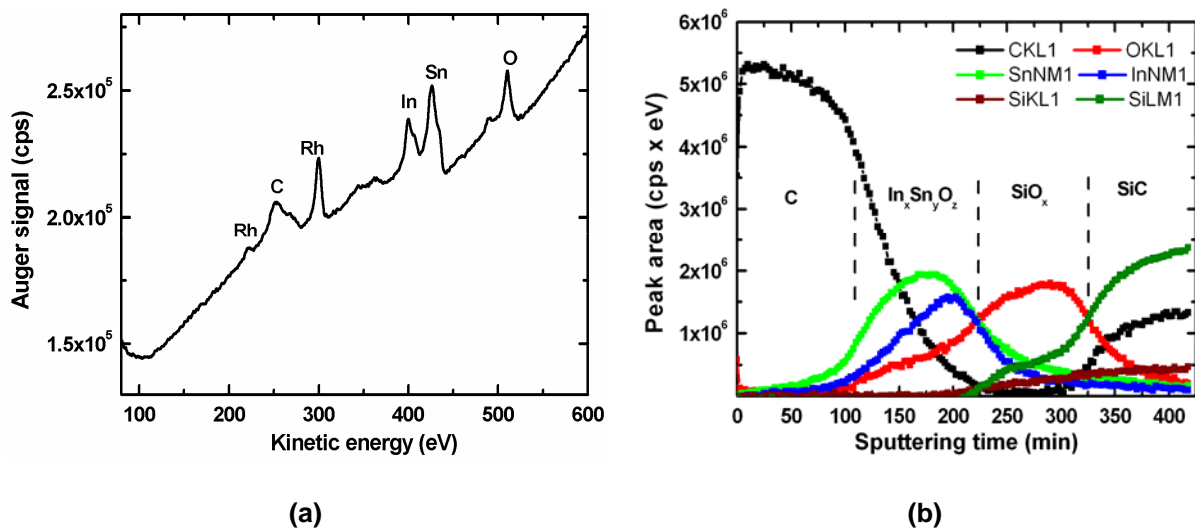


**Fig. 3.21:** (a) Typical Auger spectrum of the active sensor area. (b) Auger depth profiles of the active sensor area (Rh is not measured).

#### 3.6.2.2 $\text{NO}_x$ detection:

Fig. 3.22a provides the dependence of the response  $R$  to  $\text{NO}_x$  on the partial pressure of  $\text{NO}_x$  at different temperatures. A significant increase of the response by decreasing the temperature of operation and by increasing the gas partial pressure was observed and no complete saturation was obtained even at high partial pressures of up to 3 mbar. The maximum response to  $\text{NO}_x$  was observed at room temperature.

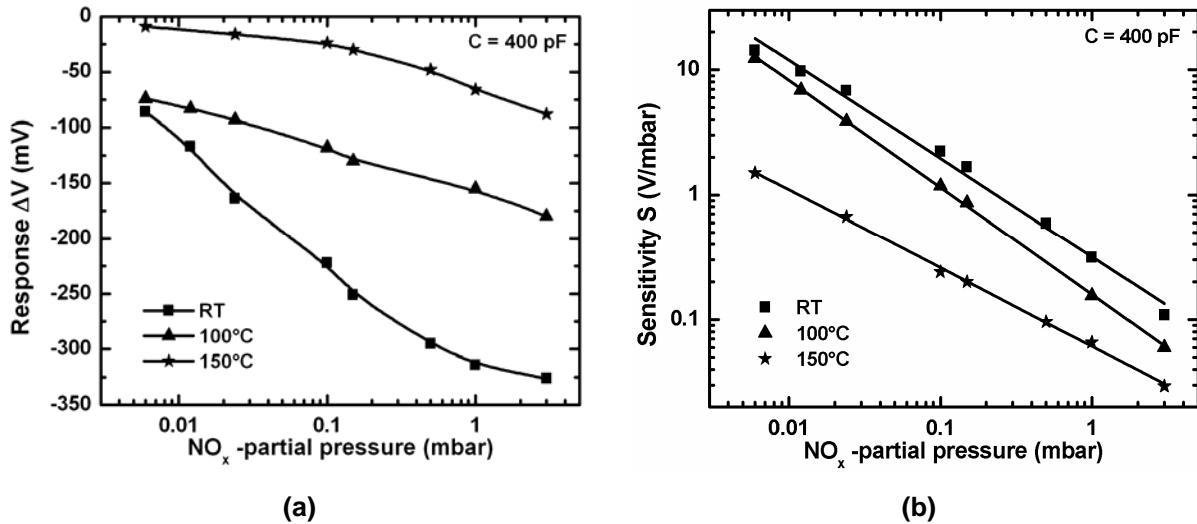


**Fig. 3.22:** The dependence of response  $R$  (a), and sensitivity  $S$  (b) on the  $\text{NO}_x$  partial pressures at different operation temperatures for the sample A1. The measurements were performed at a constant capacitance of 400 pF.

The fitting parameters of the sensitivity  $S$  to  $\text{NO}_x$  at several temperatures (Fig. 3.22b) with the Eq. (3.5) are summarized in Tab. 3.5.

**Tab. 3.5:** Fitting parameter of the sensitivity  $S$  to  $\text{NO}_x$  at several temperatures.

Temperature (°C)	$S = 10^{[a+b \log(\text{NO}_x)]}$		$R^2$
	a	b	
25	$-0.49 \pm 0.03$	$-0.79 \pm 0.03$	0.998
100	$-0.79 \pm 0.01$	$-0.86 \pm 0.008$	0.999
150	$-1.21 \pm 0.01$	$-0.63 \pm 0.01$	0.997

### 3.6.2.3 $\text{D}_2$ detection:

The response  $R$  to  $\text{D}_2$  was investigated in dependence on the operating temperature for different partial pressures of  $\text{D}_2$ . We observed a significant increase of the response by increasing the temperature of operation and by increasing the gas partial pressure and no complete saturation was observed even at high partial pressures of up to 20 mbar (Fig. 3.23a). The maximum response to  $\text{D}_2$  was observed at 300°C.

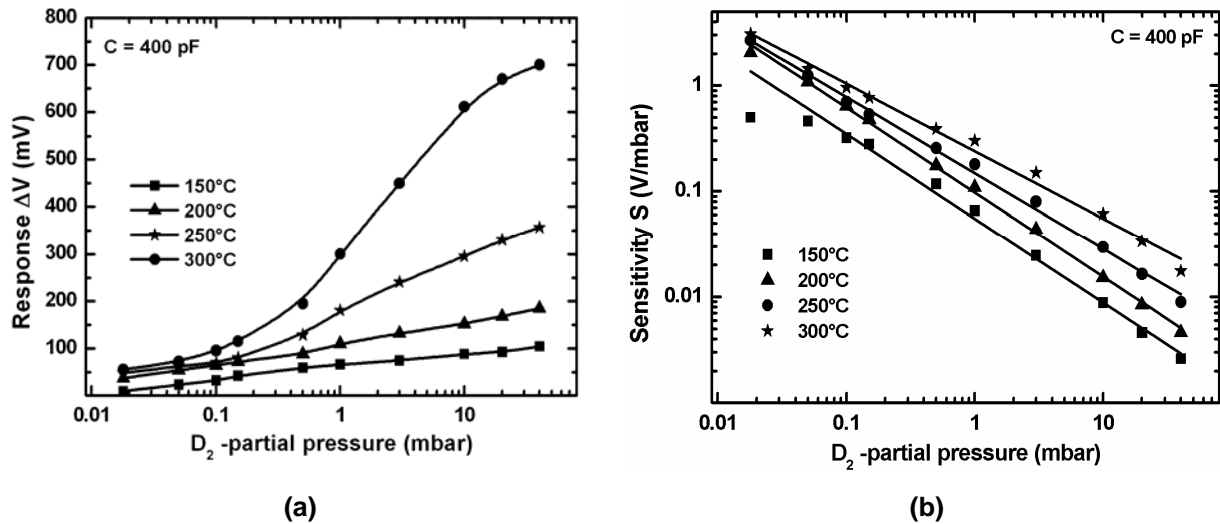


**Fig. 3.23:** The dependence of response R (a), and sensitivity S (b) to different partial pressures of pure D<sub>2</sub> on the operation temperature for the sample A1. The measurements were performed at a constant capacitance of 400 pF.

The fitting parameters of the sensitivity S to D<sub>2</sub> at several temperatures (Fig. 3.23b) with the Eq. (3.7) are presented in Tab. 3.6.

**Tab. 3.6:** Fitting parameter of the sensitivity S towards D<sub>2</sub> at several temperatures.

Temperature (°C)	$S = 10^{[a+b \log(D_2)]}$		R <sup>2</sup>
	a	b	
150	$-1.26 \pm 0.02$	$-0.79 \pm 0.02$	0.996
200	$-1.01 \pm 0.01$	$-0.8 \pm 0.01$	0.999
250	$-0.83 \pm 0.01$	$-0.72 \pm 0.01$	0.998
300	$-0.62 \pm 0.02$	$-0.64 \pm 0.02$	0.996

### 3.6.2.4 Conclusion:

Fig. 3.24 shows the dependence of the responses R to 0.1, 0.15, 1, 3 mbar of pure NO<sub>x</sub>, and D<sub>2</sub> on the operating temperature. Clearly, the optimum detection temperatures occur in the range of 25-75°C for NO<sub>x</sub>. In this range no response to O<sub>2</sub> was observed and the cross response to D<sub>2</sub> is very low indicating that the sensor is very suitable for selective detection of NO<sub>x</sub> at low temperatures. The optimum temperature of operation for detection of deuterium is determined to be between 250-300°C. In this range no significant response to NO<sub>x</sub> is observed indicating that the sensor is very suitable as D<sub>2</sub> gas sensor in this range.

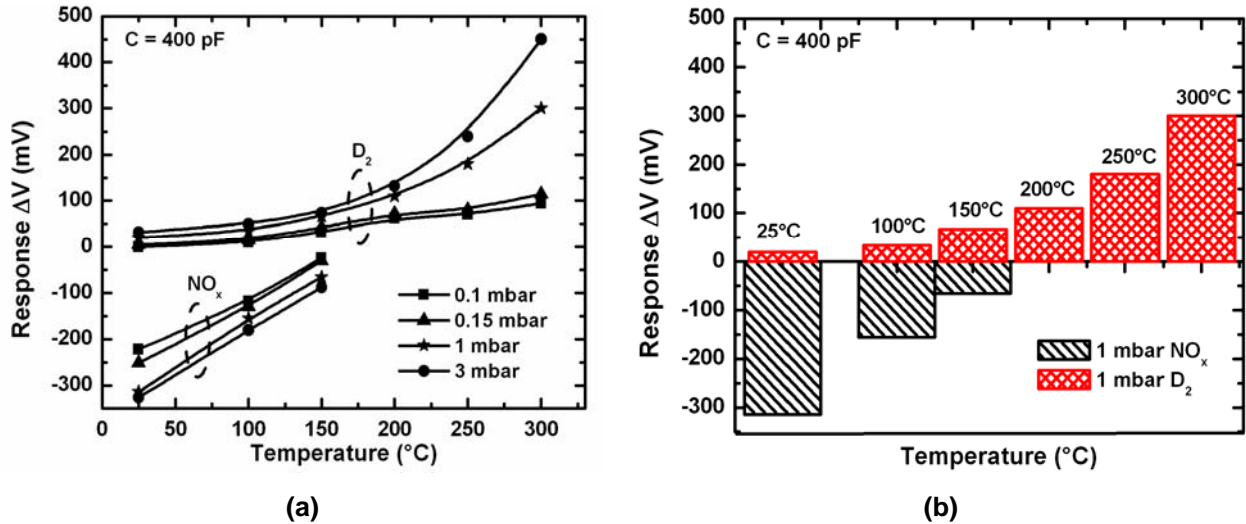


**Fig. 3.24:** (a) The dependence of the response  $R$  to 0.1, 0.15, 1, and 3 mbar of  $\text{NO}_x$  and  $\text{D}_2$ , on the operating temperature. The measurements were performed at a constant capacitance of 400 pF. (b) Block presentations for 1 mbar of both gases.

### 3.6.3 Sample B4:

#### 3.6.3.1 Chemical characterization (AES results):

Typical Auger spectrum of the active sensor area is presented in Fig. 3.25a. We can see in this figure the peaks of nitrogen, oxygen, carbon, and Rh. The AES depth profile in Fig. 3.25b shows the layers,  $\text{SiN}$ ,  $\text{SiO}_2$ ,  $\text{SiC}$  with narrow and sharp interfaces. It is clear from Fig. 3.25b that the active area of sensor is covered by carbon or carbon containing molecules with large quantities.

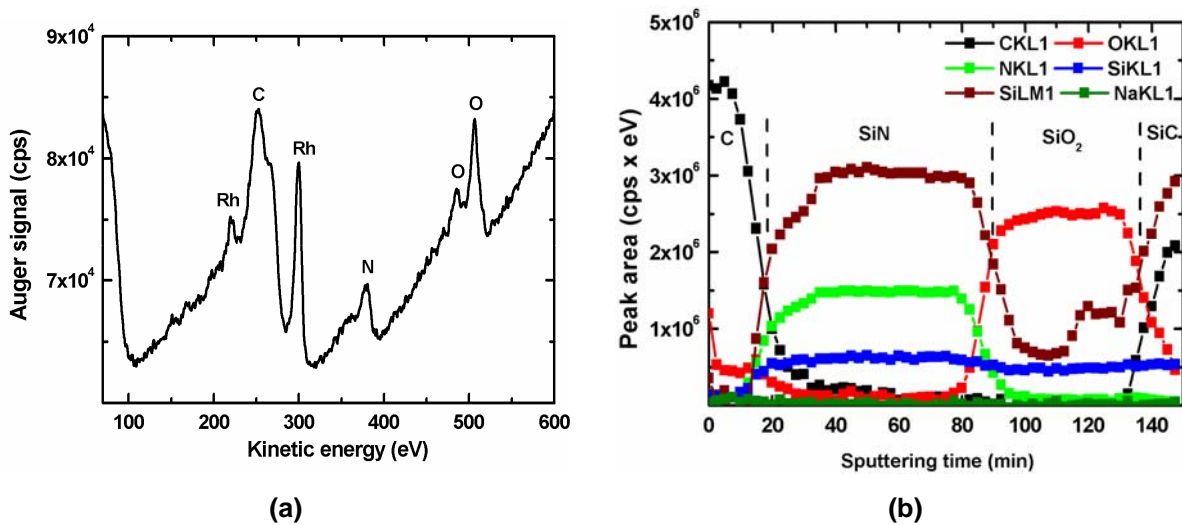


**Fig. 3.25:** Typical Auger spectrum (a) and depth profiles (b) of the active sensor area.

### 3.6.3.2 NO<sub>x</sub> detection:

Fig. 3.26a presents the dependence of the response  $R$  to NO<sub>x</sub> on the partial pressure of NO<sub>x</sub> at different temperatures. We have observed a significant increase of the response by increasing the gas partial pressure and no complete saturation was obtained even at high partial pressures of up to 3 mbar. The maximum response to NO<sub>x</sub> was observed at 100°C.

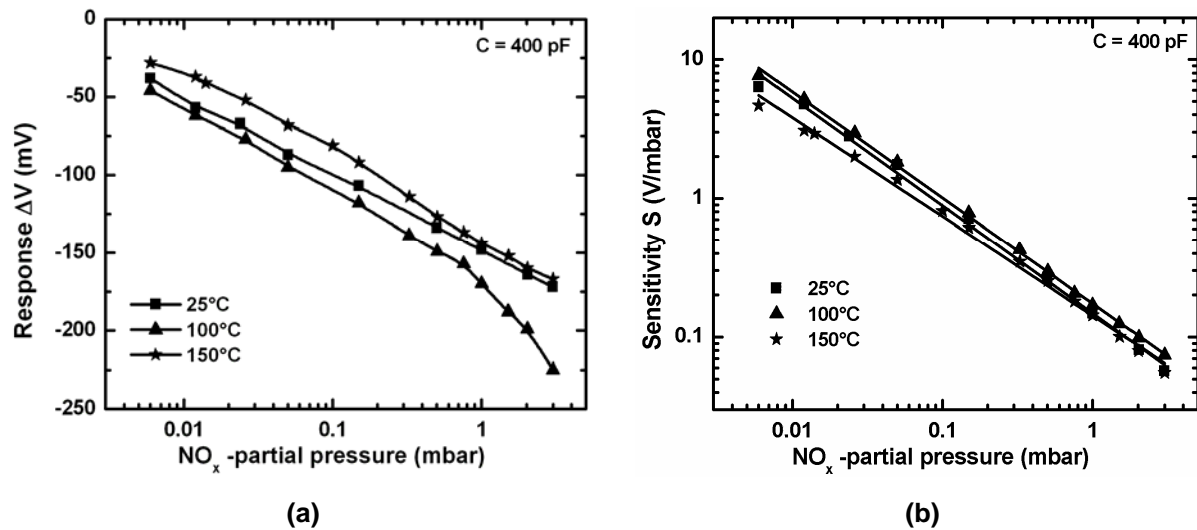


**Fig. 3.26:** The dependence of response  $R$  (a), and sensitivity  $S$  (b) on the NO<sub>x</sub> partial pressures at different operation temperatures for the sample B4. The measurements were performed at a constant capacitance of 400 pF.

Fig 3.26b shows the dependence of sensitivity on the partial pressure of NO<sub>x</sub> at different temperatures. One can see that the log/log trend fits the sensitivity in the whole NO<sub>x</sub> partial pressure range. Different fits, with Eq. (3.5) were made and the values for the coefficient  $a$ ,  $b$ , and  $R^2$  are summarized in Tab. 3.7.

**Tab. 3.7:** Fitting parameter of the sensitivity  $S$  to NO<sub>x</sub> at several temperatures.

Temperature (°C)	$S = 10^{[a+b \log(NO_x)]}$		$R^2$
	$a$	$b$	
25	$-0.83 \pm 0.02$	$-0.77 \pm 0.02$	0.998
100	$-0.76 \pm 0.01$	$-0.76 \pm 0.01$	0.999
150	$-0.84 \pm 0.01$	$-0.71 \pm 0.01$	0.997

### 3.6.3.3 O<sub>2</sub> detection:

In the second step the sensor (sample B4) was tested for the response to other oxidizing gases such as O<sub>2</sub> with partial pressures starting from 0.01 going up to 10 mbar at temperatures between room temperature and 300°C. The dependence of the response R and the sensitivity S to O<sub>2</sub> on the partial pressure of O<sub>2</sub> at different temperatures is shown in Fig. 3.27.

We observed a significant increase of the response by increasing the gas partial pressure. The maximum response to O<sub>2</sub> was observed at 200°C and no significant response to O<sub>2</sub> was observed at a temperature lower than 150°C. At 300°C and above a general decrease of the response was observed, very likely due to an increased thermal desorption of the test gas species from the sensor surface.

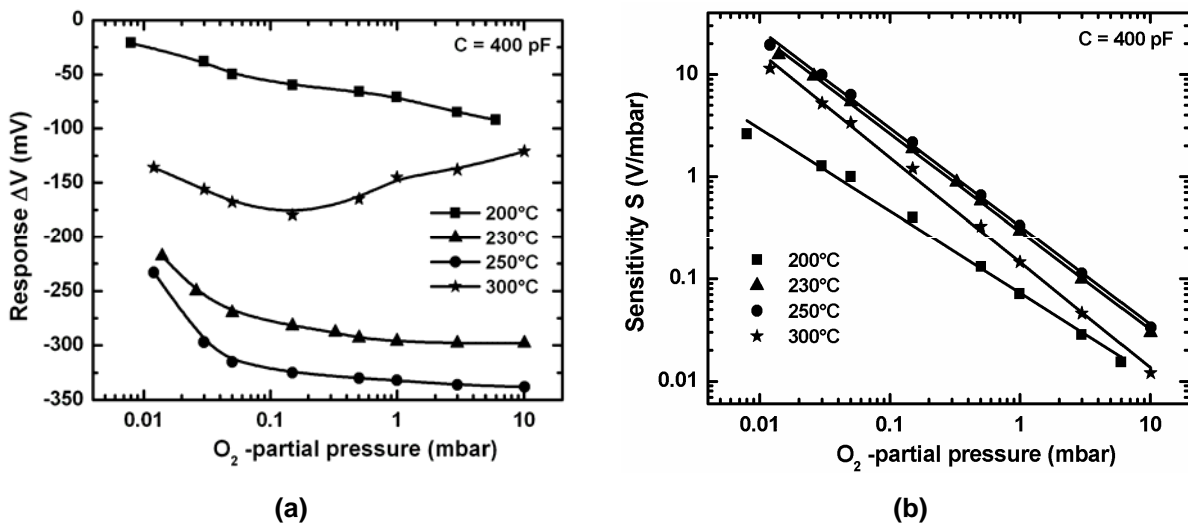


**Fig. 3.27:** The dependence of response R (a), and sensitivity S (b) to different partial pressures of pure O<sub>2</sub> on the operation temperature for the sample B4. The measurements were performed at a constant capacitance of 400 pF.

**Tab. 3.8:** Fitting parameter of the sensitivity S towards O<sub>2</sub> at several temperatures.

Temperature (°C)	$S = 10^{[a+b \log(O_2)]}$		R <sup>2</sup>
	a	b	
200	$-1.14 \pm 0.03$	$-0.8 \pm 0.03$	0.996
230	$-0.54 \pm 0.01$	$-0.96 \pm 0.01$	0.999
250	$-0.48 \pm 0.01$	$-0.96 \pm 0.01$	0.998
300	$-0.84 \pm 0.02$	$-1.026 \pm 0.02$	0.997



Different fits, with Eq. (3.6) were made for the sensitivity  $S$  (Fig. 3.27b) and the values for the coefficient  $a$ ,  $b$ , and  $R^2$  are summarized in Tab. 3.8.

### 3.6.3.4 D<sub>2</sub> detection:

In the third step the sensors were tested for the response to reducing gases such as D<sub>2</sub> with partial pressures starting from 0.004 going up to 10 mbar at temperatures between room temperature and 150°C. The dependence of the response  $R$  on the partial pressures of D<sub>2</sub> (calibration curves) at different operating temperatures is shown in Fig. 3.28a.

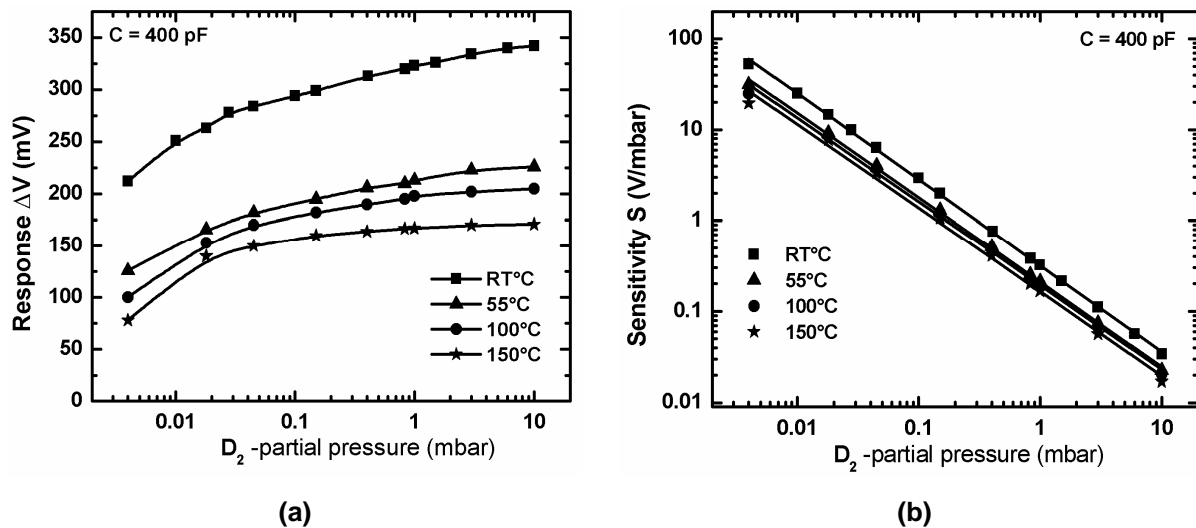


**Fig. 3.28:** The dependence of response  $R$  (a), and sensitivity  $S$  (b) on the partial pressures of pure D<sub>2</sub> at different operation temperatures for the sample B4. The measurements were performed at a constant capacitance of 400 pF.

As one can see, the responses increase non-linearly with increasing the partial pressure of D<sub>2</sub> and complete saturation was observed at a partial pressure of 3 mbar. The maximum response to D<sub>2</sub> was observed at room temperature.

Fig 3.28b plots the dependence of the sensitivity  $S$  on the partial pressures of pure D<sub>2</sub> at different operating temperatures. It can be seen from Fig 3.28b that, in all cases the sensitivity decreases with increasing the partial pressure of the D<sub>2</sub> gas. This effect is likely due to a reduction in the number of adsorption sites as the gas partial pressures are increased leading to a lower sensitivity for higher D<sub>2</sub> partial pressures. As one can see, in the range of the partial pressures investigated, the

sensitivity  $S$  is related to the gas partial pressure by means of Eq. (3.7). Fitting parameters with Eq. (3.4) for the sensitivity  $S$  towards  $D_2$  are presented in Tab. 3.9.

**Tab. 3.9:** Fitting parameter of the sensitivity  $S$  towards  $D_2$  at several temperatures.

Temperature (°C)	$S = 10^{[a+b \log(D_2)]}$		$R^2$
	a	b	
25	$-0.48 \pm 0.006$	$-0.948 \pm 0.005$	0.999
55	$-0.67 \pm 0.01$	$-0.931 \pm 0.01$	0.999
100	$-0.71 \pm 0.02$	$-0.92 \pm 0.016$	0.998
150	$-0.78 \pm 0.03$	$-0.92 \pm 0.02$	0.997

### 3.6.3.5 Conclusion:

The dependence of the responses  $R$  to 0.15, 1, and 3 mbar of pure  $NO_x$ ,  $O_2$ , and  $D_2$  on the operating temperature is shown in Fig. 3.29. It becomes obvious from Fig. 3.29 that the optimum detection temperatures occur in the range of 75-120°C for  $NO_x$ . In this range no response to  $O_2$  was observed and the cross response to  $D_2$  is very low indicating that the sensor is very suitable for selective detection of  $NO_x$  at low temperatures.

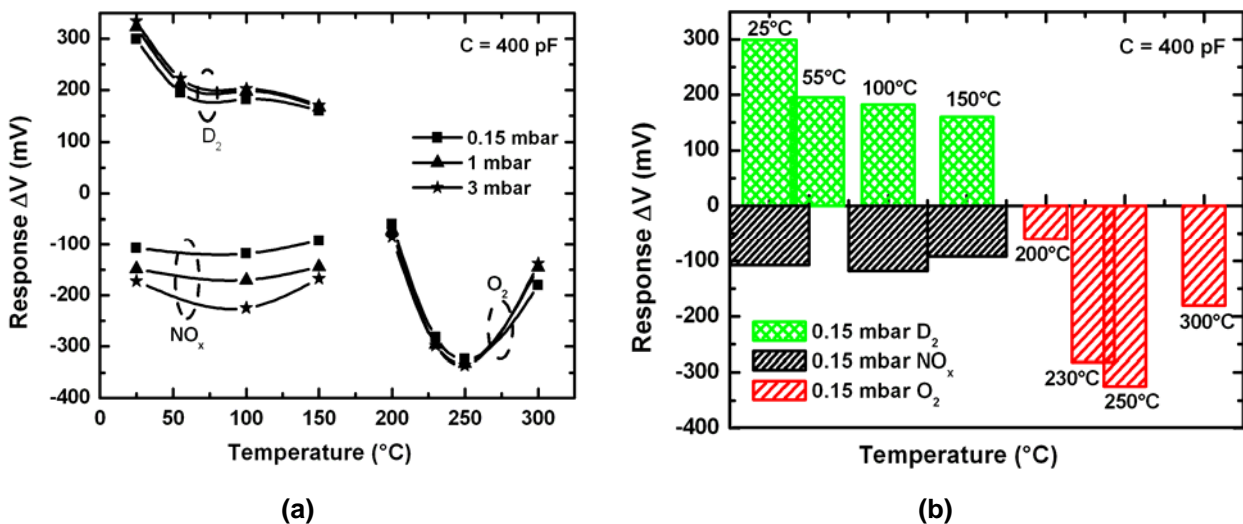


**Fig. 3.29:** (a) The dependence of the response  $R$  to 0.15, 1 and 3 mbar of  $NO_x$ ,  $O_2$ , and  $D_2$ , on the operating temperature. The measurements were performed at a constant capacitance of 400 pF. (b) Block presentations for 0.15 mbar of the all three gases.

The optimum temperature of operation for detection of deuterium is determined to be between 25-50°C. In this range no significant response to  $\text{NO}_x$  is observed indicating that the sensor is very suitable for selective  $\text{D}_2$  detection at very low temperatures. In addition, for  $\text{O}_2$  the optimum detection temperatures occur in the range of 225-275°C. In this range no response to  $\text{D}_2$  and  $\text{NO}_x$  was observed indicating that the sensor is very suitable for selective detection of  $\text{O}_2$  at high temperatures.

### 3.6.4 Discussion and Comparison:

The C-V curve of the sensor is displaced toward negative voltages in deuterium (reducing gases) and towards positive voltages in  $\text{NO}_x$  and  $\text{O}_2$  (oxidizing gases).

#### 3.6.4.1 $\text{D}_2$ detection:

The response of the MISiC sensors to hydrogen containing gases has been attributed to the formation of a polarized layer at the metal- $\text{SiO}_2$  interface [3.3], due to the reduction of the metal-oxide work function difference in hydrogen [3.14]. We use the model of Tobias *et al.* [3.15] to explain the response to  $\text{D}_2$ . Fig. 3.30 shows the distribution of charges in the MISiC sensor during exposure to  $\text{H}_2$  ( $\text{D}_2$ ) and after evacuation the quartz tube of the  $\text{H}_2$  ( $\text{D}_2$ ), respectively.

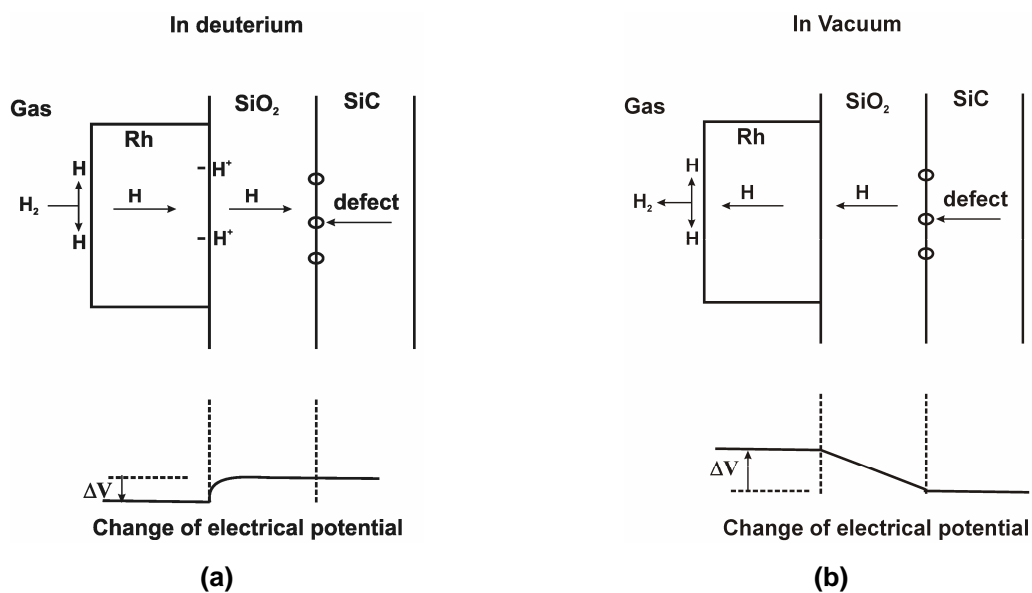


**Fig. 3.30:** Distribution of charges in the MISiC sensor during exposure to (left)  $\text{H}_2$  ( $\text{D}_2$ ) and after evacuation of the quartz tube of the  $\text{H}_2$  ( $\text{D}_2$ ) (right), respectively (adapted from [3.15]).

For an MISiC device biased at constant capacitance, the potentials in the SiC are constant, regardless of gas exposure. In a hydrogen (deuterium) ambient, the hydrogen (deuterium) is dissociating at the Rh surface and diffusing relatively fast into the sensor. A polarized layer builds up at the Rh-SiO<sub>2</sub> interface with the protons in the SiO<sub>2</sub> and the electrons in the metal. With the polarized layer present, the potential of the Rh decreases in hydrogen (deuterium). As a result, the flat band voltage of the capacitor decreases, which gives a voltage drop,  $\Delta V$ , resulting in a shift,  $\Delta V$  along the voltage axis, of the C-V curve of a capacitor. After evacuation of the quartz tube of the D<sub>2</sub>, the disappearance of the polarized layer at the metal-SiO<sub>2</sub> interface increases the potential of the Rh and the sensor signal returns to initial value after a few minutes.

#### 3.6.4.2 O<sub>2</sub> and NO<sub>x</sub> detection:

We use the model of Schalwig *et al.* [3.10] to explain the response to O<sub>2</sub> and NO<sub>x</sub>. It is supposed in Fig. 3.31a that, at the beginning, no electrical connection exists between the porous catalytic metal electrode and the semiconductor contact. Assuming that the Rh-MOSiC gas sensor is operated in an oxygen-containing gas ambient, molecular oxygen will dissociate and chemisorb as individual atoms on the Rh surface.

Oxygen atoms will also be present on the neighboring exposed patches of oxide due to spillover effects [3.16]. This spillover leaves negative ionic surface charge on the exposed patches of oxide and positive electronic charge on the Rh clusters of the porous electrode. These surface charges will be balanced by immobile positive donor and mobile negative electron charges in the semiconductor [3.10]. Therefore, an electrostatic potential between the Rh and the SiC arises due to the positive charge on the Rh electrode.

Within the band picture (Fig. 3.31a), which neglects the effects of electrode porosity, the overall effect of spillover-induced charge separation is modeled by an increase in the metal work function  $\Phi_m$  relative to the semiconductor [3.10].

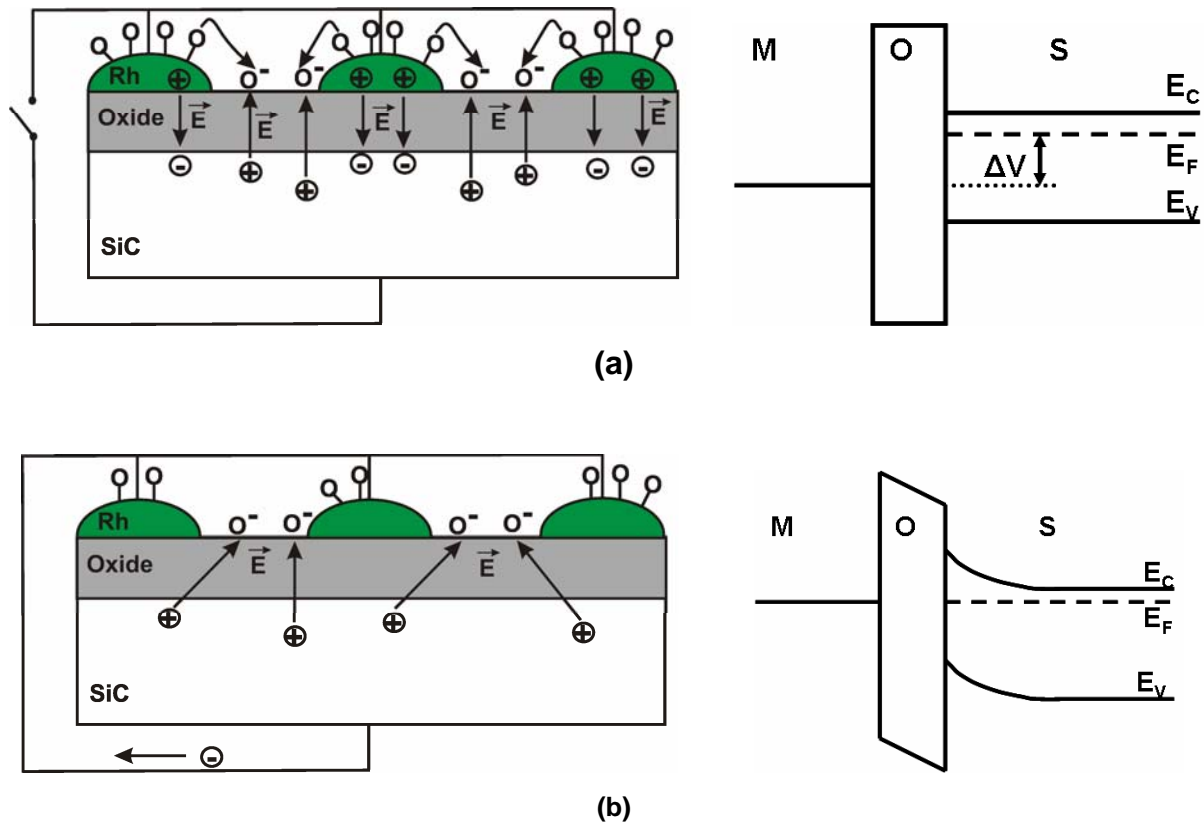


**Fig. 3.31:** Schematic drawing and band structure for the proposed oxygen sensing mechanism occurring on porous Rh electrodes of MOS field effect gas sensors. **(a)** Without electrical connection between catalytic electrode and ohmic contact. **(b)** Catalytic electrode short circuited to the ohmic contact (adapted from [3.10]).

Applying a short circuit to the device as shown in Fig. 3.31b, the Fermi levels of the semiconductor and those of the Rh surface clusters line up by transferring electronic charge from the semiconductor to the catalytic surface electrode. This transfer of electronic charge ultimately leaves negative ionic charge on the exposed surface of the device and compensating positive donor charge in the sub-surface semiconductor regions. As a consequence, an increased band bending and a widening of the semiconductor depletion layer will result. For a sensor measured under electronically stabilized capacitance conditions, a negative sensor signal results, which is consistent with the experimental results shown in Fig. 3.16a and Fig. 3.27a.

Within the band model picture, the ionosorption of surface oxygen ions can be expressed by introducing adsorption-induced surface states at the oxide surface similar to the case of polycrystalline metal oxide gas sensors. The occupation of these states will then be defined by the equilibrium between the O<sub>2</sub> concentration in

the gas phase, on the one hand, and the semiconductor Fermi energy, on the other hand [3.10]. Similarly, the sensitivity of Rh-MOSiC sensors toward  $\text{NO}_x$  can also be explained in terms of ionosorption on patches of exposed oxide. On metal oxide gas sensors, nitric dioxide normally leads to an increased resistance with respect to oxygen. This behavior is explained in terms of  $\text{NO}_x$  related surface states on the oxide surface that are energetically lower than the O-induced ones [3.10]. As a consequence, an increased band bending and a reduced conductivity across neighboring metal oxide crystallites is obtained. The model can easily be extended to the MOSiC case. Supposing that also in the case of  $\text{NO}_2$  negatively charged species, for instance,  $\text{NO}_3^-$  or  $\text{N}_2\text{O}_4^{2-}$  [3.10, 3.17], spill over to the exposed oxide areas, the energetically deeper,  $\text{NO}_2$  related adsorption states will lead to an increased negative surface charge on patches of exposed oxide and therefore to an increased band bending with respect to an oxygen-containing atmosphere.

#### 3.6.4.3 Comparison:

The responses R to 0.15 and 3 mbar of  $\text{D}_2$ ,  $\text{NO}_x$ , and  $\text{O}_2$  as a function of operating temperature for all three studied sensors are shown in Fig. 3.32, Fig. 3.33, and Fig. 3.34. Several quantitative conclusions can be drawn from these figures:

1. The sensor A4 has the best response to  $\text{NO}_x$  in the temperature range (25-125°C) with a maximum value at 25°C. indicating that an effective sensor operation at room temperature is possible.
2. At 300°C and above the sensor A1 in the best  $\text{D}_2$  gas sensor. At this temperature no response to  $\text{NO}_x$  was observed and the response to  $\text{O}_2$  is very low indicating that the sensor A1 is very suitable for selective detection of  $\text{D}_2$  at 300°C.
3. The best response to  $\text{O}_2$  in the temperature range 150-225°C was observed for the sensor A4. But in this range the response to  $\text{D}_2$  is very high. As a consequence the sensor A4 is not suitable for selective detection of  $\text{O}_2$  or  $\text{D}_2$  in this range.
4. The sensor B4 is very suitable for selective detection of  $\text{D}_2$  at room temperature since at this temperature no response to  $\text{O}_2$  is observed and the response to  $\text{NO}_x$  is very low.
5. The different responses of sensors A4 and B4 to all test gases are attributed to the differences in the insulating materials ( $\text{SiO}_2$ ,  $\text{SiN/SiO}_2$ ).

- The response to all test gases differs for the different metal microstructure (sensors A1 and A4).
- The temperature of the maximum response is dependent on the gas species being measured. This information, along with a careful choice of insulating materials and catalyst microstructure can be used to enhance device sensitivity and selectivity.

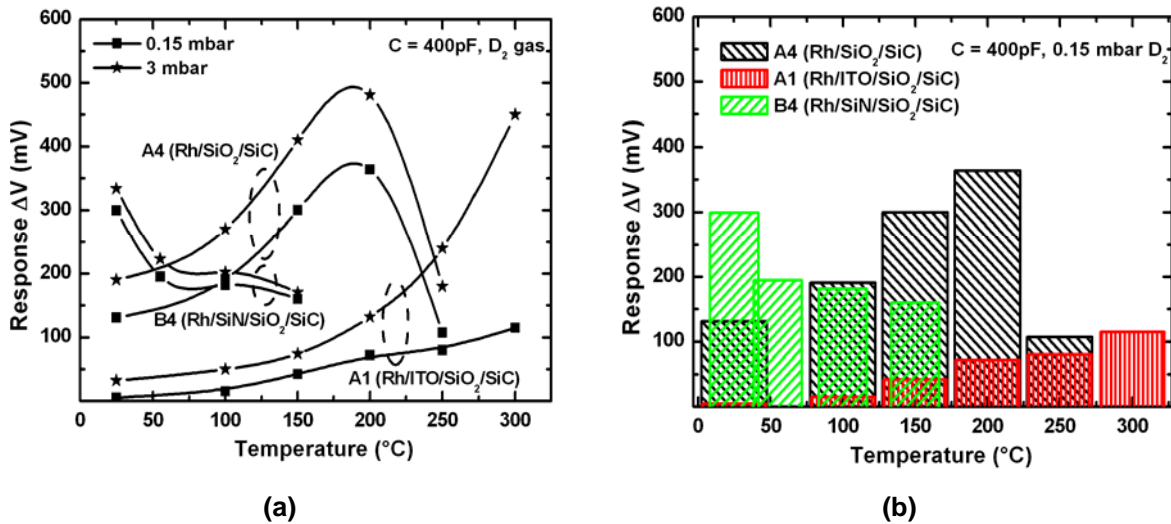


**Fig. 3.32:** (a) The dependence of the responses  $R$  of all three studied sensors investigated to 0.15, and 3 mbar of D<sub>2</sub> on the operating temperature. (b) Blocks presentation for 0.15 mbar D<sub>2</sub>.

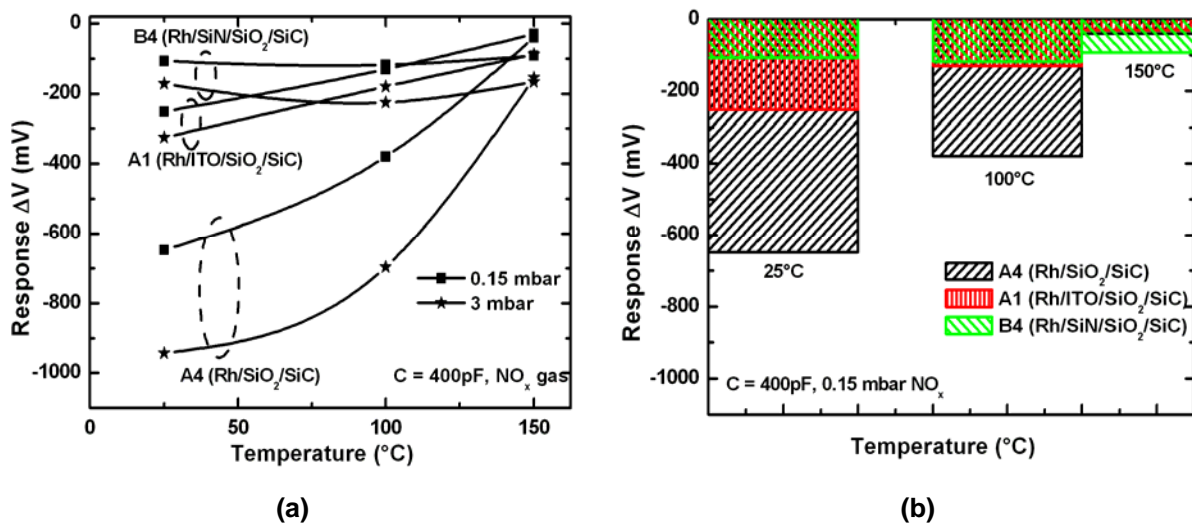


**Fig. 3.33:** (a) The dependence of the responses  $R$  of all three sensors studied to 0.15, and 3 mbar of NO<sub>x</sub> on the operating temperature. (b) Block presentations for 0.15 mbar of NO<sub>x</sub>.

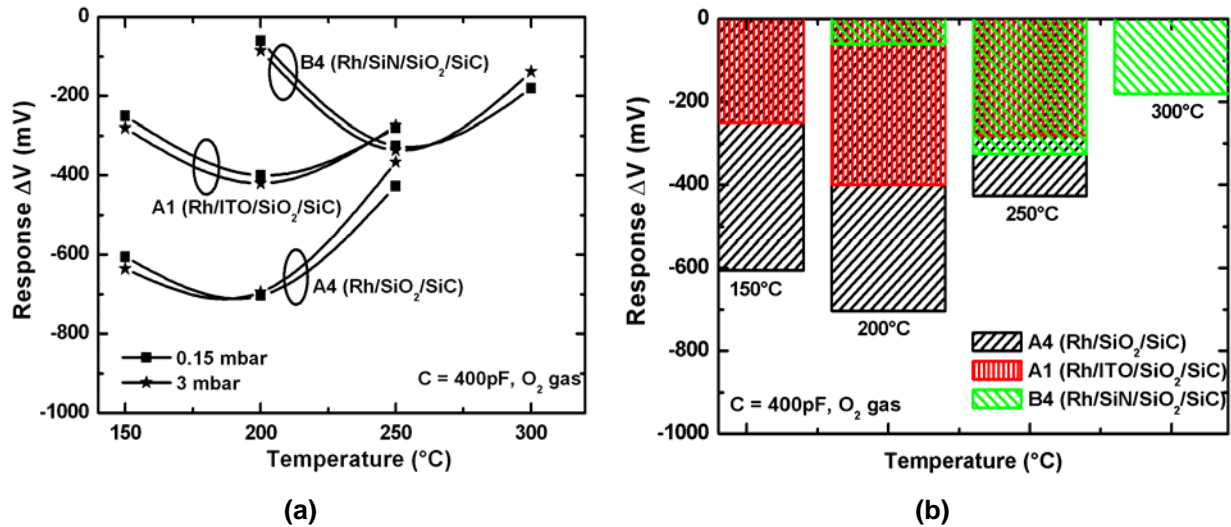


**Fig. 3.34:** (a) The dependence of the responses  $R$  of all three sensors studied to 0.15, and 3 mbar of O<sub>2</sub> on the operating temperature. (b) Block presentations for 0.15 mbar of O<sub>2</sub>.

### 3.7 Conclusion:

The response to reducing (D<sub>2</sub>) and oxidizing gases (NO<sub>x</sub>, and O<sub>2</sub>) of MOSiC and MMOOSiC structures with Rh gate with a thickness of 30 nm in dependence on the operating temperature and gas partial pressures was investigated. The response was measured as a shift in the capacitance-voltage (C-V) curve along the voltage axis. Positive and negative flat-band voltage shifts up to 1 V were observed for oxidizing and reducing gases, respectively. The most important property of the sensors studied in this chapter is that the sensors can be used as NO<sub>x</sub> gas sensor at room temperature. Depending on the type of insulator that is chosen, and the Rh structure, differences in the sensitivity properties are achieved.

### 3.8 Outlook and future work:

The following additional experiments are suggested for further investigation in this field of study:

- The fundamental properties of the gate microstructure (Rh, Rh/ITO) and the insulators (SiO<sub>2</sub>, SiN/SiO<sub>2</sub>) should be investigated by a wide set of structural characterisation techniques, including Transmission Electron Microscopy, X-ray diffraction, Raman, Fourier Transform infrared, and X-ray photoelectron spectroscopy. The combined use of the different techniques allows an improved understanding of the sensing mechanism of Rh-MOSiC gas sensors.



- The selectivity against other gases such as CO, and NH<sub>3</sub> should be investigated.
- The investigation of the stability or reliability of the sensor is needed.
- The influence of the catalytic (Rh) thickness on the gas sensing properties of the Rh-MOSiC gas sensors should be tested.

### References:

- [3.1] I. Lundström, M. S. Shivaraman, C. M. Svensson, and L. Lundqvist, "A hydrogen-sensitive MOS field-effect transistor", *Appl. Phys. Lett.* 26 (1975) 55-57.
- [3.2] J. Fogelberg, M. Eriksson, H. Dannetun, and L.-G. Petersson, "Kinetic modelling of hydrogen adsorption/absorption in thin films on hydrogen-sensitive field-effect device: Observation of larger hydrogen-induced dipoles at the Pd-SiO<sub>2</sub> interface", *J. Appl. Phys.* 78 (1995) 988-996.
- [3.3] A. Lloyd Spetz, A. Baranzahi, P. Tobias, and I. Lundström, "High temperature sensors based on metal-insulator-silicon carbide device", *phys. stat. sol. A* 162 (1997) 493-511.
- [3.4] A. Lloyd Spetz, P. Tobias, L. Uneus, H. Svenningstorp, L.-G. Ekedahl, and I. Lundström, "High temperature catalytic metal field effect transistors for industrial applications", *Sensors and Actuators B* 70 (2000) 67-76.
- [3.5] I. Lundström, M. Armgarth, and L.-G. Petersson, "Physics with catalytic metal gate chemical sensors", *CRC Crit. Rev. Solid State Mater. Sci.* 15 (1989) 201.
- [3.6] L. -G. Ekedahl, M. Eriksson, and J. Lundström, "Hydrogen Sensing mechanism of metal-insulator interfaces", *Acc. Chem. Res.* 31 (1998) 249-256 .
- [3.7] M. Wallin, H. Grönbeck, A. Lloyd Spetz, and M. Skoglundh, "Vibrational study of ammonia adsorption on Pt/SiO<sub>2</sub>", *Appl. Surf. Sci.* 235 (2004) 487-500.
- [3.8] A. Arbab, A. Spetz, Q. ul Wahab, M. Willander, and I. Lundström, "Chemical sensors for high temperatures based on silicon carbide structures", *Sensors and Mater.* 4 (1993) 173.
- [3.9] H. Dannetun, I. Lundström, and L.-G. Petersson, "Dehydrogenation of acetylene and ethylene studied on clean and oxygen covered palladium surfaces", *Surf. Sci.* 173 (1986) 148-149.
- [3.10] J. Schalwig, P. Kreisl, S. Ahlers, and G. Müller, "Response mechanism of SiC-based MOS field-effect gas sensors", *IEEE sensors J.* 2 (2002) 394-402.

- [3.11] M. Eriksson, C. Utaiwasin, A. Carlsson, and M. Löfdahl, "Gas response dependence on gate metal morphology of field-effect devices", in Proc. Transducers, Sendai, Japan, June 7-10, 1999, pp. 950-953.
- [3.12] S. M. Sze, "Physics of semiconductor devices", ISBN 0-471-09837-X, 1981.
- [3.13] E. S. Yang, "Fundamentals of semiconductor devices", McGraw-Hill, Inc., USA, ISBN 0 07-072236-6, 1978.
- [3.14] I. Lundström, and t. DiStefano, "Influence of hydrogen on the Pt-SiO<sub>2</sub>-Si structures", Solid State Comm. 19 (1976) 871-875.
- [3.15] P. Tobias, B. Golding, and N. Ghosh, "Interface state in high-temperature gas sensors based on silicon carbide", IEEE Sensor J. 2 (2003) 543-547.
- [3.16] W. C. Corner, G. M. Pajonk, and S. T. Teichner, "Spillover of sorbed species", Adv. Catalysis 34, (1986) 1-79.
- [3.17] S. R. Morrison, "Selectivity in semiconductor gas sensors", Sensors and Actuators B12 (1987) 425-440.

## Chapter 4

### 4. Study of Gas-Sensing Performances of SiC-Based FET using Mixtures of Metal Oxides as Gate Materials

#### 4.1 Introduction:

Nitrogen oxides ( $\text{NO}_x$ ) are produced from combustion processes, which are typical air pollutants.  $\text{NO}_x$  reacts with water in the atmosphere to form nitrous acid and nitric acid, which are one of the factors that cause the acid rain. Hence, detection and emission control of toxic  $\text{NO}_x$ -gases, consisting of  $\text{NO}$  and  $\text{NO}_2$ , is of great importance [4.1]. SiC-based sensors that can be used at high temperature and in corrosive atmosphere have been under development for that purpose. An electronic device based on SiC can function as a chemical sensor with the deposition of a catalytic material on a thin insulating layer on its surface. The catalytic material can be a metal such as platinum (Pt) [4.2-4.7], palladium (Pd) [4.6-4.8], iridium (Ir) [4.4-4.5, 4.7], or combinations of these [4.7]. Metal oxides can also be used as catalytic layers on devices [4.9-4.11] where the material does not need to conduct large currents. The field effect transistor (FET) is the most complicated device design tested to date but is a highly reliable design for gas sensors. In this device, an ordinary ohmic metal contact is made to the n-type source and drain regions, and the catalytic metal is used as the gate contact placed on top of an insulating layer over the channel region. In traditional FETs, small voltages applied to the gate contact can control large currents that pass through the channel region between the source and drain regions. In the case of the sensor, the small changes induced in the catalytic metal by the reactant gases can cause large changes in the source-drain current, which makes this device a very effective sensor.

In this chapter the  $\text{NO}_x$  and other gases such  $\text{O}_2$ , and  $\text{D}_2$ , sensing properties of SiC-based FETs with  $\text{In}_x\text{Sn}_y\text{O}_z$ ,  $\text{In}_x\text{V}_y\text{O}_z$  and  $\text{Pt-In}_x\text{Sn}_y\text{O}_z$  metal oxides as a catalytic gate have been investigated as a function of operation temperature. By choosing the appropriate temperature, devices that are significantly more sensitive to certain gases have been realized. In the present study, we have tried to enhance the selectivity of a semiconductor-type sensor by mixing oxides and addition of noble metal Pt to develop a sensitive and selective nitrogen oxide sensor.

## 4.2 Theory of field-effect-transistor (FET):

This section of this chapter describes the functionality of a Metal-Oxide-Semiconductor field effect transistor, commonly denoted MOSFET. The purpose of this section is to introduce fundamental concepts within semiconductor electronics and to give a basic understanding of how a MOSFET operates.

### 4.2.1 Principles of a MOSFET:

The metal insulator semiconductor field effect transistor (MISFET) is the most prominent device based on a metal insulator semiconductor (MIS) structure next to the so-called MISCAP. If the insulator layer is chosen to be an oxide like silicon dioxide it is termed MOSFET. A high temperature design is based on SiC as semiconductor.

The general working principle of a MOSFET is quite simple. A MOSFET consists of a source, a drain, and a gate. A voltage is applied between the source and drain contact resulting in a current, the source-drain current  $I_{DS}$ . The current can be regulated by a potential applied to the gate,  $V_{GS}$ .

The term metal oxide semiconductor describes the three principal layers of a MOSFET: a metal (the gate) on top of an oxide insulator and a semiconductor substrate (including source and drain) as illustrated in Fig. 4.1.

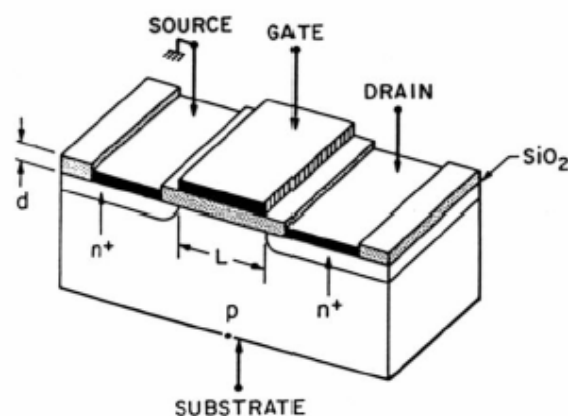
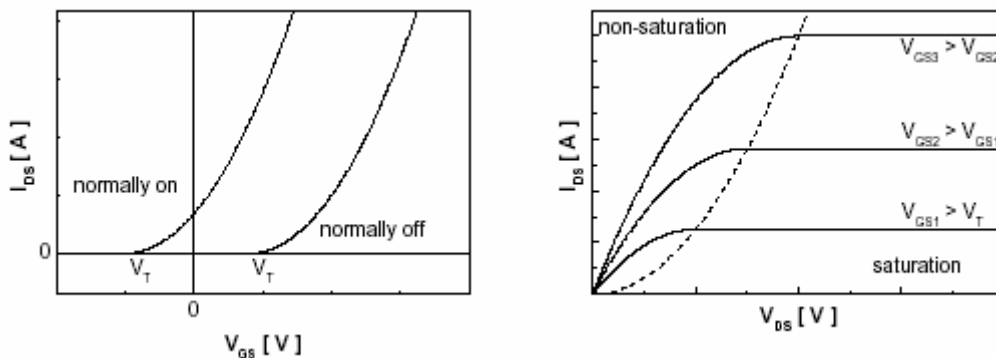


Fig. 4.1: Schematic representation of a MOSFET [4.12].

The regions of the source and drain are made of the same semiconductor material but are oppositely doped resulting in a n-p-n or p-n-p structure. The source provides

charge carriers and the drain collects charge carriers, whereas the substrate between the two acts as a conductive channel. For a n-channel MOSFET the charge carries are electrons. For a p-channel MOSFET the charge carriers are positively charged holes. An n-channel MOSFET is based on a n-p-n structure. In some designs the transistor is embedded in a transistor well to allow several independent transistors on one single substrate.

There are basically four different types of MOSFET, depending on the type of the conductive channel. If, at zero gate bias  $V_{GS}$ , a conductive n-channel exists ( $I_{DS} > 0$ ) and a negative voltage has to be applied to the gate to reduce the channel conductance, then the device is an n-channel “normally on” MOSFET (illustrated in Fig. 4.2a. If the channel conductance is very low at zero gate bias and a positive voltage larger than the threshold voltage  $V_T$  must be applied to the gate to form a n-channel, then the device is a n-channel “normally off” MOSFET. Similarly, p-channel normally on and p-channel normally of MOSFETs are available.



**Fig. 4.2:** Characteristics of a MOSFET device **(a)** Transconductance curves for a “normally on” and “normally off” MOSFET **(b)** Output conductance curves for different values of  $V_{GS}$  [4.12].

The channel geometry, charge carrier mobility, and the number of available charge carriers determine the conductance of this channel. The later can be modulated by varying the gate voltage  $V_{GS}$  or a substrate bias voltage. The electric field established by  $V_{GS}$  across the dielectric layer, in the direction traverse to the current flow, influences the type and concentration of charge carriers. Let us consider a n-channel MOSFET. If a low positive potential is applied to the gate the major carriers in the substrate (holes) are repelled and a depletion region is formed. At high potential the minor charge carriers (electrons) are attracted to the semiconductor surface (inversion layer). The inversion layer occurs if  $V_{GS} > V_T$ . Now the channel is

again conducting significantly and a current can flow due to the existing n-p-n structure. Increasing  $V_{GS}$  further increases the number of charge carriers and with it the current through the channel.

The actual current through the channel is determined by the applied source-drain potential and two regions are distinguished: the non-saturation and the saturation mode as shown in Fig. 4.2b. Two semi-quantitative equations describe these two modes. The current-voltage characteristics in the non-saturation mode ( $|V_{DS}| \leq |V_{GS} - V_T|$ ) of a long gate FET can be modelled using the square law approximation leading to:

$$I_{DS} = \mu_{eff} C_{ox} \frac{W}{L} \left( V_{GS} - V_T - \frac{V_{DS}}{2} \right) V_{DS}. \quad (4.1)$$

In saturation mode ( $|V_{DS}| \geq |V_{GS} - V_T|$ ) the current is given by:

$$I_{DS} = \mu_{eff} C_{ox} \frac{W}{2L} (V_{GS} - V_T)^2, \quad (4.2)$$

where  $\mu_{eff}$  the charge carrier mobility,  $W$ ,  $L$  the channel width and length, respectively, and  $C_{ox}$  the insulator capacitance. The drain current is near zero if the gate voltage is less than the threshold voltage.

The performance of a MOSFET device is characterised by two terms:

- The transconductance quantifies the drain current variation with a gate-source voltage variation while keeping the drain-source voltage constant. This is an important parameter as it determines the device sensitivity and contributes to the overall sensitivity of the sensor device.
- The output conductance quantifies the drain current variation with a drain-source voltage variation while keeping the gate-source voltage constant. The threshold voltage  $V_T$  as the onset of the inversion layer is determined among other factors by the properties of the materials and by the work functions of the gate material  $\Phi_M$  and the bulk semiconductor  $\Phi_S$ .

$$V_T = \Phi_M - \Phi_S - \frac{Q_i}{\epsilon_i} d_i + 2\Phi_F - \frac{Q_B}{\epsilon_i} d_i, \quad (4.3)$$

where  $Q_i$  denotes the charge of the insulator at the insulator-semiconductor interface,  $d_i$  the thickness of the insulator,  $\epsilon_i$  its permittivity,  $Q_B$  the depletion charge in the semiconductor, and  $\Phi_F$  the potential drop across the depletion region.

### 4.2.2 The GasFET:

The term chemical field effect transistor (ChemFET) is the generic term for chemical sensors based on the MOSFET design. This class is commonly divided into two major subgroups: gas sensitive field effect transistor (GasFET) for gas sensing and ion selective field effect transistor (ISFET) for sensing in liquids. The ISFET is the first MOSFET sensor and was proposed by Bergveld *et al.* [4.13].

The best-known example for (GasFET) is the Pd-FET (“Lundström FET”) reported by Lundström *et al.* [4.8]. Actually the device is a normal MOSFET with the usual aluminium gate replaced by a palladium gate. For a measurement the gate should be connected to the source plus bulk of the device. Palladium was chosen, because of its catalytic properties and its permeability to H atoms. Hydrogen in the ambient dissociatively adsorbs at the outer Pd surface and the resulting hydrogen atoms diffuse into the thin layer. This process occurs relatively fast at elevated temperatures (about 150°C). Lundström *et al.* showed that the amount of hydrogen inside the Pd is too low to influence the bulk part of its work function, but than on the other hand the hydrogen atoms are adsorbed at the Pd/SiO<sub>2</sub> interface, forming a dipole layer that thus influences the surface energy part of the work function. The magnitude of the modulation depends on the coverage  $\theta$  with H atoms of the available number of adsorption sites per unit area at the Pd/SiO<sub>2</sub> interface. The observed modulation of the threshold voltage  $\Delta V_T$  of the Pd-gate MOSFET was modelled with respect to the maximum achievable shift of the dipole-layer voltage  $\Delta X_{max}$  at maximum coverage:

$$\Delta V_T \approx \Delta X = \Delta X_{max} \theta, \quad (4.4)$$

where the coverage  $0 < \theta < 1$  was modelled as a function of the partial hydrogen pressure of the ambient,  $P_{H_2}$ , according to

$$\theta = \frac{\alpha \sqrt{P_{H_2}}}{1 + \alpha \sqrt{P_{H_2}}}, \quad (4.5)$$

where  $\alpha$  is an overall equilibrium constant which appears to be oxygen and temperature dependent.  $V_T$  is altered by the analyte gas by influencing the work function of the metal gate,  $\Phi_M$ , and consequently  $I_{DS}$ : the I-V curve is shifted by  $\Delta V$  (Fig. 4.3).

The MOSFET sensors are usually operated under the constant drain current mode, which means that the change of the drain current due to the change of the work function is compensated for by the adjustment of the gate voltage.

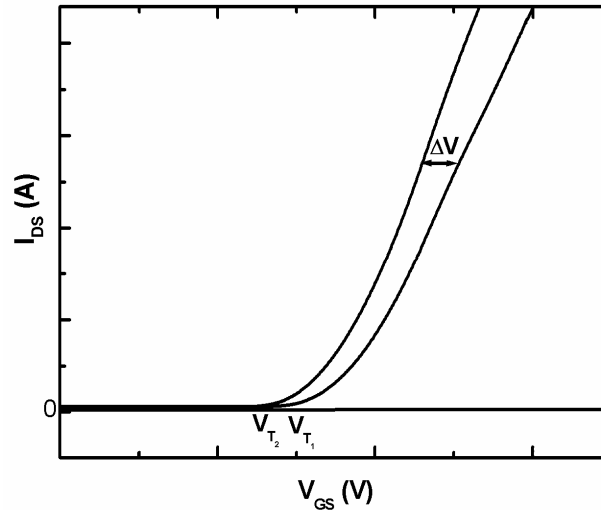


**Fig. 4.3:** A shift of the I-V curve of a GasFET (FET with Pt-In<sub>x</sub>Sn<sub>y</sub>O<sub>z</sub> gate) induced by gas adsorption and a change of work function at the metal/insulator interface.

One limitation of the Pd-FET is the fact, that only hydrogen can diffuse through the gate and therefore only few gases can be detected like hydrocarbons and ammonia. Variations in sensitivity and selectivity are possible by different operation temperatures. To overcome this limitation ultra thin, non-continuous layers of metals (among others Pt, Au, Ir) or porous materials can be used as gate materials.

The palladium gate has been replaced by SnO<sub>2</sub> [4.14], conducting polymers [4.15], ZrO<sub>2</sub> [4.16], LaF<sub>3</sub> [4.17-4.18], phthalocyanines [4.19], and porphyrins [4.20]. Apart from a modification of the gate material, structuring of the gate is applied successfully leading to the suspended gate field effect transistors (SGFET) device: the gate is suspended over the insulator and optionally coated with a sensitive material.

### 4.3 Principle of gas sensing via work function:

Field effect devices are mainly based on metal-insulator-semiconductor (MIS) capacitors. They act as capacitive voltage divider as depicted in the energy diagram of Fig. 4.4. In contrast to a conventional metal-insulator-metal (MIM) capacitor the



depletion capacitance  $C_D$  in the semiconductor is not negligible. However, above the threshold voltage  $V_T$ , which is defined for the onset of strong inversion of charge carriers at the insulator-semiconductor interface,  $C_D$  is almost constant [4.12]. Hence, a change of the potential drop between the Fermi level  $E_F$  of the semiconductor and the conduction band energy  $E_C$  of the metal-expressed as the sum of the applied gate voltage  $V_G$  and the internal potential  $V_{int}$  will act only across the insulator capacitance  $C_i$ . This yields a change in the free carrier concentration within the inversion layer of the semiconductor, which, in turn, can be measured easily.

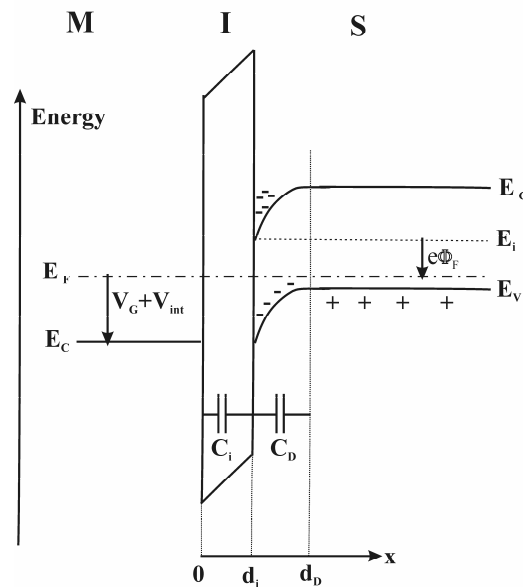


**Fig. 4.4:** Energy diagram and series capacitances of MIS device [4.21].

Strong inversion occurs when the bending of the band edges at the insulator-semiconductor interface is at the order of  $2\Phi_F$ . To achieve this condition an external threshold voltage  $V_T$  must be applied on the metal side which is expressed by [4.12]:

$$V_T = 2\Phi_F + \Phi_{MS} - \frac{1}{Cd_i} \int_0^{d_i} x\rho(x)dx + \frac{Q_D}{C} \quad (4.6)$$

where  $\Phi_F$  denotes the potential difference between the intrinsic and the Fermi level of the semiconductor,  $\Phi_{MS}$  the difference of the work functions of metal and semiconductor ( $\Phi_M - \Phi_S$ ),  $Q_D$  the change in the depletion layer of the semiconductor,  $C$  the total capacitance between metal and semiconductor,  $d_i$  the insulator thickness and  $\rho$  the insulator charge carrier concentration. For MIS structures:  $C = C_i$ .

If gas species are introduced between metal and insulator, the work function difference  $\Phi_{MS}$  changes upon chemical reactions on the surface interface, causing  $\Delta\Phi_{MS} = \Delta V_T$ , which is independent of the capacitance  $C_i$ . If a MIS transistor is fabricated, this would affect the drain current  $I_{DS}$  in the linear region of the transistor ( $V_G \ll V_{DS}$ ) according to

$$I_{DS} = \mu C_i \frac{W}{L} (V_G - V_T) V_{DS}, \quad (4.7)$$

where  $\mu$  is the electron mobility in the channel,  $C_i$  is the insulator capacitance per unit area,  $W/L$  is the channel width-to-length ratio,  $V_G$  and  $V_{DS}$  are the applied gate-source and drain-source voltages, respectively, and  $V_T$  is the threshold voltage.

#### 4.4 Device structure and fabrication:

##### 4.4.1 Devices with $\text{In}_x\text{Sn}_y\text{O}_z$ and $\text{In}_x\text{V}_y\text{O}_z$ gate:

The cross section (top) and photograph (bottom) of the sensor is shown in Fig. 4.5. The structure includes a SiC-based (FET) with  $\text{In}_x\text{Sn}_y\text{O}_z$  or  $\text{In}_x\text{V}_y\text{O}_z$  gate as a gas sensitive layer. The sensor was realized using 4H-SiC,  $n$ -type substrates, a 4  $\mu\text{m}$   $p$ -type ( $N_A = 5 \times 10^{15} \text{ cm}^{-3}$ ) epitaxial layer, and a 0.25  $\mu\text{m}$   $n$ -type ( $N_D = 1 \times 10^{17} \text{ cm}^{-3}$ ) epilayer. Inductively coupled plasma etching was used to form mesas of approximately 400 nm in height. Box profile implants were then used to form  $n^+$  regions (nitrogen implants) for the source and drain, and again to form a  $p^+$  region (Al implants) for a body contact. An annealing step was used to activate the implanted dopants at 1400°C. Next, a 50 nm  $\text{SiO}_2$  layer was realized using steam at 1100°C, followed by a 1  $\mu\text{m}$  thick high temperature oxide deposited at approximately 900°C. After patterning, another steam oxidation of 50 nm was used to form the passivation layer over the gate area. Lift-off steps were used to form ohmic contacts to the source and drain by sputtering 55 nm of Ni, and to the body contact by later sputtering 50/100/30 nm of Al/Ni/Al. In order to lower the resistance of the contacts, a rapid thermal annealing step was done at 975°C for 3 min in nitrogen.

A catalyst layer comprising equal parts of indium oxide ( $\text{InO}_x$ ) and tin oxide ( $\text{SnO}_x$ ) or  $\text{InO}_x$  and vanadium oxide ( $\text{VO}_x$ ) were then deposited by co-sputtering  $\text{InO}_x$  and  $\text{SnO}_x$  or  $\text{InO}_x$  and  $\text{VO}_x$  to form a 100 nm gate electrode. For convenience, the source and gate electrodes of these devices were shorted, and the sensitivity was determined by monitoring changes in source-drain current at various bias levels. To

prepare the catalytic films for exposure to high temperature an annealing step was used to condition the catalysts at 600°C for 10 minutes in N<sub>2</sub>. A stack of Ti/Ni/Au/Ti metalization of 50/50/400/7.5 nm was evaporated over the electrodes to form bond pads for wirebonding. Lastly a low temperature oxide was deposited over the devices at 430°C, resulting in a 60 nm SiO<sub>2</sub> layer. The sensors were then diced, and placed on TO-8 headers using ceramic-based die attach material [4.24]. The active and total areas of the sensors are 450 × 9 μm<sup>2</sup> and 1 mm<sup>2</sup>, respectively.

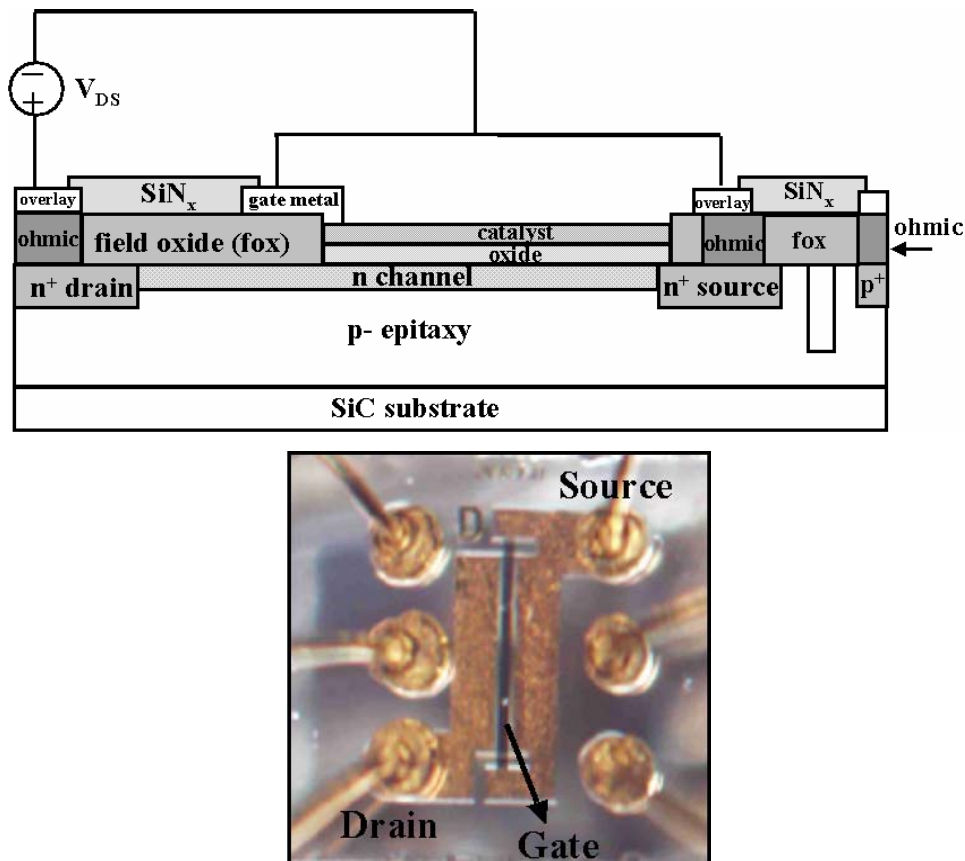


**Fig. 4.5:** Schematic cross-section (top) [4.22-4.23] and photograph (bottom) of the SiC-based FET sensor. The active and total areas are 450 × 9 μm<sup>2</sup> and 1 mm<sup>2</sup>, respectively.

#### 4.4.2 Devices with Pt-In<sub>x</sub>Sn<sub>y</sub>O<sub>z</sub> gate:

The schematic cross-section (top) and the layout (bottom) of the studied sensors are shown in Fig. 4.6. The structure includes a SiC-based (FET) with Pt-In<sub>x</sub>Sn<sub>y</sub>O<sub>z</sub> gate as a gas sensitive layer. The sensor was realized using 4H-SiC, n-type substrates, a 2.2 μm p-type (N<sub>A</sub> = 5 × 10<sup>16</sup> cm<sup>-3</sup>) epitaxial layer, and a 0.19 μm n-type (N<sub>D</sub> = 2 × 10<sup>17</sup> cm<sup>-3</sup>) epilayer.

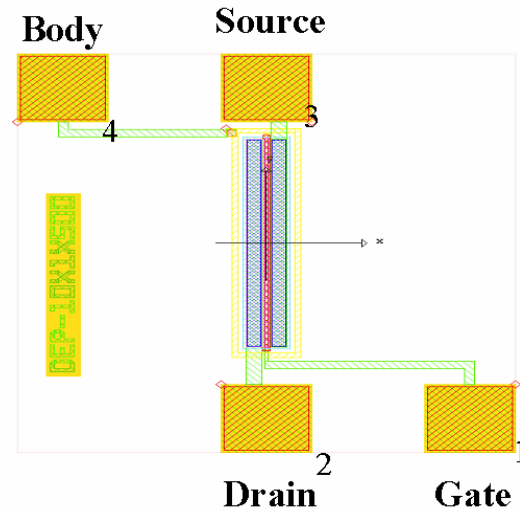
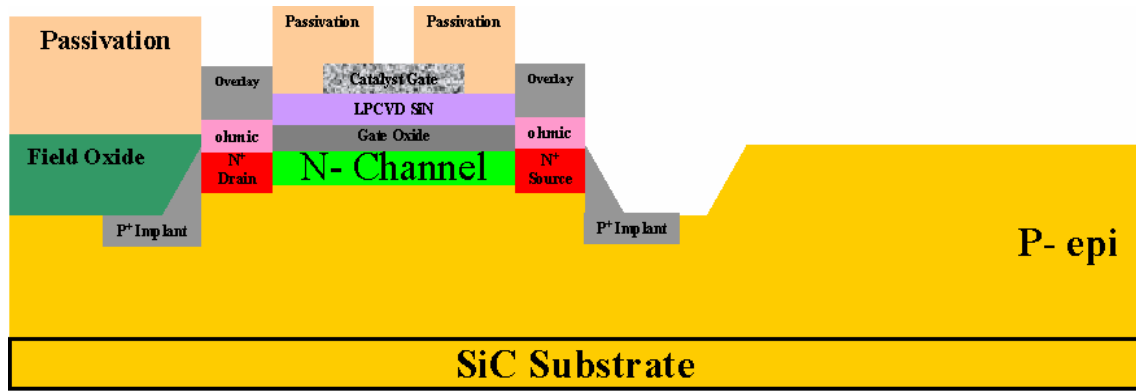


**Fig. 4.6:** Schematic cross-section (top) and the sensor layout (bottom) of the studied SiC-based FET sensor. The active area is  $4 \times 500 \mu\text{m}^2$ .

Inductively coupled plasma etching was used to form mesas of approximately 500 nm in height. Box profile implants were then used to form  $n^+$  regions (N implants) for the source and drain, and again to form a  $p^+$  region (Al implants) for a body contact. An annealing step was used to activate the implanted dopants at  $1400^\circ\text{C}$ . Next, a field oxide was realized using a high temperature ( $1100^\circ\text{C}$ ) deposition process to get a 50 nm  $\text{SiO}_2$ , followed by a 1  $\mu\text{m}$  thick high temperature oxide deposited at approximately  $900^\circ\text{C}$ , and then those were annealed.

A gate oxide was realized by deposition of 22.5 nm of  $\text{SiO}_2$  then 22.5 nm of  $\text{Si}_3\text{N}_4$ . Next, lift-off steps were used to form ohmic contacts to the source and drain by sputtering 55 nm of Ni, and to the body contact by later sputtering 50/100/30 nm of Al/Ni/Al. In order to lower the resistance of the contacts, a rapid thermal annealing step was done at  $1050^\circ\text{C}$  for 3 min in nitrogen. A catalyst layer comprising equal parts of indium oxide and tin oxide was then deposited by co-sputtering  $\text{InO}_x$  and  $\text{SnO}_x$  to form a 75 nm gate electrode, then 10 nm Pt layer was sputtered on the top

of  $\text{In}_x\text{Sn}_y\text{O}_z$  layer. To prepare the catalytic films for exposure to high temperature an annealing step was used to condition the catalysts at  $600^\circ\text{C}$  for 10 minutes in  $\text{N}_2$ . A stack of Ti/Ni/Au/Ti metalization of 50/50/1100/7.5 nm was evaporated over the electrodes to form bond pads for wirebonding. Lastly a low temperature oxide was deposited over the devices at  $430^\circ\text{C}$ , resulting in a 60 nm  $\text{SiO}_2$  layer followed by 50 nm  $\text{Si}_3\text{N}_4$ . The sensors were then diced, and placed on TO-8 headers using ceramic-based die attach material. All devices have the following dimensions:  $10\ \mu\text{m}$  = gate length,  $500\ \mu\text{m}$  = gate width, source-drain spacing =  $14\ \mu\text{m}$ . The whole device is covered with a thick passivation and there is an opening  $4 \times 500\ \mu\text{m}^2$  of the passivation above the gate.

## 4.5. Experiments:

### 4.5.1 AES measurements (surface and interface measurements):

The sensitivity of FET gas sensors is strongly influenced by the structure and the composition of the active electrode (gate electrode). Therefore, structure and composition of the  $\text{In}_x\text{Sn}_y\text{O}_z$ ,  $\text{In}_x\text{V}_y\text{O}_z$ , and  $\text{Pt-In}_x\text{Sn}_y\text{O}_z$  gates of the FET gas sensors were analyzed by Auger electron spectroscopy (AES). AES measurements have been carried out using a Thermo Microlab 350 described in Chapter 3 (section 3.5.1).

### 4.5.2 Gas sensing measurements:

For gas sensing tests, the sensors were mounted in an UHV system described in Chapter 3 (section 3.5.2). The sensors were placed directly into a quartz tube, which was pumped to a base pressure of  $4 \times 10^{-8}$  mbar. Fig. 4.7 shows schematic drawing of the UHV apparatus for this experiment and all devices mounted in it.

Current-voltage (I-V) characteristics have been carried out at different partial pressures of the test gases ( $\text{NO}_x$ ,  $\text{O}_2$ , and  $\text{D}_2$ ) above the sensors, which were heated during operation at different temperatures using a furnace. The temperature was measured by a thermocouple type K (NiCr-Ni) (see **Appendix A**) placed a few millimetres above the sensor.

We have defined the response  $R$  as the relative current variation at constant voltage expressed in percent:

$$R = \frac{I_g - I_v}{I_v} \times 100, V_{DS} = const., V_{GS} = 0 \quad (4.8)$$

and the response  $R_1$  as :

$$R_1 = \frac{I_g}{I_v}, V_{DS} = const., V_{GS} = 0 \quad (4.9)$$

where  $I_g$  and  $I_v$  are the current of the sensor in presence of gas and in vacuum, respectively.

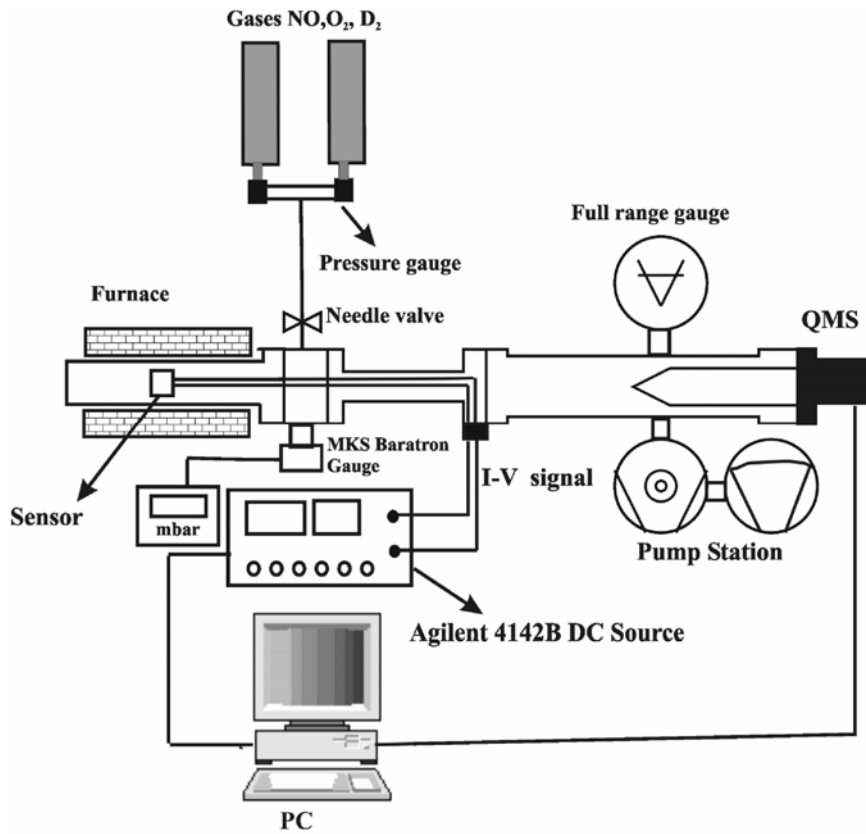


Fig. 4.7: Schematic drawing of gas measurements system.

For sensors with  $\text{Pt-In}_x\text{Sn}_y\text{O}_z$  we have other responses  $R_2$ , and  $R_3$  as:

$$R_2 = \Delta V_{th} = V_{th(v)} - V_{th(g)}, V_{DS} = const. \quad (4.10)$$

$$R_3 = \Delta V_{GS} = V_{GS(v)} - V_{GS(g)}, V_{DS} = const., I_{DS} = 1.5\text{mA} \quad (4.11)$$

where  $V_{th(g)}$  and  $V_{th(v)}$  are the threshold voltage of the sensor in presence of gas and in vacuum, respectively,  $V_{GS(g)}$  and  $V_{GS(v)}$  are the gate voltage of the sensor in presence of gas and in vacuum, respectively.

The sensitivity is given by:

$$Sensitivity = \frac{response}{C_{gas} [mbar]}, \quad (4.12)$$

## 4.6 Results and discussion:

### 4.6.1 Sensor with $In_xSn_yO_z$ gate:

#### 4.6.1.1 Chemical characterization of the gate electrode:

The  $In_xSn_yO_z$  film was analyzed by Auger electron spectroscopy. A typical Auger spectrum of the  $In_xSn_yO_z$  is shown in Fig. 4.8. The indium doublet which corresponds to MNN transitions appears at energies of 400 and 402 eV, while the oxygen peak which corresponds to KLL transitions appears at the energy of 510 eV. The tin doublet which corresponds to MNN transitions appear at energies of 426 and 432 eV. These energy values are in good agreement with those previously reported [4.25-4.28]. The C signal at 270 eV is due to contamination during the deposition process or during the transfer of the sample to the AES analyse chamber.

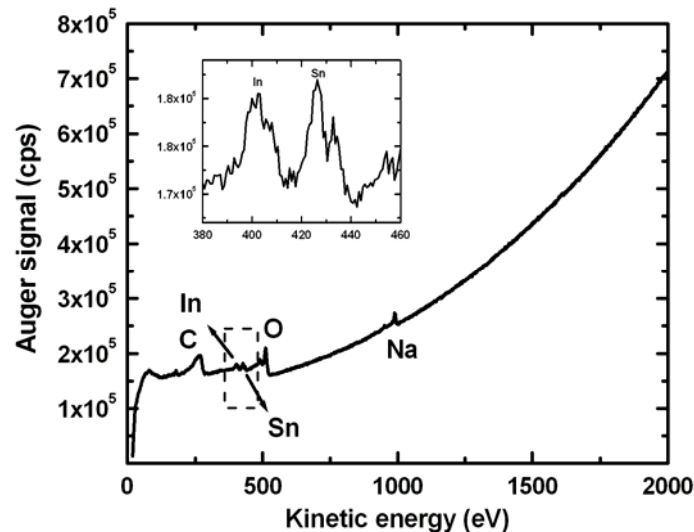


Fig. 4.8: Typical Auger spectrum of the  $In_xSn_yO_z$  gate.

Fig. 4.9 shows the Auger signal (Auger peak area) versus sputter time for the  $In_xSn_yO_z$  film. The AES depth profile revealed a strong intermixing of the both metal oxides ( $InO_x$  and  $SnO_x$ ). As seen from Fig. 4.9 the film had surface contamination, as indicated by the peak associated with sodium and carbon. The contaminants come either from the deposition process or handling of the film in air after the deposition.

A change in the oxygen peak height is a clear indication that the bonding configuration of oxygen is changing at the interface from  $\text{In}_x\text{Sn}_y\text{O}_z$  to  $\text{SiO}_x$ . In order to determine the stoichiometry of the materials  $\text{InO}_x$  and  $\text{SnO}_x$  we need to compare our AES measurements with standard samples.

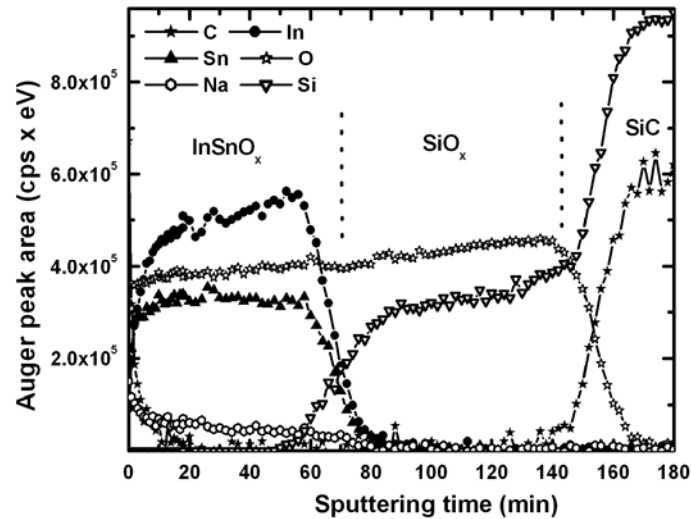


Fig. 4.9: AES depth profiles of the gate electrode.

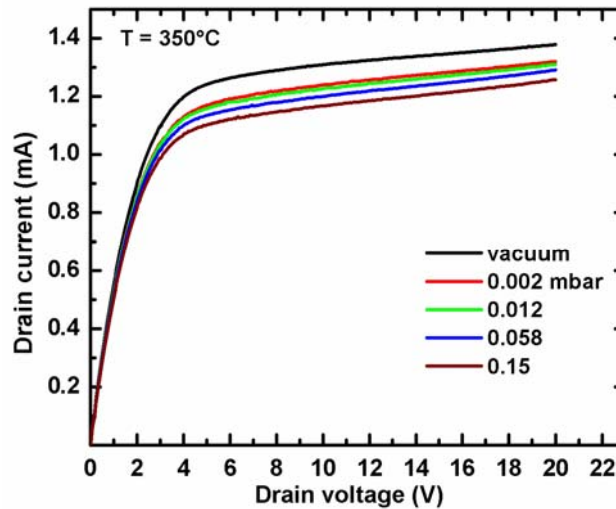
#### 4.6.1.2 NO<sub>x</sub> detection:

Fig. 4.10 shows the I-V characteristics of a SiC-based FET sensor in vacuum and in the presence of 0.002, 0.012, 0.058 and 0.15 mbar of pure NO<sub>x</sub> at 350°C. It is obvious that the exposure of the sensor to the oxidizing gas NO<sub>x</sub> results in a decrease of the source-drain current.

The response to NO<sub>x</sub> can be understood by considering the interaction between NO<sub>x</sub> and  $\text{In}_x\text{Sn}_y\text{O}_z$ . NO<sub>x</sub> molecules will affect the effective work function of the gate and thus change the current through the transistor. If NO<sub>x</sub> molecules are introduced between the catalyst and insulator, the difference of work function of the catalyst (metal oxide) and the semiconductor  $\Phi_{MS} = (\Phi_M - \Phi_S)$ , changes upon chemical reactions on the surface interface, causing a shift in the threshold voltage  $V_T$ . This would affect the source-drain current  $I_{DS}$  in the linear region of the transistor ( $V_G \ll V_{DS}$ ) according to Eq. (4.7). The increase of work function will cause a decrease in source-drain current. This is because the threshold voltage depends on the difference between the Fermi level in the semiconductor and the catalyst. As the



work function increases the threshold voltage increases and the current decreases as the  $(V_G - V_T)$  value gets lower.



**Fig. 4.10:** I-V characteristics of the sensor operated at  $350^\circ\text{C}$  in vacuum and in the presence of 0.002, 0.012, 0.058, and 0.15 of pure  $\text{NO}_x$ .

I-V characteristics in vacuum and in the presence of 0.15 mbar of pure  $\text{NO}_x$  at different temperatures are shown in Fig. 4.11. It is obvious that the operation temperature has important influence on the  $\text{NO}_x$  detection.

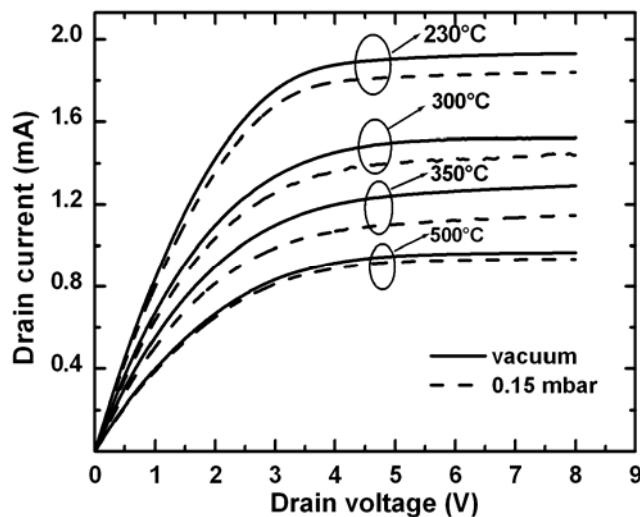


**Fig. 4.11:** I-V characteristics of the sensor in vacuum and in the presence of 0.15 mbar of pure  $\text{NO}_x$  at different operation temperatures.

The dependence of the responses  $R$  and  $R_1$  to several different partial pressures of pure  $\text{NO}_x$  on the operation temperature is presented in Fig. 4.12. The both responses increase non-linearly with increasing the partial pressure of  $\text{NO}_x$  and no complete saturation was observed even at a high partial pressure of 1 mbar. The non-linear response to increasing partial pressures of  $\text{NO}_x$  may be due to the filling of the adsorption sites on the catalytic surface, which proportionally decrease as the concentrations increase. It can be seen also from Fig. 4.12 that the responses can be enhanced by increasing the operating temperature. The maximum responses toward  $\text{NO}_x$  are observed at 350°C with this catalyst.

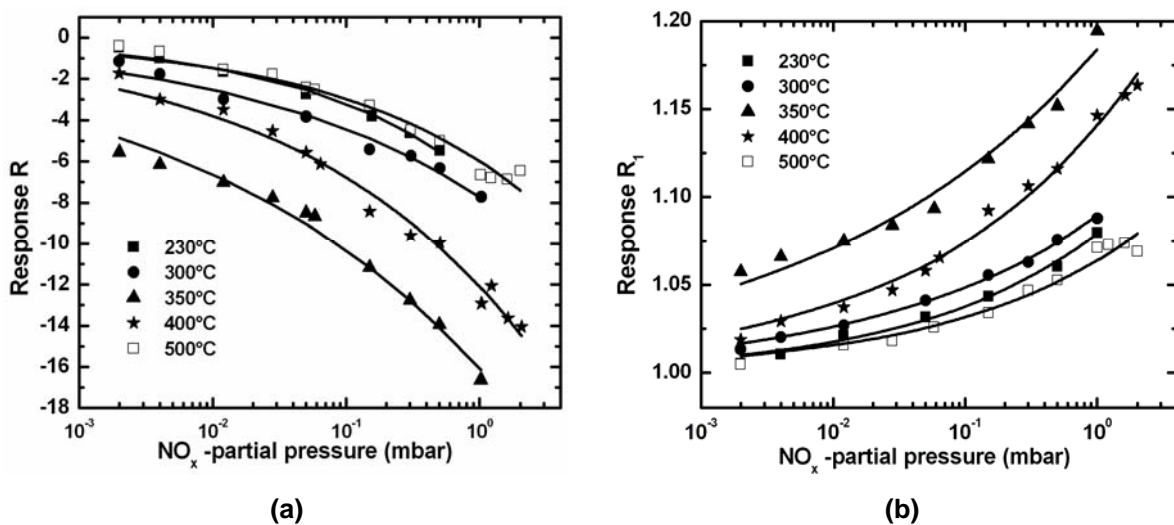


**Fig. 4.12:** Dependence of the response (a)  $R$  and (b)  $R_1$  to different partial pressures of pure  $\text{NO}_x$  on the operation temperature. The measurements were performed at a constant voltage of  $U = 8 \text{ V}$ .

This dependence of responses  $R$  and  $R_1$  on partial pressures of  $\text{NO}_x$  follows the well-known power behaviours for metal oxide semiconductor sensing films,  $R = a(P_{\text{NO}_x})^b$  [4.29] and  $R_1 = 1 + b(P_{\text{NO}_x})^c$ , where  $P_{\text{NO}_x}$  is the partial pressure,  $a$ ,  $b$ , and  $c$  are constants determined by temperature, grain size, film porosity and specifically on gas adsorption. Different fits, with this equation, were made and the values for the coefficients  $a$  and  $b$  as well as the coefficient  $R^2$  are summarized in Tab.4.1 and Tab. 4.2 for the response  $R$  and  $R_1$ , respectively. It can be seen from Fig. 4.12 that the error is noticeable in some way. We return this inaccuracy to errors in the measured values of the partial pressure.

Tab. 4.1: Fitting parameter of the response  $R$  to  $\text{NO}_x$  at several temperatures.

Temperature (°C)	Allometric1 $R = a(P_{\text{NO}_x})^b$		$R^2$
	a	b	
230	$-7.02 \pm 0.26$	$0.34 \pm 0.02$	0.990
300	$-7.74 \pm 0.27$	$0.24 \pm 0.02$	0.977
350	$-16.09 \pm 0.34$	$0.19 \pm 0.01$	0.984
400	$-12.08 \pm 0.22$	$0.25 \pm 0.01$	0.984
500	$-5.98 \pm 0.16$	$0.307 \pm 0.02$	0.969

Tab. 4.2: Fitting parameter of the response  $R_1$  curves at several temperatures.

Temperature (°C)	Allometric2 $R_1 = 1 + b(P_{\text{NO}_x})^c$		$R^2$
	b	c	
230	$0.079 \pm 0.002$	$0.332 \pm 0.02$	0.988
300	$0.089 \pm 0.001$	$0.27 \pm 0.01$	0.995
350	$0.184 \pm 0.005$	$0.207 \pm 0.01$	0.978
400	$0.140 \pm 0.002$	$0.278 \pm 0.01$	0.989
500	$0.063 \pm 0.002$	$0.309 \pm 0.02$	0.966

The dependence of the sensitivity  $S$  and  $S_1$  to several different partial pressures of pure  $\text{NO}_x$  on the operating temperature is shown in Fig. 4.13.

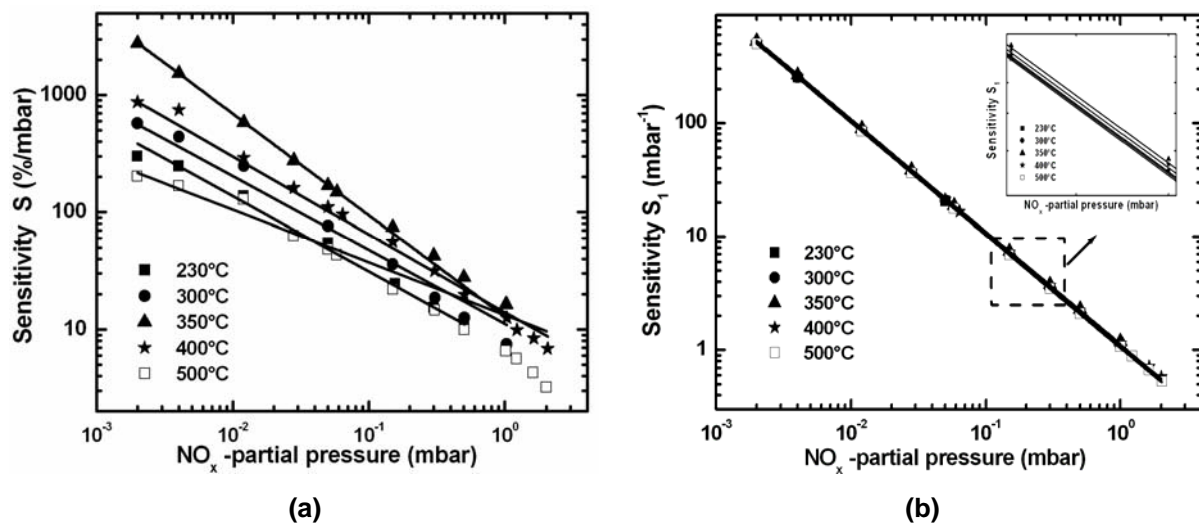


Fig. 4.13: Dependence of the sensitivity (a)  $S$  and (b)  $S_1$  to different partial pressures of pure  $\text{NO}_x$  on the operation temperature. The measurements were performed at a constant voltage of  $U = 8$  V.

It can be seen also from Fig. 4.13 that the sensitivity can be enhanced by increasing the operating temperature. In all cases the both sensitivities decrease with increasing the partial pressure of the NO<sub>x</sub> gas. This effect is likely due to a reduction in the number of adsorption sites as the gas partial pressures are increased leading to a lower sensitivity for higher NO<sub>x</sub> partial pressures. As one can see, in the range of the partial pressures investigated, the sensitivity S and S<sub>1</sub> is related to the gas partial pressure  $P_{NO_x}$  by means of the power law  $a(P_{NO_x})^b$ , where the exponent b does not depend on the gas partial pressure, and a is a constant.

Different fits, with this power expression were made for the both sensitivities S and S<sub>1</sub> and the values for the coefficient a, b, and R<sup>2</sup> are presented in Tab. 4.3 and Tab. 4.4, respectively.

**Tab. 4.3:** Fitting parameter of the sensitivity S towards NO<sub>x</sub> at several temperatures.

Temperature (°C)	Allometric1 $S = a(P_{NO_x})^b$		R <sup>2</sup>
	a	b	
230	7.14 ± 1.57	-0.64 ± 0.04	0.993
300	11.2 ± 6.14	-0.63 ± 0.09	0.967
350	12.89 ± 0.29	-0.86 ± 0.003	0.999
400	13.98 ± 6.25	-0.66 ± 0.07	0.959
500	13.28 ± 2.5	-0.45 ± 0.03	0.968

**Tab. 4.4:** Fitting parameter of the sensitivity S<sub>1</sub> curves at several temperatures.

Temperature (°C)	Allometric1 $S_1 = a(P_{NO_x})^b$		R <sup>2</sup>
	a	b	
230	1.06 ± 0.002	-0.992 ± 0.003	1
300	1.07 ± 0.003	-0.991 ± 0.0004	1
350	1.13 ± 0.004	-0.989 ± 0.0005	1
400	1.1 ± 0.005	-0.987 ± 0.0007	1
500	1.04 ± 0.001	-0.994 ± 0.0002	1

#### 4.6.1.3 O<sub>2</sub> detection:

In the second step the sensors were tested for the response to other oxidizing gases such as O<sub>2</sub> with partial pressures starting from 0.002 going up to 40 mbar at

temperatures between 230 and 500°C. Fig. 4.14 shows the I-V characteristics of the studied FET sensor in vacuum and in the presence of different partial pressures of pure O<sub>2</sub> at 450°C. It is obvious that the exposure of the sensor to the oxidizing gas O<sub>2</sub> results in a decrease of the source-drain current due to an increase in the work function of the catalytic gate and an increase in the threshold voltage of the FET.

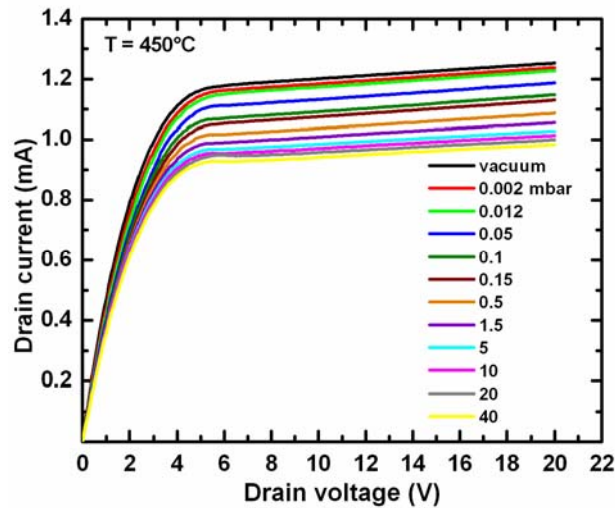


**Fig. 4.14:** I-V characteristics of the sensor operated at 450°C in vacuum and in the presence of different partial pressures of pure O<sub>2</sub>.

The dependence of the response  $R$  and  $R_1$  to different partial pressures of O<sub>2</sub> on the operating temperature is presented in Fig. 4.15.

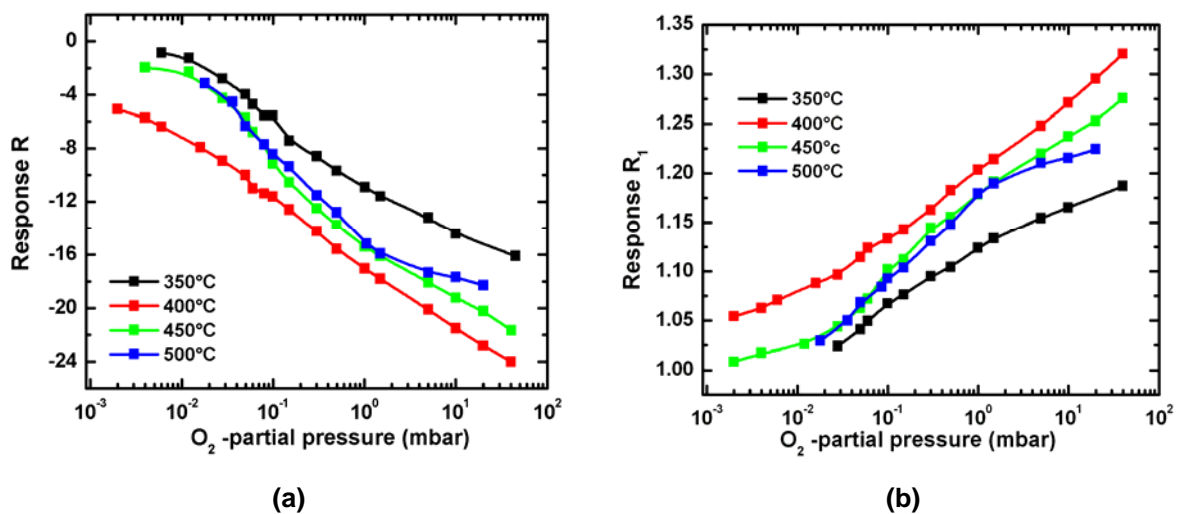


**Fig. 4.15:** Dependence of response (a)  $R$  and (b)  $R_1$  to different partial pressures of pure O<sub>2</sub> on the operation temperature. The measurements were performed at a constant voltage of  $U = 8$  V.

The response increases with increasing the partial pressure of  $O_2$ . The maximum response toward  $O_2$  is observed at  $400^\circ\text{C}$  with this catalyst. In addition, at this temperature, the responses  $R$  and  $R_1$  are found to be nearly linear with  $\log(P_{O_2})$ . In the range of the investigated partial pressures, the sensitivity  $S$  and  $S_1$  at  $400^\circ\text{C}$  was found to be related to the  $O_2$  partial pressure  $P_{O_2}$  by means of the power law  $a(P_{O_2})^b$  (Fig. 4.16), where the exponent  $b$  does not depend on the gas partial pressure, and  $a$  is a constant.

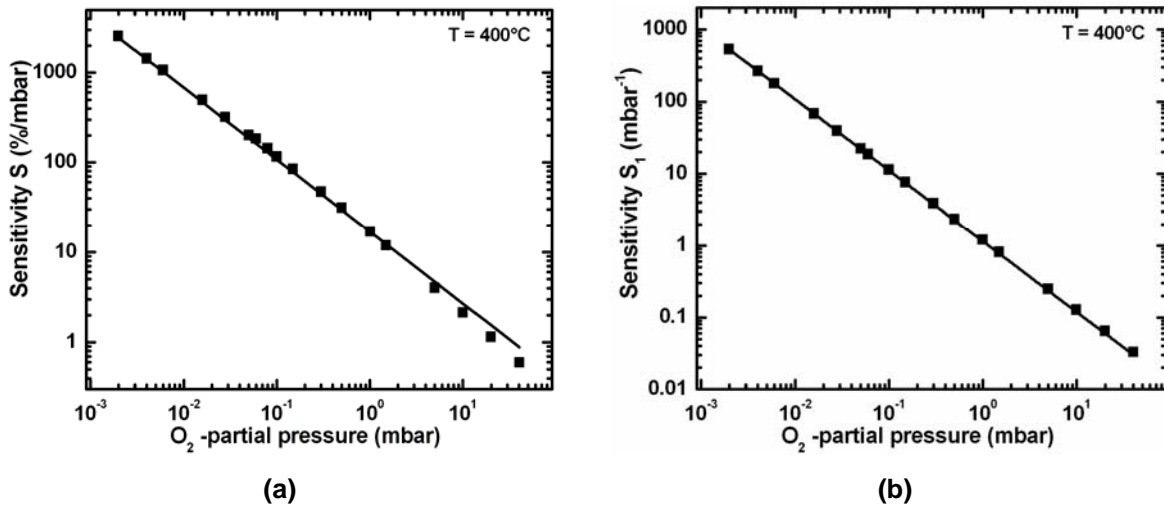


**Fig. 4.16:** Dependence of sensitivity (a)  $S$  and (b)  $S_1$  on the  $O_2$  partial pressures at operating temperature of  $400^\circ\text{C}$ . The measurements were performed at a constant voltage of  $U = 8\text{ V}$ .

Fitting, with this power expression was made for the both sensitivities  $S$  and  $S_1$  at  $400^\circ\text{C}$  and the values for the coefficient  $a$ ,  $b$ , and  $R^2$  are summarized in Tab. 4.5.

**Tab. 4.5:** Fitting parameter of the sensitivity  $S$  and  $S_1$  curve at  $400^\circ\text{C}$ .

Sensitivity	Allometric1 $S = a(P_{O_2})^b$		$R^2$
	a	b	
<b>S</b>	$17.01 \pm 1.44$	$-0.80 \pm 0.014$	0.998
<b><math>S_1</math></b>	$1.15 \pm 0.004$	$-0.98 \pm 0.0006$	1

#### 4.6.1.4 Conclusion:

The dependence of the responses  $R$  and  $R_1$  towards 0.15, 0.5 and 1 mbar of pure  $NO_x$  and  $O_2$ , on the operating temperature is presented in Fig.4.17 and Fig. 4.18,

respectively. It becomes obvious from Fig. 4.17 and Fig. 4.18 that the optimum detection temperatures occur in the range of 325-370°C for  $\text{NO}_x$ . In this range the cross response to  $\text{O}_2$  is low indicating that the sensor is suitable for selective detection of  $\text{NO}_x$ . The optimum temperature of operation for detection of  $\text{O}_2$  is determined to be between 400-500°C. In this range no significant response  $\text{NO}_x$  is observed indicating that the sensor is very suitable for selective  $\text{O}_2$  detection at very high temperatures.

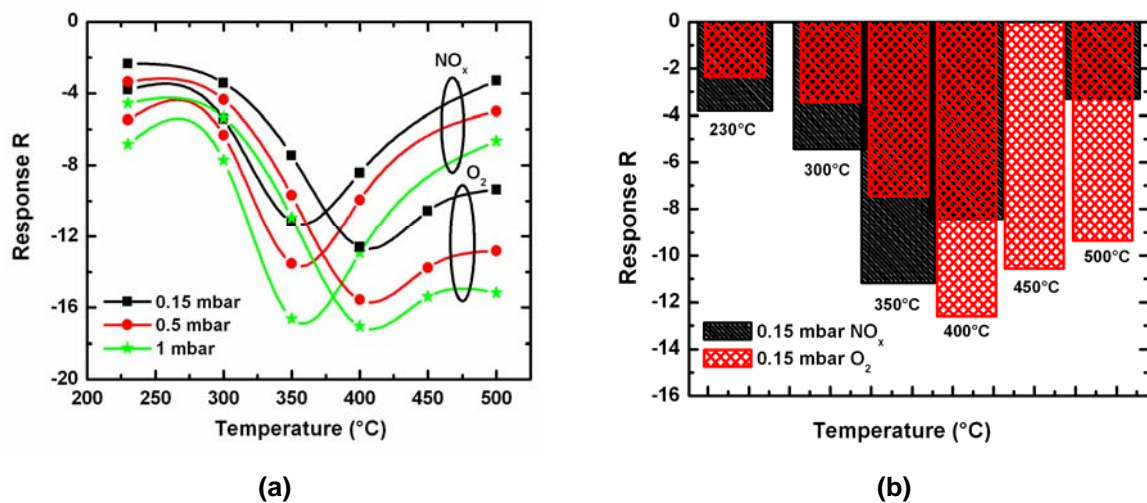


**Fig. 4.17:** (a) The dependence of the response R to 0.15, 0.5 and 1 mbar of  $\text{NO}_x$  and  $\text{O}_2$ , on the operating temperature. The measurements were performed at a constant voltage of 8 V. (b) Block presentations for 0.15 mbar of the both gases.

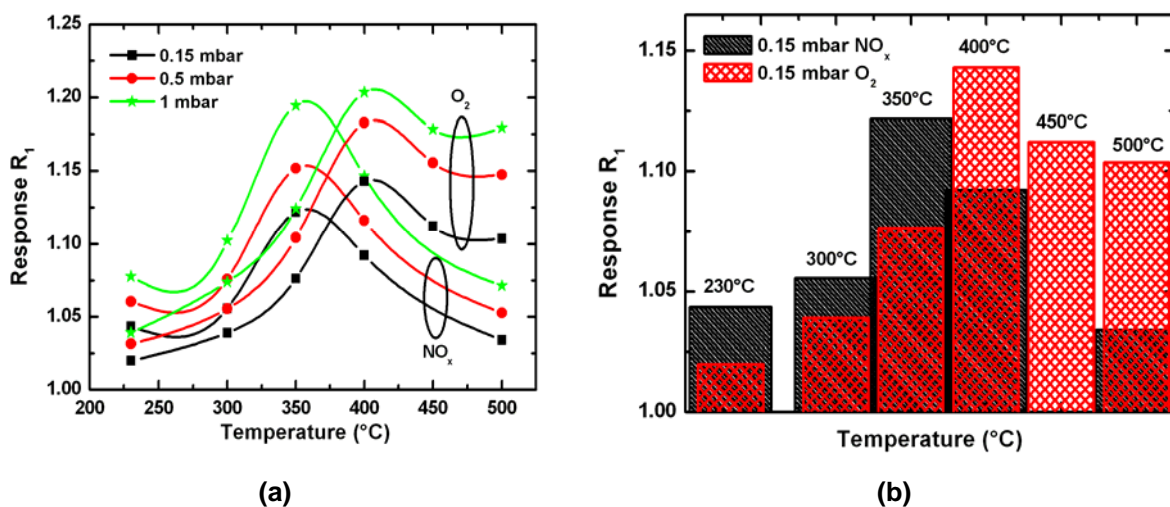


**Fig. 4.18:** (a) The dependence of the response  $R_1$  to 0.15, 0.5 and 1 mbar of  $\text{NO}_x$  and  $\text{O}_2$ , on the operating temperature. The measurements were performed at a constant voltage of 8 V. (b) Block presentations for 0.15 mbar of the both gases.

## 4.6.2 Sensor with $\text{In}_x\text{V}_y\text{O}_z$ gate:

### 4.6.2.1 Chemical characterization of the gate electrode:

The Auger spectrum of the  $\text{In}_x\text{V}_y\text{O}_z$  is shown in Fig. 4.19. The indium peaks which correspond to MNN transitions appear at energies of 402 and 452 eV, while the oxygen peak which corresponds to KLL transitions appears at the energy of 506 eV. The vanadium peaks which correspond to LMM transitions are at 464 and 485 eV.

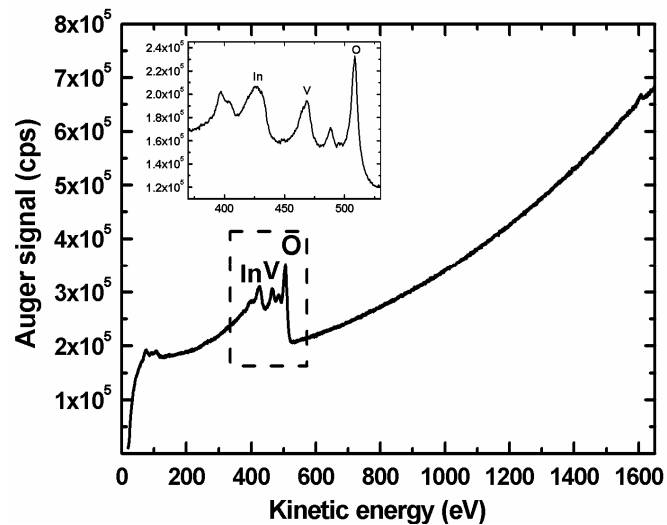


Fig. 4.19: Typical Auger spectrum of the  $\text{In}_x\text{V}_y\text{O}_z$  gate.

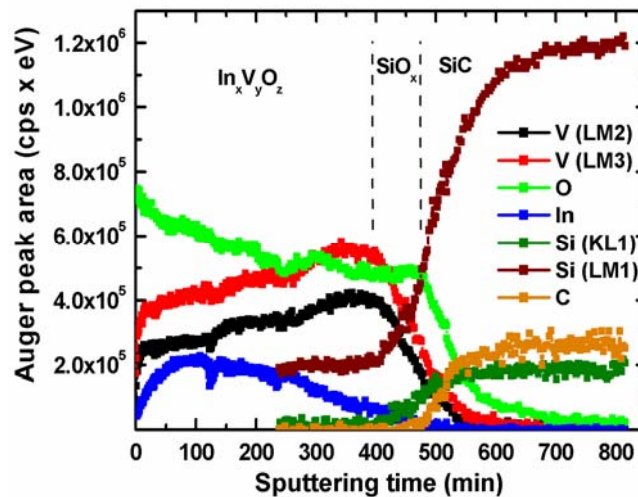


Fig. 4.20: Auger depth profiles of the gate electrode.



The AES depth profile in Fig. 4.20 shows a strong intermixing of the both metal oxides ( $\text{InO}_x$  and  $\text{VO}_x$ ). It is obvious from Fig 4.20 that the sample structure includes  $\text{In}_x\text{V}_y\text{O}_z$ ,  $\text{SiO}_x$ , and  $\text{SiC}$  layers. In addition, no contaminations were observed in the sample.

#### 4.6.2.2 $\text{NO}_x$ detection:

Firstly, the sensors were tested for the response to  $\text{NO}_x$  gas with partial pressures starting from 0.002 and going up to 2.010 mbar (pure  $\text{NO}_x$ ) in vacuum at temperatures between 230 and 400°C. Fig. 4.21 provides the I-V characteristics of the studied  $\text{SiC}$ -based FET sensor in vacuum and in the presence of different partial pressures of pure  $\text{NO}_x$  at 300°C.

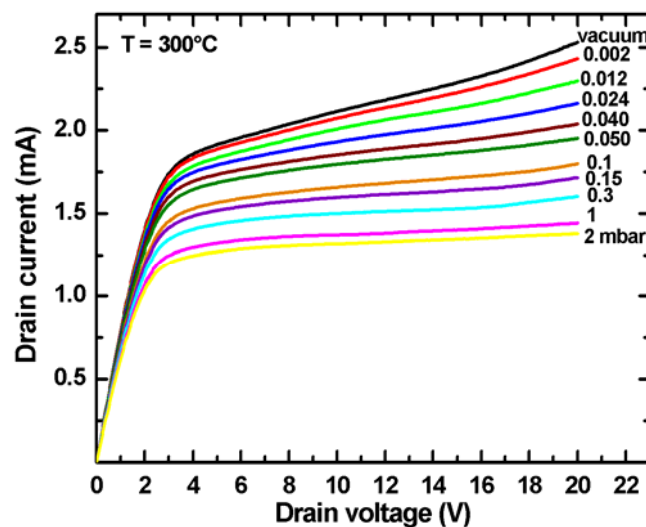


**Fig. 4.21:** I-V characteristics of the sensor operated at 300°C in vacuum and in the presence of different partial pressures of pure  $\text{NO}_x$ .

As shown in Fig 4.21, the exposure of the sensor to  $\text{NO}_x$  causes a decrease of the source-drain current due to an increase in work function of the catalytic gate and as a consequence an increase in the threshold voltage of the FET.

The response of  $\text{In}_x\text{V}_y\text{O}_z$  to 0.01 mbar of  $\text{NO}_x$  at various operation temperatures is shown in Fig. 4.22. The applied source-drain voltage is fixed at 14 V. At low operation temperatures, the sensor responds fairly fast to the test gas and shows even faster response at higher operation temperatures.

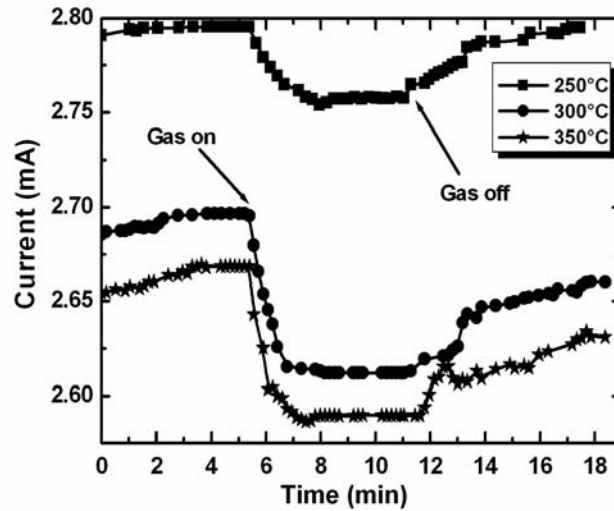


**Fig. 4.22:** Response curves towards 0.01 mbar of  $\text{NO}_x$  at various temperatures. The source-drain voltage is kept constant at 14 V.

As the operation temperature increases from 250 to 350°C, the response time decreases from 108 s to 61 s (Fig. 4.23).

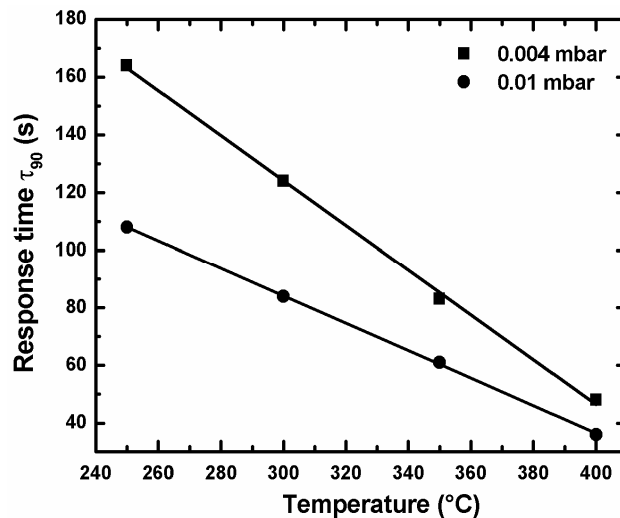


**Fig. 4.23:** The response time as a function of temperature for 0.004 and 0.01 mbar of  $\text{NO}_x$ .

In this chapter we have defined the response time  $\tau_{90}$  as the time in which the output current reaches 90% of its final value. It becomes obvious from Fig. 4.23 that the response time to both low and high  $\text{NO}_x$  partial pressures can be reduced by increasing the operating temperature. For partial pressures of 0.004 and 0.01 mbar the response time is decreasing from 164 to 48 s and from 108 to 36 s, respectively, by increasing the temperature of operation from room temperature to 400°C. Taking

into account the sensitivity and the response time, the experimental results indicate that the optimal operating temperature of the sensor for  $\text{NO}_x$  is  $300^\circ\text{C}$ .

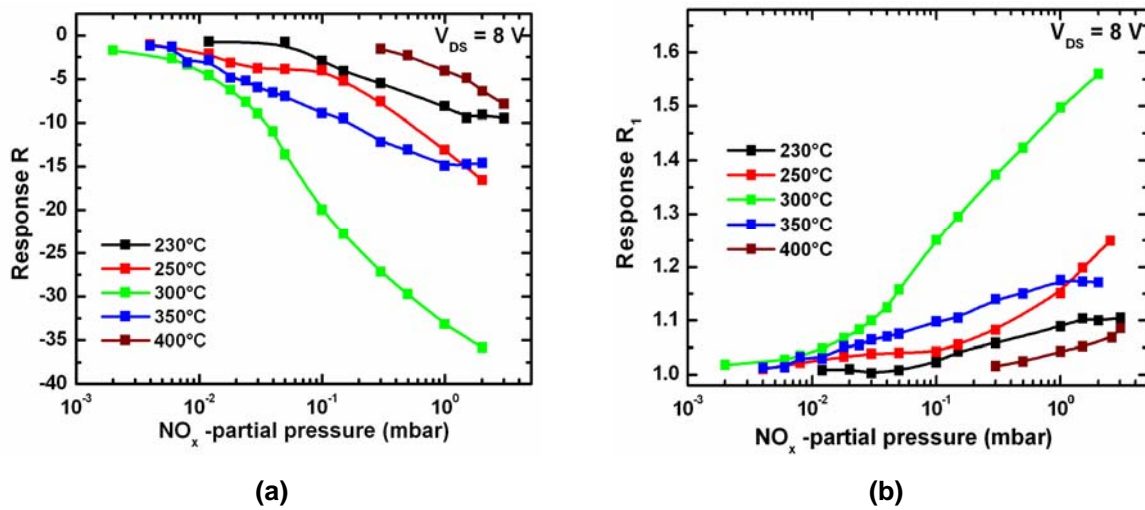


**Fig. 4.24:** The response  $R$  (a), and  $R_1$  (b) versus  $\text{NO}_x$  partial pressure of the sensor with  $\text{In}_x\text{V}_y\text{O}_z$  gate at different temperatures.

The dependence of the response  $R$  and  $R_1$  on the partial pressures of  $\text{NO}_x$  (calibration curves) on the operating temperature is shown in Fig.4.24. As one can see, both responses increase non-linearly with increasing the partial pressure of  $\text{NO}_x$  and no complete saturation was observed even at a high partial pressure of 2 mbar. The non-linear response to increasing partial pressures of  $\text{NO}_x$  may be due to the filling of the adsorption sites on the catalytic surface, which proportionally decrease as the concentrations increase.

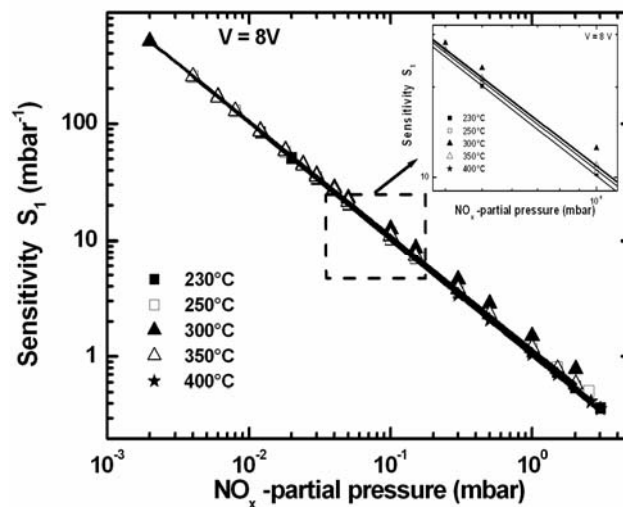


**Fig. 4.25:** The dependence of the sensitivity  $S_1$  on the partial pressure of  $\text{NO}_x$  at different operating temperatures.

Fig. 4.25 presents the dependence of the sensitivity  $S_1$  defined as  $S_1 = R_1 / P_{NO_x}$ , on the partial pressure of  $NO_x$  at different operating temperatures. We have found that the sensitivity  $S_1$  decreases linearly with increasing partial pressure. This dependence of  $S_1$  on partial pressures of  $NO_x$  was fitted with the power law  $a(P_{NO_x})^b$  and the values for the coefficients  $a$  and  $b$  as well as the coefficient  $R^2$  are summarized in Tab. 4.6.

**Tab. 4.6:** Fitting parameter of the sensitivity  $S_1$  towards  $NO_x$  at several temperatures.

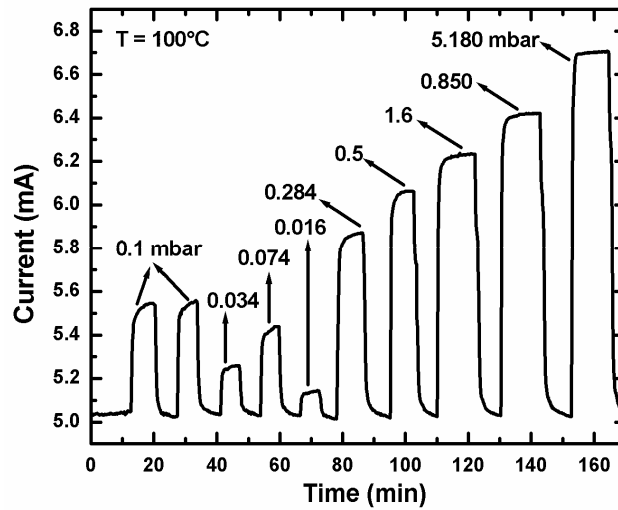
Temperature (°C)	Allometric1 $S_1 = a(P_{NO_x})^b$		$R^2$
	a	b	
230	$1.017 \pm 0.011$	$-0.997 \pm 0.002$	0.999
250	$1.093 \pm 0.004$	$-0.985 \pm 0.0007$	1
300	$1.142 \pm 0.021$	$-0.971 \pm 0.003$	0.999
350	$1.145 \pm 0.013$	$-0.977 \pm 0.002$	0.999
400	$1.042 \pm 0.002$	$-0.977 \pm 0.002$	0.999

The slope of the lines in the log-log plot (Fig. 4.25) are different and dependent on the operation temperature. A higher value of the exponent  $b$  allows an easier distinction between two partial pressures, while a lower value rises the lowest partial pressure which can be measured. If we are interested in the determination of high partial pressures, we can operate the sensor at 230°C, since the slope is higher. Otherwise, if we are interested in lower partial pressures, we should work at 300°C because at this temperature the detection limit is lower.

#### 4.6.2.3 Deuterium detection:

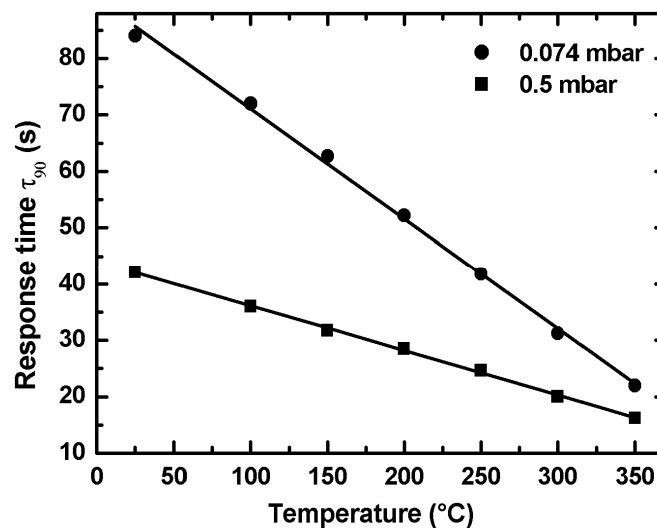
In the second step the sensors were tested for the response to deuterium with partial pressures between 0.012 and 5.180 mbar at temperatures between 25 and 350°C. When the sensor is exposed to  $D_2$ , the change of current with time is measured at a constant source-drain voltage of 14 V. Fig. 4.26 illustrates the plot of transient currents versus time upon introduction and removal of 0.1, 0.034, 0.074, 0.016, 0.284, 0.5, 0.85, 1.6, and 5.180 mbar  $D_2$  at a temperature of 100°C. The current increases when  $D_2$  is introduced into the quartz tube due to a decrease in the work function of the catalytic gate and a decrease in the threshold voltage of the FET. As

can be seen from Fig. 4.26, the source-drain current increases with increasing  $D_2$  concentration.



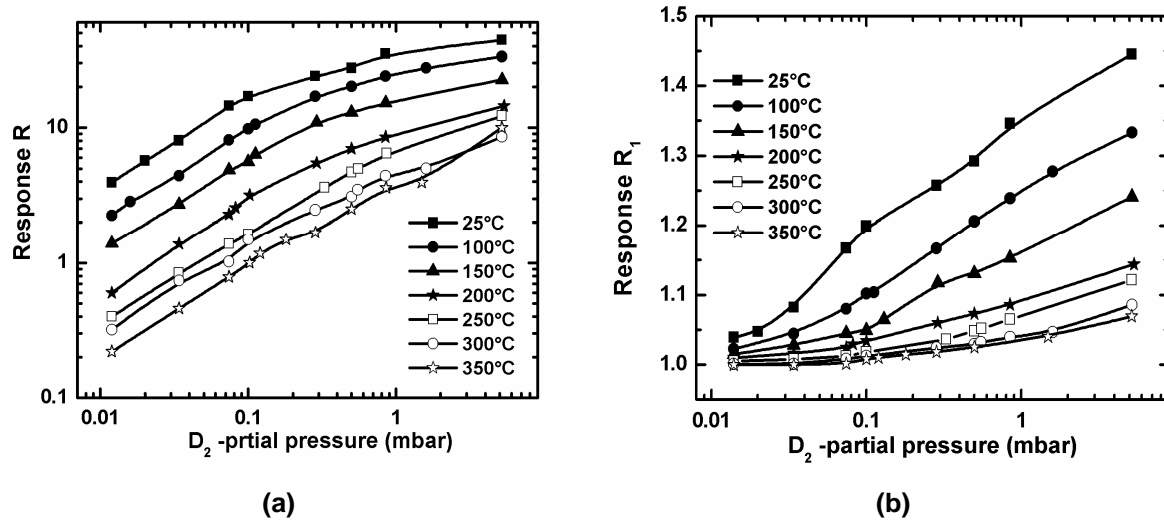
**Fig. 4.26:** Source-drain current versus time upon introduction and removal of  $D_2$  with different partial pressures and at a temperature of  $100^\circ\text{C}$ . The applied source-drain voltage is fixed at 14 V.

Fig. 4.27 reveals the response time as a function of temperature for two different partial pressures of  $D_2$ . It becomes obvious from Fig. 4.27 that the response time to both low and high  $D_2$  partial pressures can be reduced by increasing the operating temperature. For  $D_2$  partial pressures of 0.074 and 0.5 mbar the response time is decreasing linearly from 80 to 30 s and from 40 to 20 s, respectively, by increasing the temperature of operation from room temperature to  $350^\circ\text{C}$ .



**Fig. 4.27:** The response time as a function of temperature for 0.074 and 0.5 mbar of  $D_2$ .

The response  $R$  and  $R_1$  to  $D_2$  was investigated in dependence on the operating temperature for different partial pressures of  $D_2$ . We observed a significant increase of the both responses by increasing the temperature of operation and by increasing the gas partial pressure and no complete saturation was observed even at a high partial pressure of up to 5 mbar (Fig. 4.28). The maximum responses to  $D_2$  are observed at room temperature.



**Fig. 4.28:** The dependence of response  $R$  (a) and  $R_1$  (b) to different partial pressure of  $D_2$  on the operation temperature. The measurements were performed at a constant voltage of  $U = 14$  V.

Taking into account the value of response and the response time, the experimental results indicate that the optimum detection temperatures occur in the range of 25-100°C for  $D_2$ . The dependence of the sensitivity  $S$  and  $S_1$  to several different partial pressures of pure  $D_2$  on the operating temperature is presented in Fig. 4.29. It becomes obvious from Fig. 4.29 that the sensitivity can be enhanced by increasing the operating temperature. In all cases the both sensitivities decrease with increasing the partial pressure of the  $D_2$  gas. This effect is likely due to a reduction in the number of adsorption sites as the gas partial pressures are increased leading to a lower sensitivity for higher  $D_2$  partial pressures.

As shown in Fig 4.29b, the sensitivity  $S_1$  is related to the gas partial pressure  $P_{D_2}$  by means of the power law  $a(P_{D_2})^b$ , where the exponent  $b$  does not depend on the gas partial pressure, and  $a$  is a constant. Different fits, with this power expression were made for the sensitivity  $S_1$  and the values for the coefficient  $a$ ,  $b$ , and  $R^2$  are summarized in Tab. 4.7.

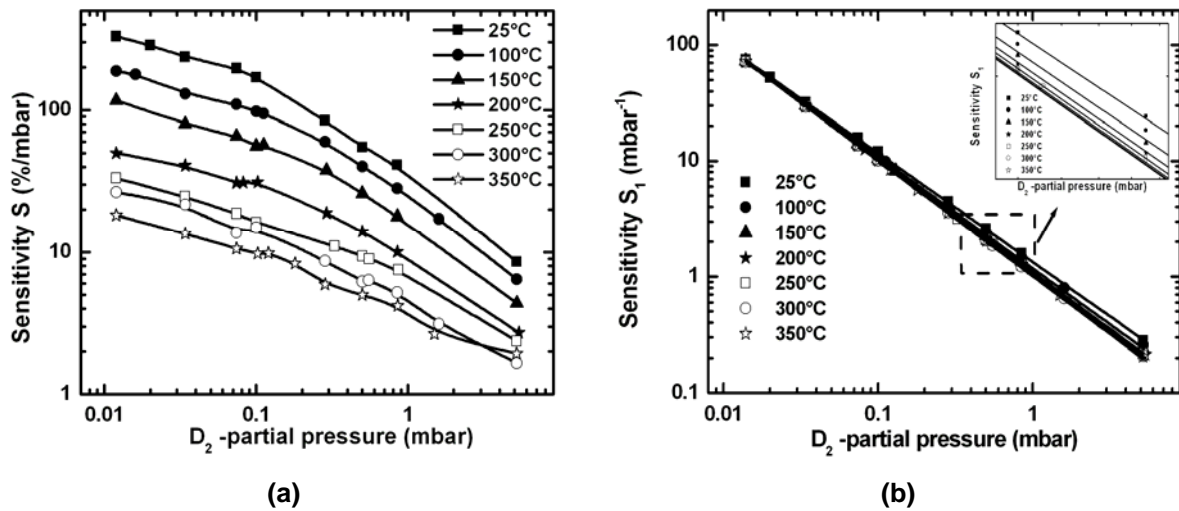


**Fig. 4.29:** The sensitivity  $S$  (a) and  $S_1$  (b) versus  $D_2$  partial pressure at different temperatures. The measurements were performed at a constant voltage of  $U = 14$  V.

**Tab. 4.7:** Fitting parameter of the sensitivity  $S_1$  to  $D_2$  at several temperatures.

Temperature (°C)	Allometric1 $S_1 = a(P_{D_2})^b$		$R^2$
	a	b	
25	$1.338 \pm 0.037$	$-0.94 \pm 0.007$	0.999
100	$1.179 \pm 0.126$	$-0.966 \pm 0.002$	0.999
150	$1.098 \pm 0.009$	$-0.98 \pm 0.002$	0.999
200	$1.053 \pm 0.005$	$-0.99 \pm 0.001$	1
250	$1.028 \pm 0.004$	$-0.994 \pm 0.001$	1
300	$1.016 \pm 0.004$	$-0.996 \pm 0.001$	1
350	$1.012 \pm 0.003$	$-0.997 \pm 0.001$	1

#### 4.6.2.4 O<sub>2</sub> detection:

Lastly, the sensors were tested for the response to other oxidizing gases such as O<sub>2</sub> with partial pressures starting from 0.002 going up to 3 mbar at temperatures between 250 and 400°C. The influence of temperature on the responses  $R$  and  $R_1$  to different partial pressures of O<sub>2</sub> is provided in Fig. 4.30. The both responses increase non-linearly with increasing the partial pressure of O<sub>2</sub> and no complete saturation was observed even at a high partial pressure of 3 mbar.

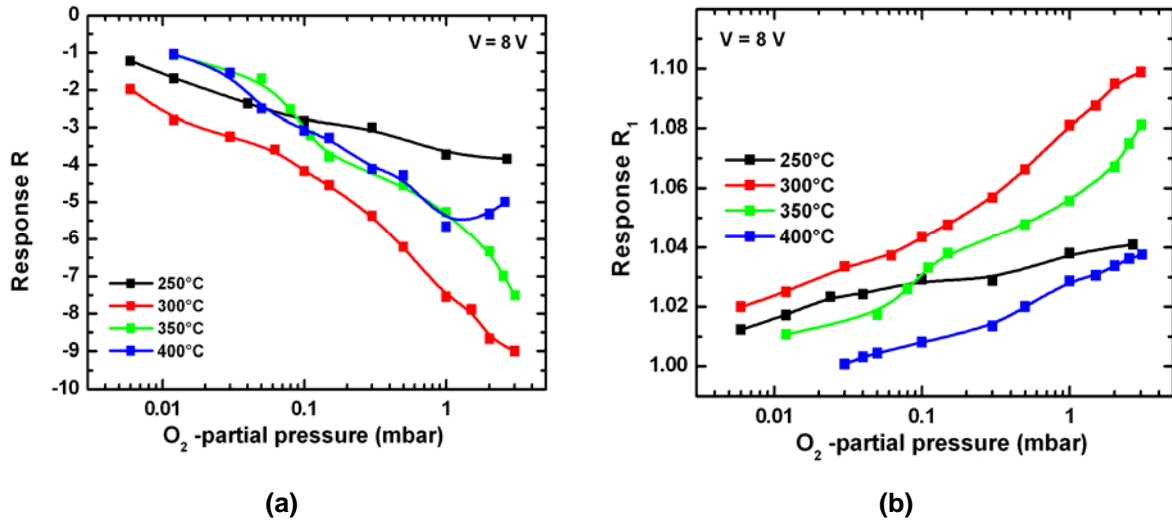


**Fig. 4.30:** The dependence of the response R (a) and  $R_1$  (b) on the  $O_2$  partial pressure of the sensor with  $In_xV_yO_z$  gate at different temperatures.

It can be seen from Fig. 4.30 that the responses can be enhanced by increasing the operating temperature. The maximum responses toward  $O_2$  are observed at 300°C for this sensor. At this temperature, fitting with the power expression  $a(P_{O_2})^b$  was made for the both sensitivities S and  $S_1$  (Fig. 4.31) and the values for the coefficient a, b, and  $R^2$  are summarized in Tab. 4.8.

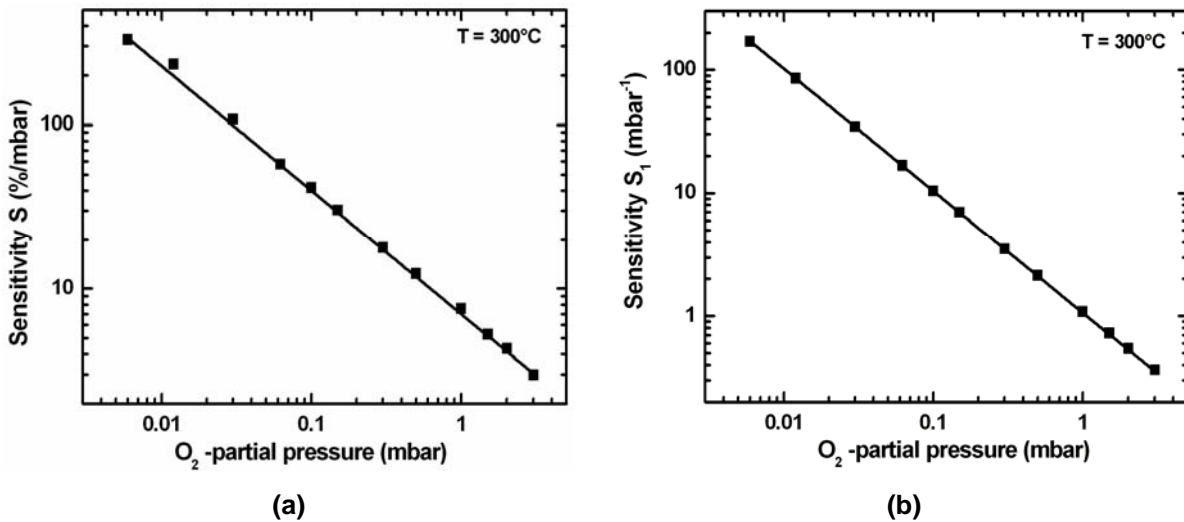


**Fig. 4.31:** Dependence of sensitivity (a) S and (b)  $S_1$  on the  $O_2$  partial pressures at operating temperature of 300°C. The measurements were performed at a constant voltage of  $U = 8\text{ V}$ .



**Tab. 4.8:** Fitting parameter of the sensitivity  $S$  and  $S_1$  towards  $O_2$  at  $300^\circ\text{C}$ .

Sensitivity	Allometric1 $a(P_{O_2})^b$		$R^2$
	a	b	
$S$	$7.006 \pm 1.442$	$-0.756 \pm 0.042$	0.989
$S_1$	$1.061 \pm 0.001$	$-0.992 \pm 0.0002$	1

#### 4.6.2.5 Conclusion:

The dependence of the responses  $R$  and  $R_1$  to 0.1, 0.5 and 1 mbar of pure  $\text{NO}_x$ ,  $\text{O}_2$ , and  $\text{D}_2$  on the operating temperature is presented in Fig. 4.32 and Fig. 4.33, respectively.

As one can see, the optimum detection temperatures occur in the range of  $275\text{--}325^\circ\text{C}$  for  $\text{NO}_x$ . In this range the cross sensitivity to  $\text{O}_2$  and  $\text{D}_2$  is very low indicating that the sensor is very suitable for selective detection of  $\text{NO}_x$ . The optimum temperature of operation for detection of deuterium is determined to be between  $25\text{--}100^\circ\text{C}$ . In this range no significant response to  $\text{O}_2$  and  $\text{NO}_x$  is observed indicating that the sensor is very suitable for selective  $\text{D}_2$  detection at very low temperatures.

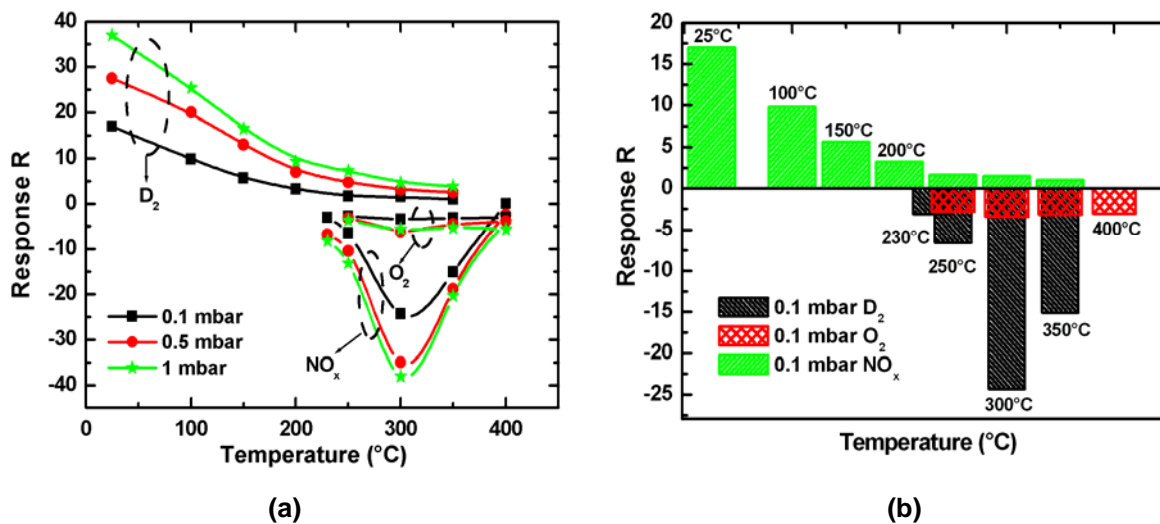


**Fig. 4.32:** (a) The dependence of the response  $R$  to 0.1, 0.5 and 1 mbar of  $\text{NO}_x$ ,  $\text{O}_2$ , and  $\text{D}_2$ , on the operating temperature. The measurements were performed at a constant voltage of 8 V. (b) Block presentations for 0.1 mbar of the all three gases.

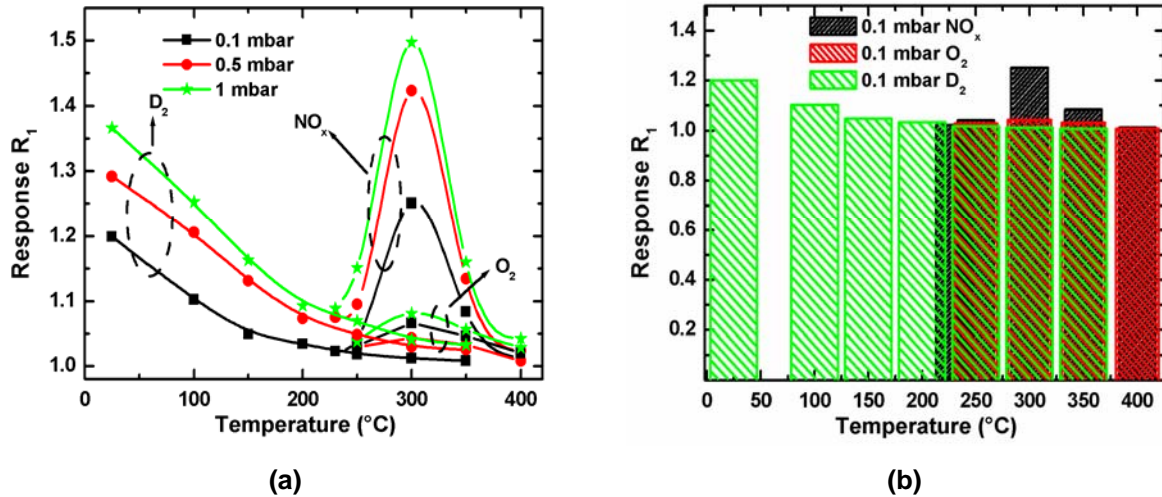


**Fig. 4.33:** (a) The dependence of the response  $R_1$  to 0.1, 0.5 and 1 mbar of  $NO_x$ ,  $O_2$ , and  $D_2$  on the operating temperature. The measurements were performed at a constant voltage of 8 V. (b) Block presentations for 0.1 mbar of the all three gases.

#### 4.6.3 Sensor with $Pt-In_xSn_yO_z$ gate (EN17):

##### 4.6.3.1 SEM and AES of the sample:

As shown in the AES spectra of Fig. 4.34, the only impurity detected from the sample surface is carbon (C) (at 270 eV), which undergoes significant reduction and becomes negligible after a short sputtering (40 s) process. This implies that the origin of the surface carbon is from the adsorption in ambient air. The indium, tin, oxygen, Pt peaks appear at energies of 402, 432, 514, and 2043 eV, respectively.

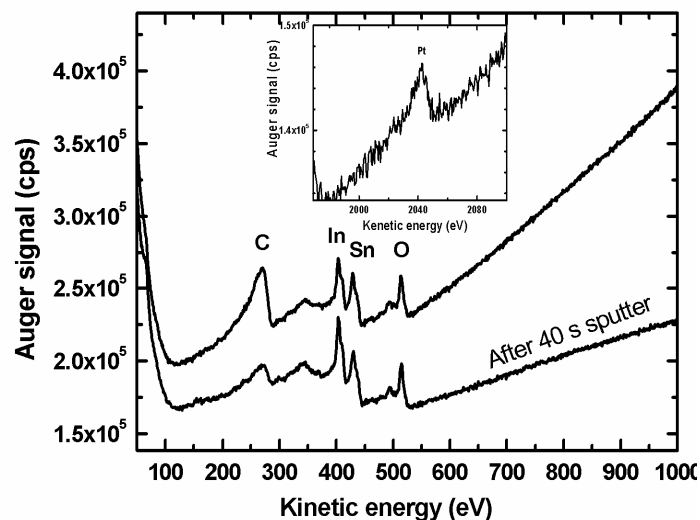


**Fig. 4.34:** Typical Auger spectrum of the  $Pt-In_xSn_yO_z$  gate.

Fig. 4.35 shows AES depth profile made on the area of the gate shown in the SEM image (Fig. 4.35b). It becomes obvious from Fig 4.35a that the sample structure includes Pt-In<sub>x</sub>Sn<sub>y</sub>O<sub>z</sub>, SiN, SiO<sub>x</sub>, and SiC layers.

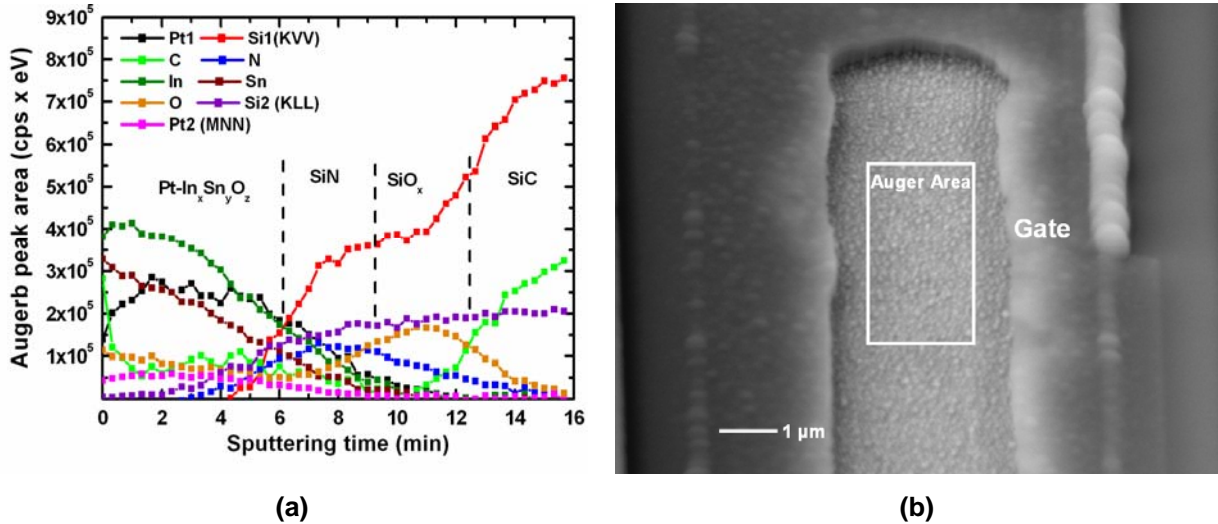


Fig. 4.35: (a) AES depth profiles of the gate area of the sensor (EN17). (b) SEM image of the gate.

#### 4.6.3.2 NO<sub>x</sub> detection:

The typical drain current vs. drain voltage ( $I_D$ - $V_D$ ) characteristics of the FET with Pt-In<sub>x</sub>Sn<sub>y</sub>O<sub>z</sub> gate under different partial pressures of NO<sub>x</sub> gas at 150, 200°C are shown in Fig. 4.36a, and b, respectively.

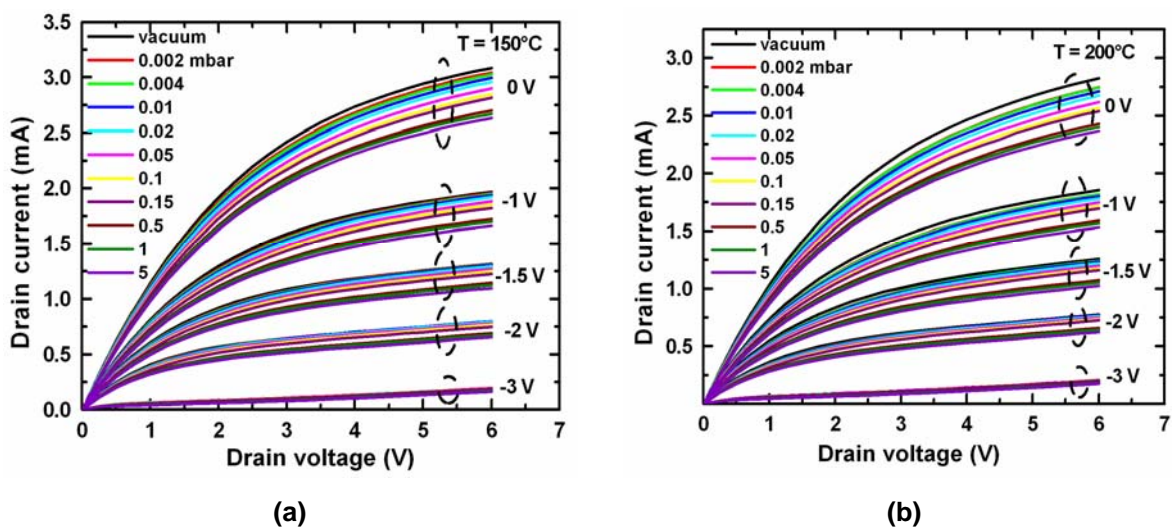
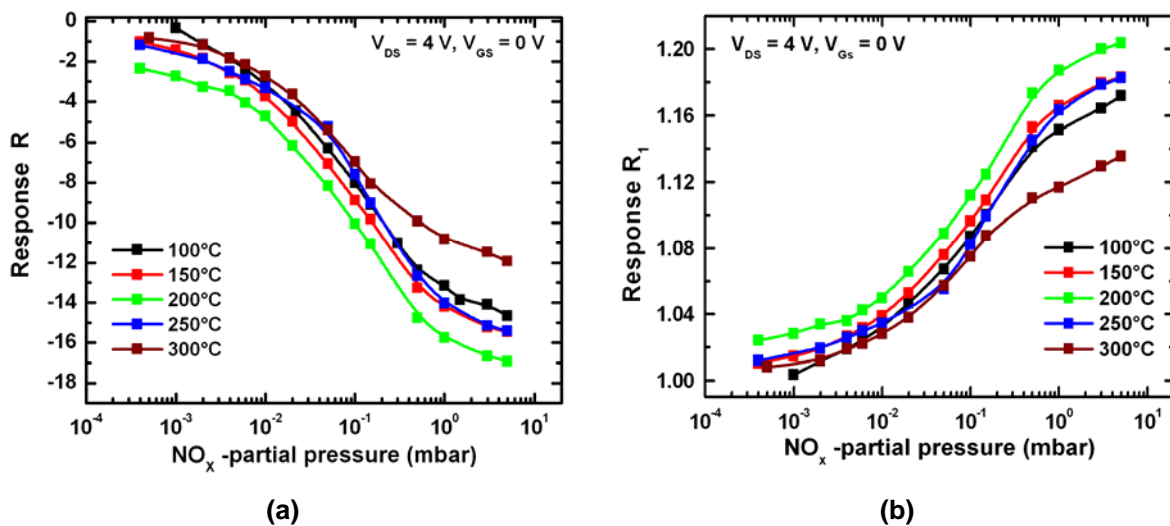


Fig. 4.36: Typical  $I_D$ - $V_D$  characteristics of the studied FET sensor under different partial pressures of NO<sub>x</sub> gas at (a) 150 and (b) 200°C.

Apparently, the studied sensor exhibits substantial current variation at  $\text{NO}_x$  ambience. As seen in Fig. 4.36, even at an extremely low  $\text{NO}_x$  partial pressure of 0.002 mbar, the current modulation can be found significantly. Under vacuum and different  $\text{NO}_x$  partial pressures of 0.002, 0.02, and 5 mbar at  $150^\circ\text{C}$  ( $200^\circ\text{C}$ ), the corresponding measured drain saturation currents are 2.73 (2.46), 2.68 (2.38), 2.59 (2.31), and 2.31 (2.04) mA, respectively, at  $V_{\text{DS}} = 4\text{ V}$  and  $V_{\text{GS}} = 0\text{ V}$ .

The response  $R$  and  $R_1$  to  $\text{NO}_x$  was investigated in dependence on the operating temperature for different partial pressures of  $\text{NO}_x$ . We observed a significant increase of the both responses by increasing the temperature of operation and the gas partial pressure and no complete saturation was observed even at a high partial pressure of up to 5 mbar (Fig. 4.37). The maximum responses to  $\text{NO}_x$  were observed at  $200^\circ\text{C}$ .



**Fig. 4.37:** The dependence of the response  $R$  (a) and  $R_1$  (b) on  $\text{NO}_x$  partial pressures at different temperatures. The applied biases are fixed at  $V_{\text{GS}} = 0\text{ V}$  and  $V_{\text{DS}} = 4\text{ V}$ .

The dependence of the sensitivity  $S$  and  $S_1$  to several different partial pressures of pure  $\text{NO}_x$  on the operating temperature is presented in Fig. 4.38. It becomes obvious from Fig. 4.38 that the sensitivity can be enhanced by increasing the operating temperature. In all cases both sensitivities decrease with increasing the partial pressure of the  $\text{NO}_x$  gas. This effect is likely due to a reduction in the number of adsorption sites as the gas partial pressures are increased leading to a lower sensitivity for higher  $\text{NO}_x$  partial pressures.

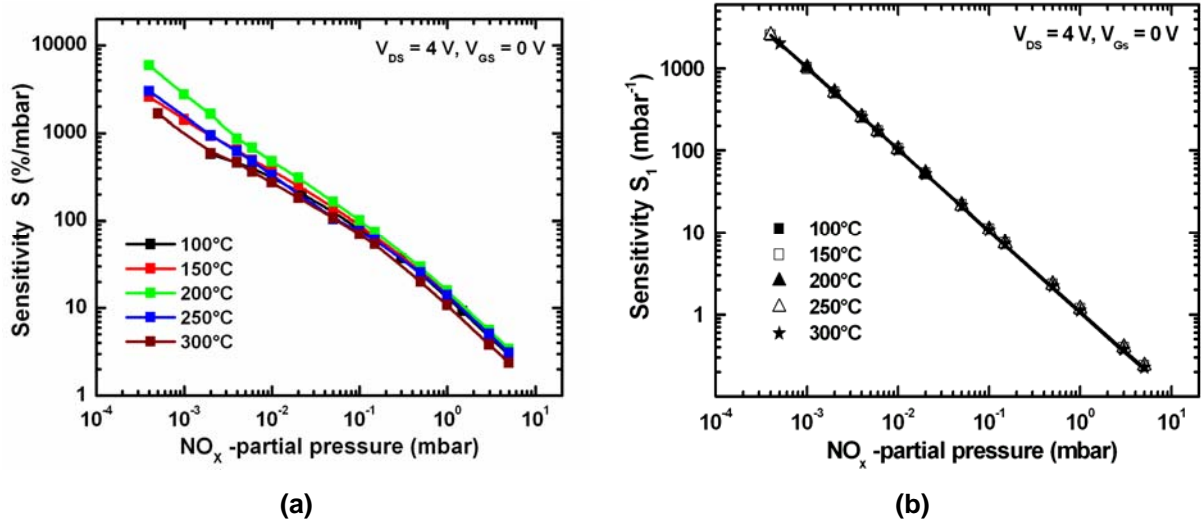


**Fig. 4.38:** The dependence of the response  $S$  (a) and  $S_1$  (b) on  $\text{NO}_x$  partial pressures at different temperatures. The applied biases are fixed at  $V_{GS} = 0$  V and  $V_{DS} = 4$  V.

As shown in Fig 4.38b the sensitivity  $S_1$  is related to the gas partial pressure  $P_{\text{NO}_x}$  by means of the power law  $a(P_{\text{NO}_x})^b$ , where the exponent  $b$  does not depend on the gas partial pressure, and  $a$  is a constant. Different fits, with this power expression were made for the sensitivity  $S_1$  and the values for the coefficient  $a$ ,  $b$ , and  $R^2$  are summarized in Tab. 4.9.

**Tab. 4.9:** Fitting parameter of the sensitivity  $S_1$  to  $\text{NO}_x$  at several temperatures.

Temperature (°C)	Allometric1 $S_1 = a(P_{\text{NO}_x})^b$		$R^2$
	a	b	
100	$1.088 \pm 0.002$	$-0.988 \pm 0.0003$	1
150	$1.057 \pm 0.004$	$-0.994 \pm 0.005$	1
200	$1.068 \pm 0.003$	$-0.9945 \pm 0.0004$	1
250	$1.055 \pm 0.002$	$-0.9946 \pm 0.0003$	1
300	$1.043 \pm 0.004$	$-0.995 \pm 0.0005$	1

The transient responses curves upon the introduction and removal of 0.03, 0.05, 0.1, and 0.3 mbar of  $\text{NO}_x$  under the applied biases of  $V_{GS} = 0$  V and  $V_{DS} = 5$  V at  $200^\circ\text{C}$  are shown in Fig. 4.39.

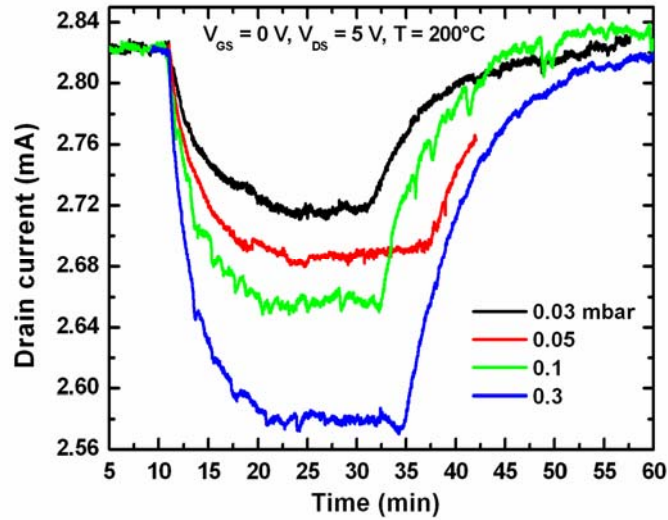


**Fig. 4.39:** Source-drain current versus time upon introduction and removal of 0.03, 0.05, 0.1, and 0.3 mbar  $\text{NO}_x$  at a temperature of  $200^\circ\text{C}$ . The applied bias are kept at  $V_{\text{GS}} = 0 \text{ V}$  and  $V_{\text{DS}} = 5 \text{ V}$ .

Upon exposing to  $\text{NO}_x$  gas, a quick  $\text{NO}_x$  sensing reaction takes place and the drain current decreases rapidly to a final steady-state value. The response time constant of adsorption ( $\tau_{90}$ ), defined as the time in which the output current reaches 90% of its final value, and ( $\tau_{70}$ ), defined as the time in which the output current reaches 70% of its final steady-state current, value are dependent on the initial rate of current variation  $d(\Delta I)/dt$ . The corresponding values of  $\tau_{90}$  ( $\tau_{70}$ ) and  $d(\Delta I)/dt$  are decreased from 514 (235) to 377(135) s and increased from 0.019 to 0.061 mA/s, respectively, as the  $\text{NO}_x$  partial pressure is increased from 0.03 to 0.3 mbar (Fig. 4.41).

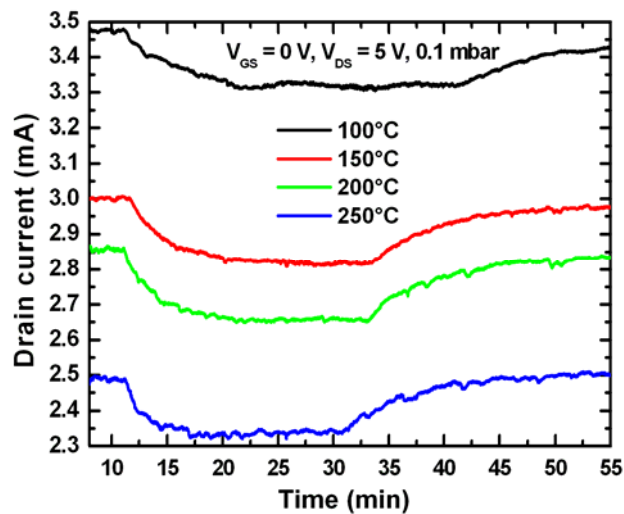


**Fig. 4.40:** Response curves towards 0.1 mbar of  $\text{NO}_x$  at various temperatures. The applied bias are kept at  $V_{\text{GS}} = 0 \text{ V}$  and  $V_{\text{DS}} = 5 \text{ V}$ .

Fig. 4.40 illustrates the transient response curves of the studied device upon the introduction and removal of 0.1 mbar of  $\text{NO}_x$  at 100, 150, 200, and 250°C. The applied bias are kept at  $V_{GS} = 0$  V and  $V_{DS} = 5$  V. At low operation temperatures, the sensor responds fairly fast to the test gas and shows even faster response at higher operation temperatures. As the operation temperature increases from 100 to 250°C, the response time  $\tau_{90}$  ( $\tau_{70}$ ) decreases from 635 (270) s to 314 (250) s (Fig.4.41).

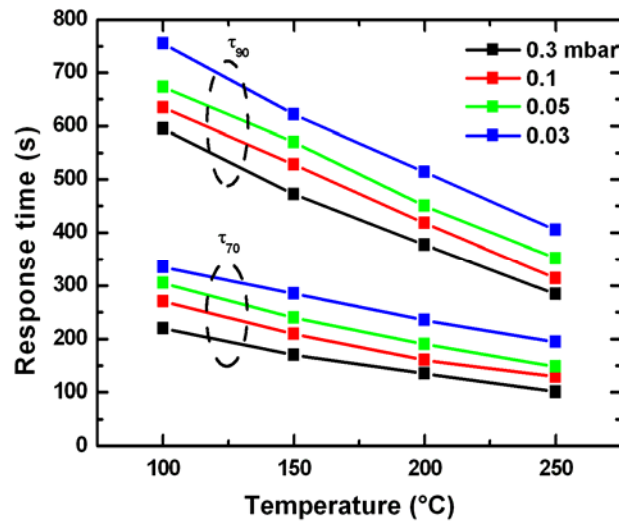


Fig. 4.41: The response time as a function of temperature for 0.03, 0.05, 0.1, and 0.3 mbar of  $\text{NO}_x$ .

#### 4.6.3.3 $\text{O}_2$ detection:

The dependence of the responses  $R$  and  $R_1$  on the partial pressure of  $\text{O}_2$  at different temperatures are presented in Fig. 4.42.

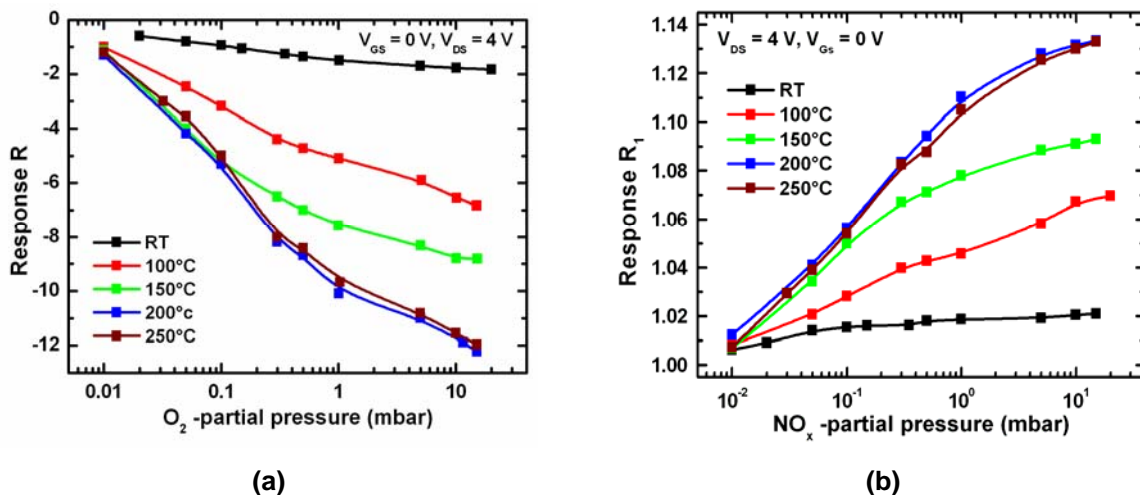
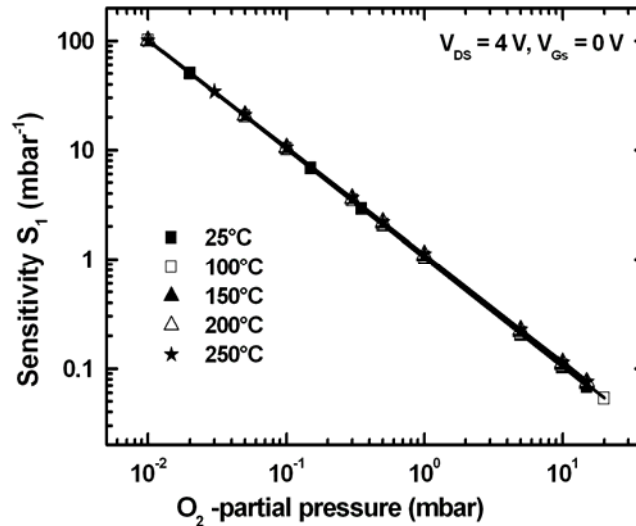


Fig. 4.42: The dependence of the response  $R$  (a) and  $R_1$  (b) on  $\text{O}_2$  partial pressures at different temperatures. The applied biases are fixed at  $V_{GS} = 0$  V and  $V_{DS} = 4$  V.

Fitting with the power expression  $a(P_{O_2})^b$  was made for the sensitivities  $S_1$  at different temperatures (Fig. 4.43) and the values for the coefficient  $a$ ,  $b$ , and  $R^2$  are summarized in Tab. 4.10.



**Fig. 4.43:** Dependence of sensitivity  $S_1$  on the  $O_2$  partial pressures at different temperature. The applied biases are fixed at  $V_{GS} = 0$  V and  $V_{DS} = 4$  V.

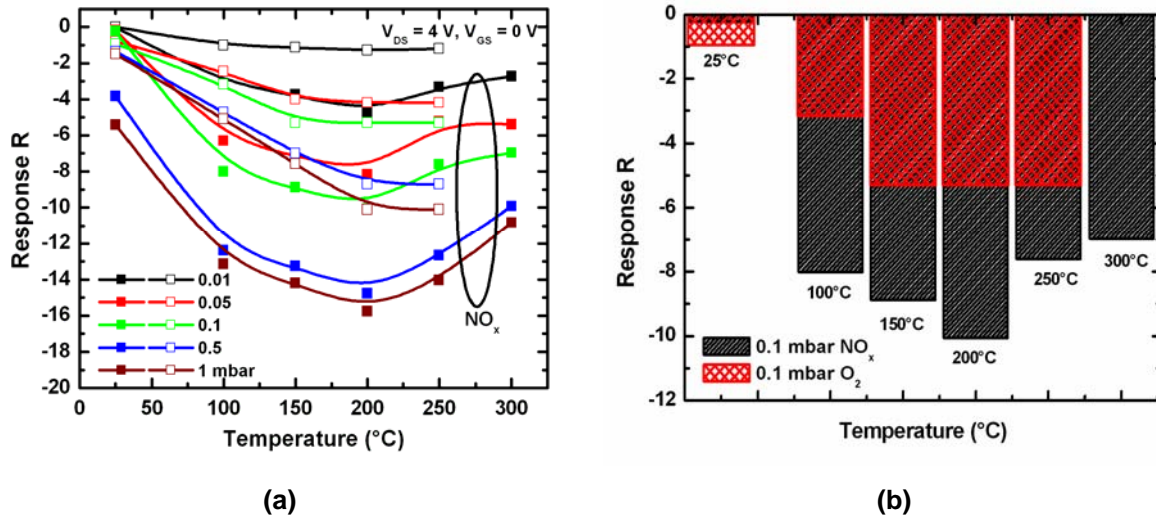
**Tab. 4.10:** Fitting parameter of the sensitivity  $S_1$  towards  $O_2$  at several temperatures.

Temperature (°C)	Allometric1 $S_1 = a(P_{O_2})^b$		$R^2$
	a	b	
25	$1.025 \pm 0.0008$	$-0.9958 \pm 0.0002$	1
100	$1.046 \pm 0.0009$	$-0.992 \pm 0.0002$	1
150	$1.089 \pm 0.0015$	$-0.9829 \pm 0.0003$	1
200	$1.1 \pm 0.0016$	$-0.982 \pm 0.0003$	1
250	$1.102 \pm 0.0007$	$-0.980 \pm 0.0001$	1

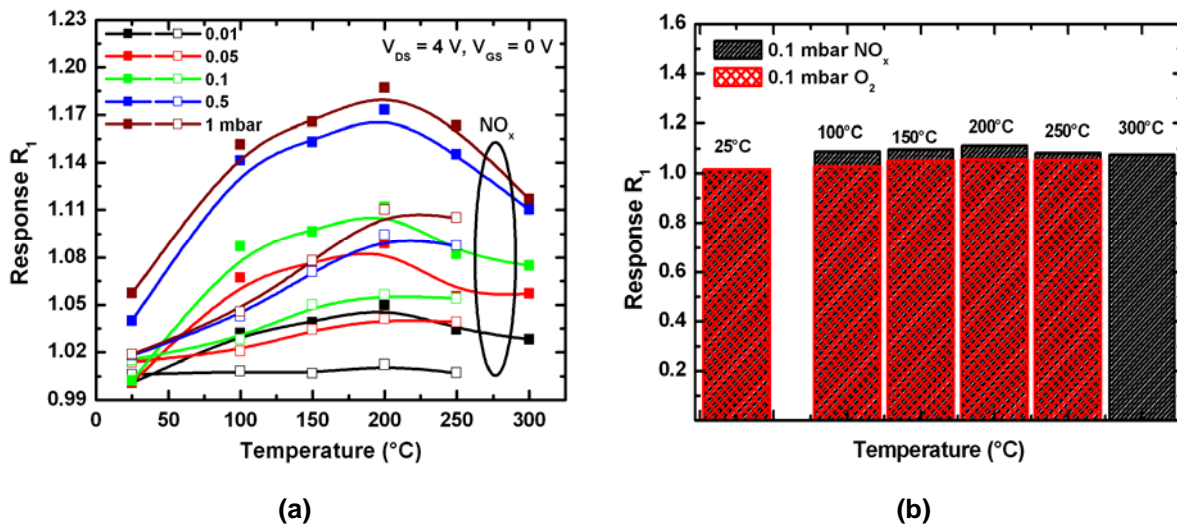
#### 4.6.3.4 Conclusion:

Fig. 4.44 and Fig.4.45 show the dependence of the responses  $R$  and  $R_1$  to 0.01, 0.05, 0.1, 0.5 and 1 mbar of pure  $NO_x$ , and  $O_2$  on the operating temperature. Clearly, the optimum detection temperatures occur in the range of 175-225°C for  $NO_x$ . In this range the cross responses to  $O_2$  is low indicating that the sensor is very suitable for selective detection of  $NO_x$ .





**Fig. 4.44:** (a) The dependence of the response  $R$  to 0.01, 0.05, 0.1, 0.5 and 1 mbar of  $\text{NO}_x$  and  $\text{O}_2$ , on the operating temperature. The applied biases are fixed at  $V_{\text{GS}} = 0 \text{ V}$  and  $V_{\text{DS}} = 4 \text{ V}$ . (b) Block presentations for 0.1 mbar of the both gases.



**Fig. 4.45:** (a) The dependence of the response  $R_1$  to 0.01, 0.05, 0.1, 0.5 and 1 mbar of  $\text{NO}_x$  and  $\text{O}_2$ , on the operating temperature. The applied biases are fixed at  $V_{\text{GS}} = 0 \text{ V}$  and  $V_{\text{DS}} = 4 \text{ V}$ . (b) Block presentations for 0.1 mbar of the both gases.

#### 4.6.4 Sensor with $\text{Pt-In}_x\text{Sn}_y\text{O}_z$ gate (EN16):

##### 4.6.4.1 SEM and AES of the sample:

AES depth profile made on the area of the gate shown in the SEM image (Fig. 4.46b) is presented in Fig. 4.46a. It can be seen in Fig. 4.46a that the sample structure includes  $\text{Pt-In}_x\text{Sn}_y\text{O}_z$ ,  $\text{SiN}$ ,  $\text{SiO}_x$ , and  $\text{SiC}$  layers.

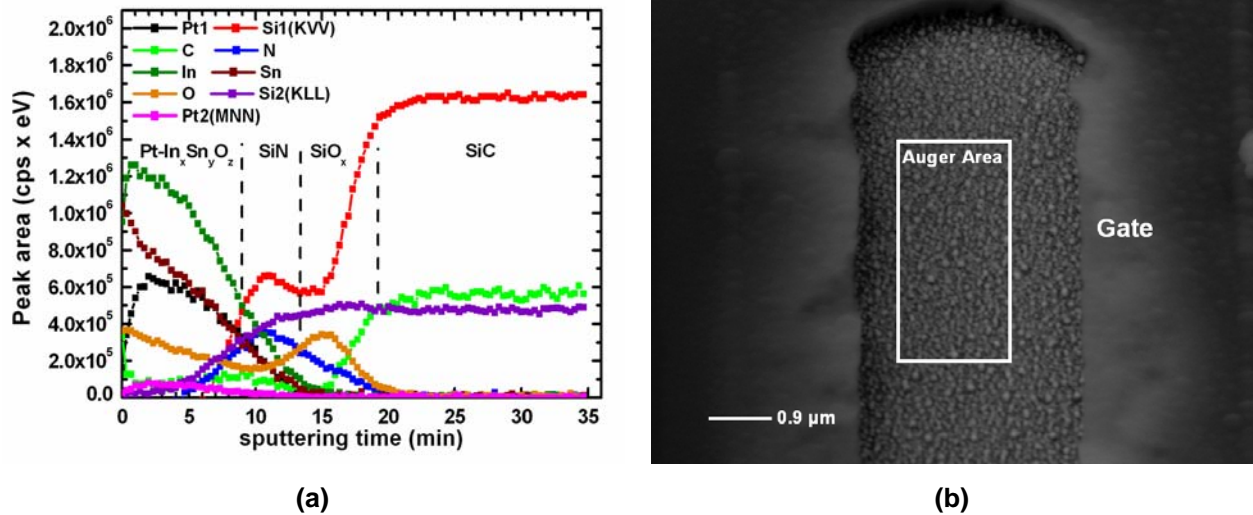


Fig. 4.46: (a) AES depth profiles of the gate area of the sensor (EN16). (b) SEM image of the gate.

#### 4.6.4.2 NO<sub>x</sub> detection:

The typical ( $I_D$ - $V_D$ ) characteristics of the Pt-In<sub>x</sub>Sn<sub>y</sub>O<sub>z</sub> gate MOSFET under different partial pressures of NO<sub>x</sub> gas at 100, 150°C are shown in Fig. 4.47a and Fig. 4.47b respectively. Apparently, the studied sensor exhibits substantial current variation at NO<sub>x</sub> ambience.

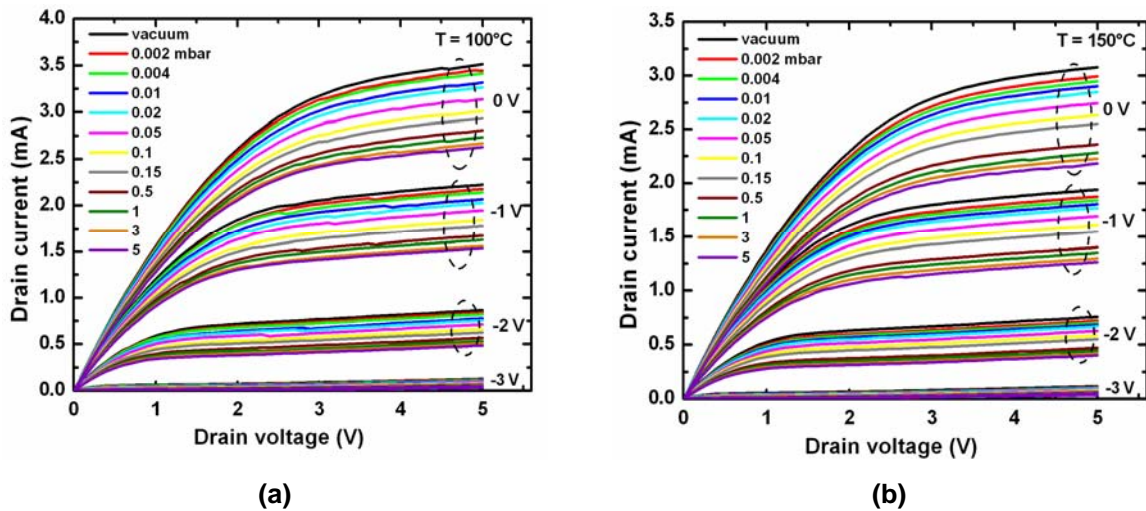


Fig. 4.47: Typical  $I_D$ - $V_D$  characteristics of the studied FET sensor under different partial pressures of NO<sub>x</sub> gas at (a) 100 and (b) 150°C.

As seen in Fig. 4.47, even at an extremely low NO<sub>x</sub> partial pressure of 0.002 mar, the current modulation can be found significantly. Under vacuum and different NO<sub>x</sub> partial pressures of 0.002, 0.02, and 5 mbar at 100°C (150°C), the

corresponding measured drain saturation currents are 3.4 (2.98) mA, 3.32 (2.89) mA, 3.15 (2.76) mA, and 2.53 (2.11) mA, respectively, at  $V_{DS} = 4V$  and  $V_{GS} = 0V$ . In addition, all I-V curves in Fig. 4.47a and Fig. 4.47b show good pinch-off and saturation characteristics.

The response  $R$  and  $R_1$  to  $NO_x$  versus  $NO_x$  partial pressure of the studied sensor at different temperatures are shown in Fig. 4.48a, and Fig. 4.48b respectively. The applied bias is fixed at the drain-source voltage of  $V_{DS} = 4 V$  and gate-source voltage of  $V_{GS} = 0 V$ . Clearly, good  $R$  and  $R_1$  values even under a very low partial pressure of 0.002 mbar are obtained for the studied sensor. Both responses  $R$  and  $R_1$  increase non-linearly with increasing partial pressure of  $NO_x$  and no complete saturation was observed even at high partial pressure of 10 mbar. The non-linear response to increasing partial pressures of  $NO_x$  may be due to the filling of the adsorption sites on the catalytic surface, which proportionally decrease as the concentrations increase.

It can be seen also from Fig. 4.48 that the response can be enhanced by increasing the operating temperature. The maximum responses  $R$  and  $R_1$  toward  $NO_x$  are observed at  $150^\circ C$  for the sensor investigated.

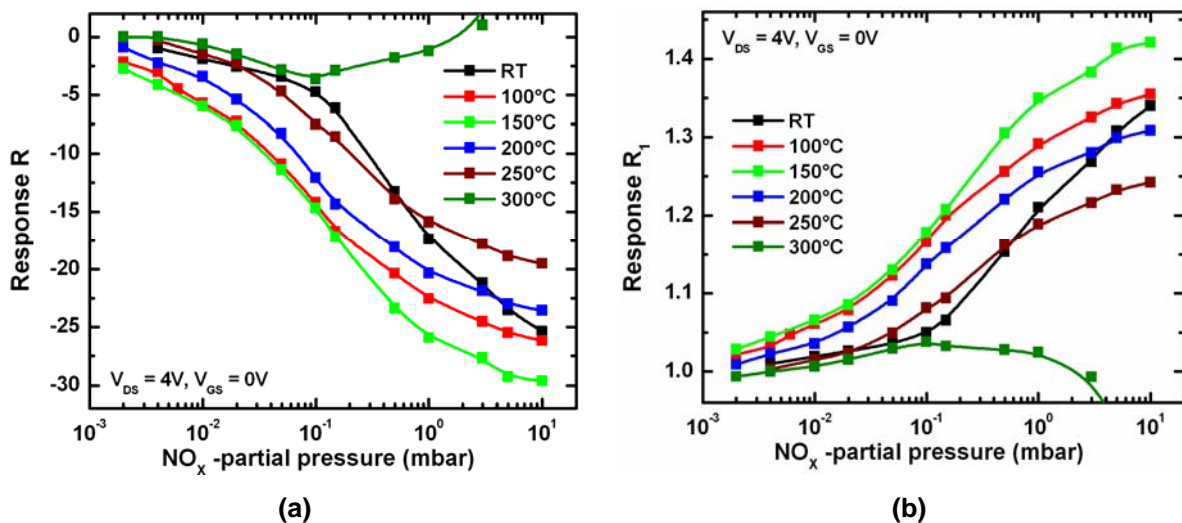


**Fig. 4.48:** The response  $R$  (a) and  $R_1$  (b) to  $NO_x$  versus  $NO_x$  partial pressure of the studied sensor at different temperatures. The applied biases are fixed at  $V_{GS} = 0 V$  and  $V_{DS} = 4 V$ .

Fig. 4.49 shows the drain saturation current  $I_{DS}$  and the transconductance  $g_m$  as a function of gate-source voltage  $V_{GS}$  of the studied sensor under different partial pressures of  $NO_x$  at  $150^\circ C$ . The threshold voltages (maximal transconductance) are -

3.25 V (21.31 mS/mm), -3.24 V (20.93 mS/mm), -3.16 V (19.82 mS/mm), -3.09 V (18.23 mS/mm), -2.96 V (15.66 mS/mm), and -2.87 V (14.65 mS/mm) under vacuum and  $\text{NO}_x$  partial pressures of 0.002, 0.02, 0.1, 1, and 10 mbar, respectively. The threshold voltage  $\Delta V_{\text{th}}$  is decreased from -17 to -379 mV as the  $\text{NO}_x$  partial pressure increased from 0.002 to 10 mbar.

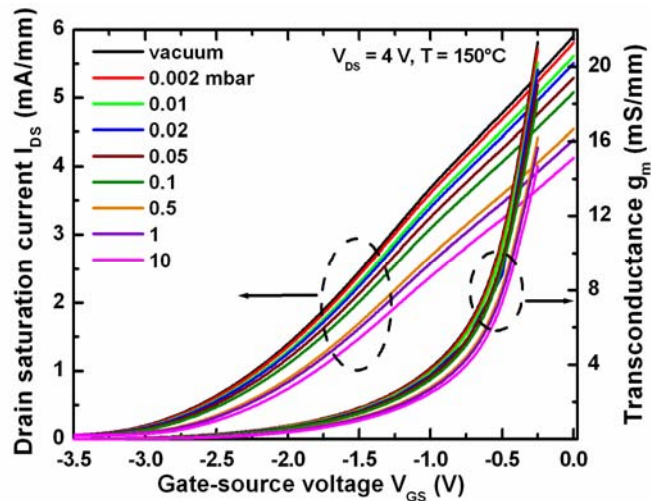


**Fig. 4.49:** The relation between the drain saturation current, transconductance, and gate-source voltage of the studied FET sensor under different partial pressures of  $\text{NO}_x$  at  $150^\circ\text{C}$ .

The response  $R_2$  (change in  $V_{\text{th}}$ ) and response  $R_3$  (change in  $V_{\text{GS}}$  at  $I_{\text{DS}} = \text{const.} = 3 \text{ mA/mm}$ ) as a function of  $\text{NO}_x$  partial pressures at different operation temperatures are presented in Fig. 4.50a and Fig. 4.50b, respectively.

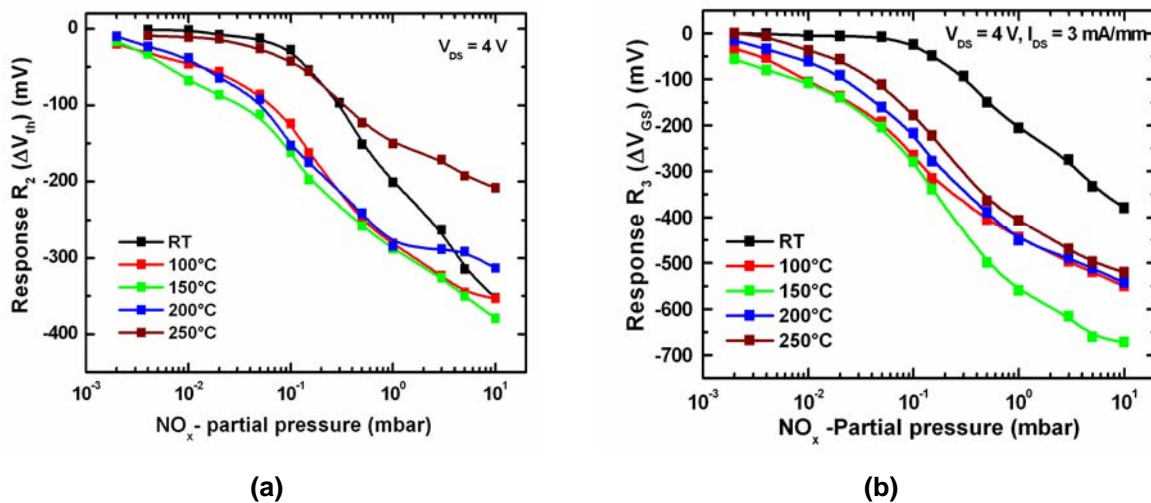


**Fig. 4.50:** The response  $R_2$  (a) and  $R_3$  (b) to  $\text{NO}_x$  as a function of  $\text{NO}_x$  partial pressures at different operation temperatures.

Clearly, good  $R_2$  and  $R_3$  values even under a very low partial pressure of 0.002 mbar are obtained for the sensor studied. Both responses  $R_2$  and  $R_3$  increase non-linearly with increasing the partial pressure of  $\text{NO}_x$  and no complete saturation was observed even at a high partial pressure of 10 mbar. It can be seen also from Fig. 4.50 that the response can be enhanced by increasing the operating temperature. The maximum responses  $R_2$  and  $R_3$  toward  $\text{NO}_x$  are observed at  $150^\circ\text{C}$  for the sensor investigated.

The dependence of the sensitivity  $S$ ,  $S_1$ ,  $S_2$ , and  $S_3$  on the partial pressure of pure  $\text{NO}_x$  at different operating temperatures is presented in Fig. 4.51. We defined the sensitivity as given by Eq. (4.12). It can be seen also from Fig. 4.51 that all sensitivities can be enhanced by increasing the operating temperature. In all cases the sensitivity decreases with increasing partial pressure of the  $\text{NO}_x$  gas.

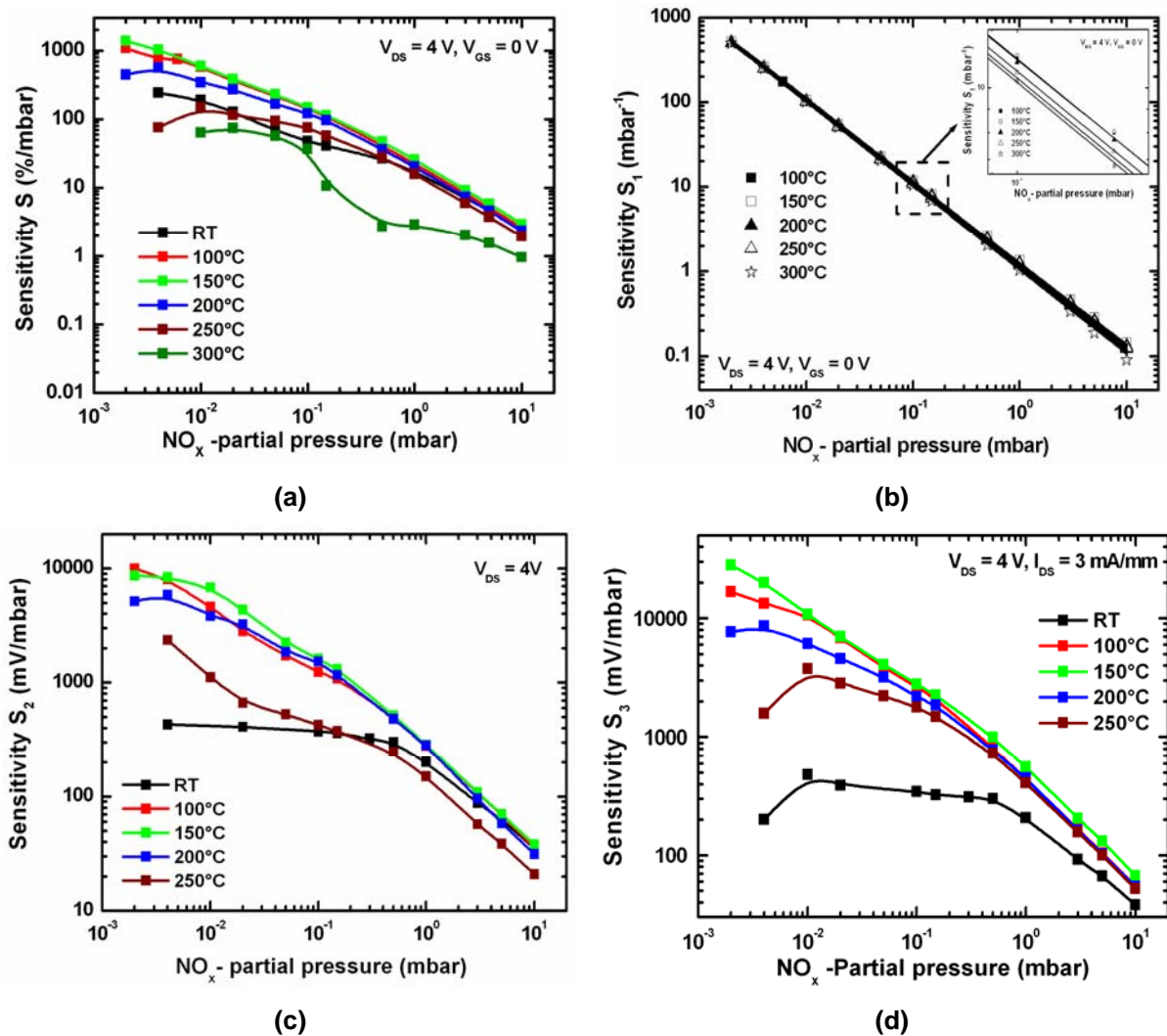


**Fig. 4.51:** The dependence of the sensitivity (a)  $S$ , (b)  $S_1$ , (c)  $S_2$ , and (d)  $S_3$  on the partial pressure of pure  $\text{NO}_x$  at different operating temperatures.

The dependence of sensitivity  $S_1$  on partial pressures of  $\text{NO}_x$  can be described with the well-known power behaviour for metal oxide semiconductor sensing films,  $a(P_{\text{NO}_x})^b$ . Different fits, with this kind of equation, were performed for the sensitivity  $S_1$  at different temperatures (Fig.4.51b). The values for the coefficients  $a$  and  $b$  as well as the coefficient  $R^2$  are summarized in Tab. 4.11.

**Tab. 4.11:** Fitting parameter of the sensitivity  $S_1$  towards  $\text{NO}_x$  at several temperatures.

Temperature (°C)	Allometric1 $S_1 = a(P_{\text{NO}_x})^b$		$R^2$
	a	b	
100	$1.165 \pm 0.012$	$-0.978 \pm 0.001$	0.998
150	$1.246 \pm 0.098$	$-0.965 \pm 0.013$	1
200	$1.137 \pm 0.007$	$-0.980 \pm 0.001$	1
250	$1.087 \pm 0.007$	$-0.985 \pm 0.001$	1
300	$1.05 \pm 0.002$	$-0.990 \pm 0.0003$	1

The slopes of the lines in the log-log plot (Fig. 4.51b) are different and dependent on the operation temperature. A higher value of the exponent  $b$  allows an easier distinction between two partial pressures, while a lower value rises the lowest partial pressure which can be measured. If we are interested in the determination of high partial pressures, we can operate the sensor at 300°C, since the slope is higher. Otherwise, if we are interested in lower partial pressures, we should work at 150°C because at this temperature the detection limit is lower.

#### 4.6.4.3 O<sub>2</sub> detection:

In second step, the sensor was tested for the response to other oxidizing gases such as O<sub>2</sub> with partial pressures starting from 0.002 going up to 10 mbar at temperatures between room temperature and 300°C. The dependence of the responses  $R$ ,  $R_1$ ,  $R_2$ , and  $R_3$  towards different partial pressures of O<sub>2</sub> on the operating temperature is presented in Fig. 4.52. All responses increase with increasing the partial pressure of O<sub>2</sub> and no saturation is observed even at a partial pressure of 10 mbar. The maximum response toward O<sub>2</sub> is observed in the range 200-250°C for the sensor studied.

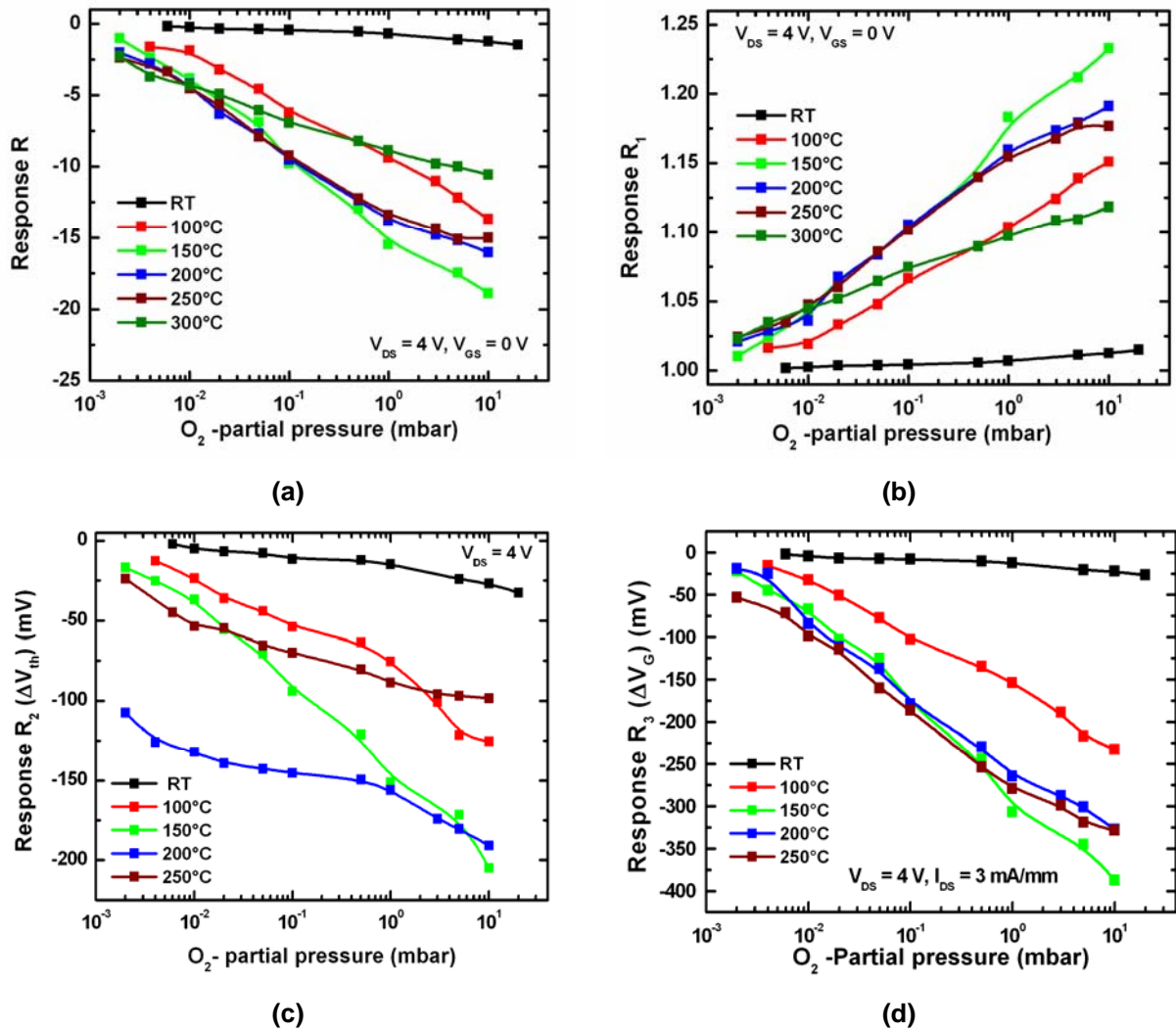


**Fig. 4.52:** The dependence of the response R (a),  $R_1$  (b),  $R_2$  (c) and  $R_3$  (d) on the  $O_2$  partial pressure of the sensor studied at different temperatures.

Fig. 4.53 presents the dependence of the sensitivities  $S$ ,  $S_1$ ,  $S_2$ , and  $S_3$  to different partial pressures of  $O_2$  on the operating temperature. Again all sensitivities increase with increasing operation temperature. In addition, in all cases the sensitivity decreases with increasing the partial pressure of  $O_2$ . It can be seen from Fig. 4.53b that the sensitivity  $S_1$  can be described by the power expression  $a(P_{O_2})^b$ . Different fits with this expression were performed for the sensitivity  $S_1$  at different temperatures (Fig. 4.53b) and the values for the coefficient  $a$ ,  $b$ , and  $R^2$  are summarized in Tab. 4.12.

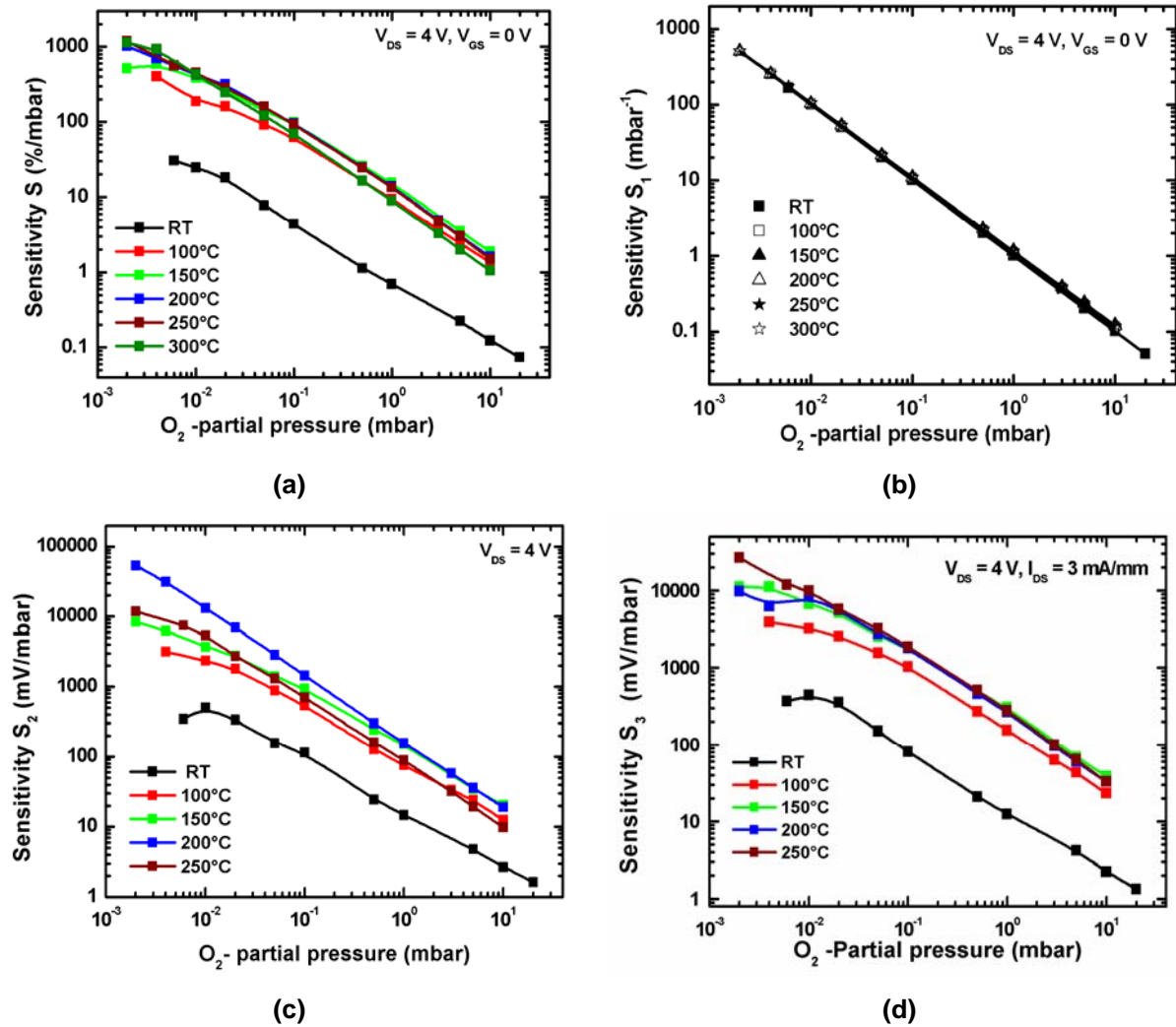


**Fig. 4.53:** The sensitivity  $S$  (a),  $S_1$  (b),  $S_2$  (c) and  $S_3$  (d) versus  $O_2$  partial pressure of the sensor studied at different temperatures.

**Tab. 4.12:** Fitting parameter of the sensitivity  $S_1$  towards  $O_2$  at several temperatures.

Temperature (°C)	Allometric1 $S_1 = a(P_{O_2})^b$		$R^2$
	a	b	
RT	$1.008 \pm 0.0004$	$-0.998 \pm 0.0001$	1
100	$1.06 \pm 0.009$	$-0.992 \pm 0.0016$	0.999
150	$1.144 \pm 0.006$	$-0.978 \pm 0.0008$	0.999
200	$1.106 \pm 0.01$	$-0.987 \pm 0.0014$	1
250	$1.107 \pm 0.007$	$-0.9873 \pm 0.001$	1
300	$1.116 \pm 0.004$	$-0.986 \pm 0.0006$	1



#### 4.6.4.4 Conclusion:

The dependence of the responses  $R$ ,  $R_1$ ,  $R_2$ , and  $R_3$  to 0.01, 0.05, 0.1, 0.5 and 1 mbar of pure  $\text{NO}_x$  and  $\text{O}_2$  on the operating temperature is shown in Fig. 4.54. It becomes obvious from Fig. 4.54 that the optimum detection temperatures occur in the range of 125-175°C for  $\text{NO}_x$ . In this range the cross responses to  $\text{O}_2$  is low indicating that the sensor is very suitable for selective detection of  $\text{NO}_x$ . In addition, in the range 260-300°C the response to  $\text{NO}_x$  decreases significantly therefore, is low and no response to  $\text{NO}_x$  was observed, therefore, the sensor can be used as  $\text{O}_2$  gas sensor in this range.

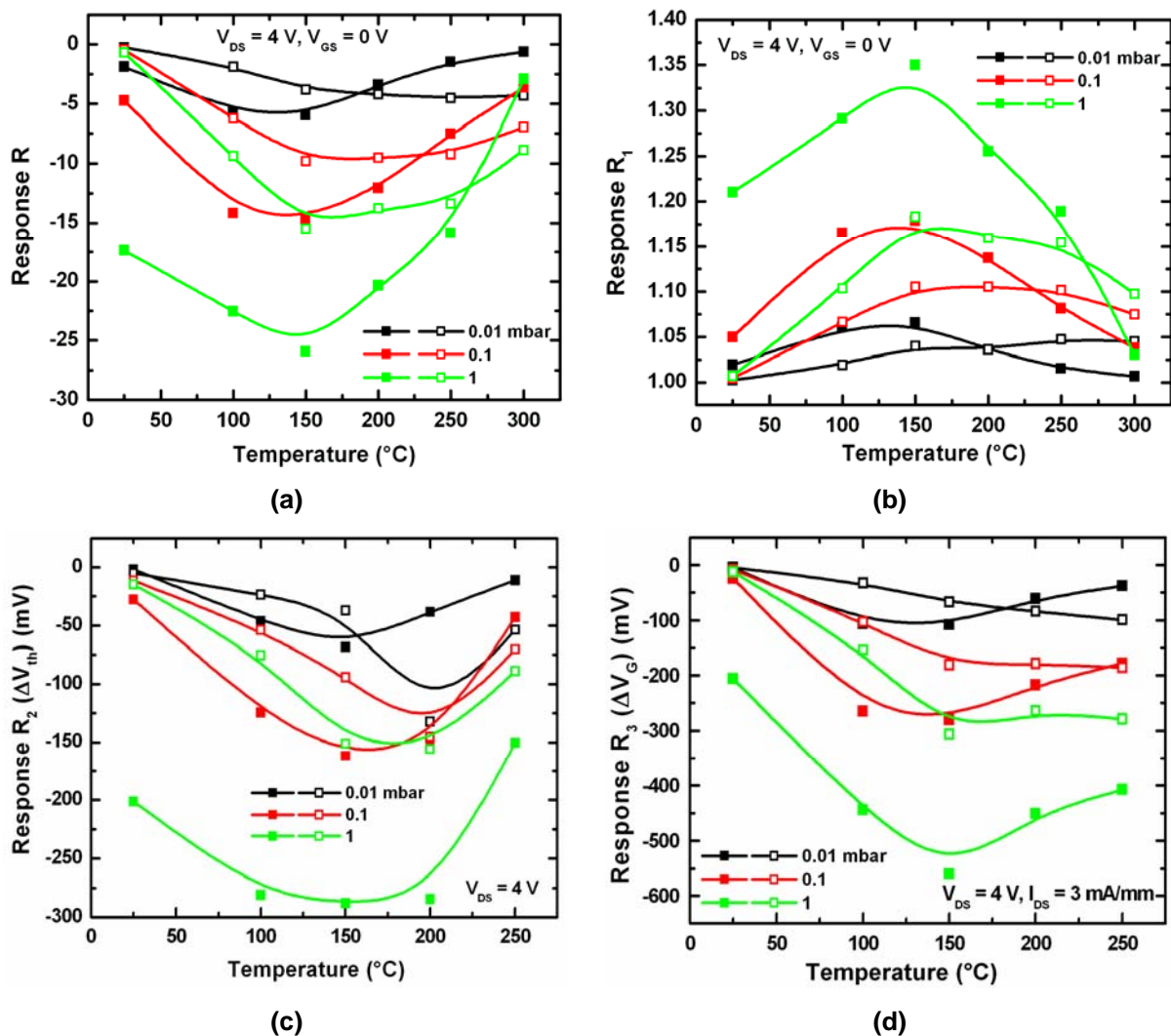


**Fig. 4.54:** The dependence of the responses  $R$  (a),  $R_1$  (b),  $R_2$  (c), and  $R_3$  (d) to 0.01, 0.05, 0.1, 0.5, and 1 mbar of  $\text{NO}_x$  (closed symbols) and  $\text{O}_2$  (open symbols), on the operating temperature.

#### 4.7 Comparison:

The responses  $R$  and  $R_1$  to 0.5 and 1 mbar of  $\text{NO}_x$  and  $\text{O}_2$  as a function of operating temperature for all studied sensors are shown in Fig. 4.55 and Fig. 4.56, respectively.

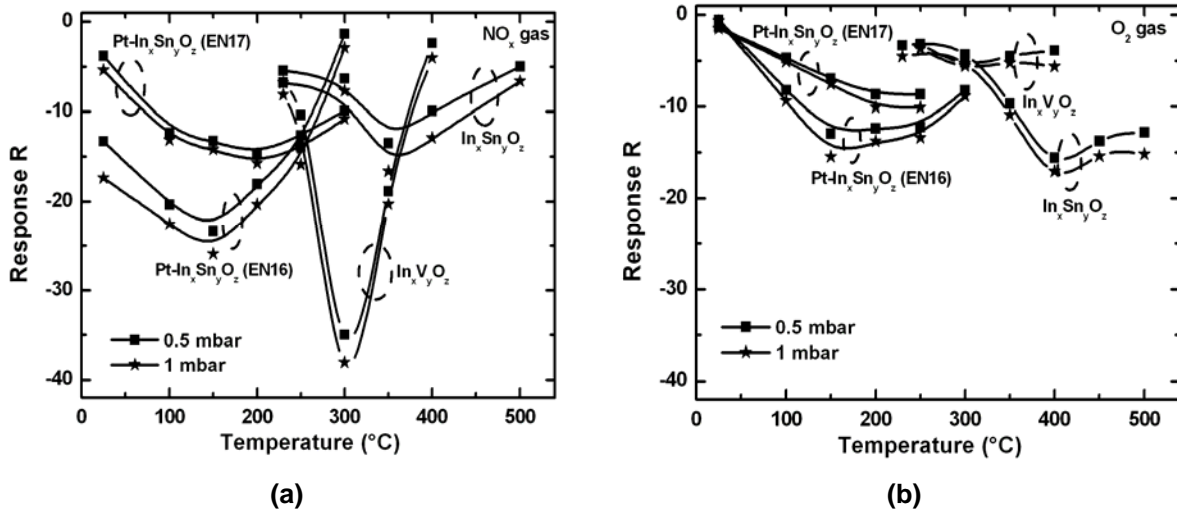


**Fig. 4.55:** The dependence of the responses  $R$  of all studied FETs to 0.5, and 1 mbar of (a)  $\text{NO}_x$  and (b)  $\text{O}_2$  on the operating temperature.

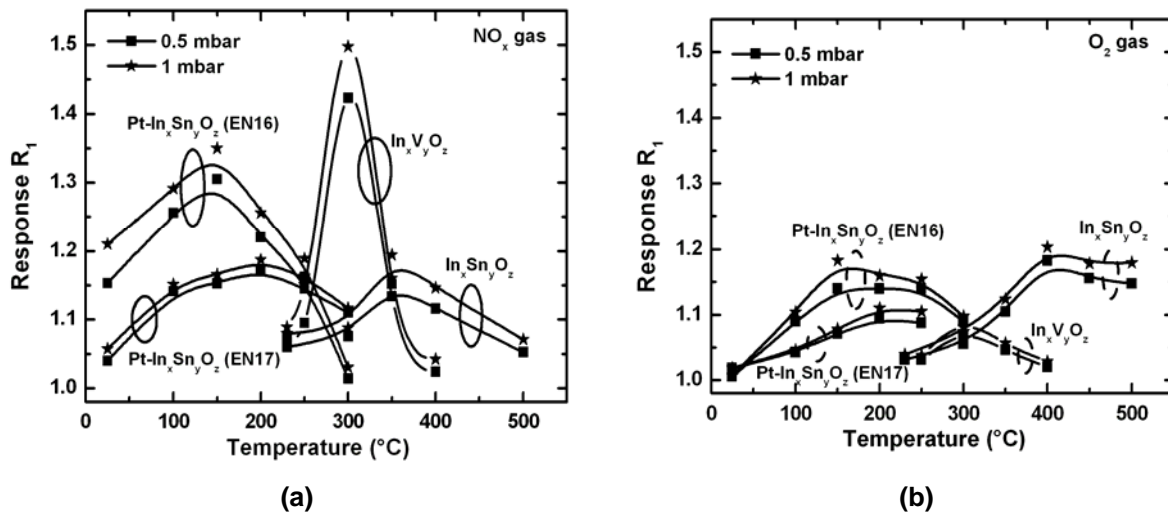


**Fig. 4.56:** The dependence of the responses  $R_1$  of all studied FETs to 0.5, and 1 mbar of (a)  $\text{NO}_x$  and (b)  $\text{O}_2$  on the operating temperature.

The experimental results indicate that:

1. The sensor with  $\text{In}_x\text{V}_y\text{O}_z$  gate has the best response in the temperature range (250-350  $^{\circ}\text{C}$ ) with a maximum value at 300  $^{\circ}\text{C}$ .

2. The response of the sensor with Pt-In<sub>x</sub>Sn<sub>y</sub>O<sub>z</sub> gate (EN16) to 1 mbar of NO<sub>x</sub> reaches the maximum, R = 25, at 150°C. However, the maximum response of the sensor with In<sub>x</sub>Sn<sub>y</sub>O<sub>z</sub> gate (without Pt) is 15 at 350°C. It becomes obvious that a small quantity of Pt enhances the response remarkably and lowers the operating temperature.
3. The temperature of the maximum response is dependent on the gas species being measured. This information, along with a careful choice of catalyst (gate material) can be used to enhance device selectivity.
4. The cross responses of the sensor with Pt-In<sub>x</sub>Sn<sub>y</sub>O<sub>z</sub> gate (EN16) and (EN17) to O<sub>2</sub> are lower than those of the sensor with In<sub>x</sub>Sn<sub>y</sub>O<sub>z</sub> gate (without Pt) (Fig. 4.55b, Fig. 4.56b). As a consequence a small quantity of Pt can enhance the selectivity.
5. The difference in the sensing properties of the two Pt-modified sensors (EN17 and EN16) depends on the different surface morphology of the Pt thin film deposited on top of the In<sub>x</sub>Sn<sub>y</sub>O<sub>z</sub> films.

It is known that the addition of noble metals (Pt, Pd,...) to metal oxide materials improve the detection of various kinds of gases via enhancement of the response and a shift of T<sub>M</sub> (the temperature at which the maximum sensitivity is observed) to lower temperatures [4.30-4.32]. This can be explained through the modification of the conductivity (via the addition of excess electrons in the conduction band, or through the addition of holes) and/or the influence on microstructure (porosity, grain size and grain boundaries).

#### 4.8 Conclusion:

The performance of SiC-based field effect transistors (FETs) with different gate materials: (i) Indium oxide and tin oxide (In<sub>x</sub>Sn<sub>y</sub>O<sub>z</sub>), (ii) Indium oxide and vanadium oxide (In<sub>x</sub>V<sub>y</sub>O<sub>z</sub>), (iii) as well as mixture of metal oxides with addition of an appropriate amount of metal additives (Pt) were investigated as NO<sub>x</sub>, O<sub>2</sub>, and D<sub>2</sub> gas detectors. The responses to these gases were investigated in dependence on the operating temperature and gas partial pressures.

The composition and microstructure of the sensing gate electrode are the key parameters that influence the sensing mechanism, and hence key performance parameters: sensitivity, selectivity, and response time. By choosing the appropriate temperature and catalyst material (gate material) devices that are sensitive to a certain gases were realized. In addition, the temperature of maximum response

varies dependent on the gas species being measured. This information, along with a careful choice of catalyst (gate material) can be used to enhance device selectivity.

#### 4.9 Outlook and future work:

For further investigation in this field of study, the following experiments are suggested:

- The fundamental properties of  $\text{In}_x\text{Sn}_y\text{O}_z$ ,  $\text{In}_x\text{V}_y\text{O}_z$  and  $\text{Pt-In}_x\text{Sn}_y\text{O}_z$  gates should be investigated by a wide set of structural characterisation techniques, including Transmission Electron Microscopy, X-ray diffraction, Raman, Fourier Transform infrared, and X-ray photoelectron spectroscopy. The combined use of the different techniques allows an improved understanding of the structural properties of the gate material, as well as the sensing mechanism.
- A further study of the selectivity against other gases such as  $\text{CO}$ , and  $\text{NH}_3$ , as well as investigation related to stability or reliability of the sensor is needed.
- For sensors with  $\text{In}_x\text{Sn}_y\text{O}_z$ , and  $\text{In}_x\text{V}_y\text{O}_z$  gates, many parameters that may affect the sensor performance still need to be optimized; these parameters include the amount of each metal oxide in the metal oxide mixtures, the thickness, grain size, and the geometry of the thin films.
- For sensors with  $\text{Pt-In}_x\text{Sn}_y\text{O}_z$  gates, the influence of the amount of doping (Pt additives) on the gas sensing properties should be studied
- The influence of the relative humidity on the performance of the sensors at different operation temperatures should be tested.
- The cross response was measured using a system that allows injection of one gas only. But the system can be developed to use two or more gases at the same time and this allows the best investigation of the selectivity.

#### Reference:

- [4.1] N. Yamazoe, and G. Sakai, "Recent trends in research for environmental gas sensors", *Trans. Inst. Elec. Jpn.* 118-E (1998) 60-63.
- [4.2] A. Samman, S. Gebremariam, L. Rimai, X. Zhang, G. W. Auner, and J. Hangan, "Platinum-aluminum nitride-silicon carbide diodes as combustible gas sensors", *J. Appl. Phys.* 87 (2000) 3101-3107.

- [4.3] A. Lloyd Spetz, M. Armgarth, and I. Lundstöm, "Hydrogen and ammonia response of metal-silicon dioxide-silicon structures with thin platinum gates", *J. Appl. Phys.* 64 (1988) 1274-1283.
- [4.4] H. Wingbrant, H. Svenningstorp, P. Salomonsson, D. Kubinski, J. H. Visser, M. Löfdahl, and A. Lloyd Spetz, "Using a MISiC-FET sensor for detecting NH<sub>3</sub> in SCR systems", *IEEE Sensors J.* 5 (2005) 1099.
- [4.5] M. Andersson<sup>1</sup>, P. Ljung, M. Mattsson, M. Löfdahl, and A. Lloyd Spetz, "Investigations on the possibilities of a MISiCFET sensor system for OBD and combustion control utilizing different catalytic gate materials", Springer Verlag, Berlin, 30-31 (2004), 365-368.
- [4.6] C. K. Kim, J. H. Lee, S. M. Choi, I. H. Noh, H. R. Kim, N. I. Cho, C. Hong, and G. E. Jang, "Pd- and Pt-SiC Schottky diodes for detection of H<sub>2</sub> and CH<sub>4</sub> at high temperature", *Sensors and Actuators B* 77 (2001) 455-462.
- [4.7] A. Lloyd Spetz, M. Eriksson, L.-G. Ekedahl, and I. Lundström, "Si and SiC based field effect devices", Conference proceeding of TAFT 2000, Nancy, France, 27-30 March (2000).
- [4.8] I. Lundström, S. Shivaraman, C. Svensson, and L. Lundkvist, "A hydrogen-sensitive MOS field-effect transistor", *Appl. Phys. Lett.* 26 (1975) 55-57.
- [4.9] G. W. Hunter, L. Y. Chen, P. G. Neudeck, D. Knight, C. C. Liu, Q. H. Wu, H. J. Zhuo, D. Makel, M. Liu, and W. A. Rauch, "Chemical gas sensors for aeronautic and space applications II", NASA/TM-1998-208504.
- [4.10] Z. Fan, and J. G. Lu, "Gate-refreshable nanowire chemical sensors", *Appl. Phys. Lett.* 86 (2005) 123510.
- [4.11] M. S. Arnold, P. Avouris, Z. W. Pan, and Z. L. Wang, "Field-effect transistors based on semiconducting oxide nanobelts", *J. Phys. Chem. B* 107 (2003) 659-663.
- [4.12] S. M. Sze, "Physics of semiconductor devices", New York, ISBN 0-471-09837-X, 1981.
- [4.13] P. Bergveld, "Development of an ion-selective solid state device for neurophysiological measurements", *IEEE Trans. Biomed. Eng.* 17 (1970) 70.
- [4.14] J. Wöllenstein, F. Ihlenfeld, M. Jaegle, G. Köhner, H. Böttner, and W.J. Becker, "Gas-sensitive p-GaAs field effect device with catalytic gate", *Sensors and Actuators B*, 68 (2000) 22-26.

- [4.15] J. V. Hatfield, J.A. Covington, and J. W. Gardner, "GasFETs incorporating conducting polymers as gate materials", *Sensors and Actuators B* 65 (2000) 253-256.
- [4.16] Y. Miyahara, Tsukada K., and H. Miyagi, "Field-effect transistor using a solid electrolyte as a new oxygen sensor", *J. Appl. Phys.* 63 (1988) 2431-2434.
- [4.17] W. I. Cho, C. W. Yi, J. B. Ju, B. W. Cho, and K. S. Yun, "Characteristics of a thin-film LaF<sub>3</sub> solid electrolyte for oxygen sensing", *Sensors and Actuators B* 5 (1991) 149-153.
- [4.18] S. K. Choi, C. W. Yi, W. I. Cho, B. C. Cho, J. B. Ju, K. S. Yun, and N. Yamazoe, "A MOSFET type sensor for oxygen sensing LaF<sub>3</sub> as a gate material", *Sensors and Actuators B* 13 (1993) 45-48.
- [4.19] M. Bouvet, G. Guillaudb, A. Leroy, A. Maillard, A. Spirkovitch, and F.-G. Tournilhac, "Phthalocyanine-based field-effect transistor as ozone sensor", *Sensors and Actuators B* 73 (2001) 63-70.
- [4.20] M. Andersson, M. Holmberg, I. Lundström, A. Lloyd-Spetz, P. Martenson, R. Paolesse, C. Falconi, E. Proiett, C. Di Natale, and A. D'Amico, "Development of a ChemFET sensor with molecular films of porphyrins as sensitive layer", *Sensors and Actuators B* (2001) 567-571.
- [4.21] I. Eisele, T. Doll, and M. Burgmaier, "Low power gas detection with FET sensors", *Sensors and Actuators B* 78 (2001) 19-25.
- [4.22] M. Ali, V. Cimalla, V. Lebedev, Th. Stauden, G. Ecke, V. Tilak, P. Sandvik and O. Ambacher, "SiC-based FET for detection of NO<sub>x</sub> and O<sub>2</sub> using InSnO<sub>x</sub> as a gate material", *Sensors and Actuators B* 122 (2007) 182-186.
- [4.23] M. Ali, V. Cimalla, V. Lebedev, Th. Stauden, Ch. Y. Wang, G. Ecke, V. Tilak, P. Sandvik and O. Ambacher, "Reactively sputtered In<sub>x</sub>V<sub>y</sub>O<sub>z</sub> films for detection of NO<sub>x</sub>, D<sub>2</sub>, and O<sub>2</sub>", *Sensors and Actuators B* 123 (2007) 779-783.
- [4.24] P. Sandvik, M. Ali, V. Tilak, K. Matocha, Th. Stauden, J. Tucker, J. Deluca, and O. Ambacher, "SiC-based MOSFET for harsh environment emissions sensors", *Conference proceeding of ICSCRM 2005*, Pittsburgh, Pennsylvania, 18-23 September (2005).
- [4.25] G. Kriakidis, N. Katsarakis, M. Bender, E. Gagaudakis, and V. Cimalla, "InO<sub>x</sub> thin films, candidates for novel chemical and optoelectronic applications", *Mater. Phys. Mech.* 1 (2000) 83-97.

- [4.26] P. W. Palmberg, G. E. Riach, R. E. Weber, and N. C. MacDonald, "Handbook of Auger Electron Spectroscopy", (Physical Electronics Industries, Minnesota, 1972).
- [4.27] R. Ramamoorthy, M. K. Kennedy, H. Nienhaus, A. Lorke, F. E. Kruis, and H. Fissan, "Surface oxidation of monodisperse SnO<sub>x</sub> nanoparticles", *Sensors and Actuators B* 88 (2003) 281-285.
- [4.28] R. Larcipretea, E. Borsella, P. D. Padova, P. Perfetti, and C. Crotti, "Surface analysis study of the oxidation of organotin films deposited by ArF excimer laser chemical vapor deposition", *J. Vac. Sci. Technol. A* 15 (1997) 2492-2501.
- [4.29] M. J. Madou, and S. R. Morrison, "Chemical sensing with solid state devices", Academic Press, New York, 1988, pp. 67-104.
- [4.30] N. Yamazoe, Y. Kurokawa, and T. Seiyaama, "Enzyme semiconductor sensor based on butyrylcholinesterase", *Sensors and Actuators B* 4 (1983) 283-286.
- [4.31] Y. Takao, Y. Iwanaga, Y. Shimizu, and M. Egashira, "Trimethylamine-sensing mechanism of TiO<sub>2</sub>-based sensors 1. Effects of metal additives on trimethylamine-sensing properties of TiO<sub>2</sub> sensors", *Sensors and Actuators B* 10 (1993) 229-234.
- [4.32] H. Kuwabara, T. Okuhara, and M. Misono, "Catalytic removal of trimethylamine, an offensive-odor component, by selective oxidative decomposition to N<sub>2</sub>, CO<sub>2</sub>, and H<sub>2</sub>O over copper-exchanged zeolites", *Chem. Lett.* 1992 (1992) 947-950.





## Chapter 5

### 5. NO<sub>x</sub> and O<sub>2</sub> Sensing Properties of In<sub>2</sub>O<sub>3</sub> Thin Films grown by MOCVD

#### 5.1 Introduction:

Demands for exact monitoring of nitrogen oxide gases (NO<sub>x</sub>), which are air pollutants released from combustion facilities and automobiles, have become more serious all over the world in recent years. For air quality monitoring or exhaust gas control, NO<sub>x</sub> is the main gas to be detected. In order to detect the partial pressure of hazardous NO<sub>x</sub> gas, there have been a lot of efforts in developing a variety of sensors such as electrochemical [5.1], SAW [5.2], and polymer based sensors [5.3]. Recently, much interest has been focused on metal oxide based sensors because of their structural simplicity, high sensitivity, short response time, small size, low cost and good compatibility with the fabrication process for microelectronic devices. The semiconductor metal oxide (SMO) gas sensors operate on the principle that a chemical reaction between the gas species to be detected and a SMO sensing film produces a change in the film's resistance. Although several different metal oxide semiconductors can be used as gas sensing materials the most popular include, tin oxide (SnO<sub>2</sub>) [5.4-5.7], tungsten trioxide (WO<sub>3</sub>) [5.4, 5.8], titanium oxide (TiO<sub>2</sub>) [5.9-5.10], zinc oxide (ZnO) [5.4, 5.11] and indium oxide (In<sub>2</sub>O<sub>3</sub>) [5.4, 5.12-5.13]. It was found that indium oxide exhibits high sensitivity to oxidizing gases, such as NO<sub>x</sub> [5.14-5.15] and O<sub>3</sub> [5.12, 5.16] and therefore can be used as active layers in detectors for these gases.

Several methods have been used to prepare In<sub>2</sub>O<sub>3</sub> thin films, such as dc and rf sputtering [5.16-5.17], reactive evaporation [5.18-5.19], evaporation of metallic indium and subsequent oxidation [5.20-5.21], chemical vapour deposition [5.22], spray pyrolysis [5.23] sol-gel [5.14] and laser ablation [5.24]. Metal organic chemical vapor deposition (MOCVD) technique is a new and low cost approach for thin film deposition of indium oxide films which offers the opportunity to control the stoichiometry and morphology by varying the process parameters.

In this chapter the NO<sub>x</sub>, and O<sub>2</sub> sensing properties of In<sub>2</sub>O<sub>3</sub> thin films grown by MOCVD technique have been investigated as a function of the operation temperature and partial pressure.

## 5.2 Fundamentals of metal oxide gas sensors:

Metal oxide semiconductor gas sensors are used to monitor the content of oxidizing and reducing gas molecules in a surrounding medium (usually air). The operation principle of such a device is to transform, directly, the value of adsorption and desorption of oxygen into an electrical signal. The electrical signal is the conductivity of the sensing layer which changes due to the attendance of different gas ambients.

A schematic of a measurements chain to detect gases by means of metal oxides is shown in Fig. 5.1. The chemisorption mechanism describes the reaction process resulting in a resistance change. A transducer, which consists of the gas-sensing film and the substrate including electrodes and heating elements, converts a chemical quantity into an electrical quantity for purposes of a measurement. The display shows the resistance change, i.e. the sensitivity of a given gas-sensing device. The principle gases for which this type of sensor has found most widespread application are the lower hydrocarbons, However CO, H<sub>2</sub>, NO<sub>x</sub> and other gases have also been measured using this technique.

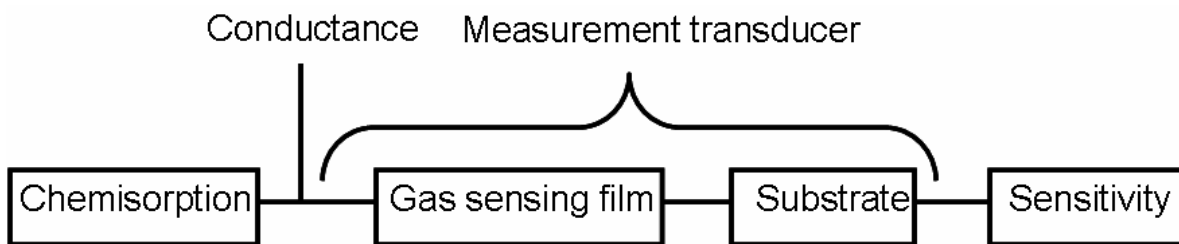


**Fig. 5.1:** Schematic of the measurements chain for gas-sensing application using metal oxides.

The principle manner in which these sensors operate can be summarised as follows: there is a finite density of electron donors (e.g. adsorbed hydrogen) and/or electron acceptor (e.g. adsorbed oxygen) bounded to the surface of a wide band gap semiconductor oxide, such as (SnO<sub>2</sub>, In<sub>2</sub>O<sub>3</sub>,...etc). The electron donors or acceptors cause the formation of surface states followed by an exchange of electrons within the interior of the semiconductor, thus forming a space charge layer close to the surface. By changing the surface concentration of the donors/acceptors, the conductivity of the space charge region is modulated.

### 5.2.1 Electrical conductivity of metal oxide semiconductor:

The charge carriers contributing to the electrical conductivity of a material are electrons, holes and ions. The overall scalar electrical conductivity is thus given by:

$$\sigma = \sum_i n_i \cdot q_i \cdot \mu_i, \quad (5.1)$$

where  $n_i$  is the carrier density,  $q_i$  is the carrier charge, and  $\mu_i$  is the mobility.

In intrinsic semiconducting metal oxides, the charge carriers are created by point defects in the bulk crystal lattice. These point defects are created by the non-stoichiometry of the metal oxide. The defects in the crystal can be Frenkel (Fig. 5.2) or Schottky defects [5.25]. Frenkel defects are caused by atoms moving their lattice positions into interstitial positions, whereas Schottky defects result from the diffusion of atoms to the semiconductor surface where they enter the gaseous phase leaving a void in the crystal. Depending on the predominant effects in the particular material, one finds oxygen voids  $V_o^*$  or interstitial metal atoms  $M_i$ . Excess oxygen yields a  $p$ -type semiconductor with mobile defect electrons (holes), excess metal yields an  $n$ -type semiconductor with mobile electrons. The charge carrier concentration thus increases with increasing proportion of oxygen ( $p$ -type) or metal ( $n$ -type) in the lattice.

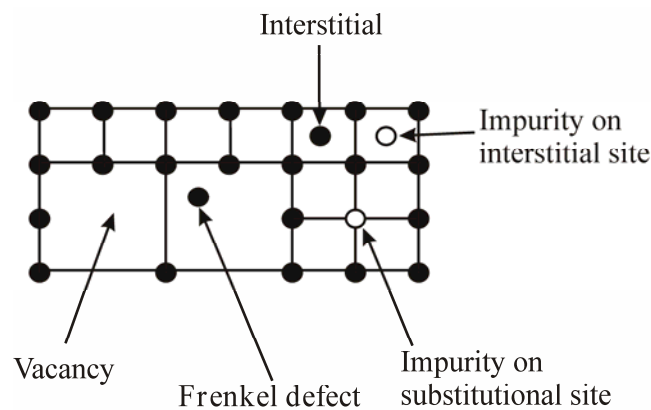


Fig. 5.2: Types of point defects on a simple crystal lattice [5.26].

The creation and equilibrium of the crystal defects is temperature dependent [5.27]. While at room temperature and up to several hundred degrees Celcius, the defect equilibrium is frozen, at high temperatures, depending on the metal oxide used

(e.g.  $\sim 800^\circ\text{C}$  for  $\text{Ga}_2\text{O}_3$ ), the lattice oxygen is in thermodynamic equilibrium with the ambient air oxygen partial pressure  $P_{\text{O}_2}$ .

The ionisation of the crystal defects is also temperature dependent. The free charge carrier concentration thus depends on the energy required for defect formation (Gibbs energy  $G_D$ ) and for ionisation  $E_I$ .

A hopping mechanism can be used to explain the electrical conductivity of semiconductors with low charge carrier mobility and high band gap [5.28]. I.e. in a p-type metal oxide the conductivity results from carrier dissociation or phonon induced hopping of holes from one void to another requiring a hopping activation energy. We thus obtain a temperature dependant carrier mobility  $\mu(T)$ . For *n*-type metal oxides similar hopping mechanisms have been postulated, where the electron hopping is hindered by defect potential barriers [5.28]. The defect concentration is again temperature dependant. At high defect concentrations electron tunneling through the potential barriers is possible. For all metal oxides we do however obtain an electrical conductivity following:

$$\sigma \cong \exp\left(\frac{E_A}{kT}\right). \quad (5.2)$$

$E_A$  being the activation energy consisting of the energy required for defect creation, the energy required for ionisation of the charge carriers and the temperature dependent hopping energy [5.29].

### 5.2.2 Structure and equivalent circuit models:

The basic structure for a metal oxide semiconductor sensor consists of a metal oxide film and contact electrodes. The film either has an amorphous or polycrystalline microstructure. To obtain an amorphous structure the film deposited at room temperature and is not heat-treated after deposition.

An amorphous film is highly disordered and exhibits no periodicity, which helps to eliminate the effects of the intercrystalline boundaries. In an equivalent circuit, it can be represented as a resistor between the two contacts (Fig. 5.3a). The dc equivalent circuit for the amorphous film in Fig. 5.3a includes the electrode finger resistance,  $R_s$ , the metal-semiconductor junction resistance,  $R_c$ , and the resistance between the two contacts,  $R_g$ .

Polycrystalline films are deposited at higher temperature or annealed after deposition. A polycrystalline film consists of many randomly orientated microcrystalline regions, each of which exhibits periodicity. Each semiconductor crystallite is connected with its neighbours by a grain boundary (Fig. 5.3b). Electrons can move across the potential barrier at each boundary. The gas-film interaction can change the barrier height and the number of free carriers, which results in a change of the electrical resistance of the film. In case of the polycrystalline film (Fig. 5.3b), it is assumed that the film consists of only a single layer of crystallites. In addition to  $R_s$  and  $R_c$ , the dc equivalent circuit includes the grain boundary resistance,  $R_{bi}$ , and the individual crystallite resistances,  $R_{gi}$  ( $i = 1, \dots, n$ ). One can combine each of the circuit elements to obtain an equivalent resistance for the sensing element. When significant interactions occur between the sensing element and the gas measured the values of the resistive circuit elements change.

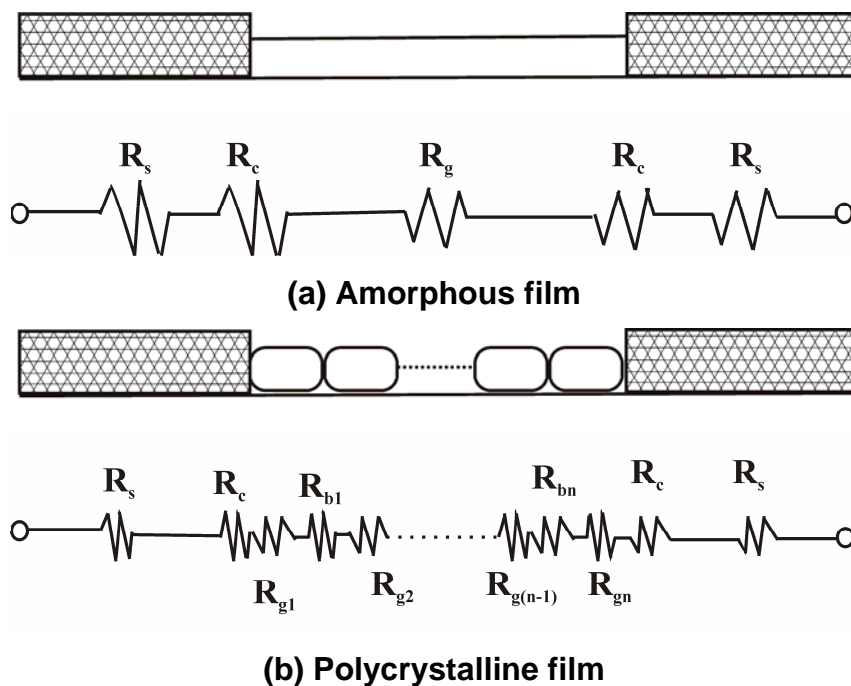


**Fig. 5.3:** Physical structure and equivalent circuit of a semiconducting metal oxide sensing element for (a) amorphous film and (b) polycrystalline film [5.30].

### 5.2.3 Sensing mechanism of metal oxide semiconductor gas sensor:

Metal oxide semiconductor gas sensors detect gases via variation in their resistance (or conductance). The gas-sensing mechanism in the case of  $n$ -type semiconductor can be described in detail via a chemisorption process combined with a charge

transfer process at the n-semiconductor surface at temperatures above 100°C. This process makes it possible to use semiconducting gas sensors having a fast and appreciable interaction of the surrounding gas molecules with the surface.

At temperatures below 100°C, the oxygen molecules are adsorbed by a physisorption process. At room temperature, the coverage of physisorbed molecules is less than one monolayer. This process is accomplished by weak van der Waals forces. The binding forces are very small (20 kJ/mol~0.2 eV per molecule) and the molecules are mobile on the surface of the semiconductor without changing their electrical properties. The low value of the physisorption enthalpy of about 20 kJ/mol causes physisorption to disappear almost totally at higher temperatures. The activation energy for diffusion jumps of physisorbed molecules is smaller than the adsorption energy. Consequently, the probability that a molecule jumps to a neighbouring site is greater than in the desorption process [5.31].

Where a metal-oxide semiconducting gas sensor is used at temperatures below 100°C, additional equipment is required. It has been demonstrated that UV light illumination can be used to enhance the sensitivity of SnO<sub>2</sub> thin film gas sensors to nitrogen dioxide (NO<sub>2</sub>) [5.32]. Photoexcitation can affect the charge carrier transport across grain boundaries by increasing the density of free carriers throughout the material and decreasing the intergrain barrier height.

At higher temperatures (>100°C), oxygen molecules are dissociated via a chemisorption process. Firstly, oxygen is connected via dipole bonding to the semiconductor surface atoms. Under this condition, electrons are removed from the semiconductor surface via a charge transfer mechanism; this is followed by the formation of chemical bonds with the semiconductor surface atoms. The bond and activation energy of the surface reaction depends on the lattice and defect structure of the surface. Active sites for a chemisorption reaction can be normal sites, adatoms, dislocation cores or impurity atoms. The reactants can be impinging gas molecules, electrons, and atoms or defects on the regular charge or on specific sites of the substrate. The chemisorption species can have an electrical charge and consist of one or more atoms. It is assumed that oxygen vacancies are primarily responsible for the chemisorption reaction. Typical chemisorption species on the surface of semiconductive metal oxides in air are  $O_2^-$ ,  $O^-$ , and  $O^{2-}$  [5.33]. The case of *n*-type semiconductive metal oxides, the formation of these oxygen adsorbates builds a space-charge region on the surfaces of the metal-oxide grains, resulting in

an electron-depleted surface layer (Fig. 5.4a). Due to the electron transfer from the grain surfaces to the adsorbates it follows:



The depth of this space-charge layer ( $L$ ) is a function of the surface coverage of oxygen adsorbates and intrinsic electron concentration in the bulk. The resistance of an n-type semiconductor gas sensor in air is therefore high, due to the development of a potential barrier to electronic conduction at each grain boundary, as shown in Fig. 5.4a.

Reducing gases (R), i.e. gases which cause a reduction of the chemisorbed oxygen on the surface of the metal-oxide, react as expressed as follows:



As an example, the reaction of CO with the surface of tin oxide is shown thus:

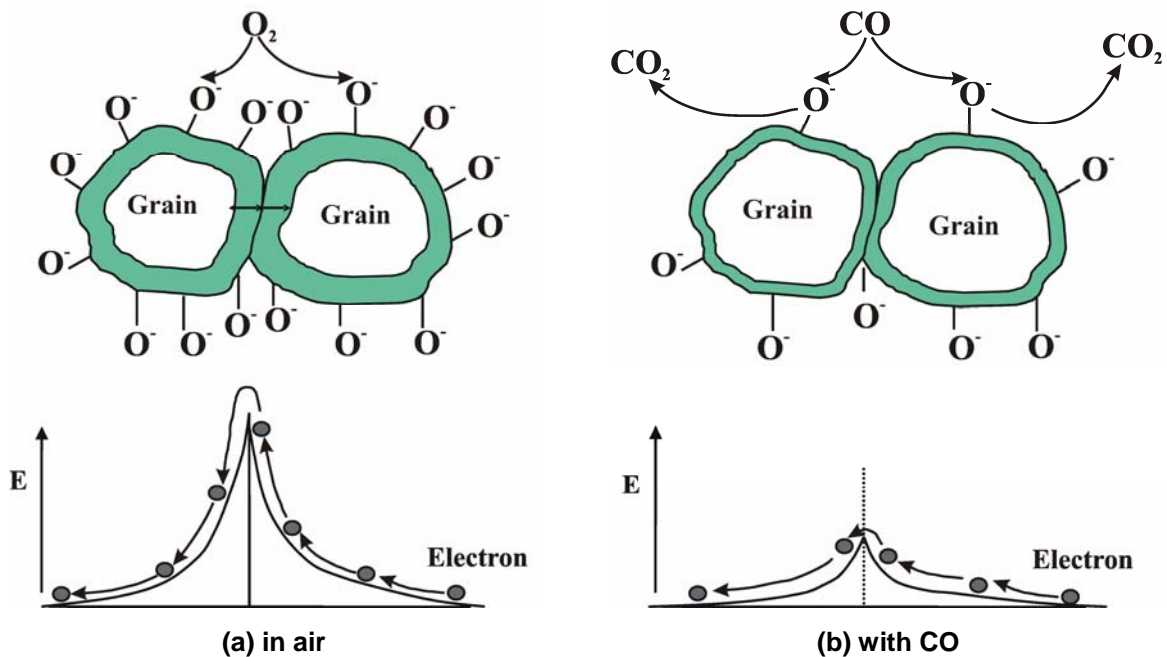


**Fig. 5.4:** Grain contact model and barrier control scheme (a) when O<sub>2</sub> molecules adsorb at the grain boundaries, a space charge region is induced. This causes a large energy barrier between the grains (below). (b) In a reducing atmosphere such CO molecules the space-charge region becomes smaller and the potential barrier decreases [5.26].

Due to the reaction with a reducing gas, free charge carriers are replaced within the conduction band, whereas the reaction product desorbs thermally from the

semiconductor surface. A lower surface coverage of the oxygen adsorbates is obtained, leading to a drop in resistance (Fig. 5.4b). As long as the oxygen partial pressure is constant, the conductivity of the semiconductor is proportional to the concentration of the reducing gas in the atmosphere, and the gas sensor can be used for detection. The metal oxides such  $\text{SnO}_2$  can also react with the oxidizing gases such as ozone ( $\text{O}_3$ ), NO and  $\text{NO}_2$ . It is assumed that NO gas in the presence of oxygen in air tends to oxidize into  $\text{NO}_2$  which can be adsorbed or can interact with the oxygen adsorbed on to the sensor surface as expressed here under [5.34]:



The NO gas molecules that have not reacted with the oxygen in air can, at the same time, be adsorbed on to the oxide surface; they then react with the adsorbed oxygen. In this case, the reaction will be:



These reactions reduce the electron concentration and, therefore, an increase in the electrical resistance occurs.

Since the charge carriers in *p*-type semiconductor metal oxides are positive holes, the resistance in air is low because of the formation of negatively charged oxygen adsorbates, and the extraction of electrons from the bulk eventually enhances the concentration of holes in the grain surface. Then, the consumption of oxygen adsorbates by reaction with reducing gases leads to an increase in resistance, which is the reverse of the case for *n*-type metal oxides. Conversely, the adsorption of oxidizing gases on *p*-type metal oxides results in a decrease in resistance.

#### 5.2.4 Effects of grain size and the geometry of grain connections:

One of the most important factors affecting sensing properties of metal oxides is the actual grain or crystallite size  $D$  of the sensor material in conjunction with the space-charge depth  $L$ . Xu *et al.* [5.35] assumed two different grain joining structures: grain boundary contacts and necks, that may coexist in the same material. In the first case, electrons should move across a potential barrier at each grain boundary, as shown in Fig. 5.4. If there are no necks structures, the gas sensitivity is controlled by the barrier height and is almost independent of the grain size. When grains are



connected by neck structures, charge carriers move through a channel formed at each neck, where the resistance is lower than in the depletion region formed close to the surface, as shown in Fig. 5.5. Since the cross-section of each channel is controlled by the space-charge depth, sensitivity in this case will be highly dependent on the grain size.

In the model developed by Xu et al. [5.35], it was assumed that necks had a diameter of  $0.8D_{gr}$ , where  $D_{gr}$  is the mean grain size, and the sensing layer is composed by grains connected mostly by necks and sometimes by grain boundary contacts. Supposing that the space-charge layer had depth  $L$ , there would be three different conduction regimes: grain boundary controlled, neck controlled and grain controlled.

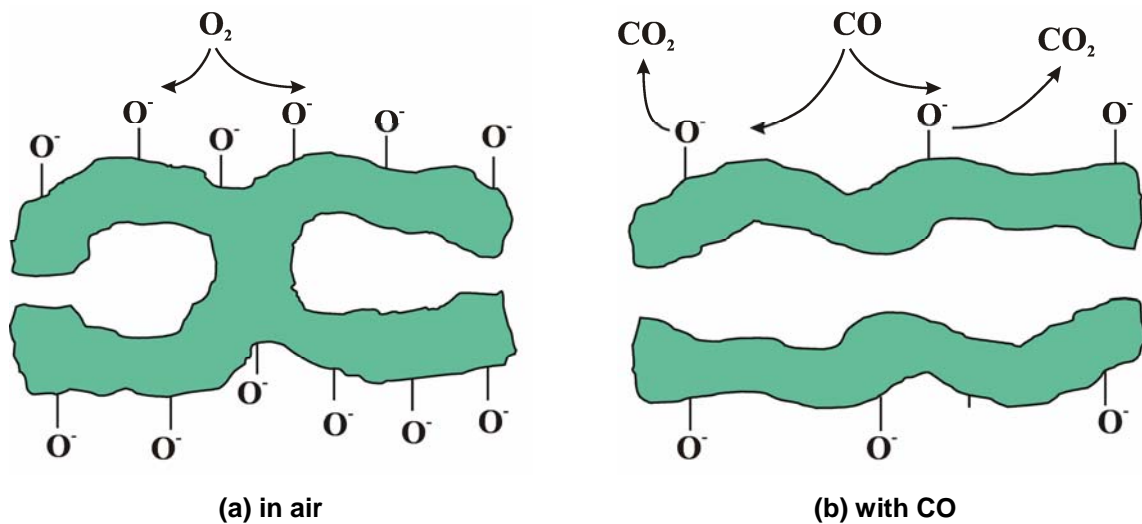


Fig. 5.5: Neck model and space charge layer formation [5.26].

Grain boundary controlled develops when  $2L$  is much smaller than  $D_{gr}$ . In this case the contact resistance between grains is much larger than the bulk resistance of the grains and thus the contact resistance variations will control the current flow through the layer. Neck control arises when  $D_{gr}$  is comparable with  $2L$ . In this case, since the space-charge layer resistance is much larger than the bulk resistance of the grain, the neck resistance will control the current flow. Finally, when  $D_{gr}$  is lower than  $2L$  the grain resistance will control the current flow.

If a compact thin film was used, instead of a porous film, a situation similar to the one described above as neck controlled could be obtained, provided that the film

thickness,  $d_f$  was comparable to the depletion layer depth,  $L$ . This case is illustrated in Fig. 5.6.

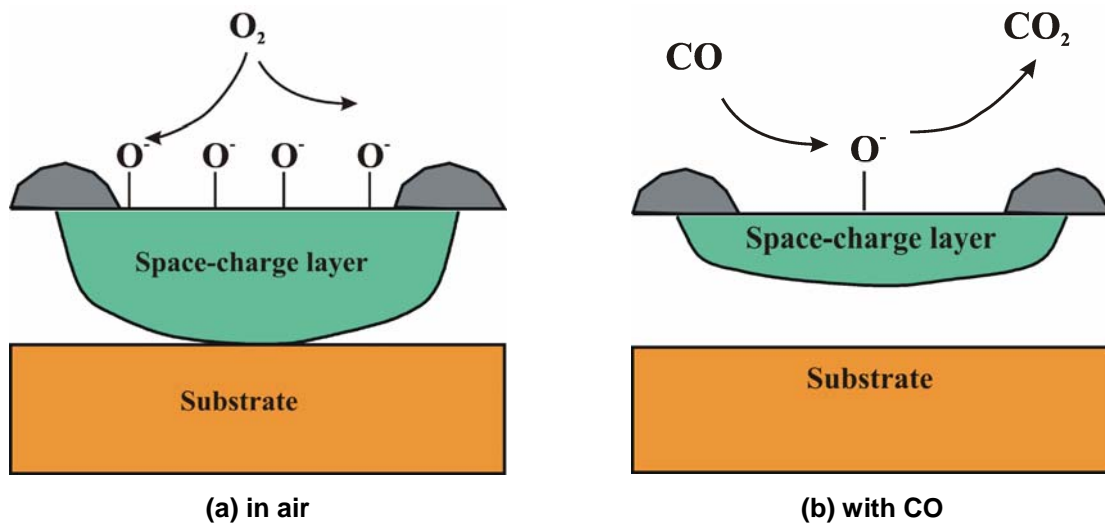


Fig. 5.6: Thickness control on very thin films [5.26] .

### 5.3 $In_2O_3$ properties:

Indium oxide is a very interesting material for many different applications. In its stoichiometric form ( $In_2O_3$ ) it behaves as an insulator. Indium oxide prepared in oxygen deficient form ( $InO_x$ ), it can reach high  $n$ -type doping levels as a result of intrinsic defects, namely, oxygen vacancies [5.36]. Thus, a variety of electrical properties can be obtained (metallic, semiconducting, or insulating behaviour) depending on the stoichiometry, without any further impurity doping. Furthermore,  $InO_x$  shows high transparency in the visible region of the electromagnetic spectrum due to a wide band gap of approximately 3.7 eV [5.37] and high reflectivity in the infrared region. This combination of electrical and optical properties favors  $InO_x$  for numerous applications as, for example, transparent conductive electrodes in flat-panel displays and solar cells, coating for architectural glasses [5.38], and grating material in optoelectronic devices [5.39].

Furthermore, indium oxide is used as semiconducting gas sensor due to its conductivity changes when it is exposed to oxidizing gases such as ozone [5.12, 5.16] and  $NO_x$  [5.14-5.15]. A wide range of deposition technologies has been used for the preparation of indium oxide films, such as dc and rf sputtering [5.16-5.17], reactive evaporation [5.18-5.19], evaporation of metallic indium and subsequent oxidation [5.20-5.21], chemical vapour deposition [5.22], spray pyrolysis [5.23] sol-gel [5.14] and laser ablation [5.24].

The crystal structure of  $\text{In}_2\text{O}_3$  at normal pressure and room temperature is a fluorite-related cubic bixbyite type with 80 atoms in the unit cell. One fourth of the anions are missing. The lattice parameter is 1.0118 nm.

Fig. 5.7 presents the crystal structure of  $\text{In}_2\text{O}_3$ . The two non-equivalent  $\text{In}^{3+}$  ion positions have six-fold symmetry. The  $\text{O}^{2-}$  ions are arranged in fourfold symmetry.  $\text{In}_2\text{O}_3$  may be intrinsically doped by introducing oxygen vacancies ( $V_o^{**}$ ) in the lattice. Each oxygen vacancy contributes with two electrons to the conduction band.

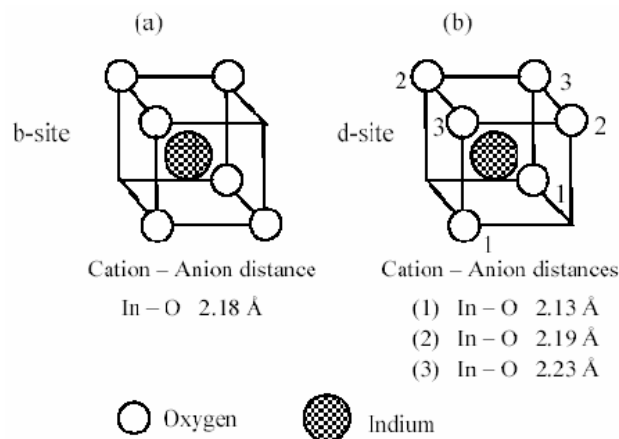


Fig. 5.7:  $\text{In}_2\text{O}_3$  crystal structure with two non-equivalent indium sites,  $\text{In}_b$  (a) and  $\text{In}_d$  (b) [5.40].

#### 5.4 Nanocrystalline materials:

Solids with a grain size of a few nanometer are normally referred to as nanocrystalline materials. Nanocrystalline (nc) materials make up a group of materials attracting a great deal of interest both from a fundamental and from an applied point of view. This is due to the fact that these materials display a large surface to bulk ratio, which distinguishes them from bulk materials.

A nanocrystalline material contains a high concentration of grain boundaries or in the case of porous films, a large internal surface compared to the case of a bulk material. These properties are of considerable importance for electrical transport, optical, and mechanical properties and gas sensing application. When it comes to the electrical transport properties of nc-materials, especially in nc-metals and heavily doped semiconductors, the electrical dc conductivity is very much affected by the microstructure and mainly by the grain boundaries. Tab. 5.1 presents some basic properties of nanocrystalline materials and their application.

**Tab. 5.1:** Some basic properties and applications of nanoparticles and nanocrystalline materials.

Property	Application
Wavelength selective optical absorption	Solar collectors
High flow stress	Jet engines
Giant magnetoresistance	Reader heads in computer
High magnetic coercive force	Data storage
Large surface-to-bulk ratio	Sensors

Nanocrystalline materials are classified into different categories depending on the number of dimensions which are nano-structured: the generally acknowledged classification is [5.41] layered nano-structures (one nano-structured dimension, 1D), filamentary structures (2D), and equiaxial nano-structured materials (3D). The realization and the study of 1D and 3D nanostructures were actively explored, whereas the 2D structures have been less investigated. For gas sensing, typically a three-dimensional (3D) nanostructure is considered. However, 3D nanostructures often highlight a tendency to change the electrical properties owing to grain coalescence, porosity modification, and grain-boundary alteration. The problem becomes still more complex because the layers must be kept at a relatively high temperature in order to guarantee the reversibility of chemical reactions at the surface. Thus, several solutions have been put forward to stabilize the nanostructure, e.g., addition of a foreign element [5.42] or phase [5.43]. A technique that renders the material sufficiently crystalline to guarantee long-term stability while maintaining a high sensitivity would be the optimal.

### 5.5 Films deposition and sensor structure:

The growth of  $\text{In}_2\text{O}_3$  thin films was carried out in a horizontal MOCVD reactor (AIXTRON 200). Trimethylindium (TMIn) and  $\text{H}_2\text{O}$  vapor were used as indium and oxygen precursors, respectively. The  $\text{In}_2\text{O}_3$  thin films were synthesized on sapphire (0001) substrates by supplying TMIn and  $\text{H}_2\text{O}$  vapor with flow rates of 15 and 1160  $\mu\text{mol}/\text{min}$ , respectively.

The substrate temperature varied in the range of 150 and 600°C. Highly-textured  $\text{In}_2\text{O}_3$  films with a thickness of  $\sim 200$  nm were obtained at a substrate temperature of 600°C by using a 10 nm thick low-temperature (300°C) grown  $\text{In}_x\text{O}_y$  nucleation layer (sample A) [5.44]. nano-structured  $\text{In}_2\text{O}_3$  with a thickness of  $\sim 10$  nm

was deposited at a substrate temperature of 200°C and process pressure of 200 mbar (sample B). Samples for gas testing were prepared by sputtering two Ni contacts onto the film surface in a gap configuration. Fig. 5.8 shows cross section of the studied sensors. The active area of the sensor was  $5 \times 1 \text{ mm}^2$ .

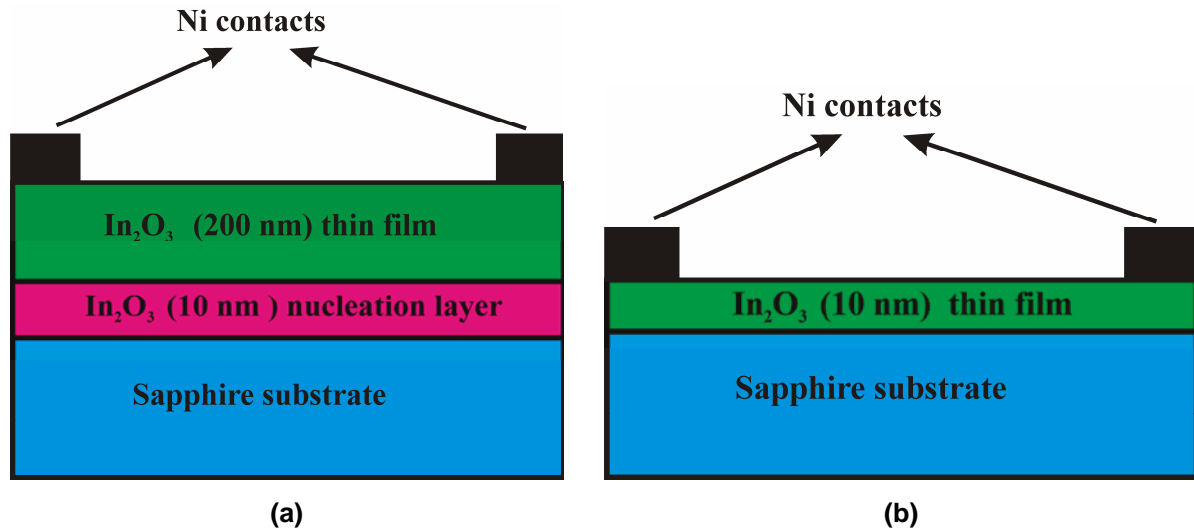


Fig. 5.8: Device cross section of the studied  $\text{In}_2\text{O}_3$  gas sensors. (a) sample A. (b) sample B.

## 5.6 Experiments:

### 5.6.1 Film characterization:

After growth, the  $\text{In}_2\text{O}_3$  thin films were *ex-situ* characterized by means of scanning electron microscopy (SEM), atomic force microscopy (AFM), high-resolution transmission electron microscopy (HRTEM) and x-ray diffraction (XRD).

### 5.6.2 Gas sensing measurements:

For gas sensing tests, the sensors were mounted in an UHV system described in chapter 3 (section 3.5.2). The sensors were placed directly into a quartz tube, which was pumped to a base pressure of  $4 \times 10^{-8}$  mbar. Fig. 5.9 shows schematic drawing of the UHV apparatus for this experiment and all devices mounted in it. For measurements of the response and dynamic behaviour of the sensors, a source-measure-unit (model 2000, Keithley Instr./Germany) with an external voltage source was used. The instruments were connected via an IEEE-488 bus to the computer.

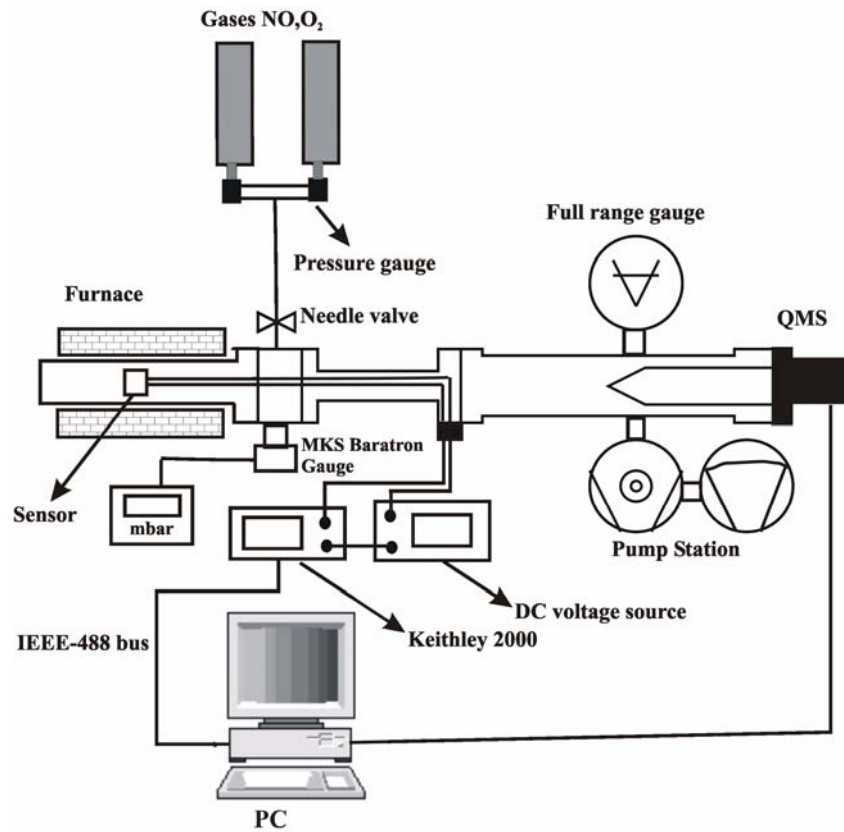


Fig. 5.9: Schematic drawing of gas measurements system.

The sensor resistance is determined under various partial pressures of the test gases and temperatures by applying a constant ac voltage and measuring the current  $I$ . The response and recovery of the films exposed to different gas partial pressures were obtained by plotting their resistance as a function of time. The recovery process has been accelerated by UV-light ( $\lambda = 365$  nm) with an output power of 1.4 mW. The sensors were heated during operation at different temperatures using a furnace. The temperature was measured by a thermocouple type K (NiCr-Ni) (see **Appendix A**) placed a few millimetres above the sensor. The operating temperature was varied from room temperature to 300°C to determine the optimum response, which was defined by:

$$R = \frac{R_g}{R_v}, \quad (5.9)$$

where  $R_v$  is the stable base resistance in vacuum (after 20 min UV-light exposure) and  $R_g$  the resistance after 10 min of gas exposure.

The sensitivity  $S$  is given by:

$$S = \frac{R}{C_g [\text{mbar}]}, \quad (5.10)$$

where  $C_g$  is the gas partial pressure in mbar.

## 5.7 Results and discussion:

### 5.7.1 Characterization of the $\text{In}_2\text{O}_3$ thin films:

Fig. 5.10 presents the grain size in dependence on the substrate temperature in the range of 150 and 600°C. The grain size increases from ~ 3 nm up to ~ 270 nm by increasing the substrate temperature from 150 to 600°C.

The activation energy of the first part between 150 and 400°C was determined to be  $0.5 \pm 0.03$  eV. At high substrate temperatures, well developed grains having a triangle or square shape, which correspond to the (111) and (100) oriented  $\text{In}_2\text{O}_3$  grains, respectively, can be observed. It was also reported that large grains which are in-plane rotated by 30° with respect to each other can be deposited at high substrate temperatures by MOCVD [5.44]

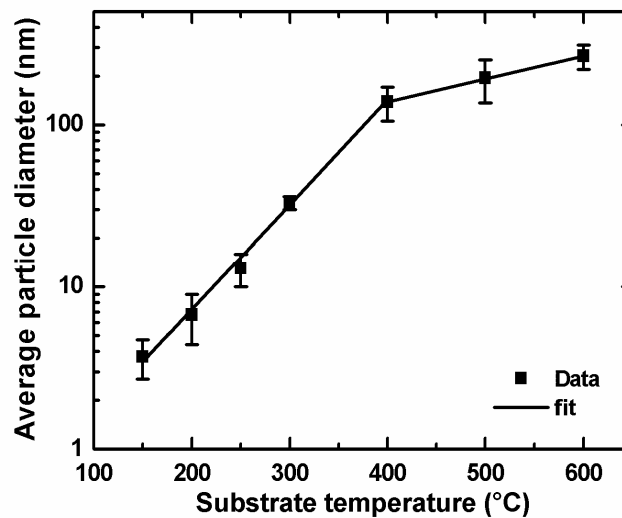
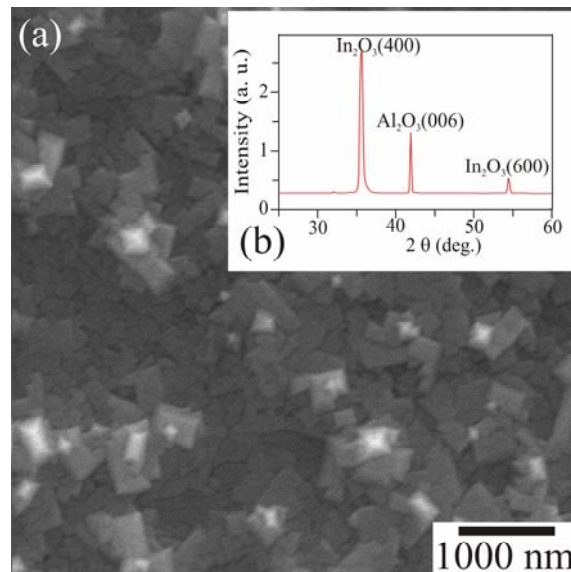


Fig. 5.10: Particle size dependence on the substrate temperature.

### Sample A: Polycrystalline $\text{In}_2\text{O}_3$ (thickness: 200 nm, grain size: 270 nm):

Fig. 5.11a shows the SEM image of a highly-textured  $\text{In}_2\text{O}_3$  thin film with the thickness of ~ 200 nm. Well developed grains which are in-plane rotated by 30° with respect to each other [5.44] can be apparently seen in the SEM image. The surface

root-mean-square roughness was determined to be  $\sim 4$  nm by atomic force microscopy. By using a low-temperature deposited  $\text{In}_2\text{O}_3$  nucleation layer followed by the high-temperature process, highly textured  $\text{In}_2\text{O}_3$  films were obtained. A Cu  $K\alpha$  X-ray diffraction pattern of the *as deposited*  $\text{In}_2\text{O}_3$  films is shown in Fig. 5.11b. The diffraction pattern revealed two peaks at  $35.49^\circ$  and  $54.46^\circ$ , corresponding to the (400) and (600) diffraction peaks of body-centered cubic indium oxide, respectively.



**Fig. 5.11:** (a) SEM image of highly-textured  $\text{In}_2\text{O}_3$  thin films. (b)  $\theta$ - $2\theta$  XRD pattern of the bcc- $\text{In}_2\text{O}_3$  thin films deposited on the (0001) sapphire substrate.

### Sample B (Nano-structured $\text{In}_2\text{O}_3$ thin films (thickness: 10 nm, grain size: 7 nm)):

Fig. 5.12a shows the HRTEM image of nano-structured  $\text{In}_2\text{O}_3$  thin films with a thickness of  $\sim 10$  nm. The particle containing layer was deposited at a substrate temperature of  $200^\circ\text{C}$  and process pressure of 200 mbar by MOCVD. The particles having an orientation of (222) and (400) can be obviously seen in Fig. 5.12a. A fast-Fourier filtered image of the  $\sim 10$  nm particle containing layer is presented in the inset of Fig. 2 (a). Typical ring structure reveals the two main planes corresponding to (222) and (400) of cubic  $\text{In}_2\text{O}_3$  phase. A number of HRTEM micrographs taken from different sample areas were analyzed to obtain the size distribution of the deposited particles, as shown in Fig. 5.12b. The mean diameter of the  $\text{In}_2\text{O}_3$  nanoparticles were derived to be  $\sim 7$  nm for the layers grown at  $200^\circ\text{C}$ .



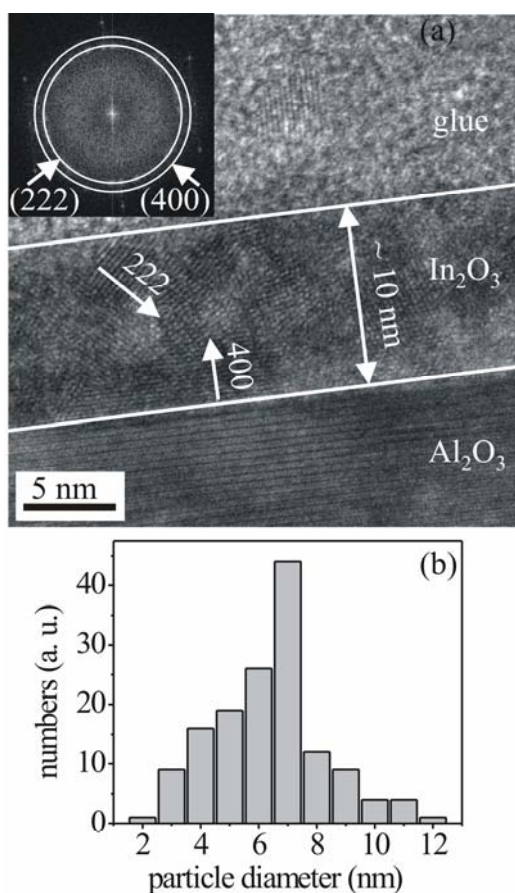


**Fig. 5.12:** (a) HRTEM image of as grown nano-structured  $\text{In}_2\text{O}_3$  thin film with a thickness of  $\sim 10$  nm. The inset shows the fast-Fourier filtered image of the thin film. (b) Size contribution of the  $\text{In}_2\text{O}_3$  nanoparticles.

## 5.7.2 Gas sensitivity:

### 5.7.2.1 Sample A:

#### 5.7.2.1.1 $\text{NO}_x$ detection:

Firstly, the sensors were tested for the response to  $\text{NO}_x$  gas with partial pressures starting from 0.002 to 10 mbar (pure  $\text{NO}_x$ ) at temperatures between room temperature and  $250^\circ\text{C}$ . Fig. 5.13 presents the resistance variation versus time as a function of the successive increase of  $\text{NO}_x$  partial pressure at a working temperature of  $150^\circ\text{C}$ . The resistance of  $\text{In}_2\text{O}_3$  thin films increases after exposure to the oxidizing gas  $\text{NO}_x$  and it returns to the initial value when the  $\text{NO}_x$  gas is removed.

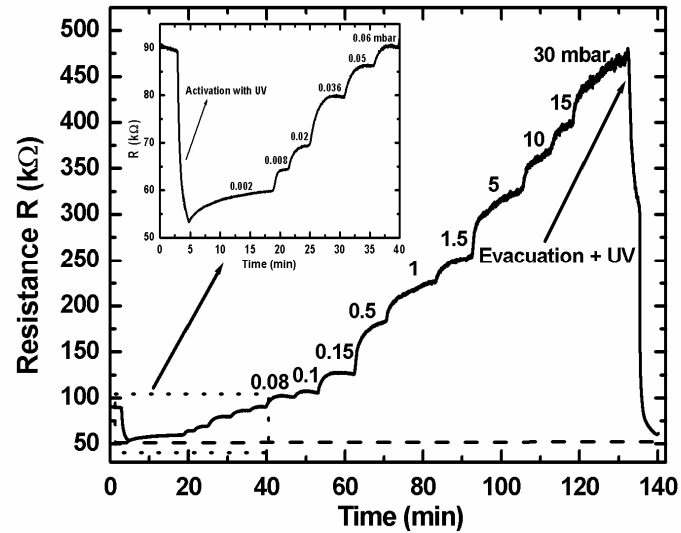


**Fig. 5.13:** Resistance variation versus time as a function of successive increase of  $\text{NO}_x$  partial pressure at a working temperature of  $150^\circ\text{C}$ .

It is well known that *n*-type semiconductor have higher resistance in an oxygen or  $\text{NO}_x$  ( $\text{NO}$  and  $\text{NO}_2$ ) ambient as compared to that in vacuum [5.45]. This is because if an electronegative molecule such as oxygen or  $\text{NO}_x$  is approaching the semiconductor surface and its electron affinity  $\chi$  is larger than the semiconductor work function  $\Phi_s$ , the molecule will tend to pick up an electron from the semiconductor conduction band and become chemisorbed at the surface. The net result of the chemisorption of the acceptor-type gas such as oxygen or  $\text{NO}_x$  on *n*-type semiconductor surface is a decrease in electron concentration in the conduction band near the semiconductor surface, and hence a decrease in the conductance close to the surface.

The variations of normalized resistances at five different operation temperatures for 0.01 mbar  $\text{NO}_x$  exposure is shown in Fig.5.14. At low operating temperature, the sensor responded slowly and higher operating temperature caused faster response. At the same time, if the temperature is higher, the interaction will be stronger. Therefore, the recovery time becomes longer at higher operation temperatures.

In particular, as the operating temperature increases from room temperature to  $250^\circ\text{C}$ , the response time decreases from 11 min to 15 s but the recovery time increases from 100 s to 40 min as shown in Fig. 5.15.

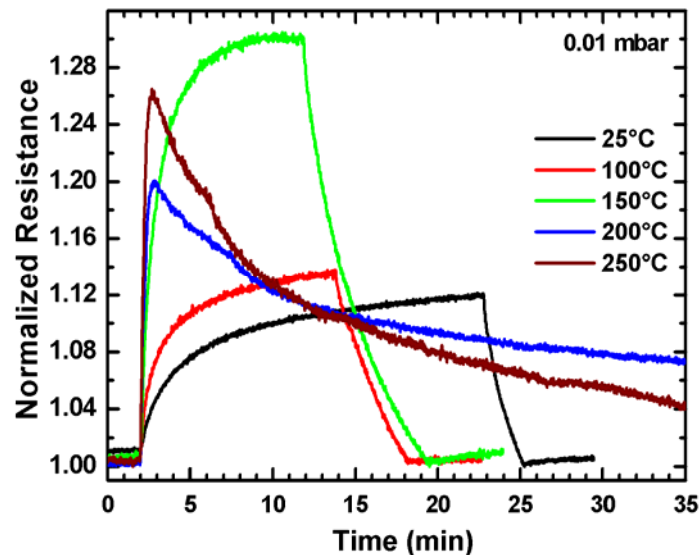


**Fig. 5.14:** Variation of the magnitude of normalized resistance at five different operation temperatures for 0.01 mbar  $\text{NO}_x$ .

In this work we have defined the response time as the time required for the sample resistance to reach 90% of the equilibrium value, while we define the recovery time as the time necessary for the sample to return to 10% above its original resistance in vacuum.

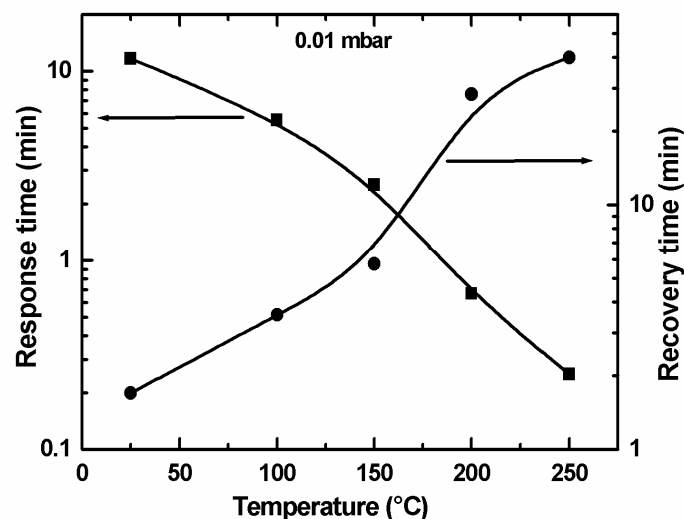


**Fig. 5.15:** The response and recovery times as a function of temperature for 0.01 mbar of  $\text{NO}_x$ .

Fig. 5.16 provides the response and recovery of  $\text{In}_2\text{O}_3$  thin films upon introduction and removal of varying  $\text{NO}_x$  partial pressures at room temperature and  $100^\circ\text{C}$ , respectively. The response (recovery) was found to become faster (slower) with

increasing gas partial pressure. But the film resistance can return to exactly its initial value after a few minutes. Taking into account the response amplitude and the response, as well as the recovery times, the experimental results indicate that the optimal operating temperature of the sensor for  $\text{NO}_x$  is  $150^\circ\text{C}$  (Fig. 5.14).

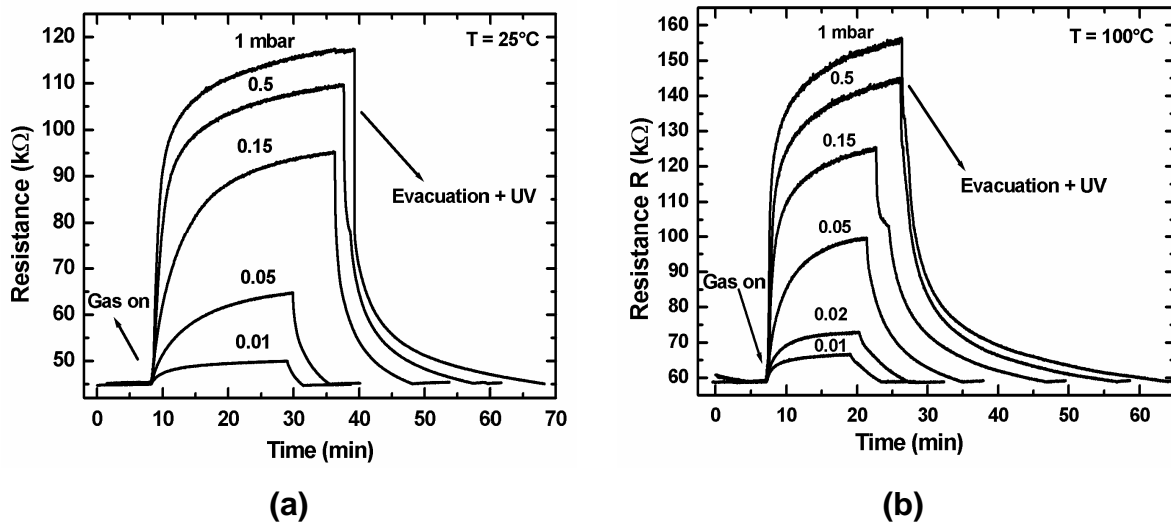


**Fig. 5.16:** The changes of resistance versus time upon introduction and removal of varying  $\text{NO}_x$  partial pressures at **(a)** room temperature and **(b)**  $100^\circ\text{C}$ .

Temperature is a very important parameter of the sensor because, if it is different for various gaseous species, it can be related to the selectivity. When it is in a low range of values it offers the possibility to perform a sensor with a low cost of energy consumption. Fig. 5.17 shows the dependence of response  $R$  and the sensitivity  $S$  on the partial pressure of  $\text{NO}_x$  (calibration curves) at different operating temperatures.

We have found that the response to  $\text{NO}_x$  increases non-linearly with increasing partial pressure and no complete saturation was observed even at partial pressures of up to 30 mbar. The non-linear response to increasing partial pressures of  $\text{NO}_x$  may be due to the filling of adsorption sites on the  $\text{In}_2\text{O}_3$  surface, which proportionally decrease as the concentrations increase.

This dependence of the sensitivity  $S$  on partial pressures of  $\text{NO}_x$  follows the well-known power law for metal-oxide semiconductor sensing films,  $a(P_{\text{NO}_x})^b$  [5.46]. Different fits, with this equation, were made and the values for the coefficients  $a$  and  $b$  as well as the coefficient  $R^2$  are summarized in Tab. 5.2.

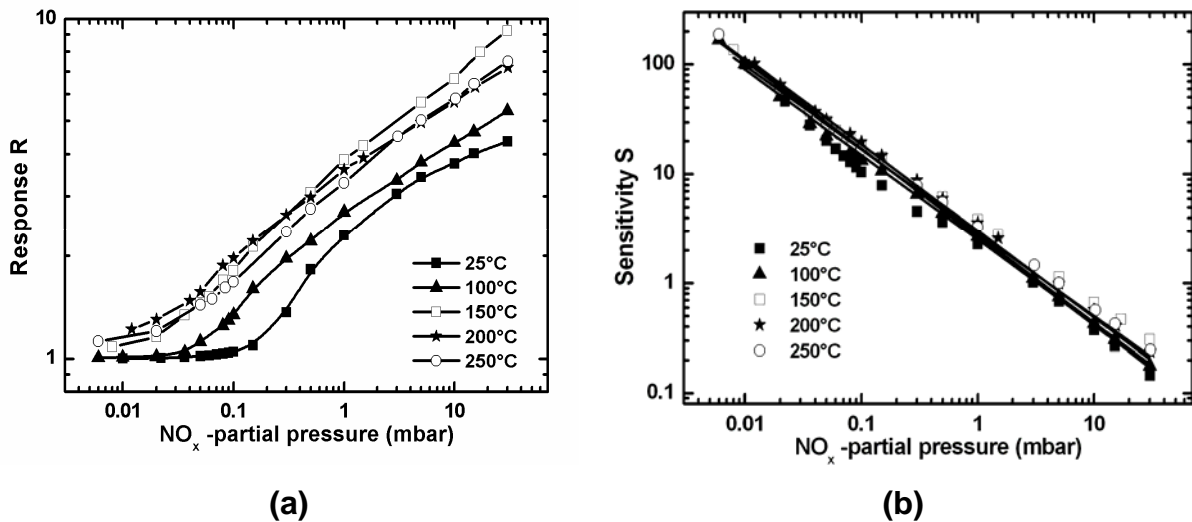


**Fig. 5.17:** The dependence of response R (a) and the sensitivity S (b) on the partial pressures of NO<sub>x</sub> at different temperatures.

The slopes of the lines in the log-log plot (Fig. 5.17b) are different and dependent on the operation temperature. A higher value of the exponent  $b$  allows an easier distinction between two partial pressures, while a lower value rises the lowest partial pressure which can be measured. If we are interested in the determination of high partial pressures, we can operate the sensor at 150°C, since the slope is higher. Otherwise, if we are interested in lower partial pressures, we should work at 250°C because at this temperature the detection limit is lower.

**Tab. 5.2:** Fitting parameter of the sensitivity S curves at several temperatures.

Temperature (°C)	Allometric1 $S = a(P_{NO_x})^b$		R <sup>2</sup>
	a	b	
25	2.51 ± 0.48	-0.77 ± 0.05	0.968
100	2.74 ± 0.47	-0.79 ± 0.03	0.987
150	2.90 ± 0.67	-0.76 ± 0.05	0.974
200	3.01 ± 0.14	-0.79 ± 0.01	0.998
250	2.67 ± 0.65	-0.8 ± 0.05	0.984

#### 5.7.2.1.2 O<sub>2</sub> detection:

In the second step the sensors were tested for the response to O<sub>2</sub> gas with partial pressures ranging from 0.006 up to 30 mbar (pure O<sub>2</sub>) at temperatures between 25

and 300°C. The dependence of the response  $R$  and the sensitivity  $S$  on the partial pressure of  $O_2$  at different operating temperatures is shown in Fig. 5.18.

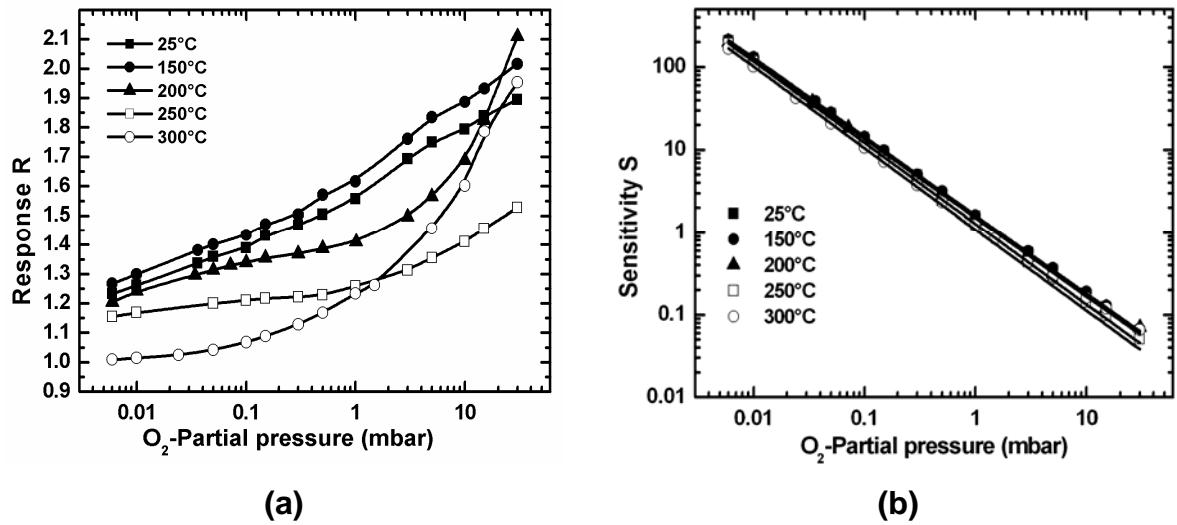


**Fig. 5.18:** The dependence of response and sensitivity on the partial pressures of  $O_2$  at different operating temperatures.

The response increases with increasing partial pressure of  $O_2$ . The maximum response to  $O_2$  is observed at 150°C. We have found that the sensitivity  $S$  decreases linearly with increasing partial pressure. This dependence of  $S$  on partial pressures of  $O_2$  was fitted with the power law  $a(P_{O_2})^b$  and the values for the coefficients  $a$  and  $b$  as well as the coefficient  $R^2$  are summarized in Tab. 5.3.

**Tab. 5.3:** Fitting parameter of the sensitivity  $S$  curves at several temperatures.

Temperature (°C)	Allometric1 $S = a(P_{O_2})^b$		$R^2$
	a	b	
25	$1.55 \pm 0.002$	$-0.95 \pm 0.0003$	1
150	$1.61 \pm 0.004$	$-0.95 \pm 0.0005$	1
200	$1.51 \pm 0.018$	$-0.95 \pm 0.002$	0.999
250	$1.27 \pm 0.006$	$-0.98 \pm 0.001$	1
300	$1.08 \pm 0.008$	$-0.98 \pm 0.001$	0.999

### 5.7.2.1.3 Conclusion:

The dependence of the response to 0.1, 0.15, 0.3 and 1 mbar of pure  $\text{NO}_x$  and  $\text{O}_2$ , on the operating temperature is presented in Fig. 5.19. It becomes obvious from Fig. 5.19 that the optimum detection temperatures occur in the range of 150–200°C for  $\text{NO}_x$  considering the response and the response time. In this range of temperatures the response to  $\text{O}_2$  is very low indicating that the sensor is very suitable for selective detection of  $\text{NO}_x$ .

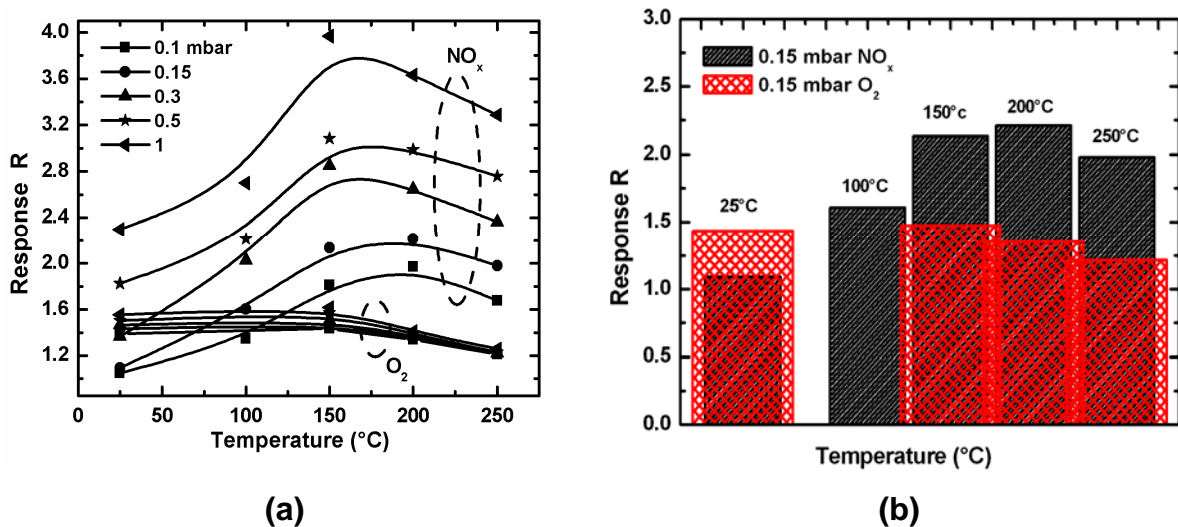


**Fig. 5.19:** (a) the dependence of the response to 0.1, 0.15, 0.3 and 1 mbar of pure  $\text{NO}_x$ , and  $\text{O}_2$ , on the operating temperature. (b) Block presentations for 0.15 mbar of the both gases.

### 5.7.2.2 Sample B:

#### 5.7.2.2.1 $\text{NO}_x$ detection:

The sample B was tested for the response to  $\text{NO}_x$  with partial pressures from 0.0002 up to 200 mbar at temperatures varied from room temperature to 250°C. Fig. 5.20 shows the resistance changes of sample B due to step by step injection of increasing  $\text{NO}$  partial pressures at operating temperatures of room temperature and 200°C, respectively.

As shown in Fig. 5.20a, the resistance of  $\text{In}_2\text{O}_3$  thin films increases after exposure to the oxidizing gas  $\text{NO}_x$  and it returns to the initial value after removal of  $\text{NO}_x$  gas under UV-irradiation. To reduce the recovery time especially at low operating temperatures, UV-light ( $\lambda = 365 \text{ nm}$ ) was used to irradiate the sensor

during the removal of  $\text{NO}_x$  gas. By increasing the operation temperature to  $200^\circ\text{C}$  lower partial pressures of  $\text{NO}_x$  down to 0.0002 mbar can be detected (Fig. 5.20b) and the resistance changes increase greatly.

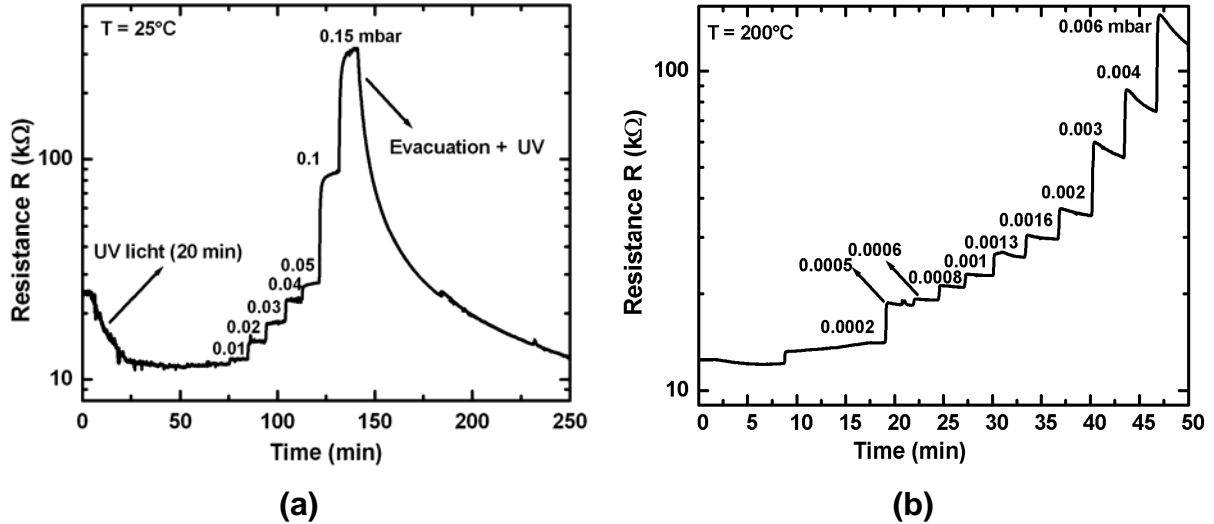


**Fig. 5.20:** Resistance variation versus time as a function of successive increase of  $\text{NO}_x$  partial pressure at a working temperatures of  $25^\circ\text{C}$  (a) and  $200^\circ\text{C}$  (b).

Fig. 5.21 provides the variation of normalized resistances at different operation temperatures for 0.004 mbar  $\text{NO}_x$ . At low operating temperature, the sensor responded slowly and higher operating temperature caused faster response.

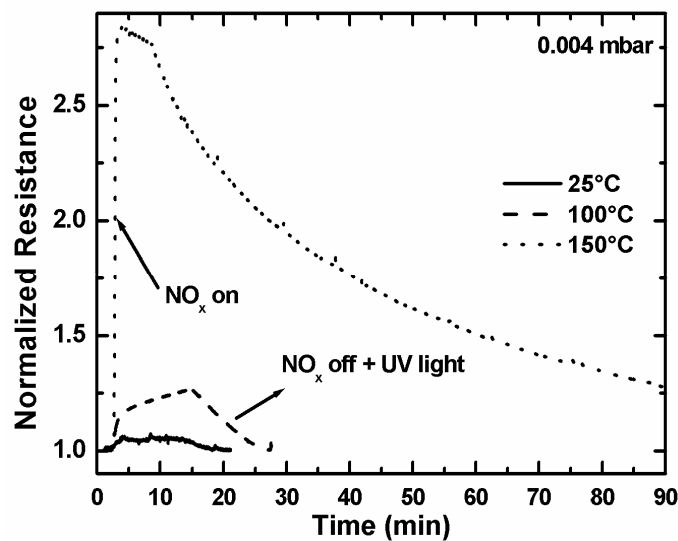


**Fig. 5.21:** Variation of the magnitude of normalized resistance at different operation temperatures for 0.004 mbar  $\text{NO}_x$ .



The dependence of the response and recovery times on the operation temperature for 0.004 mbar  $\text{NO}_x$  exposure is shown in Fig. 5.22.

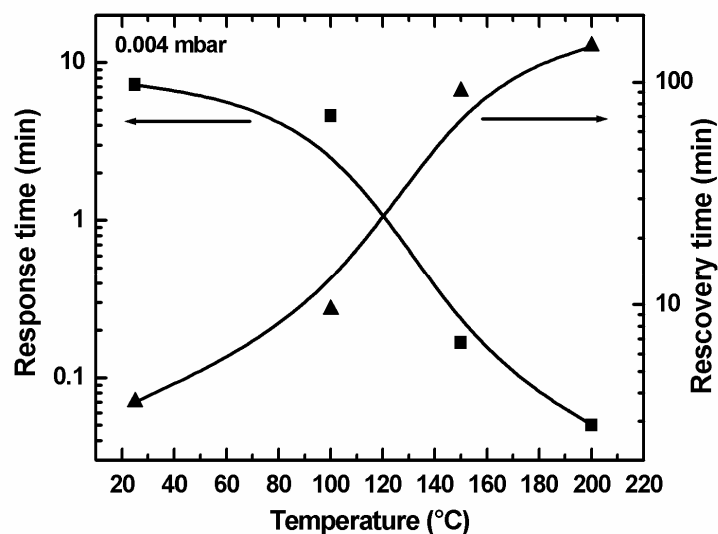


**Fig. 5.22:** The response and recovery times as a function of temperature for 0.004 mbar of  $\text{NO}_x$ .

There was a sharp decrease in the value of response time from  $\sim 6$  min to 3 s with an increase of the operating temperature ranging from 25 to 200°C, while the recovery time rose from  $\sim 3$  up to 140 min. It is believed that the interaction is stronger, if the temperature is higher. Therefore, the recovery time becomes longer at higher operating temperatures.

The response of  $\text{In}_2\text{O}_3$  (sample B) to different low partial pressures of  $\text{NO}_x$  at an operation temperature of 150°C is presented in Fig. 5.23. Fig. 5.23a displays the sensor response after introducing the  $\text{NO}_x$ -gas with partial pressures from 0.0003 to 0.0008 mbar into the chamber. The resistance change increases while the response time decreases by a rise of  $\text{NO}_x$  partial pressure. The resistance change after removal of  $\text{NO}_x$ -gas under simultaneous UV-irradiation is demonstrated in Fig. 5.23b.

The film resistance exactly returns to its initial value after a few minutes. It must be mentioned here that at low operating temperatures (RT, 100°C) the reactivation of the sensor surface is mainly caused by the UV-irradiation. The UV-irradiation used for the reactivation of sensors, especially at low operating temperature (RT) has been reported elsewhere. [5.44] However, at high operating temperature (150°C and 200°C), the thermal energy is sufficient to reset the sensor resistance to the initial

value. The UV-irradiation has only a little influence on the sensor response, because at high operating temperatures the desorption processes dominates.

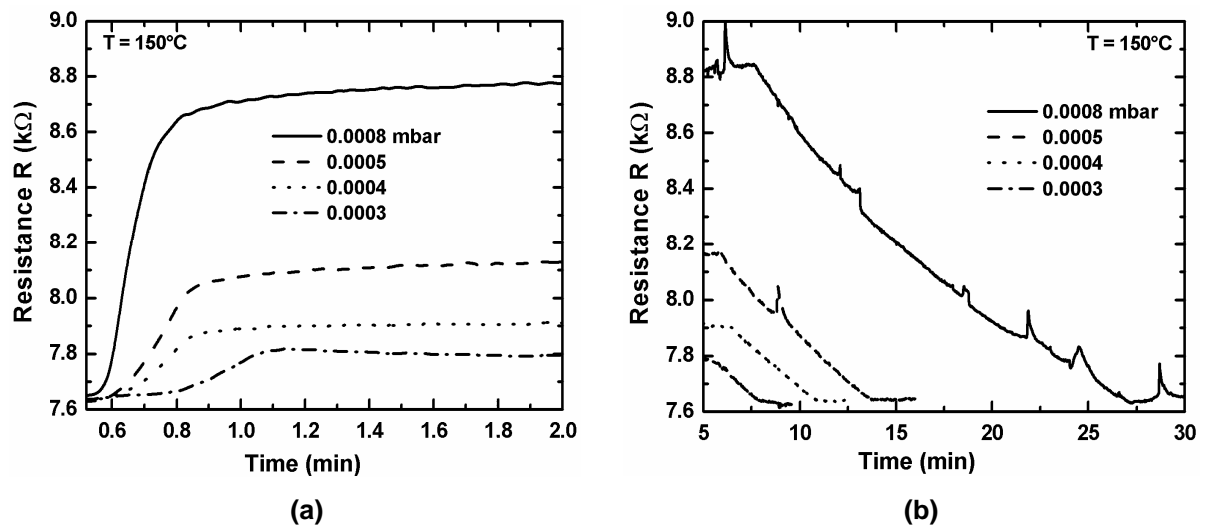


**Fig. 5.23:** The changes of resistance versus time upon introduction (a) and removal (b) of varying NO<sub>x</sub> partial pressures at 150°C.

The dependence of the response and recovery times on the NO<sub>x</sub> partial pressures at an operating temperature of 150°C is presented in Fig 5.24.

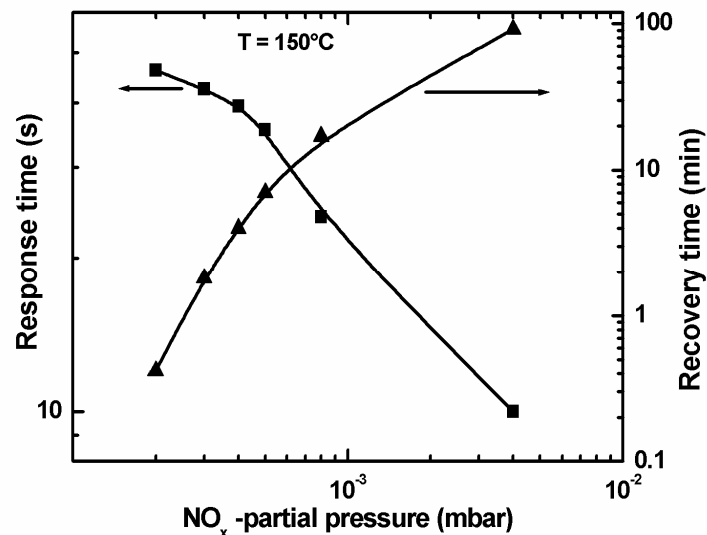


**Fig. 5.24:** The response and recovery times as a function of NO<sub>x</sub> partial pressure at an operation temperature of 150°C.

The response (recovery) was found to become faster (slower) by increasing gas partial pressure. In spite of the exposure of the sensor to very low partial pressures of

$\text{NO}_x$ , the response time is lower than one minute. By increasing the gas partial pressure to 0.004 mbar, the response time is decreased to 10 s. However, the recovery time varied from 0.5 to 90 min by increasing  $\text{NO}_x$  partial pressures from 0.0003 up to 0.004 mbar.

The dependence of response  $R$  and the sensitivity  $S$  on the partial pressure of  $\text{NO}_x$  (calibration curves) at different operating temperatures is presented in Fig. 5.25. At low partial pressures of  $\text{NO}_x$  ( $< 0.001$  mbar), the sensor showed relatively low response to  $\text{NO}_x$  gas. The corresponding response of the sensor operated at  $100^\circ\text{C}$  was lower than 1.1 at a partial pressure of 0.002 mbar, while the response of the sensor operated at  $200^\circ\text{C}$  increased up to  $\sim 3.1$  at the same partial pressure. We have found that the response to  $\text{NO}_x$  increases non-linearly with increasing partial pressure and no saturation was observed even at partial pressure of up to 0.2 mbar. The non-linear response to increasing partial pressures of  $\text{NO}_x$  may be due to the filling of adsorption sites on the  $\text{In}_2\text{O}_3$  surface, which decreases as the concentrations increases. The maximum response to  $\text{NO}_x$  is observed at  $200^\circ\text{C}$  for partial pressures in the range 0.002-0.05 mbar.

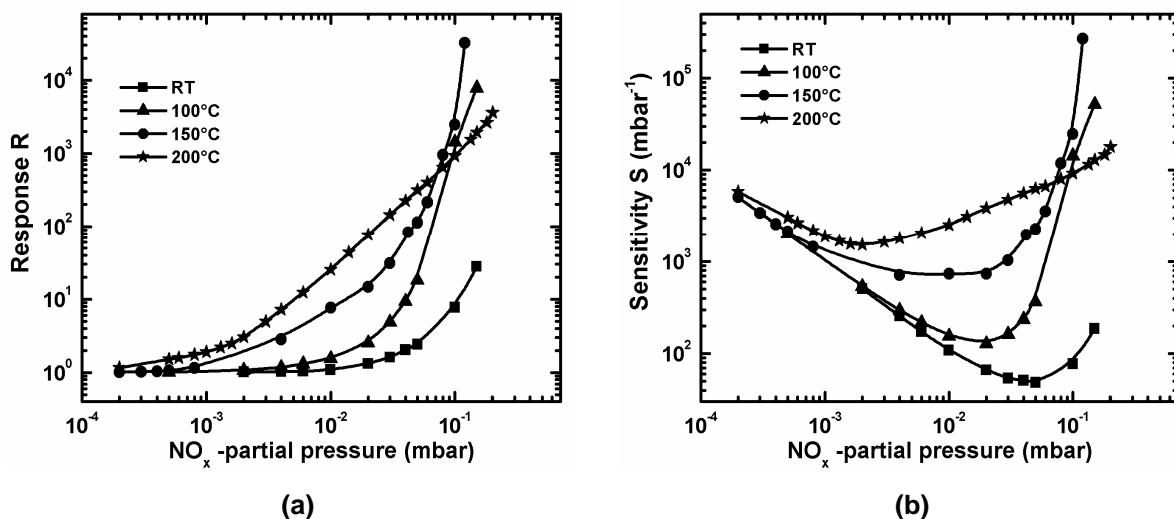


**Fig. 5.25:** The dependence of response  $R$  (a) and the sensitivity  $S$  (b) on the  $\text{NO}_x$  partial pressure at different temperatures.

#### 5.7.2.2.2 $\text{O}_2$ detection:

In the second step the sensors were tested for the response to  $\text{O}_2$  gas with partial pressures ranging from 0.001 up to 10 mbar at operating temperatures between  $25$  and  $200^\circ\text{C}$ . The results are presented in Fig. 5.26. Generally, the response increases with

increasing  $O_2$  partial pressures. The maximum response to  $O_2$  is observed at  $150^\circ\text{C}$ . The lowest limit for detection of  $O_2$  concentration is  $\sim 0.001$  mbar. At low operating temperatures ( $25$  and  $100^\circ\text{C}$ ), the  $\text{In}_2\text{O}_3$  sensor showed nearly no response to  $O_2$  gas at partial pressure of up to  $0.3$  mbar. The corresponding response was  $\sim 1.3$  at  $100^\circ\text{C}$ .

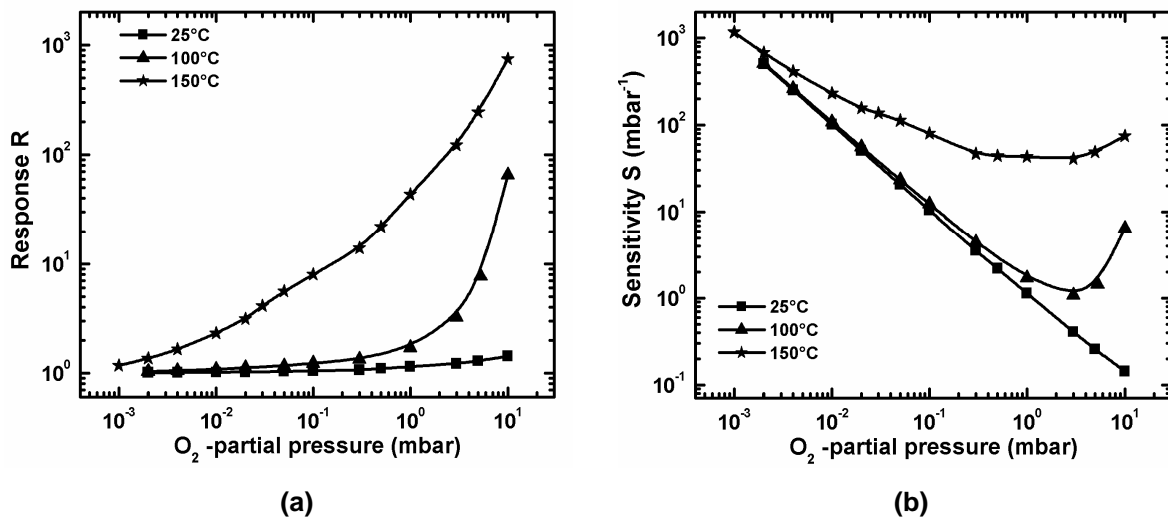


**Fig. 5.26:** The dependence of response R **(a)** and the sensitivity S **(b)** on the  $O_2$  partial pressure at different temperatures.

### 5.7.2.2.3 Conclusion:

Fig. 5.27 presents the dependence of the response to  $0.004$ ,  $0.01$ ,  $0.1$  and  $0.15$  mbar of pure  $\text{NO}_x$  and  $O_2$ , on the operating temperature. It becomes obvious from Fig. 5.27 that the optimum detection temperatures occur in the range of  $100$ - $175^\circ\text{C}$  for  $\text{NO}_x$  considering the response and the response time. In this range of temperatures the response to  $O_2$  is very low indicating that the sensor is very suitable for selective detection of  $\text{NO}_x$ .

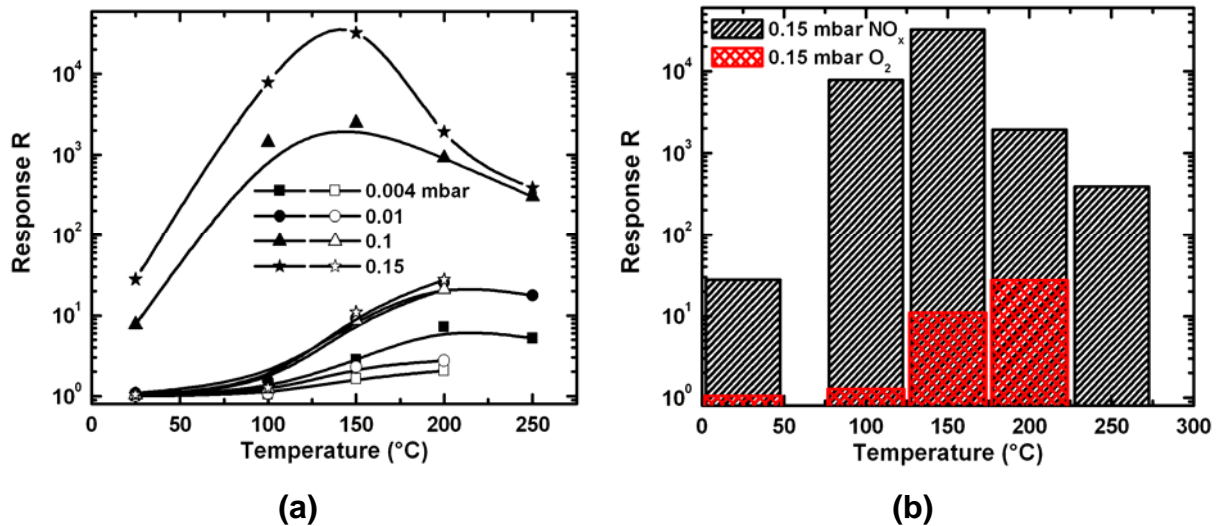


**Fig. 5.27:** (a) The dependence of the response to 0.004, 0.05, 0.1 and 0.15 mbar of pure  $\text{NO}_x$  (closed symbols), and  $\text{O}_2$  (open symbols), on the operating temperature. (b) Block presentations for 0.15 mbar of both gases.

### 5.7.2.3: Comparison between polycrystalline and nano-structured $\text{In}_2\text{O}_3$ :

The oxygen partial pressure in our gas test chamber is less than  $8 \times 10^{-10}$  mbar. Therefore, our results for  $\text{NO}_x$  detection disagree with the results reported by Akiyama *et al.* [5.47] on  $\text{WO}_3$  thin films. In fact, these authors report that  $\text{WO}_3$  is almost insensitive to  $\text{NO}_x$  gas when the oxygen concentration in the test gas is less than 1%. The behavior of our analyzed  $\text{In}_2\text{O}_3$  thin films can be explained considering the mechanism of  $\text{NO}_x$  adsorption on  $\text{TiO}_2$  and  $\text{ZnO}$  films proposed by Boccuzzi *et al.* [5.48]. We hypothesize a dissociative chemisorption process of  $\text{NO}_x$  with participation by free electrons or electrons trapped in oxygen vacancies present in the films:



accompanied by the following successive reactions:



Therefore,  $\text{NO}_x$  behaves as an oxidizing gas, increasing the resistance in  $n$ -type semiconductors.

Fig. 5.28 presents the dependence of the response of the both samples (A and B) to 0.1 and 0.15 mbar of pure  $\text{NO}_x$  and  $\text{O}_2$ , on the operating temperature. It is clearly evident that sample B exhibits the best response to both  $\text{NO}_x$  and  $\text{O}_2$ . At

150°C, the response of the sample B to 0.15 mbar of  $\text{NO}_x$  is over four orders of magnitude higher in comparison to the polycrystalline (sample A). Additionally, at 200°C the response of sample B to 0.15 mbar of  $\text{O}_2$  is over one order of magnitude higher than the one of the polycrystalline (sample A).

The higher response of sample B to both  $\text{NO}_x$  and  $\text{O}_2$  is most probably due to the enlarged overall active surface area of the sensing layer as a consequence of the small grain size (higher surface to volume ratio) so that the relative interactive surface area is larger.

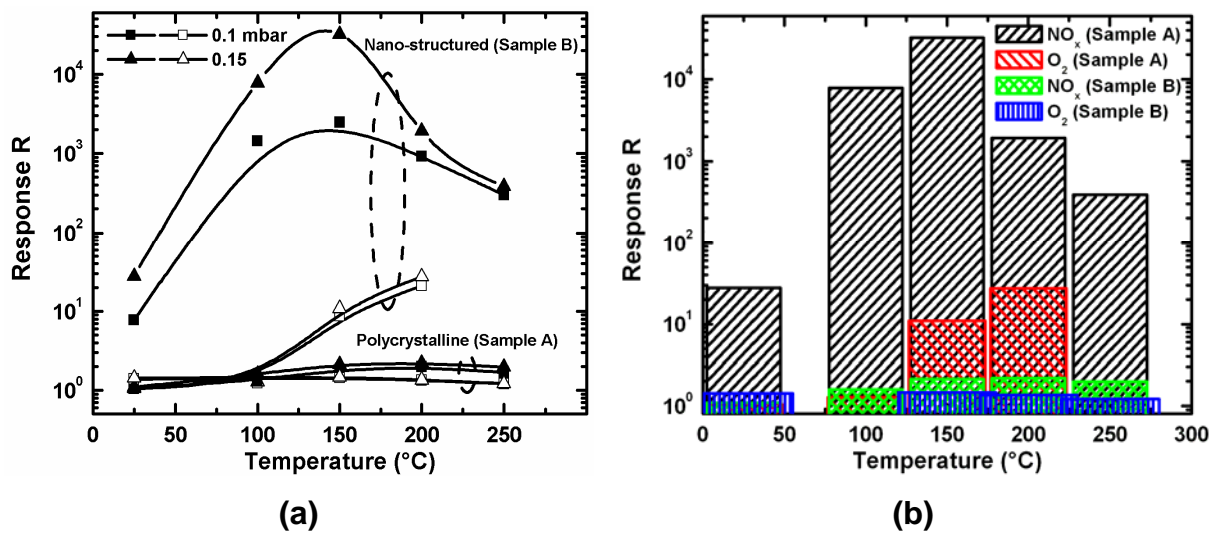


**Fig. 5.28:** (a) The dependence of the response of both samples (A and B) to 0.1 and 0.15 mbar of pure  $\text{NO}_x$  (closed symbols), and  $\text{O}_2$  (open symbols), on the operating temperature. (b) Block presentations for 0.15 mbar of both gases.

Several researchers [5.35, 5.49-5.50] have recently reported a substantial increase of performance in semiconducting metal oxide sensors as the grain size is reduced to the “nano-scale” level. The explanation for this phenomenon rests in the fact that chemisorption (i.e., the underlying principle of these sensors) is primarily a surface effect. To maximize the opportunities for surface reactions to occur, a high ratio of surface area to volume is needed. An inverse relationship exists between surface area and particle size; hence, ultra-fine-grained materials that offer very high surface area are desirable.

In polycrystalline materials, grain boundaries typically contribute most of the resistance, and conduction is controlled by the height of the energy barrier established at the grain boundary due to the conduction band bending into the space

charge layer. Large grain size significantly reduces the concentration of grain boundaries, which in turn reduces sensitivity to changes in the gaseous environment. Boundary layer effects are also present where “necking” of individual grains occurs. In this case, the resistance is controlled by the width of the bulk conduction channel, which narrows as the space charge layer forms. The population of such sites also increases with decreasing grain size, as does the likelihood that such interconnections will be of small enough size to enable the presence of boundary layer effects. Consequently, both mechanisms contribute best when the individual grains are very small, thereby increasing the sensor response.

### 5.8 Conclusion:

The response of  $\text{In}_2\text{O}_3$  thin films grown by MOCVD to  $\text{NO}_x$  and  $\text{O}_2$  gases was investigated as a function of operating temperature for different partial pressures of the test gases.  $\text{NO}_x$  behaves as an oxidizing gas, increasing the resistance in n-type semiconductors. The analysis of resistance variation indicates that the adsorption mechanism of  $\text{NO}_x$  gas on  $\text{In}_2\text{O}_3$  films does not involve oxygen. According to the conclusion of Boccuzzi *et al.* [5.48] for  $\text{TiO}_2$  and  $\text{ZnO}$  films, a dissociative chemisorption process of NO with participation by free electrons or electrons trapped in oxygen vacancies occurs.

In particular, nano-structured  $\text{In}_2\text{O}_3$  thin films were found to have the higher response to  $\text{NO}_x$ . This is most probably due to the enlarged overall active surface area of the sensing layer as a consequence of the small grain size (better surface to volume ratio) so that the relative interactive surface area is larger, and the density of charge carriers per volume is higher. We have found that reducing the grain size of the sensing material to the sub-10-nm regime can have a substantial effect on performance.

The optimum detection temperatures of the nano-structured  $\text{In}_2\text{O}_3$  occur in the range of 100-175°C for  $\text{NO}_x$  considering the sensitivity and the response time. In this range of temperatures the response to  $\text{O}_2$  is very low indicating that the sensor is very suitable for selective detection of  $\text{NO}_x$  at low temperatures. In addition, nano-structured  $\text{In}_2\text{O}_3$  thin films were found to be more suitable to be used in the field of application for detecting low partial pressures.

### 5.9 Outlook and future work:

For further investigation in this field of study, the following additional experiments are suggested:

- With regard to sensor properties a further study of the selectivity against reducing gases such as CO and H<sub>2</sub>, and other oxidizing gases as well as the stability and reliability of the sensor is needed.
- The influence of the relative humidity on the response and the selectivity of the sensors at different operation temperatures must be studied.
- Adsorption of gas species on the gate of AlGaIn/GaN high electron mobility transistors (HEMTs) leads to enhancement or depletion effects in the two dimensional electron gas (2DEG). Nano-structure In<sub>2</sub>O<sub>3</sub> can be used to develop very sensitive but robust sensors for the detection of NO<sub>x</sub>.
- The influence of the addition of amount of noble metals (Pt, Pd,...) or other metal oxides to In<sub>2</sub>O<sub>3</sub> thin films on the gas sensing properties should be studied.

### References:

- [5.1] N. Yamazoe, and N. Miura, "Environmental gas sensing", *Sensors and Actuators B* 20 (1994) 95-102.
- [5.2] M. S. Nieuwenhuizen, and A. J. Nederlof, "Preliminary results with silicon-based surface acoustic wave chemical sensor for NO<sub>2</sub>", *Sensors and Actuators B* 19 (1989) 385-392.
- [5.3] C. J. Liu, S. Y. Wang, J. C. Hsieh, and Y. H. Ju, "Gas sensing properties of vacuum deposited titanyl phthalocyanine film", *Sensors and Actuator B* 65 (200) 371-374.
- [5.4] T. Seiyman, A. Kato, K. Fujiishi, and M. Negatani, "A new detector for gaseous components using semiconductive thin films", *Anal. Chem.* 34 (1962) 1502-1503.
- [5.5] A. A. Tomchenko, G. P. Harmer, B. T. Marquis, and J. W. Allen, "Semiconducting metal oxide sensor array for the selective detection of combustion gases", *Sensors and Actuators B* 93 (2003) 126-134.



- [5.6] C.-D. Feng, Y. Shimizu, and M. Egashira, "Effect of gas sensing diffusion process on sensing properties of SnO<sub>2</sub> thin film sensors in a SiO<sub>2</sub>/SnO<sub>2</sub> layer-built structure fabricated by sol-gel process", *J. Electrochem. Soc.* 141 (1994) 220-225.
- [5.7] T. Hyodo, S. Abe, Y. Shimizu, and M. Egashira, "Gas-sensing properties of ordered mesoporous SnO<sub>2</sub> and effects of coatings thereof", *Sensors and Actuators B* 93 (2003) 590-600.
- [5.8] S. C. Moulzolf, L. J. LeGore, and R. J. Lad, "Heteroepitaxial growth of tungsten trioxide films on sapphire substrate for chemical gas sensor", *Thin Solid Film* 400 (2001) 56-63.
- [5.9] Y. Yamada, Y. Sano, Y. Masuoka, T. Nakamura, and K. Yamashita, "NO<sub>2</sub> Sensing Characteristics of Nb Doped TiO<sub>2</sub> Thin Films and their Electronic Properties", *Sensors and Actuators B* 66 (2000).164-166.
- [5.10] L. Zheng, M. Xu, and T. Xu, "TiO<sub>2-x</sub> Thin films as oxygen sensor", *Sensors and Actuators B* 66 (2000) 28-30.
- [5.11] M. Egashira, Y. Shimizu, Y. Takao, and S. Sako, "Variations in I-V characteristics of oxide semiconductors induced by oxidizing gases", *Sensors and Actuators B* 35-36 (1996) 62-67.
- [5.12] T. Doll, A. Fuchs, I. Eisele, G. Faglia, S. Groppelli, and G. Sberveglieri, "Conductivity and work function ozone sensors based on indium oxide", *Sensors and Actuators B* 49 (1998) 63-67.
- [5.13] B. P. J. de Lacy Costello, R. J. Ewen, N. M. Ratcliffe, and P. S. Sivanand, "Thick film organic vapour sensors based on binary mixtures of metal oxides", *Sens. Actuators B* 92 (2003) 159-166.
- [5.14] A. Gurlo, M. Ivanovskaya, A. Pfau, U. Weimar and W. Göpel, "Sol-gel prepared In<sub>2</sub>O<sub>3</sub> thin films", *Thin Solid Films* 307 (1997) 288-293.
- [5.15] M. Liess, "Electric field-induced migration of chemisorbed gas molecules on a sensitive film-a new chemical sensor", *Thin Solid Film* 410 (2002) 183-187.
- [5.16] G. Kiriakidis, M. Bender, N. Katsarakis, E. Gagoudaskis, E. Hourdakis, E. Douloufakis, and V. Cimalla, "Ozone sensing properties of polycrystalline indium oxide films at room temperature", *phys. stat. sol. (a)* 185 (2001) 27-32.
- [5.17] A. N. H. Alajili, and S. C. Bayliss, "A study of the optical, electrical and structural properties of reactively sputtered InO<sub>x</sub> and ITO<sub>x</sub> thin films", *Thin Solid Film* 305 (1997) 116-123.

- [5.18] P. Thilakau and J. Kumar, "Reactive thermal deposition of indium oxide and tin-doped indium oxide thin films on inp substrates", *Thin Solid Films* 292 (1997) 50-54.
- [5.19] K. G. Copchandran, B. Joseph, J. T. Abraham, P. Koshy and V. K. Vaidyan, "The preparation of transparent electrically conducting indium oxide films by reactive vacuum evaporation", *Vacuum* 48 (1997) 547-550.
- [5.20] K. B. Sundaram and G. K. Bhagavat, "Preparation and properties of indium oxide films", *phys. stat. sol. (a)* 63 (1981) K15-K18.
- [5.21] V. Damodara Das, S. Kirupavathy, L. Damodare and N. Lakshminarayan, "Optical and electrical investigations of indium oxide thin films prepared by thermal oxidation of indium thin films", *J. Appl. Phys.* 79 (1996) 8521-8530.
- [5.22] A. P. Mammana, E. S. Braga, I. Torriani and R. P. Anderson, "Structural characterization of transparent semiconducting thin films of SnO<sub>2</sub> and In<sub>2</sub>O<sub>3</sub>", *Thin Solid Films* 85 (1981) 355-359.
- [5.23] W. Siefert, "Properties of thin In<sub>2</sub>O<sub>3</sub> and SnO<sub>2</sub> films prepared by corona spray pyrolysis, and a discussion of the spray pyrolysis process", *Thin Solid Films* 120 (1984) 275-282.
- [5.24] S. Mailis, C. Grivas, D. Gill, L. Boutsikaris, N.A. Vainos, C. Xirouchaki, G. Vasiliou, N. Garawal, G. Kiriakidis and H. Fritzsche, "Dynamic holography in indium Oxide and Indium-Tin-Oxide Thin Films", *Optical Memory and Neural Networks* 5 (1996) 191-196.
- [5.25] V. Demarne and R. Sanjinés, "Thin film semiconducting metal oxide gas sensors", *Gas Sensors*, G. Sberveglieri (ed.), Kluwer Academic Publishers, Dordrecht, The Netherlands, 1992, pp.89-106.
- [5.26] J. Pires, "Thin films for gas sensors", PhD thesis, Minho University, Braga, Portugal, 2003.
- [5.27] V. L. Bonc-Bruevic and S. G. Kalasnikov, "Halbleiterphysik", Deutscher Verlag der Wissenschaften, Berlin 1982.
- [5.28] M. Fleischer, "Präparation und Charakterisierung von Ga<sub>2</sub>O<sub>3</sub> Dünnschichten, Untersuchung der gassensitiven elektrischen Leitfähigkeitseigenschaften", Technische Universität München, Dissertation, 1992.
- [5.29] A. Bielanski and J. Haber, "Oxygen in catalysis on transition metal oxides", *Catal. Rev.-Sci. Eng.* 19 (1979) 1-41.

- [5.30] S. Pitcher, J. A. Thiele, H. Ren and J. F. Vetelino, "Current/voltage characteristics of a semiconductor metal oxide gas sensor", *Sensors and Actuators B* 93 (2003) 454-462.
- [5.31] E. Fromm, "Kinetics of metal-gas interactions at low temperature", Springer-Verlag Berlin-Heidelberg, 16 (1998).
- [5.32] E. Comini, G. Faglia and G. Sberveglieri, "UV light activation of tin oxide thin films for NO<sub>2</sub> sensing at low temperatures", *Sensors and Actuators B* 78 (2001) 73-77.
- [5.33] N. Yamazoe, J. Fuchigami, M. Kishikawa, and T. Seiyama, "Interactions of tin oxide surface with O<sub>2</sub>, H<sub>2</sub>O and H<sub>2</sub>", *Surf. Sci.* 86 (1979) 335-344.
- [5.34] S. Capone, R. Rella, P. Siciliano, and L. Vasanelli, "A comparison between V<sub>2</sub>O<sub>5</sub> and WO<sub>3</sub> thin films as sensitive elements for NO detection", *Thin Solid Films* 350 (1999) 264-268.
- [5.35] C. Xu, J. Tamaki, N. Miura, and N. Yamazoe, "Grain size effects on gas sensitivity of porous SnO<sub>2</sub>-based elements", *Sensors and Actuators B* 3 (1991) 147-155.
- [5.36] P. Thilakan and J. Kumar, "Oxidation dependent crystallization behaviour of IO and ITO thin films deposited by reactive thermal deposition technique", *Mater. Sci. Eng. B* 55 (1998) 195-200.
- [5.37] C. Xirouchaki, G. Kiriakidis, T. F. Pedersen, and H. Fritzsche, "Photoreduction and oxidation of as-deposited microcrystalline indium oxide", *J. Appl. Phys.* 79 (1996) 9349-9352.
- [5.38] C. G. Granqvist, "Transparent Conductive Electrodes for Electrochromic Devices: A Review", *Appl. Phys. A: Solids. Surf.* 57 (1993) 19-24.
- [5.39] S. Pissadakis, S. Mailis, L. Reekie, J. S. Wilkinson, R. W. Eason, N. A. Vainos, K. Moschovis, and G. Kiriakidis, "Permanent holographic recording in indium oxide thin films using 193 nm excimer laser radiation", *Appl. Phys. A: Mater. Sci. Process.* 69 (1999) 333-336.
- [5.40] J. Ederth, "Electrical transport in nanoparticle thin films of gold and indium tin oxide", PhD thesis, Uppsala university, Uppsala, Sweden, 2003.
- [5.41] C. Suryanarayana and C. C. Koch, "Nanocrystalline materials-current research and future directions", *Hyperfine Interact.* 130 (2000) 5-44.

- [5.42] N. Bovini, M. C. Carotta, V. Guidi, C. Malaga, G. Martinelli, L. Paglialonga, and M. Sacerdoti, "Doping of a nanostructured titania thick film: structural and electrical investigations", *Sensors and Actuators*, B 68 (2000) 274-280.
- [5.43] E. Comini, G. Sberveglieri, M. Ferroni, V. Guidi, C. Frigeri, and D. J. Boscarino, "Production and characterization of titanium and iron oxide nano-sized thin films", *J. Mater. Res.* 16 (2001) 1559-1564.
- [5.44] Ch. Y. Wang, V. Cimalla, H. Romanus, Th. Kups, G. Ecke, Th. Stauden, M. Ali, V. Lebedev, J. Pezoldt, and O. Ambacher, "Phase selective growth and properties of rhombohedral and cubic indium oxide", *Appl. Phys. Lett.* 89 (2006) 011904-1-3.
- [5.45] S. -C. Chang, "Thin-film semiconductor NO<sub>x</sub> sensor", *IEEE Trans. Elec. Dev.* ED26 (1979) 1875-1880.
- [5.46] M. J. Madou, S. R. Morrison, "Chemical sensing with solid state devices", Academic Press, New York, 1988, pp. 67-104.
- [5.47] M. Akiyama, Z. Zhang, J. Tamaki, N. Miura, N. Yamazoe, and T. Harata, "Tungsten oxide-based semiconductor sensor for detection of nitrogen oxides in combustion exhaust", *Sensors and Actuators B* 14 (1993) 619-620.
- [5.48] F. Boccuzzi, E. Guglielminotti, and A. Chiorino, "IR study of gas-sensor materials: NO interaction on ZnO and TiO<sub>2</sub>, pure or modified by metals", *Sensors and Actuators B* 7 (1992) 645-650.
- [5.49] Z. H. Jin, H. J. Zhou, Z. L. Jin, R. F. Savinelli, and C. C. Liu, "Application of nano-crystalline porous tin oxide thin film for CO sensing", *Sensors and Actuators B* 52 (1998) 188-194.
- [5.50] O. K. Varghese, L. K. Malhotra, and G. L. Sharma, "High ethanol sensitivity in sol-gel derived SnO<sub>2</sub> thin films", *Sensors and Actuators B* 55 (1999) 161-165.

## Chapter 6

### 6. Comparison and Conclusion

The gas sensors studied in this thesis can be classified into three groups:

#### I. H<sub>2</sub> (D<sub>2</sub>) gas sensors:

The members of this group are:

1. Pt/GaN Schottky diodes with different Pt thickness and areas.
2. Rh/SiO<sub>2</sub>/SiC capacitor (sample A4).
3. Rh/ITO/SiO<sub>2</sub>/SiC capacitor (sample A1).
4. Rh/SiN/SiO<sub>2</sub>/SiC capacitor (sample B4).
5. SiC-based FET with In<sub>x</sub>V<sub>y</sub>O<sub>z</sub> gate.

#### II: NO<sub>x</sub> gas sensors:

This group includes:

1. Rh/SiO<sub>2</sub>/SiC capacitor (sample A4).
2. Rh/ITO/SiO<sub>2</sub>/SiC capacitor (sample A1).
3. Rh/SiN/SiO<sub>2</sub>/SiC capacitor (sample B4).
4. SiC-based FET with In<sub>x</sub>Sn<sub>y</sub>O<sub>z</sub> gate.
5. SiC-based FET with In<sub>x</sub>V<sub>y</sub>O<sub>z</sub> gate.
6. SiC-based FET with Pt-In<sub>x</sub>Sn<sub>y</sub>O<sub>z</sub> gate (EN17).
7. SiC-based FET with Pt-In<sub>x</sub>Sn<sub>y</sub>O<sub>z</sub> gate (EN16).
8. Polycrystalline In<sub>2</sub>O<sub>3</sub> thin film (sample A).
9. Nano-structured In<sub>2</sub>O<sub>3</sub> thin film (sample B).

#### III: O<sub>2</sub> gas sensors:

In this group we had the following sensors:

1. Rh/SiO<sub>2</sub>/SiC capacitor (sample A4).
2. Rh/ITO/SiO<sub>2</sub>/SiC capacitor (sample A1).
3. Rh/SiN/SiO<sub>2</sub>/SiC capacitor (sample B4).
4. SiC-based FET with In<sub>x</sub>Sn<sub>y</sub>O<sub>z</sub> gate.
5. SiC-based FET with Pt-In<sub>x</sub>Sn<sub>y</sub>O<sub>z</sub> gate (EN16).

## 6. Nano-structured $\text{In}_2\text{O}_3$ thin film (sample B).

### 6.1. Comparison of all sensors studied:

Since the sensitivity (S), selectivity (SE), response time  $\tau_{\text{res}}$ , recovery time  $\tau_{\text{rec}}$ , and the range of operating temperature for the optimum detection  $T_{\text{opt}}$  are the most important parameters that decide which sensor is better than the others we have arranged our results in Tab. 6.1 to enable an easy comparison.

**Tab. 6.1:** Comparison of the sensors studied according to the most important parameters.

Group	Sensor	$T_{\text{opt}}$ ( $^{\circ}\text{C}$ )	S	SE	$\tau_{\text{res}}$	$\tau_{\text{rec}}$
<b><math>\text{H}_2</math> (<math>\text{D}_2</math>) gas sensors</b>	Pt/GaN Schottky diodes	300-325	++++	+++	+++	+++
	Rh/ $\text{SiO}_2$ /SiC capacitor (A4)	115-140	+++	++	++	++
	Rh/ITO/ $\text{SiO}_2$ /SiC capacitor (A1)	250-300	+++	+++	+++	++
	Rh/SiN/ $\text{SiO}_2$ /SiC capacitor (B4)	25-50	++	++	++	++
	FET with $\text{In}_x\text{V}_y\text{O}_z$ gate	25-100	++++	++++	+++	+++
<b><math>\text{NO}_x</math> gas sensors</b>	Rh/ $\text{SiO}_2$ /SiC capacitor (A4)	25-75	++++	++++	++	++
	Rh/ITO/ $\text{SiO}_2$ /SiC capacitor (A1)	25-75	+++	++++	++	++
	Rh/SiN/ $\text{SiO}_2$ /SiC capacitor (B4)	75-120	++	+	++	++
	FET with $\text{In}_x\text{Sn}_y\text{O}_z$ gate	325-370	++	++	+++	+++
	FET with $\text{In}_x\text{V}_y\text{O}_z$ gate	275-325	++++	++++	+++	+++
	FET with Pt- $\text{In}_x\text{Sn}_y\text{O}_z$ gate (EN17)	175-225	++	++	++	++
	FET with Pt- $\text{In}_x\text{Sn}_y\text{O}_z$ gate (EN16)	125-175	+++	++	++	++
	Polycrystalline $\text{In}_2\text{O}_3$ (sample A)	150-200	++	++++	++	-
Nano-structured $\text{In}_2\text{O}_3$ (sample B)	100-175	++++	++++	+++	--	
<b><math>\text{O}_2</math> gas sensors</b>	Rh/ $\text{SiO}_2$ /SiC capacitor (A4)	225-250	++++	++	+++	+++
	Rh/ITO/ $\text{SiO}_2$ /SiC capacitor (A1)	150-225	+++	+++	+++	+++
	Rh/SiN/ $\text{SiO}_2$ /SiC capacitor (B4)	225-275	++	+++	+++	+++
	FET with $\text{In}_x\text{Sn}_y\text{O}_z$ gate	400-500	+++	+++	+++	+++
	FET with Pt- $\text{In}_x\text{Sn}_y\text{O}_z$ gate (EN16)	260-300	+++	++	++	++
	Nano-structured $\text{In}_2\text{O}_3$ (sample B)	200-250	++	+	++	++

+: reasonable; ++: good; +++: very good; ++++: excellent; -: bad; --: very bad.

When we compare the sensors in the first group we can easily conclude that the best  $\text{H}_2$  ( $\text{D}_2$ ) sensors are Pt/GaN Schottky diodes and FET with  $\text{In}_x\text{V}_y\text{O}_z$  gate. But when the  $T_{\text{opt}}$  are compared we can see that the sensor FET with  $\text{In}_x\text{V}_y\text{O}_z$  gate is better for

low temperature sensing applications with the consequence of low power consumption, what makes this sensor cheap in operation.

In the second group the sensors (FET with  $\text{In}_x\text{V}_y\text{O}_z$  gate) and (Rh/SiO<sub>2</sub>/SiC capacitor (A4)) are the best. But when operation at low temperatures is required, the second should be preferred. However, the recovery time of the sensor (nano-structured  $\text{In}_2\text{O}_3$  (sample B)) is not acceptable although it has an excellent sensitivity and selectivity as well as a very good response time. So the improvement of its recovery time should be the subject of future investigations.

In the third group we find that all sensors have good parameters, so the selection of one of them depends on the field of application.

## 6.2. Comparison with other results present in the literature:

### 6.2.1. H<sub>2</sub> gas sensors:

The results from other researchers who have studied H<sub>2</sub> gas sensors are listed in Tab. 6.2.

**Tab. 6.2:** Comparison with other results of H<sub>2</sub> gas sensors present in the literature.

Sensor	Sensitive layer		C[H <sub>2</sub> ] (ppm)	T (°C)	Response/ Sensitivity	$\tau_{res}$ (s)	Ref.
	Thickness (nm)	Deposition method					
Pt/GaN Schottky diode	75	e-beam evaporation	2000	500	R = 400 mV	-	[6.1]
Pt/GaN Schottky diode	8-40	e-beam evaporation	2000	310	R = 250 mV	-	This thesis
Pt/GaN Schottky diode	15	e-beam evaporation	10%	150	R = 200 mV	-	[6.2]
Pt/GaN Schottky diode	8	e-beam evaporation	1%	310	R = 325 mV	-	This thesis
Pt/SiC Schottky diode	100	dc-magnetron sputtering	1000	300	R <sub>2</sub> = 0.3-0.75	-	[6.3]
Pt/GaN Schottky diode	8-40	e-beam evaporation	1000	310	R <sub>2</sub> = 0.3-1.2	-	This thesis

Sensor	Sensitive layer		C[H <sub>2</sub> ] (ppm)	T (°C)	Response/ Sensitivity	$\tau_{res}$ (s)	Ref.
	Thickness (nm)	Deposition method					
Pt/SiO <sub>2</sub> /SiC capacitor	100	e-beam evaporation	10%	425	R = 440 mV at 180 pF	2400	[6.4]
					R = 230 mV at 180 pF	60	
Rh/SiO <sub>2</sub> /SiC capacitor	30	e-beam evaporation	1%	200	R = 500 mV at 400 pF	120	This thesis
Rh/ITO/SiO <sub>2</sub> /SiC capacitor		sputtering	4%	300	R = 700 mV at 400 pF	85	
Rh/SiN/SiO <sub>2</sub> /SiC capacitor		e-beam evaporation	1%	25	R = 350 mV at 400 pF	650	
Pt-SiO <sub>2</sub> -Si capacitor	20	e-beam evaporation	1000	140	R = 900 mV	-	[6.5]
		dc-magnetron sputtering	1000	140	R = 220 mV		
Rh/SiO <sub>2</sub> /SiC capacitor	30	e-beam evaporation	1000	200	R = 450 mV	-	This thesis
Rh/ITO/SiO <sub>2</sub> /SiC capacitor		sputtering		300	R = 300 mV		
Rh/SiN/SiO <sub>2</sub> /SiC capacitor		e-beam evaporation		25	R = 325 mV		
Pt-AlGaIn/GaN Schottky diode	25	e-beam evaporation	5%	800	R <sub>2</sub> = 1.75	-	[6.6]
Pt/GaN Schottky diode	8	e-beam evaporation	1%	310	R <sub>2</sub> = 4-5	-	This thesis
Pd-Pt/SiO <sub>2</sub> /Si	12+12	e-beam evaporation	1%	140	R = 500 mV	-	[6.7]
Pd-Pt/Si <sub>3</sub> N <sub>4</sub> /SiO <sub>2</sub> /Si					R = 250 mV		
Pd-Pt/Al <sub>2</sub> O <sub>3</sub> /SiO <sub>2</sub> /Si					R = 600 mV		
Pd-Pt-Ta <sub>2</sub> O <sub>5</sub> /SiO <sub>2</sub> /Si					R = 620 mV		
Rh/SiO <sub>2</sub> /SiC capacitor	30	e-beam evaporation	1%	200	R = 500 mV	-	This thesis
Rh/ITO/SiO <sub>2</sub> /SiC capacitor		sputtering		300	R = 650 mV		
Rh/SiN/SiO <sub>2</sub> /SiC capacitor		e-beam evaporation		25	R = 350 mV		
Pd/poros-GaAs	100	chemical solution	500	100	R <sub>6</sub> = 50	-	[6.8]
Pt/GaN Schottky diode	8-40	e-beam evaporation	1%	310	R <sub>6</sub> = 12-45	-	This thesis



Sensor	Sensitive layer		C[H <sub>2</sub> ] (ppm)	T (°C)	Response/ Sensitivity	$\tau_{res}$ (s)	Ref.
	Thickness (nm)	Deposition method					
Pt-TaSi <sub>x</sub> /SiO <sub>x</sub> N <sub>y</sub> /SiC Schottky diode	100	dc-magnetron sputtering	1000	150	R <sub>2</sub> = 1.2	-	[6.9]
			800	300	R = 75 mV		
Pt/GaN Schottky diode	8-40	e-beam evaporation	1000	150	R <sub>2</sub> = 0.4-3.4	-	This thesis
			800	300	R = 40-150 mV		
3C-SiC/SOI resistive	-	LPCVD	10%	400	R = 10	-	[6.10]
FET with In <sub>x</sub> V <sub>y</sub> O <sub>z</sub> gate	-	sputtering	0.5%	25	R = 44.3	-	This thesis
Ru/3C-SiC Schottky diode	100	e-beam evaporation	1%	400	R = 200 mV R <sub>1</sub> = 0.7 mA	12.3	[6.11]
Pt/GaN Schottky diode	8-40	e-beam evaporation	1%	310	R = 210-350 R <sub>1</sub> = 2-10	5-10	This thesis

From Tab. 6.2 the following results can be obtained:

➤ For the H<sub>2</sub> gas sensors based on Schottky diodes, we find that our sensors provide better sensitivity which was achieved by three different approaches:

### 1. The reduction of catalytic metal thickness:

The comparison between our sensors and the other sensors shows that the reduction of catalytic metal thickness down to 8 nm provides a higher sensitivity as presented in references [6.2] and [6.6] due to the higher grain boundary density of the thinner catalytic metal.

### 2. The use of e-beam evaporation as deposition method:

Our sensors with a catalytic metal deposited by e-beam evaporation have the highest sensitivity by comparison to the sensors used sputtering instead of evaporation presented in references [6.3] and [6.9]. The high sensitivity of our detectors is due to high quality of the catalytic film. As well known, the atomic structure of the catalytic metal surface will affect the surface reactions and thus affect the sensitivity of the sensor [6.5].

### 3. The selection of Pt as a catalytic metal:

The high sensitivity provided by our sensors that use Pt as a catalytic metal when compared to similar sensors presented in [6.11] which use Ru instead of Pt indicates that Pt is better than Ru for H<sub>2</sub> sensing applications.

- Our H<sub>2</sub> gas sensors based on MOS capacitors provide better sensitivity due to our selection of Rh as a catalytic gate.
- Finally, our FETs with In<sub>x</sub>V<sub>y</sub>O<sub>z</sub> gate provide four times higher sensitivity and can be used at lower temperatures.

In general our H<sub>2</sub> gas sensors exhibit a sensitivity that is higher in comparison to the sensors having the same structure. When we consider the operation temperature we find that most of our sensors can be used at lower temperatures that means lower power consumption.

### 6.2.2. NO<sub>x</sub> gas sensors:

For NO<sub>x</sub> gas sensors we have summarized the results from other researcher as shown in the Tab. 6.3.

**Tab. 6.3:** Comparison with other results of NO<sub>x</sub> gas sensors present in the literature.

Sensor	Sensitive layer		C[NO <sub>x</sub> ] (ppm)	T (°C)	Response/ Sensitivity	τ <sub>res</sub> (s)	Ref.
	Thickness (nm)	Deposition method					
V <sub>2</sub> O <sub>3</sub> thin films	-	sputtering	100	290	R = 1.92	-	[6.12]
Polycrystalline In <sub>2</sub> O <sub>3</sub>	200	MOCVD	100	200	R = 1.97	-	This thesis
Nano-structured In <sub>2</sub> O <sub>3</sub>	10			200	R = 917	-	
TiO <sub>2</sub> thin films	-	reactive sputtering	10	500	R = 2	-	[6.13]
Nano-structured In <sub>2</sub> O <sub>3</sub>	10	MOCVD	10	200	R = 25.4	-	This thesis
Nano-structured SnO <sub>2</sub>	-	sol-gel	1000	300	R = 2.9	1080	[6.14]
CuO-doped SnO <sub>2</sub>	-			200	R = 4.3	180	
Polycrystalline In <sub>2</sub> O <sub>3</sub>	200	MOCVD	1000	150	R = 3.85	125	This thesis
Nano-structured In <sub>2</sub> O <sub>3</sub>	10			150	R > 2200	< 1	
In <sub>2</sub> O <sub>3</sub> thin films	120	rf sputtering	25	400	R = 15	τ <sub>50</sub> = 234	[6.15]
Nano-structured In <sub>2</sub> O <sub>3</sub>	10	MOCVD	25	200	R = 100	< 1	This thesis

Sensor	Sensitive layer		C[NO <sub>x</sub> ] (ppm)	T (°C)	Response/ Sensitivity	τ <sub>res</sub> (s)	Ref.
	Thickness (nm)	Deposition method					
Au/SiO <sub>2</sub> /Si capacitor	50	thermal evaporation	200	200	R = 500 mV	600	[6.16]
Rh/SiO <sub>2</sub> /SiC capacitor	30	e-beam evaporation	200	25	R = 700 mV	330	This thesis
Rh/SiN/SiO <sub>2</sub> /SiC capacitor				100	R = 175 mV	400	
Rh/ITO/SiO <sub>2</sub> /SiC capacitor		sputtering		25	R = 275 mV	360	
WO <sub>3</sub> thin films	-	dip-coating	10	300	R = 30	< 60	[6.17]
Nano-structured In <sub>2</sub> O <sub>3</sub>	10	MOCVD	10	200	R = 43	< 1	This thesis
Pt-MOSiC capacitor	45-150	evaporation	1000	500	R = 280 mV	-	[6.18]
Rh/SiO <sub>2</sub> /SiC capacitor	30	e-beam evaporation	1000	25	R = 800 mV	-	This thesis
Rh/SiN/SiO <sub>2</sub> /SiC capacitor				100	R = 200 mV		
Rh/ITO/SiO <sub>2</sub> /SiC capacitor		sputtering		25	R = 325 mV		
WO <sub>3</sub> thin films	150	dc-magnetron sputtering	10	250	R = 6.5	-	[6.19]
Nano-structured In <sub>2</sub> O <sub>3</sub>	10	MOCVD	10	200	R = 43	-	This thesis
Pt/SiC Schottky diode	20-40	sputtering	300	300	R = 1.5	60	[6.20]
FET with In <sub>x</sub> Sn <sub>y</sub> O <sub>z</sub> gate	100	sputtering	300	350	R = 12	42	This thesis
FET with In <sub>x</sub> V <sub>y</sub> O <sub>z</sub> gate				300	R = 27	55	
FET with Pt-In <sub>x</sub> Sn <sub>y</sub> O <sub>z</sub> gate (EN17)	10 (Pt) + 75 (In <sub>x</sub> Sn <sub>y</sub> O <sub>z</sub> )			200	R = 14	350	
FET with Pt-In <sub>x</sub> Sn <sub>y</sub> O <sub>z</sub> gate (EN16)				150	R = 20	354	

Sensor	Sensitive layer		C[NO <sub>x</sub> ] (ppm)	T (°C)	Response/ Sensitivity	τ <sub>res</sub> (s)	Ref.
	Thickness (nm)	Deposition method					
SnO <sub>2</sub> thick films	-	drop-coating	25	100	R = 9.39	-	[6.21]
ZnO thick films				300	R = 9.4		
WO <sub>3</sub> thick films				200	R = 8.92		
In <sub>2</sub> O <sub>3</sub> thick films				200	R = 17		
CuO thick films				200	R = 1.03		
Nano-structured In <sub>2</sub> O <sub>3</sub>	10	MOCVD	25	200	R = 110	-	This thesis
Polycrystalline In <sub>2</sub> O <sub>3</sub>	200			200	R = 1.38		
FET with In <sub>x</sub> Sn <sub>y</sub> O <sub>z</sub> gate	100	sputtering	25	350	R <sub>1</sub> = 1.075	-	This thesis
FET with In <sub>x</sub> V <sub>y</sub> O <sub>z</sub> gate				300	R <sub>1</sub> = 1.07		
FET with Pt-In <sub>x</sub> Sn <sub>y</sub> O <sub>z</sub> gate (EN17)	10 (Pt) + 75 (In <sub>x</sub> Sn <sub>y</sub> O <sub>z</sub> )			200	R <sub>1</sub> = 1.06		
FET with Pt-In <sub>x</sub> Sn <sub>y</sub> O <sub>z</sub> gate (EN16)				150	R <sub>1</sub> = 1.074		
WO <sub>3</sub> thin films				-	rf sputtering		
Pt-WO <sub>3</sub> thin films	R = 11.73						
Au-WO <sub>3</sub> thin films	R = 1.3						
Ag-WO <sub>3</sub> thin films	R = 7.57						
Ti-WO <sub>3</sub> thin films	R = 2.53						
SnO <sub>2</sub> -WO <sub>3</sub> thin films	R = 2.75						
ZnO-WO <sub>3</sub> thin films	R = 3.12						
ITO-WO <sub>3</sub> thin films	R = 1.12						
Nano-structured In <sub>2</sub> O <sub>3</sub>	10	MOCVD	10	200	R = 25.4	-	This thesis
Polycrystalline In <sub>2</sub> O <sub>3</sub>	200			200	R = 1.22		
SiC-FET with Pt gate	40	e-beam evaporation	40	525	ΔI = 17 μA	-	[6.23]
FET with In <sub>x</sub> Sn <sub>y</sub> O <sub>z</sub> gate	100	sputtering	40	350	ΔI = 120 μA	-	This thesis
FET with In <sub>x</sub> V <sub>y</sub> O <sub>z</sub> gate				300	ΔI = 245- 300 μA		
FET with Pt-In <sub>x</sub> Sn <sub>y</sub> O <sub>z</sub> gate (EN17)	10 (Pt) + 75 (In <sub>x</sub> Sn <sub>y</sub> O <sub>z</sub> )			200	ΔI = 185 μA		
FET with Pt-In <sub>x</sub> Sn <sub>y</sub> O <sub>z</sub> gate (EN16)				150	ΔI = 260 μA		

Tab. 6.3 shows the following:

➤ For NO<sub>x</sub> resistive gas sensors based on metal oxides: The sensitivity of our sensors using nano-structured In<sub>2</sub>O<sub>3</sub> deposited by MOCVD is noticeably higher than

the other sensors using different metal oxides deposited by various deposition methods. Even when compared to other sensors those also use the same metal oxide ( $\text{In}_2\text{O}_3$ ) our sensor provide the highest sensitivity, lower operating temperature and shorter response times. This is due to the enlarged overall active surface area of the sensing layer as a consequence of the small grain size (better surface to volume ratio).

➤ Similar to  $\text{H}_2$  gas sensors our  $\text{NO}_x$  gas sensors based on MOS capacitors by comparison with similar sensors presented in references [6.16] and [6.18], provide better sensitivity due to our selection of Rh as a catalytic gate. But the most additional important property of these sensors is that they can be used at room temperature.

➤ Our SiC-based FETs  $\text{NO}_x$  gas sensors provided higher sensitivity too, in comparison to other SiC-based FETs and Schottky diodes presented in [6.23] and [6.20], respectively. This was achieved by using a mixture of metal oxides  $\text{In}_x\text{Sn}_y\text{O}_z$  and  $\text{In}_x\text{V}_y\text{O}_z$  as well as mixture of metal oxides  $\text{In}_x\text{Sn}_y\text{O}_z$  with addition of an appropriate amount of metal additives (Pt) as catalytic gates.

Generally, in comparison to other  $\text{NO}_x$  detectors, our sensors operate at lower temperature and providing higher sensitivity.

### 6.2.3. $\text{O}_2$ gas sensors:

Tab. 6.4 shows some comparable properties of our  $\text{O}_2$  gas sensors and the properties of similar  $\text{O}_2$  gas sensors studied by other groups.

**Tab. 6.4:** Comparison with other results of  $\text{O}_2$  gas sensors present in the literature.

Sensor	Sensitive layer		C[ $\text{O}_2$ ] ppm	T (°C)	Response/ Sensitivity	$\tau_{\text{res}}$ (s)	Ref.
	Thickness (nm)	Deposition method					
Resistive $\text{SnO}_2$	grain size 6.5	sputtering	1%	273	R = 12	-	[6.24]
Nano-structured $\text{In}_2\text{O}_3$	grain size 7	MOCVD	1%	150	R = 300	-	This thesis

Sensor	Sensitive layer		C[O <sub>2</sub> ] ppm	T (°C)	Response/ Sensitivity	$\tau_{res}$ (s)	Ref.
	Thickness (nm)	Deposition method					
Nanosized SnO <sub>2</sub>	particle size 24	mechanochemical	1%	300	R = 12	120- 180	[6.25]
Nano-structured In <sub>2</sub> O <sub>3</sub>	grain size 7	MOCVD	1%	150	R = 300	35	This thesis
Pt-MOSiC capacitor	45-150	evaporation	1%	600	R = 120 mV	-	[6.18]
Rh/SiO <sub>2</sub> /SiC capacitor (A4)	30	e-beam evaporation	1%	200	R = 675 mV	-	This thesis
Rh/SiN/SiO <sub>2</sub> /SiC capacitor (B4)				250	R = 330 mV		
Rh/ITO/SiO <sub>2</sub> /SiC capacitor (A1)		sputtering		200	R = 480 mV		
MoO <sub>3</sub> thin films	-	sol-gel	1000	370	R = 39	60	[6.26]
MO <sub>3</sub> thin films				400	R = 7.5	240	
TiO <sub>2</sub> thin films				420	R = 28	120	
Nano-structured In <sub>2</sub> O <sub>3</sub>	200	MOCVD	1000	150	R = 40	45	This thesis
SnO <sub>2</sub>	-	mechanochemical	1000	450	R = 1.45	-	[6.27]
Fe-doped SnO <sub>2</sub>					R = 1.38		
Polycrystalline In <sub>2</sub> O <sub>3</sub>	200	MOCVD	1000	150	R = 1.6	-	This thesis
Nano-structured In <sub>2</sub> O <sub>3</sub>	10			150	R = 40		
Ga <sub>2</sub> O <sub>3</sub>	-	sputtering	4000	1000	R = 1.2	-	[6.28]
FET with In <sub>x</sub> Sn <sub>y</sub> O <sub>z</sub> gate	-	sputtering	4000	400	R = 1.25	-	This thesis
FET with Pt-In <sub>x</sub> Sn <sub>y</sub> O <sub>z</sub> gate (EN16)				150	R = 1.225		
Nano-structured In <sub>2</sub> O <sub>3</sub>		MOCVD		150	R = 400		
Polycrystalline In <sub>2</sub> O <sub>3</sub>				150	R = 1.85		
Al <sub>2</sub> O <sub>3</sub> /SiO <sub>2</sub>	-	sputtering	2000	1000	R = 2.8	-	[6.28]
Nano-structured In <sub>2</sub> O <sub>3</sub>	-	MOCVD	2000	150	R = 100	-	This thesis

➤ Similar to H<sub>2</sub> and NO<sub>x</sub> gas sensors our O<sub>2</sub> gas sensors based on MOS capacitors compared to similar sensors presented in [6.18], have better sensitivity due to Rh

selected as a catalytic gate and can be operated at lower temperatures making the power consumption lower.

- The situation of our O<sub>2</sub> resistive gas sensor based on nano-structured In<sub>2</sub>O<sub>3</sub> did not differ from that of our NO<sub>x</sub> resistive gas sensor which exhibit higher sensitivity and lower operation temperatures in comparison to results presented in [6.24-6.28].
- In relation to the SiC-based FETs O<sub>2</sub> gas sensors, Tab. 6.4 shows that our sensor sensitivity is higher than the sensitivity of resistive O<sub>2</sub> sensors presented in [6.28].

### 6.3. Conclusion:

Field effect devices (Schottky diodes, MOS capacitors, and MOSFET transistors) based on wide band gap semiconductors like SiC and GaN as well as resistive gas sensors based In<sub>2</sub>O<sub>3</sub>, have been developed as H<sub>2</sub>, NO<sub>x</sub>, and O<sub>2</sub> gas sensors.

In chapter 2: The sensitivity to hydrogen of Pt/GaN Schottky diodes was investigated in dependence on the active area, the Pt thickness and the operating temperature. A significant increase of the sensitivity and a decrease of the response and recovery times by increasing the temperature of operation to about 350°C and by decreasing the Pt thickness down to 8 nm were observed. By decreasing the catalytic metal thickness down to 8 nm, the use of e-beam evaporation as deposition method of the catalytic metal, and the selection of Pt as catalytic metal, caused better sensitivity in comparison to the other sensors presented in the literature.

In chapter 3: The responses to D<sub>2</sub>, NO<sub>x</sub>, and O<sub>2</sub> of MOSiC and MMOOSiC structures were investigated in dependence on the operating temperature and gas partial pressures. The most important property of these sensors is that they can be used as NO<sub>x</sub> gas sensor at room temperature. Depending on the type of insulator that is chosen and the Rh structure, differences in the sensitivity are observed. The selection of Rh as a catalytic gate provided better sensitivity to H<sub>2</sub>, NO<sub>x</sub>, and O<sub>2</sub> by comparison to similar sensors having the same structure described in the scientific literature.

In chapter 4: SiC-based FETs were investigated as NO<sub>x</sub>, and O<sub>2</sub> gas detectors. The responses to these gases were investigated in dependence on the operating temperature and gas partial pressures. By using a mixture of metal oxides In<sub>x</sub>Sn<sub>y</sub>O<sub>z</sub> and In<sub>x</sub>V<sub>y</sub>O<sub>z</sub> as well as mixture of metal oxides In<sub>x</sub>Sn<sub>y</sub>O<sub>z</sub> with addition of an appropriate amount of metal additives (Pt) as catalytic gates our NO<sub>x</sub> and O<sub>2</sub> SiC-

based FETs gas sensors provided higher sensitivity and lower operation temperatures in comparison to other SiC-based FETs presented in the literature.

In chapter 5: Polycrystalline and nano-structured  $\text{In}_2\text{O}_3$  thin films were investigated as  $\text{NO}_x$  and  $\text{O}_2$  gas sensors exhibiting higher sensitivity and lower operation temperatures when compared to other sensors using different metal oxides deposited by various deposition methods. The higher sensitivity of the nano-structured  $\text{In}_2\text{O}_3$  is due to the enlarged overall active surface area of the sensing layer as a consequence of the small grain size (better surface to volume ratio).

The best  $\text{H}_2$  ( $\text{D}_2$ ) sensors studied in this work are Pt/GaN Schottky diodes and FET with  $\text{In}_x\text{V}_y\text{O}_z$  gate taking in account, sensitivity, selectivity, and the response and recovery times. In addition, the sensor FET with  $\text{In}_x\text{V}_y\text{O}_z$  gate is better for low temperature sensing applications.

Sensors (FET with  $\text{In}_x\text{V}_y\text{O}_z$  gate) and (Rh/ $\text{SiO}_2$ /SiC capacitor (A4)) are the best  $\text{NO}_x$  sensors presented in this work. When operation at low temperatures is required, the second should be preferred. However, the recovery time of the  $\text{NO}_x$  sensor (nano-structured  $\text{In}_2\text{O}_3$  (sample B)) is not acceptable although it has an excellent sensitivity and selectivity as well as a very good response time. So the improvement of its recovery time should be the subject of future investigations.

All  $\text{O}_2$  sensors investigated in this thesis have good parameters, so the selection of one of them depends on the field of application.

As a final result we can conclude that the sensors we have improved are comparable to those obtained by other researchers and have been published in the literature.



**References:**

- [6.1] J. Schalwig, G. Müller, M. Eickhoff, O. Ambacher, and M. Stutzmann, "Group III-nitride-based gas sensors for combustion monitoring", *Mater. Sci. Eng. B* 93 (2002) 207-214.
- [6.2] J. Kim, F. Ren, B. P. Gila, C. R. Abernathy, and S. J. Pearton, "Reversible barrier height changes in hydrogen-sensitive Pd/GaN and Pt/GaN diodes", *Appl. Phys. Lett.* 82 (2003) 739-741.
- [6.3] J. P. Xu, P. T. Lai, D. G. Zhong, and C. L. Chan, "Improved hydrogen sensitive properties of MISiC Schottky sensor with thin NO-grown oxynitride as gate insulator", *IEEE electron device Lett.* 24 (2003) 13-15.
- [6.4] P. Tobias, B. Golding, and N. Ghosh, "Interface state in high-temperature gas sensors based on silicon carbide", *IEEE Sensor J.* 2 (2003) 543-547.
- [6.5] A. E. Abom, R. T. Haasch, N. Hellgren, N. Finnegan, L. Hultman, and M. Eriksson, "Characterization of the metal-insulator interface of field-effect chemical sensors", *J. Appl. Phys.* 93 (2003) 9760-9768.
- [6.6] J. Song, W. Lu, J. S. Flynn, and G. R. Brandes, "Pt-AlGaN/GaN Schottky diodes operated at 800°C for hydrogen sensing", *Appl. Phys. Lett.* 87 (2005). 133501-1-3.
- [6.7] M. Eriksson, A. Salomonsson, and I. Lundström, "The influence of the insulator surface properties on the hydrogen response of field gas sensors", *J. Appl. Phys.* 98 (2005) 034903-1-6.
- [6.8] A. Salehi, A. Nikfarjam, D. J. Kalantari, "Pd/porous-GaAs Schottky contact for hydrogen sensing application", *Sensors and Actuators B* 113 (2006) 419-427.
- [6.9] W. M. Tang, P. T. Lai, J. P. Xu, C. L. Chan, "Enhanced hydrogen-sensing characteristics of MISiC Schottky-diode hydrogen sensor trichloroethylene oxidation", *Sensors and Actuators A* 119 (2005) 63-67.
- [6.10] T. J. Fawcett, J. T. Wolan, M. Reyes, S. E. Sadow, and A. Lloyd Spetz, "Thermal detection mechanism of SiC based hydrogen resistive sensors", *Appl. Phys. Lett.* 89 (2006) 182102-1-3.
- [6.11] S. Roy, C. Jacob, and S. Basu, "Studies on Ru/3C-SiC Schottky junction for high temperature hydrogen sensors", *J. Electrochem. Soc.* 150 (2003) H135-H139.
- [6.12] S. Capone, R. Rella, P. Siciliano, and L. Vasanelli, "A comparison between V<sub>2</sub>O<sub>5</sub> and WO<sub>3</sub> thin films as sensitive elements for NO detection", *Thin Solid Films* 350 (1999) 264-268.

- [6.13] T. Gessner, K. Gottfried, R. Hoffmann, C. Kaufmann, U. Weiss, E. Charetin, P. Hauptmann, R. Lucklum, B. Zimmermann, U. Dietel, G. Springer, and M. Vogel, "Metal oxide gas sensor for high temperature application", *Microsystem Technology* 6 (2000) 169-174.
- [6.14] G. Zhang, M. Liu, "Effect of particle size and dopant on properties of SnO<sub>2</sub>-based gas sensors", *Sensors and Actuators B* 69 (2000) 144-152.
- [6.15] H. Steffes, C. Imawan, F. Solzbacher, E. Obemeier, "Fabrication parameters and NO<sub>2</sub> sensitivity of reactively RF-sputtered In<sub>2</sub>O<sub>3</sub> thin films", *Sensors and Actuators B* 68 (2000) 249-253.
- [6.16] D. Filippini, R. Aragon, and U. Weimar, "NO<sub>2</sub> sensitive gate metal-oxide-semiconductor capacitors", *J. Appl. Phys.* 90 (2001) 1883-1886.
- [6.17] W. Y. Chung, "Tungsten oxide thin films prepared for NO<sub>2</sub> sensors by using the hydrothermal method and dip coating", *Journal of the Korea Physical Society* 41 (2002) L181-L183.
- [6.18] J. Schalwig, P. Kreisl, S. Ahlers, and G. Müller, "Response mechanism of SiC-based MOS field-effect gas sensors", *IEEE sensor J.* 2 (2002) 394-402.
- [6.19] X. He, J. Li, X. Gao, and L. Wang, "NO<sub>2</sub> sensing characteristics of WO<sub>3</sub> thin film microgas sensor", *Sensors and Actuators B* 93 (2003) 463-467.
- [6.20] Shabbir A. Khan, Elder A. de Vasconcelos, Y. Hasegawa, and T. Katsube, "High-temperature thin-catalytic gate devices for combustion emissions control", *Brazilian Journal of Physics* 34 (2004) 577-580.
- [6.21] A. A. Tomchenko, G. P. Harmer, B. T. Marquis, J. W. Allen, "Semiconducting metal oxide sensor array for the selective detection of combustion gases", *Sensors and Actuators B* 93 (2003) 126-134.
- [6.22] M. Stankova, X. Vilanova, J. Caldere, E. Liobet, J. Brezmes, I. Gracia, C. Cane, X. Correig, "Sensitivity and selectivity improvement of rf sputtered WO<sub>3</sub> microhotplate gas sensors", *Sensors and Actuators B* 113 (2006) 241-248.
- [6.23] K. Matocha, V. Tilak, P. Sandvik, J. Tucker, "High-temperature SiC MOSFET gas sensor", in: *Proceedings of the MRS Fall Meeting*, 828 (2004) A7.9.
- [6.24] J. P. Santos, J. A. de Agapito, "The interaction of oxygen with nanocrystalline SnO<sub>2</sub> thin films in the framework of the electron theory of adsorption", *Thin Solid Films* 338 (1999) 276-280.

- [6.25] L. M. Cukrov, P. G. McComick, K. Galatsis, W. Wlodarski, "Gas sensing properties of nanosized tin oxide synthesised by mechanochemical processing", *Sensors and Actuators B* 77 (2001) 491-495.
- [6.26] K. Galatsis, Y. X. Li, W. Wlodarski, E. Comini, G. Sberveglieri, C. Canalini, S. Cantucci, and M. Passacantando, "Comparison of single and binary oxide MoO<sub>3</sub>, TiO<sub>2</sub>, and WO<sub>3</sub> sol-gel gas sensors", *Sensors and Actuators B* 83 (2002) 276-280.
- [6.27] K. Galatsis, L. Curkrov, , W. Wlodarski, P. McCormick, K. Kalantar-zadeh, E. Comini, G. Sberveglieri, C. Canalini, S. Cantucci, and M. Passacantando, "Comparison of single and binary oxide MoO<sub>3</sub>, TiO<sub>2</sub>, and WO<sub>3</sub> sol-gel gas sensors", *Sensors and Actuators B* 83 (2002) 276-280.
- [6.28] C. Baban, Y. Toyoda, M. Ogita, "Oxygen sensor based on Ga<sub>2</sub>O<sub>3</sub> films operating at high temperature", *Journal of Optoelectronics and Advanced Materials* 7 (2005) 891-896.



## Appendix A

Thermocouple type K and S [A.1, A.2]:

Type	NiCr-Ni (K)	Pt10%Rh-Pt (S)	Type	NiCr-Ni (K)	Pt10%Rh-Pt (S)
°C	mV	mV	°C	mV	mV
25	1	0.143	600	24.905	5.239
50	2.023	0.299	625	25.967	5.495
75	3.059	0.467	650	27.025	5.753
100	4.096	0.646	675	28.079	6.013
125	5.124	0.834	700	29.129	6.275
150	6.138	1.029	725	30.174	6.539
175	7.140	1.232	750	31.213	6.806
200	8.138	1.441	800	33.275	7.345
225	9.141	1.655	825	34.297	7.618
250	10.153	1.874	850	35.313	7.893
275	11.176	2.096	875	36.323	8.170
300	12.209	2.323	900	37.326	8.449
325	13.248	2.553	925	38.323	8.731
350	14.293	2.786	950	39.314	9.014
375	15.343	3.021	975	40.298	9.300
400	16.397	3.259	1000	41.276	9.587
425	17.455	3.500	1100	45.119	10.757
450	18.516	3.742	1200	48.838	11.951
475	19.579	3.987	1250	50.644	12.554
500	20.644	4.233	1300	-	13.159
525	21.710	4.482	1400	-	14.373
550	22.776	4.732	1500	-	15.582
575	23.842	4.984	1600	-	16.777

[A.1] <http://www.thermometricscorp.com/thertypk.html>.

[A.2] <http://www.thermometricscorp.com/thertyps1to5.html>.



## Appendix B

B.1. Relative ion currents from fragment ions for ionization energy of 90 eV [B.1].

(m/e)	H <sub>2</sub>	He	CH <sub>4</sub>	H <sub>2</sub> O	Ne	N <sub>2</sub>	CO	C <sub>2</sub> H <sub>6</sub>	O <sub>2</sub>	Ar	CO <sub>2</sub>	C <sub>3</sub> H <sub>8</sub>
1												
2	3											
4	100	100	16.5	2.4				9.6				5.0
12			3.0				6.3	0.7				0.6
13			7.8					1.2			9.7	0.9
14			16.0			14	0.8	3.3				2.3
15			85.0									
16			100	1.8				4.7				7.2
17			1.2	26			2.8		18		16.0	
18												
20				100	100							
22					10.2					22.6	2.1	
25								3.8				0.8
26								22.2				9.8
27								33.4				43.5
28								100				61.0
29						100	100	20.0			13.0	100
30						0.7	1.2	22.2				21.7
31												
32									100			
34									0.4			
36										0.34		
37												4.6
38										0.06		6.7
39												20.2
40												2.6
41									100			15.0
42												4.8
43												22.8
44											100	24.0
45											1.2	0.8

## B.2. Sensitivity for QMA 200 [B.1]

Gas	Mass number of the basis peak	Sensitivity for basis peak $\times 10^{-5}$ [A/mbar]	Sum of the fragment ions $\times 10^{-5}$ [A/mbar]
He	4	6.4	-
Ne	20	6.4	7.2
Ar	40	24	30
Kr	84	6.8	17
H <sub>2</sub>	2	13	-
N <sub>2</sub>	28	20	23
CO	28	20	22
O <sub>2</sub>	32	14	16
CO <sub>2</sub>	44	13	19
CH <sub>4</sub>	16	28	54
C <sub>2</sub> H <sub>6</sub>	28	34	68
C <sub>3</sub> H <sub>8</sub>	29	26	74
C <sub>4</sub> H <sub>10</sub> (n)	43	22	74
C <sub>4</sub> H <sub>10</sub> (iso)	43	24	68
H <sub>2</sub> O	18	20	26

[B.1] *Fa. Balzers*: Partialdruckmessung in der Vakuumtechnik, Firmenbroschüre.



## **Erklärung**

Ich versichere, dass ich die vorliegende Arbeit ohne unzulässige Hilfe Dritter und ohne Benutzung anderer als der angegebenen Hilfsmittel angefertigt habe. Die aus anderen Quellen direkt oder indirekt übernommenen Daten und Konzepte sind unter Angabe der Quelle gekennzeichnet.

Bei der Auswahl und Auswertung folgenden Materials haben mir die nachstehend aufgeführten Personen in der jeweils beschriebenen Weise unentgeltlich geholfen:

1. Prof.-Dr. Oliver Ambacher - Betreuer,
2. Dr. -Ing. Volker Cimalla - Betreuer,
3. Dr. -Ing Gernot Ecke - Durchführung der AES Messungen,
4. Dr. -Ing Henry Romanus - Durchführung der SEM Messungen.

Weitere Personen waren an der inhaltlich-materiellen Erstellung der vorliegenden Arbeit nicht beteiligt. Insbesondere habe ich hierfür nicht die entgeltliche Hilfe von Vermittlungs- bzw. Beratungsdiensten (Promotionsberater oder anderer Personen) in Anspruch genommen. Niemand hat von mir unmittelbar oder mittelbar geldwerte Leistungen für Arbeiten erhalten, die im Zusammenhang mit dem Inhalte der vorgelegten Dissertation stehen.

Die Arbeit wurde bisher weder im In- noch im Ausland in gleicher oder ähnlicher Form einer Prüfungsbehörde vorgelegt.

Ich bin darauf hingewiesen worden, dass die Unrichtigkeit der vorstehenden Erklärung als Täuschungsversuch angesehen wird und den erfolglosen Abbruch des Promotionsverfahrens zu Folge hat.

**(Ort, Datum)**

Ilmenau, den 28.06.2007

**Unterschrift**

**Thesen zur Dissertation “Wide band gap materials and devices for NO<sub>x</sub>, H<sub>2</sub>, and O<sub>2</sub> gas sensing applications”, vorgelegt von Dipl.-Ing. Majdeddin Ali**

- 1) Selektive Erkennung von Stickoxiden (NO<sub>x</sub>) bei niedrigen Temperaturen durch den Einsatz von nanostrukturierten Metalloxid-Dünnschichten.
- 2) Die Reduzierung der Korngröße der Indiumoxid-Dünneschichten auf unter 10 nm hat erhebliche Auswirkung auf die Empfindlichkeit auf NO<sub>x</sub> von In<sub>2</sub>O<sub>3</sub>-basierenden resistiven Gassensoren.
- 3) Entwicklung und Optimierung von AlGaIn/GaN-basierenden HEMTs zum Nachweis von NO<sub>x</sub>-Gasen durch den Einsatz von nanostrukturierten In<sub>2</sub>O<sub>3</sub>-Dünnschichten als gassensitives Gate.
- 4) Charakterisierung und Weiterentwicklung von NO<sub>x</sub>-Gassensoren auf der Basis von SiC-basierten Feldeffekttransistoren mit verschiedenen Gemischen aus Metalloxiden für das Gate.
- 5) Die Zugabe einer entsprechenden Menge Metallzusätzen (Pt,Pd,...) beeinflusst die Empfindlichkeit, die Selektivität, und die Ansprech- und Erholzeiten von nanostrukturierten In<sub>2</sub>O<sub>3</sub>-basierenden Gassensoren.
- 6) Die Mikrostruktur der Gateelektrode von SiC-basierten FETs ist entscheidend für den Detektionsmechanismus und somit die entscheidenden Leistungsparameter des Sensors: Empfindlichkeit, Selektivität und Reaktionszeit.
- 7) In<sub>2</sub>O<sub>3</sub>-basierende resistive Gassensoren besitzen hohe Empfindlichkeit auf NO<sub>x</sub>, gute Selektivität, schnelle Reaktionszeit und relative lange Erholzeiten. Für eine effektive Entwicklung solcher NO<sub>x</sub>-Gassensoren ist eine Reduzierung der Erholzeit notwendig.
- 8) Die Mikrostruktur des Gates der Gassensoren (Schottky Dioden, MOS Kapazitäten, und SiC-basierte FETs) muss mit der Hilfe von TEM, AFM, und Röntgenbeugung optimiert werden.
- 9) Feuchtigkeit auf In<sub>2</sub>O<sub>3</sub>-basierenden resistiven Gassensoren und die Feldeffektgassensoren (Pt/GaN Schottky Dioden, MOS Kapazitäten, MOSFET Transistoren) in Anwesenheit von reduzierenden und oxidierenden Gasen reduziert die Empfindlichkeit.
- 10) Die Anwendung von Rhodium (Rh) als Gateelektrode von Schottky Dioden, MOS Kapazitäten und MOSFET Transistoren ermöglicht die Entwicklung von Gassensoren für die Detektion von Stickoxiden (NO<sub>x</sub>) bei niedrigen Temperaturen.

## Lebenslauf

**Vorname:** Majdeddin  
**Nachname** Ali  
**Geburtsdatum** 08.09.1976  
**Geburtsort** Homs, Syrien  
**Familienstand:** verheiratet  
**Nationalität:** syrisch  
**Anschrift:** Geschwister-Scholl-Str. 8d, 98693 Ilmenau

**1982 - 1991** Grund- und Mittelschule in Homs  
**1991 - 1994** Oberschule in Homs mit dem Abschluss:  
Reifezeugnis des naturwissenschaftlichen Zweiges  
**1994 - 1999** Studium an der Aleppo Universität in Aleppo mit dem Abschluss:  
Bachelor in Elektrotechnik und Elektronik  
**1999 - 2001** Studium an der Aleppo Universität in Aleppo mit dem Abschluss:  
Diplom Ingenieur in Elektrotechnik und Elektronik  
**02.2000 - 03.2001** wissenschaftlicher Mitarbeiter an der Al-Baath Universität in Homs  
**10.2001 - 04.2002** Deutschkurs (Grundstufe) an der TU Ilmenau  
**04.2002 - 07.2002** Deutschkurs (Mittelstufe) an der TU Dresden mit dem Abschluss:  
DSH Zeugnis  
**2003 - 2007** Doktorand und wissenschaftlicher Mitarbeiter am Fachgebiet  
Nanotechnologie, Institut für Mikro- und Nanoelektronik der  
Technischen Universität Ilmenau  
Anfertigung der Dissertation mit dem Thema: Wide band gap  
materials and devices for NO<sub>x</sub>, H<sub>2</sub> and O<sub>2</sub> gas sensing applications